

APPLIED COMPUTATIONAL ELECTROMAGNETICS SOCIETY JOURNAL

**Special Issue on Magnetic Bearing
and Magnetic Levitation**

Guest Editors:

Antonino Musolino, Rocco Rizzo,
and Luca Sani
DESTEC, University of Pisa, Italy

August 2017
Vol. 32 No. 8
ISSN 1054-4887

The ACES Journal is abstracted in INSPEC, in Engineering Index, DTIC, Science Citation Index Expanded, the Research Alert, and to Current Contents/Engineering, Computing & Technology.

The illustrations on the front cover have been obtained from the research groups at the Department of Electrical Engineering, The University of Mississippi.

THE APPLIED COMPUTATIONAL ELECTROMAGNETICS SOCIETY

<http://aces-society.org>

EDITOR-IN-CHIEF

Atef Elsherbeni

Colorado School of Mines, EE Dept.
Golden, CO 80401, USA

ASSOCIATE EDITORS-IN-CHIEF

Sami Barmada

University of Pisa. ESE Dept.
Pisa, Italy, 56122

Mohamed Bakr

McMaster University, ECE Dept.
Hamilton, ON, L8S 4K1, Canada

Antonio Musolino

University of Pisa
56126 Pisa, Italy

Mohammed Hadi

Kuwait University, EE Dept.
Safat, Kuwait

Abdul Arkadan

Marquette University, ECE Dept.
Milwaukee, WI 53201, USA

Marco Arjona López

La Laguna Institute of Technology
Torreon, Coahuila 27266, Mexico

Alistair Duffy

De Montfort University
Leicester, UK

Paolo Mezzanotte

University of Perugia
I-06125 Perugia, Italy

EDITORIAL ASSISTANTS

Matthew J. Inman

University of Mississippi, EE Dept.
University, MS 38677, USA

Shanell Lopez

Colorado School of Mines, EE Dept.
Golden, CO 80401, USA

EMERITUS EDITORS-IN-CHIEF

Duncan C. Baker

EE Dept. U. of Pretoria
0002 Pretoria, South Africa

Ahmed Kishk

Concordia University, ECS Dept.
Montreal, QC H3G 1M8, Canada

Allen Glisson

University of Mississippi, EE Dept.
University, MS 38677, USA

Robert M. Bevensen

Box 812
Alamo, CA 94507-0516, USA

David E. Stein

USAF Scientific Advisory Board
Washington, DC 20330, USA

EMERITUS ASSOCIATE EDITORS-IN-CHIEF

Yasushi Kanai

Niigata Inst. of Technology
Kashiwazaki, Japan

Alexander Yakovlev

University of Mississippi, EE Dept.
University, MS 38677, USA

Levent Gurel

Bilkent University
Ankara, Turkey

Mohamed Abouzahra

MIT Lincoln Laboratory
Lexington, MA, USA

Ozlem Kilic

Catholic University of America
Washington, DC 20064, USA

Erdem Topsakal

Mississippi State University, EE Dept.
Mississippi State, MS 39762, USA

Fan Yang

Tsinghua University, EE Dept.
Beijing 100084, China

EMERITUS EDITORIAL ASSISTANTS

Khaled ElMaghoub
Trimble Navigation/MIT
Boston, MA 02125, USA

Christina Bonnington
University of Mississippi, EE Dept.
University, MS 38677, USA

Anne Graham
University of Mississippi, EE Dept.
University, MS 38677, USA

Mohamed Al Sharkawy
Arab Academy for Science and Technology, ECE Dept.
Alexandria, Egypt

AUGUST 2017 REVIEWERS

Vincenzo di Dio
Efrén Díez Jiménez
Atef Z. Elsherbeni
Antonino Musolino

Rocco Rizzo
Luca Sani
Vitawat Sittakul

THE APPLIED COMPUTATIONAL ELECTROMAGNETICS SOCIETY
JOURNAL

Vol. 32 No. 8

August 2017

TABLE OF CONTENTS

| | |
|--|-----|
| Stability Analysis for a Flywheel Supported on Magnetic Bearings with Delayed Feedback Control Ling L. Zhang and Jian H. Huang | 642 |
| Nonlinear Position-Flux Zero-Bias Control for AMB System with Disturbance Arkadiusz Mystkowski and Ewa Pawluszewicz | 650 |
| Six-Axis Rotor Magnetic Suspension Principle for Permanent Magnet Synchronous Motor with Control of the Positive, Negative and Zero-Sequence Current Components Gael Messenger and Andreas Binder | 657 |
| Magnetic Propulsion Force Calculation of a 2-DoF Large Stroke Actuator for High-Precision Magnetic Levitation System Mousa Lahdo, Tom Ströhla, and Sergej Kovalev | 663 |
| Magneto-Mechanical Model of Passive Magnetic Axial Bearings versus the Eccentricity Error, Part I: Physical Mathematical Model Roberto Muscia | 670 |
| Magneto-Mechanical Model of Passive Magnetic Axial Bearings versus the Eccentricity Error, Part II: Application and Results Roberto Muscia | 678 |
| Performance of Yokeless Heteropolar Electrodynamic Bearings Corentin Dumont, Virginie Kluyskens, and Bruno Dehez..... | 685 |
| Modeling and Discussing an Interconnected Flux Magnetic Bearing Domingos F. B. David, José A. Santisteban, and Afonso C. Del Nero Gomes | 691 |
| Crucial Parameters and Optimization of High-Speed Bearingless Drives Hubert Mitterhofer and Siegfried Silber | 697 |
| Performance Tests of a Permanent Magnet Thrust Bearing for a Hydropower Synchronous Generator Test-Rig J. José Pérez-Loya, C. Johan D. Abrahamsson, Fredrik Evestedt, and Urban Lundin | 704 |

| | |
|---|-----|
| Vibration Isolation of Magnetic Suspended Platform with Double Closed-loop PID Control Mao Tang, Jin Zhou, Chaowu Jin, and Yuanping Xu | 712 |
| Sensorless Control for a Three-pole Active Magnetic Bearing System Shyh-Leh Chen and Kang-Yu Liu..... | 720 |
| Algorithm for Accounting for Inner Damping in a Computer Model of Dynamics of a Flexible Rotor on Active Magnetic Bearings Viktor F. Ovchinnikov, Mikhail Y. Nikolaev, and Vasily N. Litvinov | 726 |
| A Stepped Magnetic Suspension System (SMSS) Evgeni Frishman..... | 731 |
| Coupled Electromechanical Analysis of a Permanent-Magnet Bearing Vincenzo Di Dio and Luca Sani..... | 736 |

Stability Analysis for a Flywheel Supported on Magnetic Bearings with Delayed Feedback Control

Ling L. Zhang^{1,2} and Jian H. Huang¹

¹ College of Science
National University of Defense Technology, Changsha, Hunan, 410073, P. R. China
z002005@163.com, jhhuang32@nudt.edu.cn

² Department of Information Technology
Hunan Women's University, Changsha, Hunan, 410004, P. R. China
linglingmath@gmail.com

Abstract — In this paper, the model of the rotor dynamics of the flywheel is given using a rigid rotor supported on magnetic bearings. The phase lag of the control loop is modeled by a simple time delay. Limits of stability and the associated vibration frequencies are described in terms of nondimensional magnetic bearing stiffness and damping and nondimensional parameters of flywheel speed and time delay. Compared to the theoretical values, the simulation results and experimental measurements show the stability boundaries of the PD controller have the same qualitative tendencies.

Index Terms — Flywheel, magnetic bearing, PD controller, stability, time delay.

I. INTRODUCTION

As a new type of attitude control actuator of spacecraft, the magnetic levitation flywheel has many advantages such as no friction, high energy density, long life capability for up to 90 percent depth of discharge, peaking or pulse power capability and so on. Flywheels can be also an alternative to batteries and reaction wheels for the space system. Therefore magnetic levitation flywheel is an important direction of space technology development.

Since 1960's, developed countries have begun to work on the magnetic levitation flywheel [1-4]. After decades of development, the magnetic suspension flywheel technology have made great progress in the magnetic bearing structure design and optimization, the dynamics and mechanics analysis, modeling and model identification, control method, high performance sensors and power amplifier and so on; but there are still many technical difficulties. The vibration suppression control of maglev flywheel is a key to display the maglev flywheel space applications such as low loss, high precision, long life and other advantages [5].

The magnetic bearing system uses magnetic forces

to levitate the shaft between opposing magnetic poles. The rotor is attracted to one pole or the other pole and is inherently unstable, then the magnetic bearing system of a flywheel is stabilized with an active control system. In the process of eddy current proximity sensors, anti-alias filters, digital controller, re-construction filter, power amplifier, the magnetic bearing forces, each of the components involved in the magnetic bearing and control system has a time delay associated with the components. The total time delay is the sum of the individual time delays [6]. Time-delayed systems, which have been studied for various applications and control systems, may admit rich dynamics, including bifurcations and chaotic motions [7-11]. Hosek [12] developed a single-step automatic tuning algorithm as a means of increasing robustness against uncertainties and variations in the mechanical properties of the absorber arrangement. In studying the stability robustness of systems with multiple independent and uncertain delays, Fazelinia [13, 14] used the building hypersurfaces to arrive at the complete stability robustness picture in the domain of the delays. In recent years, some scholars began to study the characteristics of magnetic suspension flywheel from a dynamics behavior aspect, thus providing theoretical guidance to suppress vibration [15-19]. Based on decentralized PD controller, Polajzer [15] and Kascak [6] established the coupled dynamics model for the active magnetic bearing and analyzed the rotor critical speed using the Hopf bifurcation theory; Zhang [16] studied the global bifurcation and chaotic vibration for time-varying stiffness of the magnetic bearing, and discussed the bifurcation of the average equation using the normal form theory. Zhang [17] derived the averaged equation using the perturbation analysis method, then studied the transient and steady-state vibration response of the nonlinear magnetic bearing with the numerical simulation method. In these above research, only a few papers consider the effect of the time delay on the

stability of the magnetic flywheel.

According to the details of the flywheel mechanical design and the performance requirements, many different approaches have been used, varying from PID to modal or adaptive methods [20]. For example, Pichot [21] discussed the benefits of a notch filter based controller in comparison to a PID control for a large flywheel. Palazollo [22] developed a modal control system which was applied to a 60,000 rpm flywheel. In this paper, we will use a P-D controller which causes the magnetic bearing to produce two forces: one is proportional to the displacement and the other is proportional to the derivative of the displacement, the velocity.

This paper theoretically describes the stability boundaries of the magnetic bearing controller which levitates the high speed flywheel rotor. In Section 2, based on current stiffness and displacement stiffness of magnetic bearing, linear motion differential equation for maglev flywheel is established. Section 3 analyzes the stability limits and the associated vibration frequencies about two variables of these system parameters and control parameters. We give the simulation and experiment results in Section 4 and compare them to the theoretical values. Finally, the main conclusions drawn in this paper are summarized in Section 5.

II. FLYWHEEL STABILITY ANALYSIS

Figure 1 shows the rotor displacement of magnetic suspension flywheel with four axes and lateral axis of a flywheel [23]. The magnetic bearing sensors $s_1 - s_4$ are installed on the forward whirl and $s_5 - s_8$ on the backward whirl, and the distance of the up and down sensor planes is l . The magnetic bearing axis is OZ and the direction of radial axis points to the sensor measurement point. From Fig. 1, the displacement signals of the rotor $u_1 - u_8$ are measured by the eight sensor measurement points of the magnetic suspension flywheel with four axes. By the differential process, we can get the displacement signals of the flywheel rotor x_1, x_2, y_1 and y_2 , as follows:

$$x_1 = \frac{u_1 - u_3}{k_s}, \quad y_1 = \frac{u_2 - u_4}{k_s},$$

$$x_2 = \frac{u_5 - u_7}{k_s}, \quad y_2 = \frac{u_8 - u_6}{k_s},$$

where k_s represents the sensor gain.

Denote the displacement of the center of mass by x and y , then,

$$x = \frac{x_1 + x_2}{2}, \quad y = \frac{y_1 + y_2}{2}.$$

Denote the angles motion of the center of mass about X and Y axes respectively:

$$\alpha = \frac{y_2 - y_1}{l}, \quad \beta = \frac{x_2 - x_1}{l}.$$

In the definition of the angles, we use the upper plane parameters minus the under plane parameters, therefore β denotes the positive direction along the Y axis and α represents the negative direction along the X axis.

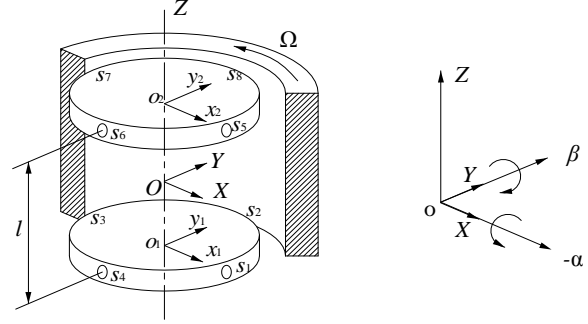


Fig. 1. The rotor displacement of magnetic suspension flywheel with four axes and lateral axis of a flywheel.

The control currents i_1, i_2, i_3, i_4 are applied to the port voltage of the electromagnet according to these four position signals, the induced forces are:

$$F_{x1} = k_x x_1 + k_i i_1, \quad F_{x2} = k_x x_2 + k_i i_2, \quad (1)$$

$$F_{y1} = k_x y_1 + k_i i_3, \quad F_{y2} = k_x y_2 + k_i i_4, \quad (2)$$

where k_x and k_i represent the control gains of the displacement and the current respectively.

The rotor dynamics of the flywheel can be described in terms of the motion of the center of mass and rotations about the center of mass. For small displacements the lateral motion is uncoupled from the axial motion. The lateral equations of motion of the center of mass are:

$$\frac{m}{2}(\ddot{x}_1 + \ddot{x}_2) = k_x x_1 + k_i i_1 + k_x x_2 + k_i i_2, \quad (3)$$

$$\frac{m}{2}(\ddot{y}_1 + \ddot{y}_2) = k_x y_1 + k_i i_3 + k_x y_2 + k_i i_4, \quad (4)$$

where m is the mass of the flywheel rotor.

For small rotations, the equations of angular motion about the center of mass are:

$$J_d \ddot{\alpha} + J_p \Omega \dot{\beta} = \frac{l}{2} [(k_x y_2 + k_i i_4) - (k_x y_1 + k_i i_3)], \quad (5)$$

$$J_d \ddot{\beta} - J_p \Omega \dot{\alpha} = \frac{l}{2} [(k_x x_2 + k_i i_2) - (k_x x_1 + k_i i_1)], \quad (6)$$

where Ω is a circular frequency of the flywheel, J_d and J_p are the transverse and polar moments of inertia respectively. $J_p \Omega \dot{\alpha}$ and $J_p \Omega \dot{\beta}$ are the gyro items.

Using P-D controller, the control currents are as follows:

$$i_1 = k_p x_1 + k_d \dot{x}_1, \quad i_2 = k_p x_2 + k_d \dot{x}_2, \quad (7)$$

$$i_3 = k_p y_1 + k_d \dot{y}_1, \quad i_4 = k_p y_2 + k_d \dot{y}_2, \quad (8)$$

where k_p and k_d are proportional and derivative feed-

back control gains respectively. Combining Equations (3)-(8), we have:

$$\frac{m}{2}(\ddot{x}_1 + \ddot{x}_2) = (k_x + k_i k_p)(x_1 + x_2) + k_i k_d(\dot{x}_1 + \dot{x}_2), \quad (9)$$

$$\frac{m}{2}(\ddot{y}_1 + \ddot{y}_2) = (k_x + k_i k_p)(y_1 + y_2) + k_i k_d(\dot{y}_1 + \dot{y}_2), \quad (10)$$

$$J_d \ddot{\alpha} + J_p \Omega \dot{\beta} = \frac{l^2}{2}(k_x + k_i k_p)\alpha + \frac{l^2}{2}k_i k_d \dot{\alpha}, \quad (11)$$

$$J_d \ddot{\beta} - J_p \Omega \dot{\alpha} = \frac{l^2}{2}(k_x + k_i k_p)\beta + \frac{l^2}{2}k_i k_d \dot{\beta}. \quad (12)$$

The solution for the motion of the center of mass and that for the rotation about the center of mass is of the same form, if the shaft speed Ω is set equal to zero [24, 25]. Therefore only motion of the rotation about the center of mass will be solved. The classical small signal stability analysis assumes an eigenvalue solution of the equation of motion.

A centralized controller decouples the motion of the center of mass and the rotation about the center of mass. The controller terms have a time delay associated with the various components in the control loop. Let $x(t) = [\alpha, \dot{\alpha}, \beta, \dot{\beta}]^T$, and the equations of motion become:

$$\dot{x}(t) = Px(t) + Qx(t - \tau), \quad (13)$$

where

$$P = \begin{pmatrix} 0 & 1 & 0 & 0 \\ \frac{l^2 k_x}{2J_d} & 0 & 0 & -\frac{J_p \Omega}{J_d} \\ 0 & 0 & 0 & 1 \\ 0 & \frac{J_p \Omega}{J_d} & \frac{l^2 k_x}{2J_d} & 0 \end{pmatrix}, Q = \begin{pmatrix} 0 & 0 & 0 & 0 \\ \frac{l^2 k_i k_p}{2J_d} & \frac{l^2 k_i k_d}{2J_d} & 0 & 0 \\ 0 & 0 & 0 & 0 \\ 0 & 0 & \frac{l^2 k_i k_p}{2J_d} & \frac{l^2 k_i k_d}{2J_d} \end{pmatrix}.$$

If the characteristic solution is assumed to be:

$$x(t) = Ae^{\lambda t}.$$

We only consider the first term of the corresponding characteristic Equation of (13):

$$J_d \lambda^2 - i\Omega J_p \lambda - \frac{l^2}{2}k_i k_d \lambda e^{-\lambda \tau} - \frac{l^2}{2}k_i k_p e^{-\lambda \tau} - \frac{l^2}{2}k_x = 0. \quad (14)$$

The characteristic equation does not have a real solution unless Ω is zero. If the eigenvalue is complex, let $\lambda = \mu + i\omega$. The vibrations grow in time and the system is unstable with $\mu > 0$ and the vibrations decay in time and the system is stable with $\mu < 0$. $\mu = 0$ defines the stability boundary. Substituting $\lambda = i\omega$ into [14] and separating the real and imaginary parts of [14], we obtain:

$$\begin{aligned} -J_d \omega^2 + \Omega J_p \omega - \frac{l^2}{2}k_x - \frac{l^2}{2}k_i k_p \cos \omega \tau - \frac{l^2}{2}k_i k_d \omega \sin \omega \tau &= 0 \\ \frac{l^2}{2}k_i k_p \sin \omega \tau - \frac{l^2}{2}k_i k_d \omega \cos \omega \tau &= 0. \end{aligned}$$

From the above imaginary and the real parts equations respectively, we can get the expression of τ

and Ω , that is Equations (15) and (16). By means of solving the real and the imaginary parts equations group, we would get the expressions of the control parameters k_p and k_d ((17) and (18)):

$$\tau = \frac{1}{\omega} \arctan \frac{k_d \omega}{k_p} + k\pi, k = 0, 1, 2, 3, \dots, \quad (15)$$

$$\Omega = \frac{1}{J_p \omega} (J_d \omega^2 + \frac{l^2}{2}(k_x + k_i(k_p \cos \omega \tau + k_d \omega \sin \omega \tau))), \quad (16)$$

$$k_p = -\frac{2}{l^2 k_i} \sqrt{(J_d \omega^2 - \Omega J_p \omega + \frac{l^2}{2}k_x)^2 - (\frac{l^2}{2}k_i k_d \omega)^2}, \quad (17)$$

$$k_d = -\frac{2}{l^2 k_i \omega} \sqrt{(J_d \omega^2 - \Omega J_p \omega + \frac{l^2}{2}k_x)^2 - (\frac{l^2}{2}k_i k_p)^2}. \quad (18)$$

Combing (15) with another one of (16), (17) and (18), we can get the stability boundary. For example, Equations (15) and (16) define the non-dimensional flywheel speed and the time delay at the transition between stable and unstable operation of the flywheel; Equations (15) and (17) describe curves in the k_p, τ parameter space which are parameterized by ω . Similarly, we can get any two variables from the transformation of the real part and the image part equations, for example,

$$k_d = \frac{2 \sin \omega \tau}{l^2 k_i \omega} (-J_d \omega^2 + \Omega J_p \omega - \frac{l^2}{2}k_x), k_p = k_d \omega \cot \omega \tau. \quad (19)$$

From (19), we can get the stability boundary for the flywheel in the k_p, k_d parameters space.

We will illustrate these results with two examples. The realistic values for the physical parameters are given in Table 1. For magnetic suspension flywheel system, the gyro effect is very small when the rotor is static or rotates at low speed. Therefore by dividing into four single degree of freedom, the appropriate stiffness and damping can make the rotor suspend stably in this case. In this paper, the rotate speed is about 20π rad/s, which is below the critical value, and then the effect of the rotor is omitted.

Table 1: Physical parameter values

| J_d | J_p | m | l | k_i | k_x | k_s |
|-----------------------|-----------------------|-----|--------|---------|-----------|---------|
| 0.01kg·m ² | 0.02kg·m ² | 4kg | 0.016m | -150N/A | 650000N/m | 8000V/m |

Case (1)

With the proportional gain $k_p = 0.7$ and the shaft speed $\Omega = 20\pi$, we use (15) and (18) with $k = 0$ to plot the time delay τ and the derivative gain k_d as ω is varied (Fig. 2). We do not show the curves with $k > 0$ as they all lie on the right of the corresponding curve with $k = 0$, and hence, do not form part of the stability boundary.

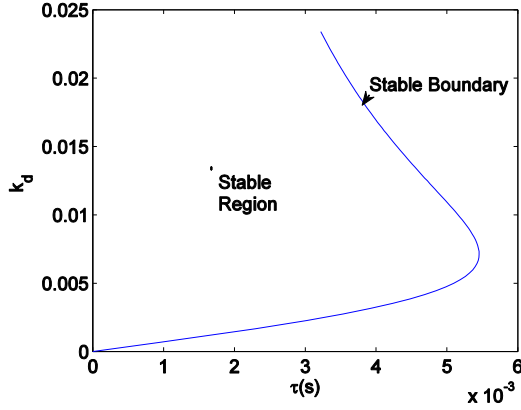


Fig. 2. The correlation of stability limits of a flywheel supported on magnetic bearings with time delay for $k_p = 0.7$, $\Omega = 20\pi$.

Case (2)

With the time delay $\tau = 0.001s$ and the shaft speed $\Omega = 20\pi$, we use (17) and (18) to plot the proportional gain k_p and the derivative gain k_d as ω is varied. Figure 3 shows both the static and dynamic stability for a magnetic flywheel with time delay. The proportional gain k_p for the static stability analysis is given by (14) with $\lambda = 0$. For both the static and dynamic stability analysis, if the real part of the eigenvalue μ is defined positive, the vibrations grow in time and the system is unstable. If μ is negative, the vibration will decay in time and the flywheel system is stable. $\mu = 0$ defines the stability boundary.

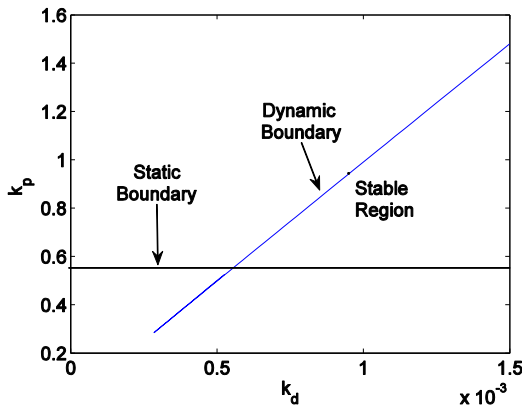


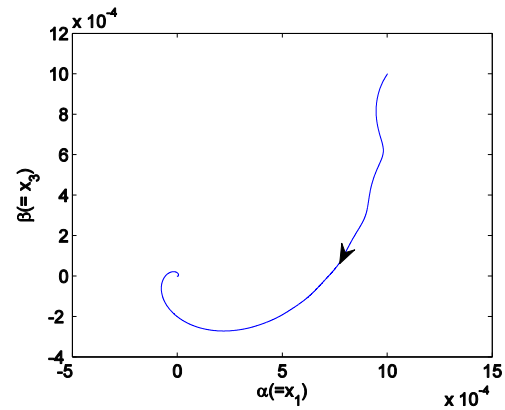
Fig. 3. The correlation of stability limits frequency of a flywheel supported on magnetic bearings with time delay for $\tau = 0.001s$, $\Omega = 20\pi$.

III. NUMERICAL SIMULATIONS

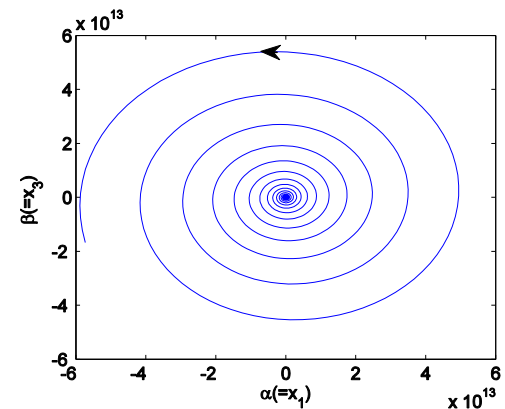
In this section, we consider the flywheel system (11)-(12) with the physical parameters given in Table 1.

According to the two examples in Section II (Fig. 2 and Fig. 3), we will compare these theoretical results with numerical simulations of the system (11)-(12). Using the DDE Toolbox for Matlab, we can get the numerical solutions for the angular motions α, β of the center of mass about X and Y axes and draw their trajectory.

Together with (15) and (18), if the time delay and the derivative gain change, we will study the stability of the flywheel system with $k_p = 0.7$, $\Omega = 20\pi$. Choosing the point $(\tau, k_d) = (0.004, 0.01)$ which lies in the stable region of Fig. 2, from Fig. 4 (a), the angular motions α, β of the center of mass about X and Y axes approach the trivial solution, indicating that it is asymptotically stable. Then we adjust the parameter k_d as 0.02 and the time delay τ remains the same, that is the point $(\tau, k_d) = (0.004, 0.02)$ is out of the stable region of Fig. 2, the values of α, β grow quickly, which suggests that the flywheel system is unstable from Fig. 4 (b). If the derivative gain $k_d = 0.02$ remains unchanged and the time delay changes as $\tau = 0.003s$, that is the point $(\tau, k_d) = (0.003, 0.02)$ lies in the stable region of Fig. 2 again, the flywheel system will restore to the stable operation from Fig. 4 (c).



(a) $\tau = 0.004s$, $k_d = 0.01$



(b) $\tau = 0.004s$, $k_d = 0.02$

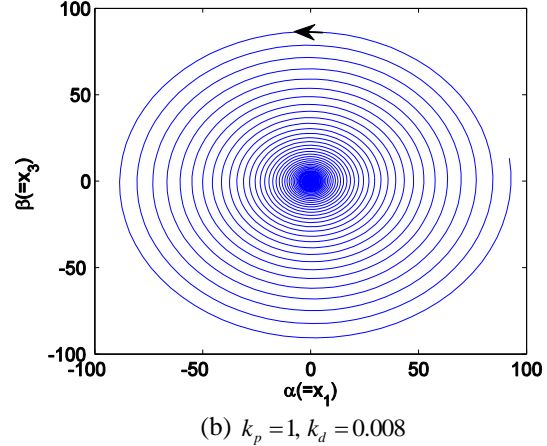
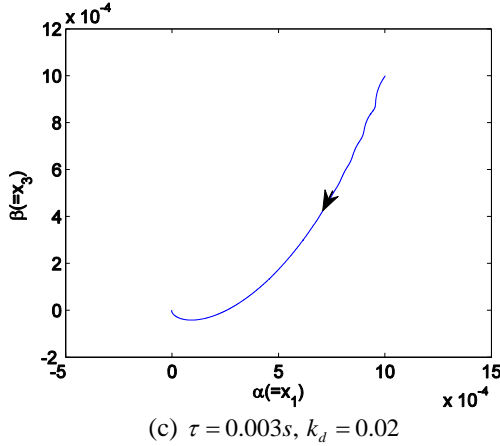


Fig. 4. Numerical simulations of the maglev flywheel system (13), τ and k_d as indicated. (a), (b), and (c) are (pseudo) phase portraits of the angular motions (α and β) of the center of mass about X and Y axes.

In another example of Section II, with (19), $\tau = 0.001s$, $\Omega = 20\pi$. Choosing the point $(k_p, k_d) = (1, 0.02)$ which lies in the stable region of Fig. 3, from Fig. 5 (a), the angular motions α, β of the center of mass about X and Y axes approach the trivial solution, indicating that the equilibrium point is stable. Then we adjust the parameter k_p as 0.008 and the derivative gain k_d remains unchanged, that is the point $(k_p, k_d) = (1, 0.008)$ is out of the stable region of Fig. 3, the values of α, β grow rapidly, which suggests that the flywheel system loses the stability from Fig. 5 (b). If the derivative gain $k_d = 0.008$ remains the same, the proportional gain changes as $k_p = 0.6$, that is the point $(k_p, k_d) = (0.6, 0.008)$ lies in the stable region of Fig. 3 again, the flywheel system will restore the stability from Fig. 5 (c).

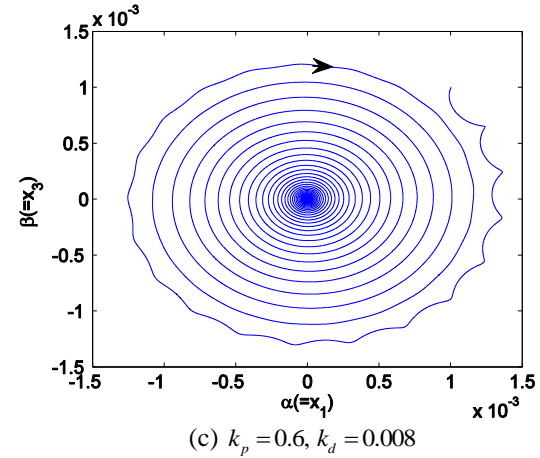
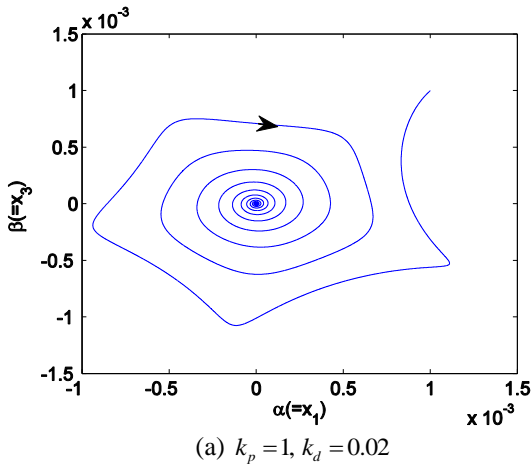


Fig. 5. Numerical simulations of the maglev flywheel system (13). k_p and k_d as indicated. (a), (b), and (c) are (pseudo) phase portraits of the angular motions (α and β) of the center of mass about X and Y axes.

Thus, the numerical simulations agree with the stable boundary diagrams of Figs. 2, 3 as predicted by the theory. When the values of the time delay, the shaft speed and the control parameters fall in the stable region (Fig. 2 and Fig. 3), the numerical solutions for the magnetic flywheel system will tend to be stable (Figs. 4 (a), (c) and Figs. 5 (a), (c)). If these values in the unstable region, the numerical solutions for the magnetic flywheel system will lose their stability (Fig. 4 (b) and Fig. 5 (b)). These results suggest that the magnetic flywheel will remain stable in the experiment and practical application by choosing the appropriate parameters values according the theoretical results.

IV. EXPERIMENT

Test was performed in Changsha. We will use the physical parameters given in Table 1 and choose $k_p = 0.07$, $\Omega = 20\pi$.

For a given time delay, the derivative gain is varied noting the region of stable operation. The measured result for the forward whirl is shown as Fig. 6 (a), which describes the correlation of stability data of the forward whirl shown on Fig. 2. The region of stable operation is limited at small time delay by the derivative gain. That is, there is no stable region of operation if the time delay at a high value. Then using $\tau = 0.001$, $\Omega = 20\pi$, for a given derivative gain, the proportional gain is varied noting the region of stable operation. The measured result Fig. 6 (b) shows the correlation of stability data of the forward whirl shown on Fig. 3. There is no stable region of operation if the proportional gain at a low value. The measured result for the forward whirl is shown in Fig. 6. The experiment results have the similar shaped regions of stability compared to the theoretical simulation.

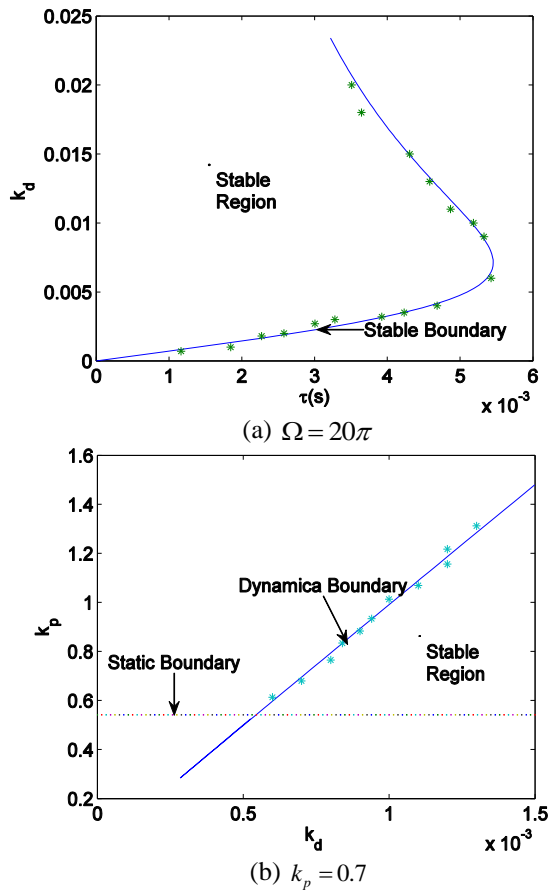


Fig. 6. The measured result for the forward whirl compared to the theoretical simulation.

We have tried different pairs of k_p and Ω and the shapes of the curves defined by (15) and (18) and their behaviors as k_p and Ω are varied are similar to what is shown in Fig. 7. Figure 7 (a) shows the stability region

for Ω fixed and varying k_p . Increasing the value of k_p decreases the size of the stability region. Figure 7 (b) shows the stability region for k_p fixed and varying Ω . Increasing Ω decreases the size of the stability region.

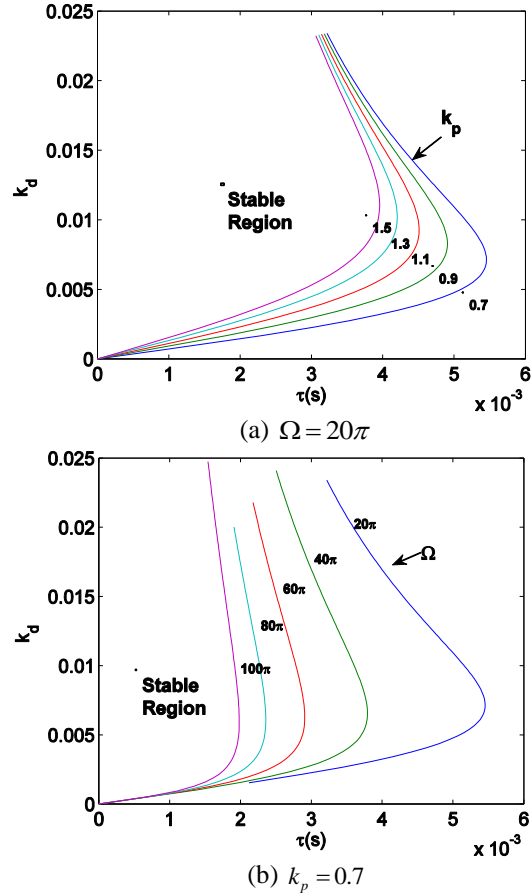


Fig.7. The stability map for a flywheel supported on magnetic bearings with time delay for various values of the proportional gain k_p or the shaft speed Ω .

Note that in all cases, the range of values of k_d for which the flywheel system is stable decreases as τ increases and there is a critical value of τ , τ_c , such that the equilibrium point is unstable for any k_d if $\tau > \tau_c$, where τ_c is the τ value at the maximum.

V. CONCLUSIONS

In this paper, the stability boundaries of the suspension system of a magnetic flywheel with time-delayed proportional, derivative feedback are studied.

According to the characteristic equation of the flywheel system, we get the stable region in the any two parameters spaces of τ, Ω, k_p, k_d . For example, a set of values of the time delay and the derivative feedback gain

for which the flywheel system is stable can then be described. For the parameter values that we investigated, the larger the proportional gain, the smaller the region of the stability; the larger the shaft speed, the smaller the region of the stability. At the same time, we should also control the time delay of the system, if the time delay larger than the critical value, the equilibrium position is unstable for any derivative gain. Numerical simulations of the full model confirmed the predictions of the analysis. Experimental measurements showed that the results of the modeling have the same qualitative tendencies as theoretical analysis.

To completely understand the dynamic behavior of the flywheel system, further research needs be carried out. Although the magnetic flywheel has the similar magnetic bearing system with the magnetic train [26, 27], but the principle of the flywheel is more complicated for considering the motion of the center mass and rotations about the center of mass. In the next step, with DR (delayed resonator) and CTCR (Cluster Treatment of Characteristic Roots) [12-14], we will carry up a more detailed stability treatment of delayed flywheel system to increase robustness against uncertainties and variations. Therefore it would be interesting to extend the dynamical behaviors research of the flywheel system such as Hopf bifurcation, chaotic behavior and so on.

ACKNOWLEDGMENT

This work was supported by National Natural Science Foundation of China (11301173) and Natural Science Foundation of Hunan Province (14JJ3143), Scientific Research Key Project of Hunan Provincial Education Department (16A106) and China Postdoctoral Science Foundation (2014M562651, 2016T90977).

REFERENCES

- [1] P. Poubeau, *Satellite momentum wheel*, United States Patent: 3955858, May 1976.
- [2] S. Michael, R. Thomas, and B. Enrico, "The challenges of miniaturisation for a magnetic bearing wheel," *Proceedings of 9th European Space Mechanisms and Tribology Symposium*, Liege, Belgium, pp. 17-24, Sep. 2001.
- [3] G. Bernd, E. Markus, and K. R. Hans, "Gimballing magnetic bearing reaction wheel with digital controller," *Proceedings of the 11th European Space Mechanisms and Tribology Symposium*, Lucerne, Switzerland, pp. 1-6, Sep. 2005.
- [4] B. C. Han, "Modeling and analysis of novel integrated radial hybrid magnetic bearing for magnetic bearing reaction wheel," *Chinese Journal of Mechanical Engineering*, vol. 23, pp. 655-662, Nov. 2010.
- [5] L. Y. Xiang, S. G. Zuo, and L. C. He, "Electric vehicles to reduce vibration caused by the radial force," *The Applied Computational Electromagnetics Society*, vol. 29, pp. 340-350, Sep. 2014.
- [6] A. F. Kacsak, G. V. Brown, and Q. H. Jansen, "Stability limits of a PD controller for a flywheel supported on rigid rotor and magnetic bearings," *AIAA Guidance, Navigation and Control Conference and Exhibition*, San Francisco, California, pp. 5956, Aug. 2005.
- [7] J. Wu, *Theory and Applications of Partial Functional Differential Equations*. Springer, New York, 1996.
- [8] S. Guo, Y. Chen, and J. Wu, "Two-parameter bifurcations in a network of two neurons with multiple delays," *J. Differential Equations*, vol. 244, pp. 444-486, Jan. 2008.
- [9] B. Hassard, N. Kazarinoff, and Y. Wan, *Theory and Applications of Hopf Bifurcation*. Cambridge University Press, Cambridge, 1981.
- [10] O. M. Ramahi, "Analysis of conventional and novel delay lines: A numerical study," *The Applied Computational Electromagnetics Society*, vol. 18, pp. 181-190, Aug. 2003.
- [11] P. Orlov, T. Gazizov, and A. Zabolotsky, "Short pulse propagation along microstrip meander delay lines with design constraints: Comparative analysis of the quasi-static and electromagnetic approaches," *The Applied Computational Electromagnetics Society*, vol. 31, pp. 238-243, Mar. 2016.
- [12] M. Hosek and N. Olgac, "A single-step automatic tuning algorithm for the delayed resonator vibration absorber," *IEEE Transactions on Mechatronics*, vol. 7, pp. 245-255, July 2002.
- [13] H. Fazelinia, R. Sipahi, and N. Olgac, "Stability analysis of multiple time delayed systems using 'building block' concept," *Proceeding of the 2006 American Control Conference*, Minnesota, USA pp. 2393-2398, 2006.
- [14] H. Fazelinia, R. Sipahi, and N. Olgac, "Stability robustness analysis of multiple time-delayed systems using 'building block' concept," *IEEE Transactions on Automatic Control*, vol. 52, pp. 799-810, May 2007.
- [15] B. Polajzer, J. Ritonja, and G. Stumberger, "Decentralized PI/PD position control for active magnetic bearings," *Electrical Engineering*, vol. 89, pp. 53-59, Oct. 2006.
- [16] W. Zhang, J. W. Zu, and F. X. Wang, "Global bifurcations and chaos for a rotor-active magnetic bearing system with time-varying stiffness," *Chaos Solitons & Fractals*, vol. 35, pp. 586-608, May 2008.
- [17] W. Zhang and J. W. Zu, "Transient and steady nonlinear for a rotor-active magnetic bearing system with time-varying stiffness," *Chaos Solitons & Fractals*, vol. 38, pp. 1152-1167, Feb. 2008.

- [18] M. P. Aghababa and H. P. Aghababa, "Chaos suppression of rotational machine systems via finite-time control method," *Nonlinear Dynamics*, vol. 69, pp. 1881-1888, Apr. 2012.
- [19] H. C. Gui, L. Jin, and S. J. Xu, "On the attitude stabilization of a rigid spacecraft using two skew control moment gyros," *Nonlinear Dynamics*, vol. 79, pp. 2079-2097, Mar. 2015.
- [20] Z. W. Liu, R. S. Chen, and J. Q. Chen, "Using adaptive cross approximation for efficient calculation of monostatic scattering with multiple incident angles," *The Applied Computational Electromagnetics Society*, vol. 26, pp. 325-333, Apr. 2011.
- [21] M. A. Pichot, J. P. Kajs, and J. P. Murhy, "Active magnetic bearings for energy storage systems for combat vehicles," *IEEE Transactions on Magnetics*, vol. 37, pp. 318-323, Jan. 2001.
- [22] A. Palazzolo, *System and methods for controlling suspension using a magnetic field*, U.S. Patent: 6323614B1, 2001.
- [23] X. F. Chen, *Research on vibration analysis and inhibitory control of magnetic suspension flywheel system*, Ph.D., National University of Defense Technology, 2011.
- [24] H. W. Wang and J. Q. Liu, "Stability and bifurcation analysis in a magnetic bearing system with time delays," *Chaos, Solitons & Fractals*, vol. 26, pp. 813-825, Mar. 2005.
- [25] J. C. Ji, "Stability and Hopf bifurcation of a magnetic bearing system with time delays," *Journal of Sound and Vibration*, vol. 259, pp. 845-856, Apr. 2003.
- [26] L. L. Zhang, S. A. Campbell, and L. H. Huang, "Nonlinear analysis of a maglev system with time-delayed feedback control," *Physica D*, vol. 240, pp. 1761-1770, July 2011.
- [27] L. L. Zhang, Z. Z. Zhang, and L. H. Huang, "Double Hopf bifurcation of time-delayed feedback control for maglev system," *Nonlinear Dynamics*, vol. 69, pp. 961-967, Mar. 2012.



Ling-Ling Zhang was born in 1982. She received the M.Sc. and Ph.D. degrees in Mathematics from Hunan University, China, in 2007 and 2010, respectively. She is a Postdoctoral Fellow from 2014 to 2017 in College of Science from National University of Defense Technology. She is currently an Associated Professor of Hunan Women's University. Her research interest is the stability and control of maglev system.



Jian-Hua Huang was born in 1968. He received the M.Sc. and Ph.D. degrees in Mathematics from Central China Normal University, China, in 1996 and 2002, respectively. He is currently a Professor of National University of Defense Technology. His main research interests are random dynamical systems and infinite dimensional dynamical systems.

Nonlinear Position-Flux Zero-Bias Control for AMB System with Disturbance

Arkadiusz Mystkowski* and Ewa Pawluszewicz

Bialystok University of Technology, Department of Automatic Control and Robotics, Bialystok, Poland
a.mystkowski@pb.edu.pl, e.pawluszewicz@pb.edu.pl

Abstract — This study presents two novel nonlinear controllers for a single one-degree-of-freedom (1-DOF) active magnetic bearing (AMB) system operated in zero-bias mode with externally bounded disturbance. Recently developed controllers are complicated and inherently difficult to implement. The simple and low-order controllers proposed in this paper are designed using nonlinear feedback tools, including Lyapunov-based techniques and control Lyapunov functions (CLFs). The control objective is to globally stabilize the mass position of the nonlinear flux-controlled AMB system with control voltage saturation. The zero-bias AMB control model is derived from the voltage switching strategy. The developed CLF-based controllers are verified by numerical calculations.

Index Terms — Active magnetic bearing, control Lyapunov function, nonlinear flux controller, zero-bias control.

I. INTRODUCTION

The active magnetic bearing (AMB) control system with classical large bias current is a well-known linear control problem, and as a result, PID controllers, \mathcal{H}_∞ -based control and μ -synthesis methods can be applied, e.g., see author references: [1, 2, 3]. However, large bias-current or a bias-flux implies power loss, where the loss mechanisms are generally proportional to the square of the electromagnetic force. Moreover, a large bias causes heat dissipation and further changes the electromagnets' parameters. In order to improve the energy efficiency of the AMB system, zero-bias flux control can be applied. In this system, the dynamics become strongly nonlinear. Therefore, nonlinear control methods can be applied in order to design a stable AMB system with zero-bias or low-bias [4÷11]. All of the aforementioned approaches are fundamentally based on position-current or position-flux state feedbacks.

In particular, a nonlinear and uncertain flux-controlled AMB system operated with zero-bias was considered in paper [10]. The major parametric uncertainties of the AMB such as: magnetic saturation perturbation, bias flux (preomagnetization) and uncertain losses increase the nonlinearity of the AMB system. In

response to this problem, paper [10] presents the robust stability and robustness analyses of a nonlinear closed-loop AMB system with inherent uncertainties. The so-called *small gain theorem* can be used to calculate the robust stability of an uncertain AMB system [10].

Flux-based control with zero-bias increases the nonlinearity of an AMB system. Nonlinear control approaches intended for AMBs have been developed [12, 13]. In the last century, stability concepts pertaining to nonlinear systems were formulated by Lyapunov and were first expounded upon by Malkin in 1952 [14]. Later, Lyapunov functions were applied, for example, to the passivity theorem and to dissipative systems in 1972 [15] as well as to solving optimal and inverse optimal control problems. The Lyapunov technique has been extended to control systems in [16÷19], for example. Since characterizing stability in terms of the smooth Lyapunov function is not possible in some cases, the stabilizing feedback design should be used. This is the main reason for using the so-called control Lyapunov function (CLF). Its concept was introduced by Artstein and Sontag in 1983 [20, 21]. The idea of CLF-based control is to select a Lyapunov function $V(x)$ and then to try to find a feedback control $u(x)$ that renders $dV(x, u)/dt$, defined negatively. Thus, by choosing a suitable $V(x)$, and when $V(x)$ is the CLF, we can find a stabilizing control law $u(x)$ for the system feedback [22]. The CLF-based control concept was extended to dynamic systems with known disturbance [23÷25], where $V(x)$ is the RCLF (a robust CLF), if, for a bounded disturbance, ω ensures that $\dot{V}(x, u, \omega) < 0$ [17, 26]. The linear \mathcal{H}_∞ control method was used to solve a disturbance attenuation problem in a nonlinear system which is analogous to the RCLF [27, 28].

The main aim of the present work is to show simple nonlinear controllers that contribute improvements to flux-controlled AMB systems operated in zero-bias mode in comparison with existing approaches. The proposed nonlinear control laws are based on the control Lyapunov function (CLF) and are effective in AMB zero-bias control systems with control voltage saturation. However, the control law based on Artstein-Sontag's theorem includes Lie derivative terms and leads to a complex solution [29]. The main advantages of the

proposed controllers, if compared with CLF based on Artstein-Sontag's theorem, are that they are simpler and inherently easier to implement in low-power micro-controller AMB hardware. Performed simulations show that simple low-order controllers based on CLF give satisfactory results in comparison with complex solutions based on Artstein-Sontag's theorem [29]. In comparison with previous solutions [29, 30], the obtained control laws ensure similar or even better transient responses and better disturbance attenuation.

The paper is organized as follows. Section 2 presents a simplified one-dimensional active magnetic bearing (AMB) system. Section 3 formulates conditions for zero-bias flux-feedback control and flux-switching strategy. Section 4 proposes Lyapunov-based controllers and describes control law design functions. Section 5 provides numerical examples which prove the control laws proposed in Section 4. Finally, Section 6 closes the paper with some concluding remarks.

II. THE 1-DOF AMB MODEL

Let us consider the simplified 1-DOF (one-degree-of-freedom) AMB model that consists of two opposite and presumably identical electromagnetic actuators (electromagnets), which generate attractive forces, F_1 and F_2 , on the rotor [31]. To control the position x of the rotor mass m to the stable state $x=0$, the voltage inputs of the electromagnets, v_1 and v_2 , are used to design the control law, see Fig. 1.

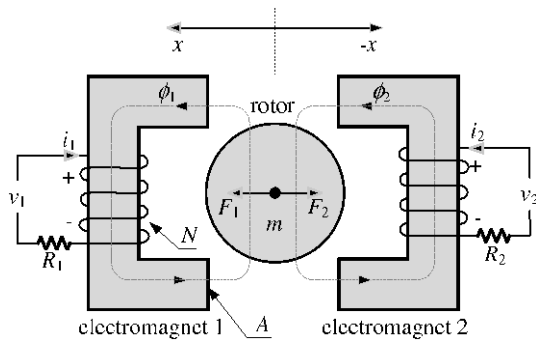


Fig. 1. Simplified one-dimensional AMB.

The 1-DOF model of the AMB is nonlinear where mechanical and electrical dynamics are coupled. Consider Fig. 1, in which, neglecting gravity (for the horizontal rotor control direction), the dynamic equation is given by [31]:

$$F_j = \frac{\cos \alpha}{\mu_0 A} \Phi_j^2, \quad \text{for } j = 1, 2, \quad (1)$$

where F_j is the total force generated by each electromagnet, Φ_j is the total magnetic flux through each active coil, A is the cross-sectional area of each electromagnet pole, α is the angle at which

electromagnetic force acts, and μ_0 is the permeability of free space ($=1.25 \times 10^{-6}$ H/m).

The total flux generated by the j -th electromagnet is $\Phi_j = \Phi_0 + \phi_j$. In the case of zero-bias operation, the bias flux Φ_0 equals zero, and the total flux equals control flux ϕ_j . Then, we define the *generalized control flux* as:

$$\phi := \phi_1 - \phi_2$$

$$\phi := \frac{1}{N} \left(\int_0^t (v_1 - Ri_1) dt - \int_0^t (v_2 - Ri_2) dt \right), \quad (2)$$

where N denotes the number of turns of the coil of each electromagnet.

If $\Phi_0 = 0$, then according to (1), the mass motion equation is given by:

$$\frac{d^2}{dt^2} x = \frac{\cos \alpha}{\mu_0 mA} (\phi_1^2 - \phi_2^2). \quad (3)$$

The electrical dynamics of the AMB system are given by the governing equation [31]:

$$v_j = N \frac{d\phi_j}{dt} + Ri_j, \quad j = 1, 2, \quad (4)$$

where R is the electromagnet's resistance. Then Eq. (4) can be rewritten in an equivalent form as:

$$\dot{\Phi}_j = \dot{\phi}_j = \frac{1}{N} (v_j - Ri_j), \quad j = 1, 2. \quad (5)$$

III. ZERO-BIAS FLUX-FEEDBACK CONTROL

In the case of zero-bias control, the nonlinear flux/force characteristic has a dead zone near the origin (low dynamic response of the AMB) [32]. This means that the slope of the magnetic force vs. flux curve near the origin is zero, and we need a large change in flux in order to generate a small control force. According to (5), the flux depends on the control voltage and current. Voltage commands are limited in real applications and voltage saturation is another problem. In short, zero-bias nonlinear control with voltage saturation is a challenging task.

In zero-bias control, the control force F_j depends on control flux ϕ_j which fulfils the following condition of the switching scheme [29, 30]:

$$\begin{aligned} \phi &= \phi_1, \quad \phi_2 = 0 \quad \text{when } \phi \geq 0 \\ \phi &= -\phi_2, \quad \phi_1 = 0 \quad \text{when } \phi < 0 \end{aligned} \quad (6)$$

The ϕ described by (6) is called a *generalized flux*. The switching scheme allows us to minimize control fluxes ϕ_1 and ϕ_2 , since at least one of the control fluxes is zero at the starting time. This means that at least one of the electromagnets is inactive at any given instant of time. The system minimizes energy and power losses [31, 33].

For zero-bias, based on (3), according to the generalized complementary flux condition (8), the total generalized attractive force is given by:

$$F(\Phi) = \frac{\Phi |\Phi|}{\mu_0 mA}, \quad (7)$$

where generalized attractive force $F = F_1 - F_2$. The system's nonlinearity in (7) is given by *non-decreasing function*

$\eta(\Phi)=\Phi|\Phi|$. The general form of the flux-based control law is given by:

$$u_\phi = -f_\phi(\phi_r - \phi), \quad (8)$$

where ϕ_r is the flux reference and f_ϕ is a nonlinear control function which also ensures bounds of ϕ_j such that:

$$\lim_{t \rightarrow \infty} \phi_j(t) = \min\{\phi_1(0), \phi_2(0)\}. \quad (9)$$

Fluxes ϕ_1 and ϕ_2 remain bounded, and condition (9) represents convergence of ϕ_j , which is ensured if system (3)–(4) is asymptotically stable. The nonlinear and fast dynamic flux controller generates the required fluxes in the AMB's structure due to nonlinear characteristics of controlled flux ϕ versus generated total force F . Typically, when cascaded control is applied, the linearizing flux controller works in the inner control flux loop. The transfer function for the low level control feedback rule in the s -domain is given by:

$$P(s) = \frac{\phi(s)}{\phi_r(s)}. \quad (10)$$

The AMB closed-loop system (10) is used in the case of local force control in electromagnets. However, in this work, we present not a local, but a global nonlinear rotor position controller.

From the simple analysis presented above, it follows that, for the dynamics of system (3) with the *generalized control flux* given by (2), under switching strategy (6), and with state coordinates defined as:

$$x_1 = x, \quad x_2 = \dot{x}, \quad x_3 = \phi, \quad (11)$$

then the state-space AMB dynamic model is given by:

$$\begin{cases} \frac{d}{dt} x_1 = x_2 \\ \frac{d}{dt} x_2 = \frac{\cos \alpha}{\mu_0 m A} |x_3| x_3, \\ \frac{d}{dt} x_3 = \frac{1}{N} (v - Ri) \end{cases} \quad (12)$$

where $v = v_1 - v_2$ is the *generalized control voltage* and $i = i_1 - i_2$ is the *generalized current*.

IV. LYAPUNOV-BASED CONTROL

A. Problem statement - AMB model with disturbance

In this section we will find the CLF that will make the AMB system globally stable with respect to additive measurement disturbances. It is well known that bounded disturbances in a nonlinear system can cause severe forms of instability [24]. Moreover, a nonlinear control law that guarantees global stability of a nonlinear system under perfect state feedback will not ensure global robustness to state measurement disturbances. There are many classes of systems for which stabilizability is preserved in the presence of state measurement disturbances, e.g., strict feedback systems [34].

In order to simplify notation, and to work with a system having the minimum number of parameters, let us introduce the following non-dimensionalized state and control variables along with a non-dimensionalized time [29, 30]:

$$\begin{aligned} x_1 &:= \frac{x}{g_0}, \quad x_2 := \frac{\dot{x}}{\Phi_{\text{sat}} \sqrt{g_0 / \mu_0 m A}}, \quad x_3 := \frac{\phi}{\Phi_{\text{sat}}} \\ u &:= \frac{v \sqrt{g_0 \mu_0 m A}}{N \Phi_{\text{sat}}^2}, \quad \tau := t \frac{\Phi_{\text{sat}}}{\sqrt{g_0 \mu_0 m A}}, \quad w = \frac{\omega}{\omega_{\text{max}}} \end{aligned} \quad (13)$$

where g_0 is the nominal air gap (clearance), u – the non-dimensionalized control variable, Φ_{sat} – the saturation flux, τ denotes non-dimensionalized time, w is an external non-dimensionalized input, and ω is the bounded disturbance with its maximum value ω_{max} .

Importantly, the AMB system parameters in (13) are constant and their nominal values and absolute boundary values are given in Table 1.

Let us assume that w is a known bounded disturbance and impact via state x_1 to the AMB system. Then, in accordance with (13), the model of the AMB system with disturbance input $w \in \mathbb{R}$ is written in the state-space:

$$\begin{cases} \frac{d}{d\tau} x_1 = x_2 + x_1 w \\ \frac{d}{d\tau} x_2 = x_3 |x_3|, \\ \frac{d}{d\tau} x_3 = u \end{cases} \quad (14)$$

where x_1, x_2, x_3 are defined by (13) and u is a control input. In this way, variables x_1, x_2 and x_3 indirectly relate to the position x [m] of the rotor mass, velocity \dot{x} [m/s] and electromagnetic flux ϕ [Wb], respectively.

However, the disturbance w and the control voltage are always limited in the AMB system. Moreover, in AMB applications, since the electromagnet coils are typically driven by power amplifiers, these amplifiers must be configured to operate in voltage mode or current mode with saturation. In a real AMB system, the voltage input is bounded as $u(t) = \text{sat}(v(t))$, where $\text{sat}(v(t))$ is the saturation function of voltage $v(t)$ defined here as:

$$\text{sat}(v(t)) = \begin{cases} -v_{\text{lim}} & \text{if } v(t) < -v_{\text{lim}} \\ v(t) & \text{if } -v_{\text{lim}} \leq v(t) \leq v_{\text{lim}}, \\ v_{\text{lim}} & \text{if } v(t) > v_{\text{lim}} \end{cases}$$

where v_{lim} is the voltage input limit and refers to v_{sat} (saturation voltage value) given in Table 1.

B. CLF for AMB with disturbance

Note that system (14) is the control affine system of the form:

$$\dot{x} = f(x) + g(x)u + h(x)w, \quad (15)$$

where $u \in \mathbb{R}$ – control input, w – bounded independent disturbance input, and vector fields $f: \mathbb{R}^3 \rightarrow \mathbb{R}^3$ and $g: \mathbb{R}^3 \rightarrow \mathbb{R}^3, h: \mathbb{R}^3 \rightarrow \mathbb{R}^3$ are given by $f(x) = [x_2 \quad x_3^{[2]} \quad 0]^T$, $g(x) = [0 \quad 0 \quad 1]^T$, $h(x) = [x_1 \quad 0 \quad 0]^T$ with $x_3^{[2]} := x_3^2 \text{sgn}(x_3) = x_3 |x_3|$.

Recall that system,

$$\dot{x} = f(x) + g(x)u, \quad (16)$$

is asymptotically stabilizable with respect to the equilibrium pair (x_0, u_0) , where $x_0 = x(0)$, if there exists a feedback law $u = \alpha(x)$, $\alpha(x_0) = u_0$, defined on a

neighbourhood U_{x_0} of x_0 such that α is continuously differentiable on $U_{x_0} \setminus \{x_0\}$, for which the closed-loop system,

$$\dot{x}(t) = (f + \alpha g)(x(t)), \quad (17)$$

is locally asymptotically stable (with respect to x_0). Recall also that (see [16, 21]) a real continuous function defined on open set $X \subset \mathbb{R}^n$ is a local control Lyapunov function for system (17) (relative to the equilibrium state x_0), if it satisfies the following properties:

- (i) V is proper at x_0 , i.e., $\{x \in X: V(x) \leq \varepsilon\}$ is a compact subset of some neighborhood U_{x_0} of x_0 for each sufficiently small $\varepsilon > 0$.
- (ii) V is positive defined on U_{x_0} : $V(x_0) = 0$ and $V(x) > 0$ for each $x \in U_{x_0}$, $x \neq x_0$.
- (iii) $L_f V(x) < 0$ for each $x \neq x_0$, $x \in U_{x_0}$, such that $L_g V(x) = 0$, where $L_g V(x) := \nabla V(x) \cdot g(x)$ denotes the Lie derivative of V with respect to g , and $L_f V(x)$ is the Lie derivative of V with respect to f .

The pair (f, g) of vector fields f and g given by (16) that satisfies conditions (i)-(iii) is called a *control Lyapunov pair*. If the origin of (15) has CLF, then there exists a control law that renders the system asymptotically stable.

Proposition 1 [10]:

If the system (15) is stabilized by a feedback $u = \alpha(x) + k^T x$, where $k = (k_1, \dots, k_m)$, $k_i, i = 1, \dots, m$, are roots of a Hurwitz polynomial p , and α is continuously differentiable on $U_0 \setminus \{0\}$, then the pair (f, g) satisfies the Lyapunov condition (i.e., conditions (i) and (ii) given above) at the origin.

After applying the control law $u = \alpha(x) + k^T x$ to (15), we obtain the system:

$$\dot{x} = f(x) + g(x)(\alpha(x) + k^T x) + h(x)w, \quad (18)$$

with external disturbance input w .

Case 1

Let us assume that the nominal system $\dot{x} = f(x) + g(x)u$ is stabilizable and the CLF for nominal system (17) is known. We assume that for all $x \neq 0$ there is a positive, proper function $V \in \mathbb{R}_+$ such that,

$$\nabla V(x)[f(x) + g(x)u] < 0. \quad (19)$$

Then, this nominal control law must be redesigned to account for disturbance w in the actual system. Let us emphasize that the nominal CLF is chosen independently of any knowledge of the disturbance input matrix $h(x)$. Then after including function $h(x)$ in inequality (19), and to keep system (15) (with disturbance w) stable, function V must satisfy:

$$\nabla V(x)[f(x) + g(x)u + h(x)w] < 0, \forall x \neq 0. \quad (20)$$

Let us assume that CLF describes the kinetic energy of system (14), i.e.,

$$V = \frac{1}{2}(3x_1^2 + 2x_2^2 + x_3^2). \quad (21)$$

Then,

$$\begin{aligned} \nabla V(x)[f(x) + g(x)u + h(x)w] = \\ 3x_1^2 w + 2x_2 x_3 |x_3| + 3x_1 x_2 + x_3 u, \end{aligned} \quad (22)$$

and the control law, which fulfils condition (20), is chosen as:

$$u = -\text{sat}(3x_1^2 x_3 + 2x_2 |x_3| + 3x_1 x_2 x_3 + x_3 - u_0), \quad (23)$$

where $u_0 = -k_1 x_1 - k_2 x_2$ with k_1, k_2 – roots of some Hurwitz polynomial, and saturation function is given according to saturated control voltage defined as $\text{sat}(v(t))$ in order to enforce the constraint on the maximum voltage allowed.

In this way, one obtains a globally stable closed-loop system with $|x_3| > \xi \geq x_1 x_2$, and for bounded disturbance $w < x_2(x_3^2 - 1)/x_1$, where ξ is a positive design constant. In fact, note that AMB system (14), with non-dimensional variables $[x_1, x_2, x_3]$ given by (13) and for the absolute maximum values of the physical AMB parameters collected in Table 1, is on the stability border. Then, the complementary sensitivity function S for these values also has its maximum value and system (14) is the most sensitive to disturbance w . Therefore, the inequality $w < x_2(x_3^2 - 1)/x_1$ should be met for maximum system variables, and it is easy to check that it holds true if $w < 0.1377$. Then, including the non-dimensionalized value in (13) and maximum value of $|\omega|_{\max} = 0.0001$ [m] (see Table 1), we get that $\omega < 0.00001377$. Thus, it is implied that the above inequality is always true.

Note that in this case, the condition: $|x_3| > \xi$ follows from the fact that, in the case of an AMB system operated in zero-bias mode, we need a large change in flux resulting in large voltage commands (7) in order to produce a small control force. Design coefficient ξ is a part of the AMB control system and its value depends on the parameters of the AMB system (which are given in Table 1). The condition $\xi \geq x_1 x_2$ is always met in the flux-controlled AMB.

Case 2

The stabilization problem for system (15) is solved if we can assign negative value to the time derivative of function V , thus the stability condition is given by:

$$L_f V(x) + L_g V(x) + L_h V(x) < 0, \quad (24)$$

where we suppose that function V is given by (21).

Following (24) and for CLF given by (21), with condition: $|x_3| > \xi \geq x_1 x_2$, the stable feedback loop can be written as $L_f V + L_g V + L_h V = 3x_1^2 w + 2x_2 x_3 |x_3| + 3x_1 x_2 + x_3 u$. Then, the second control law is selected as:

$$u = -\text{sat}\left(\frac{1}{2}(-3x_1^2 - 2x_2 x_3 |x_3| - 3x_1 x_2 + x_3) - u_0\right), \quad (25)$$

with, as previously, $u_0 = -k_1 x_1 - k_2 x_2$ where k_1, k_2 are roots of some Hurwitz polynomial, and the saturation function in (23) is given according to saturated control voltage defined as $\text{sat}(v(t))$ in order to enforce the

constraint on the maximum voltage allowed.

V. NUMERICAL EXAMPLES

This section presents results obtained for AMB system (12) after applying zero-bias flux control with switching scheme (6) and with external disturbance ω . In this way, the first equation of AMB system (12) is replaced with $\frac{d}{dt}x_1 = x_2 + x_1\omega$. The possibilities of compensating for disturbance ω are investigated with control laws (23) and (25). The simplified 1-DOF model of the AMB (given in Fig. 1) was extended by magnetic saturation, coil resistance, voltage saturation and geometrical specifications such as: nominal air gap, number of coil turns over a single pole of the AMB stator, pole area, permeability of air, and electromagnetic force acting angle. The data for these AMB specifications are collected in Table 1. Variable x is the rotor displacement from the centre point (when $x=0$), and g_0 is the nominal width of the air gap.

Table 1: AMB specification

| Symbol | Value | Meaning |
|-------------------------|-----------|------------------------------------|
| $ x _{max}$ [m] | 0.00025 | Maximum rotor position |
| $ \dot{x} _{max}$ [m/s] | 0.05 | Maximum speed |
| $ \phi _{max}$ [Wb] | 0.0005 | Maximum control flux |
| $ \omega _{max}$ [m] | 0.0001 | Maximum rotor position disturbance |
| g_0 [m] | 0.00058 | Nominal width of air gap |
| m [kg] | 2.5 | Rotor mass |
| N | 108 | Number of coil turns |
| R [Ω] | 0.5 | Coil resistance |
| A [m ²] | 0.0014 | Electromagnet pole area |
| α [deg] | 22.5 | Electromagnetic force acting angle |
| Φ_{sat} [Wb] | 0.0022 | Saturation flux |
| B_{sat} [T] | 1.6 | Saturation flux density |
| v_{sat} [V] | ± 150 | Saturation voltage |
| i_{sat} [A] | ± 5 | Saturation current |

The AMB model detailed above, with dynamics (14) and switching scheme (6), was applied in Matlab/Simulink[®] software. Numerical simulations were performed for position-flux zero-bias control, for bias flux Φ_0 equalling zero. The system's trajectories and control input are illustrated for the given nonlinear controllers with zero-bias and voltage constraints. For this purpose, the initial conditions are assumed to be as follows: $\{\phi_1(0), \phi_2(0)\} = \{0,0\}$ and $\{x(0), \dot{x}(0), \phi(0)\} = \{0,0,0\}$. All simulations are performed with optimized gains k_1 and k_2 equal to 0.92 and 9.94, as previously done in work [10]. The amplitude of step disturbance w equals 0.1 [mm] in all simulations.

The AMB system's responses to disturbance w , in zero-bias mode, for selected controller gains: $k_1 = 0.92, 1, 1.5$ and $k_2 = 9.94, 5, 5$ are presented in Fig. 2. Disturbance ω is successfully compensated with zero overshoot where the control voltage amplitude does not exceed 100 [V].

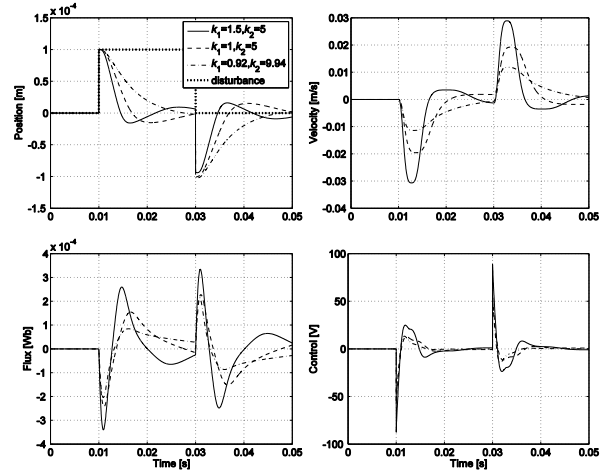


Fig. 2. Responses of closed-loop system with zero-bias to disturbances employing control law (23) for selected gains k_1 and k_2 .

Figures 3 and 4 show the results of simulations using control laws (23) and (25), with optimized controller gains: $k_1 = 0.92$ and $k_2 = 9.94$. Figure 3 shows the AMB system's responses to disturbance ω , and Fig. 4 shows voltage v_1, v_2 and flux ϕ_1, ϕ_2 trajectories according to each active electromagnet.

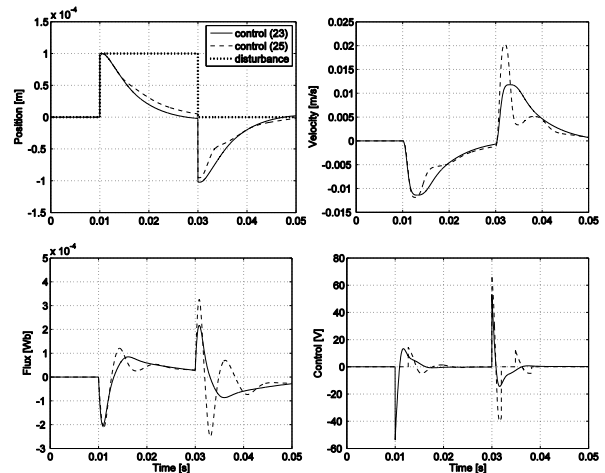


Fig. 3. Comparison of step responses between closed-loop systems employing (23) and (25) controllers for $k_1=0.92, k_2=9.94$ with zero-bias.

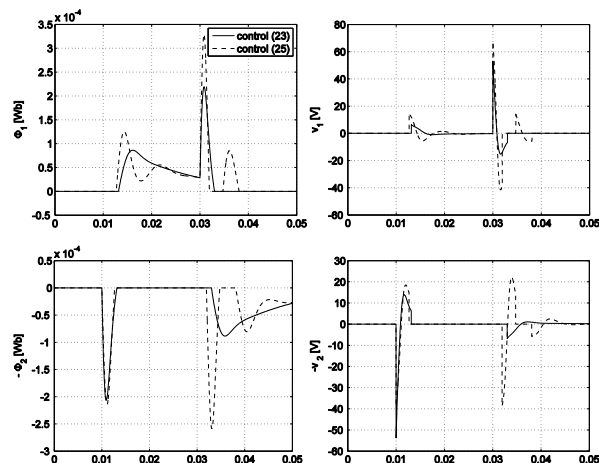


Fig. 4. Voltage switching rule with zero-bias and control laws (23) and (25) for $k_1=0.92$, $k_2=9.94$.

Figure 4 presents the idea of the voltage switching strategy used in zero-bias control with CLF and the flux and voltage signal responses to disturbance ω . In the results given (see Figs. 3 and 4), the maximum voltage is about 60 [V], and the settling time is equal to 0.02 [s].

For example, the saturation level in [33] and [35] is set to 30 [V], and in [30] $v_{\max}=10$ [V]. But in [30], the settling time for rotor position is equal to 0.2 [s], which is 10 times longer than in our simulation results. However, in light of the given results, one may conclude that higher values of control voltage lead to shorter settling times. As observed in Figs. 2 and 3, the settling time decreases as voltage saturation level increases, as expected.

VI. CONCLUSIONS

In this paper, nonlinear CLF-based controllers have been proposed and effectively applied to the AMB flux-controlled system with zero-bias and control voltage saturation. Specifically, when using the switching voltage rule with zero-bias operation, one must preclude the singularities present in the control law. The stability of the two designs has been discussed. The desired control performance was achieved despite control voltage saturation. Simulation results have shown that the novel and simple low-order controllers based on CLF gave equivalent results compared to high-order complex control, e.g., based on Artstein-Sontag's theorem [29] or as given in [30]. The dynamic performance of the proposed control laws as well as the AMB system's responses are similar to the ideal model case.

Future investigations into this topic will focus on a Lyapunov-based nonlinear dynamic output feedback control method for a 5-DOF AMB system. The fabricated test rig of the whole system and its details can be found in work [3, 36]. In the first step, the rotor will be assumed

to be rigid for simplicity. In the second step, the nonlinear Lyapunov controller will be considered for control of the 5-DOF flexible rotor.

ACKNOWLEDGMENT

This work has been supported under *University Work* of Dept. of Automatic Control and Robotics, Faculty of Mechanical Eng., Bialystok University of Technology, no. S/WM/1/2017 and also supported by the Polish Ministry of Science and Higher Education (MNiSW).

ORCID

Arkadiusz Mystkowski, <http://orcid.org/0000-0002-5742-7609>

REFERENCES

- [1] Z. Gosiewski and A. Mystkowski, "Robust control of active magnetic suspension: Analytical and experimental results," *Mechanical Systems & Signal Processing*, vol. 22, pp. 1297-1303, 2008.
- [2] A. Mystkowski, "Mu-synthesis for magnetic bearings of flywheel," *Proc. in Applied Mathematics and Mechanics (PAMM)*, Wiley Online Library, vol. 9, pp. 631-632, 2009.
- [3] A. Mystkowski, "mu-synthesis control of flexible modes of AMB rotor," *Acta Mechanica et Automatica*, vol. 4, pp. 83-90, 2010.
- [4] Y. Ariga, K. Nonami, and T. Kamiyama, "Nonlinear zero-power control of an electrical power storing flywheel (derivation of nonlinear control ignoring the gyro-effect)," *Journal of Japan AEM Society*, vol. 8, pp. 403-410, 2000.
- [5] H. Bleuler, D. Yischer, G. Schweitzer, et al., "New concepts for cost-effective magnetic bearing control," *Automatica*, vol. 30, pp. 871-876, 1994.
- [6] A. Charara, J. De Miras, and B. Caron, "Nonlinear control of a magnetic levitation system without premagnetization," *IEEE Trans. Contr. Syst. Technol.*, vol. 4, pp. 513-523, 1996.
- [7] R. P. Jastrzebski, A. Smirnov, A. Mystkowski, and O. Pyrhönen, "Cascaded position-flux controller for AMB system operating at zero bias," *Energies*, vol. 7, pp. 3561-3575, 2014.
- [8] K. Z. Liu, A. Ikai, A. Ogata, and O. Saito, "A nonlinear switching control method for magnetic bearing systems - Minimizing the power consumption," in *Proc. of the 15th IFAC World Conference*, Barcelona, Spain, 21-26 July 2002.
- [9] N. Motee, M. S. De Queiroz, Y. Fang, and D. M. Dawson, "Active magnetic bearing control with zero steady-state power loss," in *Proc. of ACC'2002*, Anchorage, Alaska, USA, pp. 827-832, 8-10 May 2002.
- [10] A. Mystkowski, E. Pawluszewicz, and E.

- Dragašius, "Robust nonlinear position-flux zero-bias control for uncertain AMB system," *Int. J. of Contr.*, vol. 88, pp. 1619-1629, 2015.
- [11] M. N. Sahinkaya and A. E. Hartavi, "Variable bias current in magnetic bearings for energy optimization," *IEEE Trans. on Mag.*, vol. 43, pp. 1052-1060, 2007.
- [12] J. Lévine, J. Lottin, and J. C. Ponstart, "A nonlinear approach to the control of magnetic bearings," *IEEE Trans. Contr. Syst. Technol.*, vol. 4, pp. 524-544, 1996.
- [13] P. J. Moylan and B. D. O. Anderson, "Nonlinear regulator theory and an inverse optimal control problem," *IEEE Trans. on Automatic Control*, vol. 18, pp. 460-465, 1973.
- [14] I. G. Malkin, *The Theory of Stability of Motion*. Moscow: Gostekhizdat, 1952.
- [15] J. Willems, "Dissipative dynamical systems - Parts I and II," *Archive for Rational Mechanics and Analysis*, vol. 45, pp. 321-393, 1972.
- [16] A. Bressan and B. Piccoli, *Introduction to the Mathematical Theory of Control*. Springfield: American Institute of Mathematical Sciences, 2007.
- [17] F. Clarke, "Lyapunov functions and feedback in nonlinear control, optimal control, stabilization and nonsmooth analysis," *Lecture Notes in Control and Information Science*, vol. 301, pp. 267-282, 2004.
- [18] R. Marino and P. Tomei, *Nonlinear Control Design – Geometric, Adaptive and Robust*. UK: Prentice Hall International, 1995.
- [19] E. D. Sontag, *Mathematical Control Theory, Deterministic Finite Dimensional Systems*. 2nd ed., New York: Springer, 1998.
- [20] Z. Artstein, "Stabilization with relaxed controls," *Nonlinear Analysis*, vol. 7, pp. 1163-1173, 1983.
- [21] E. D. Sontag, "Lyapunov-like characterization of asymptotic controllability," *SIAM Journal of Control and Optimization*, vol. 21, pp. 462-471, 1983.
- [22] E. D. Sontag, "A universal construction of Artstein's theorem on nonlinear stabilization," *Systems and Control Letters*, vol. 13, pp. 117-123, 1989.
- [23] R. A. Freeman and P. V. Kokotović, "Inverse optimality in robust stabilization," *SIAM Journal of Control and Optimization*, vol. 34, pp. 1365-1391, 1996.
- [24] R. A. Freeman and P. V. Kokotović, *Robust Nonlinear Control Design – State-Space and Lyapunov Techniques*. Boston: Birkhäuser, 1996.
- [25] R. A. Freeman and P. V. Kokotović, Design of 'softer' robust nonlinear control laws," *Automatica*, vol. 29, pp. 1425-1437, 1993.
- [26] I. Kanellakopoulos, P. V. Kokotović, and A. S. Morse, "A toolkit for nonlinear feedback design," *Systems and Control Letters*, vol. 18, pp. 83-92, 1992.
- [27] J. W. Helton and M. R. James, *Extending \mathcal{H}_∞ Control to Nonlinear Systems*. Philadelphia: SIAM Frontiers in Applied Mathematics, 1999.
- [28] A. Isidori and W. Kang, " \mathcal{H}_∞ control via measurement feedback for general nonlinear systems," *IEEE Trans. on Automatic Control*, vol. 40, pp. 466-472, 1995.
- [29] P. Tsiotras and B. C. Wilson, "Zero- and low-bias control designs for active magnetic bearings," *IEEE Trans. Contr. Syst. Technol.*, vol. 11, pp. 889-904, 2003.
- [30] P. Tsiotras and M. Arcak, "Low-bias control of AMB subject to voltage saturation: state-feedback and observer designs," *Proc. of the 41st IEEE Conf. on Decision and Contr.*, Las Vegas, NV, USA, pp. 2474-2479, 10-13 December 2002.
- [31] G. Schweitzer and E. H. Maslen, *Magnetic Bearings: Theory, Design, and Application to Rotating Machinery*. Berlin Heidelberg: Springer-Verlag, 2009.
- [32] E. Maslen, P. Hermann, and M. Scott, "Practical limits to the performance of magnetic bearings: Peak force, slew rate and displacement sensitivity," *ASME Journal on Tribology*, vol. 111, pp. 331-336, 1989.
- [33] C. Knospe, "The nonlinear control benchmark experiment," *Proc. of the American Control Conference*, Chicago, IL, pp. 2134-2138, 28-30 June 2000.
- [34] R. A. Freeman, "Global robustness of nonlinear systems to state measurement disturbances," *Proc. of the 32nd IEEE Conference on Decision and Control*, San Antonio, Texas, USA, pp. 1507-1512, 15-17 December 1993.
- [35] J. D. Lindlau and C. Knospe, "Feedback linearization of an active magnetic bearing with voltage control," *IEEE Transactions on Control Systems Technology*, vol. 10, pp. 21-31, 2002.
- [36] Z. Gosiewski and A. Mystkowski, "The robust control of magnetic bearings for rotating machinery," *Solid State Phenomena*, vol. 113, pp. 125-130, 2006.

Six-Axis Rotor Magnetic Suspension Principle for Permanent Magnet Synchronous Motor with Control of the Positive, Negative and Zero-Sequence Current Components

Gael Messenger and Andreas Binder

Institute of Electrical Energy Conversion
Darmstadt University of Technology, Darmstadt, 64283, Germany
gmessenger@ew.tu-darmstadt.de, abinder@ew.tu-darmstadt.de

Abstract — A novel magnetic levitation principle, applicable for two- and four-pole high-speed permanent magnet synchronous motors, is presented. The drive consists of two half-motors, in which two asymmetric star-connected windings are arranged. An additional active magnetic bearing part is inserted to control the axial displacement. The two coils of the axial magnetic bearing are fed by the zero-sequence current components of the star-connected windings. The proper control of the positive, the negative, and the zero-sequence currents permits to set the torque, the radial levitation forces and the axial levitation force, respectively.

Index Terms — Magnetic suspension, permanent magnet synchronous motor, self-bearing motor, symmetrical components.

I. INTRODUCTION

In the past decades, different levitation principles were investigated to achieve rotor suspension with forces of magnetic origin. This paper focuses on a solution with active control of the six degrees of freedom of the rotor, suitable for high-speed drives. Active self-bearing suspension is considered to be an alternative to active magnetic bearings, where the same iron stack is used for the generation of the torque and of the levitation forces [1]. While most self-bearing motors generate only radial suspension forces [1], some unconventional motor designs enable to generate also an axial thrust. A solution is presented in [2], where axial forces are generated by two opposing half-motors with conical air-gap. The axial displacement is controlled actively using a three-point d-current control in each half-motor. In [3], a different approach is proposed, with again two conical half-motors, but here the permanent magnet field is controlled in the synchronous coordinate system. Four conventional windings are required, two for the torque and the axial force, and two for the two radial forces of the two half-motors. Axial flux motor alternatives are proposed in [4] and [5], where the axial thrust results from the difference

of the main field on both sides of an axial flux motor. A Lorentz-force based application can be found in [6], where the two counteracting axial thrusts of two conically shaped skewed windings are used to generate a net axial force. A much simpler Lorentz-force based solution is presented in [7]. This latest prototype is composed of two cylindrical half-rotors. Two oppositely skewed windings are brought in two half motors, so that a q -current feeding results simultaneously in a torque and an axial thrust. The net torque is produced by a common q -current feeding, while the net axial thrust results from an opposite q -current feeding. In this paper, an alternative topology is presented, with a thrust bearing as a magnetic active part, fed by two zero-sequence current components from two double star windings. This topology, restricted to two- and four-pole motors, is extended from the motor design presented in [8]. Whereas the previous design [8], requires an additional axial magnetic bearing and the corresponding power electronics, the feeding of the magnetic bearing in the proposed design is achieved through the drive winding itself. As a result, all the terminals are used to generate the torque, the radial and the axial levitation forces simultaneously. In steady-state condition, these components correspond to the positive, the negative and the zero-sequence current components, respectively, in each of the three-phase windings. The first part of the paper describes the different windings in the different active parts, and their feeding. It describes in particular the thrust bearing coils to generate an axial force and their connection to the main windings. The second part focuses on the integration of the zero-sequence current control into the existing control, presented in [8]. It presents a new set of coordinate systems, relevant for the field orientation control. The third part presents an extension of the voltage modulators, which enables to impress a zero-sequence voltage. It is demonstrated, that with simple transformations the determination of the pulse widths to impress the positive and negative sequence voltages is similar to the familiar space vector

modulation. The determination of the zero-sequence voltage is explained in the fourth part. In particular, the problem of over-modulation is addressed.

II. WINDING CONFIGURATION AND FEEDING

In order to achieve the suspension and speed control of a free rotating body, the six degrees of freedom (DOF) need to be actively controlled. To do so, the torque, the axial force and two sets of two radial forces, on two parallel, but distinct planes, are produced by several electromagnetic actuators. The configuration of the proposed magnetic active parts is represented in Fig. 1.

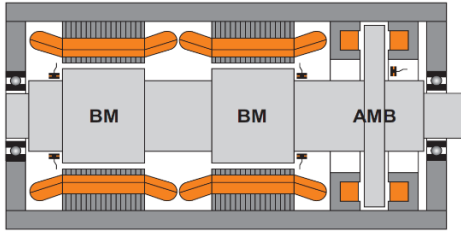


Fig. 1. Schematic representation of the proposed motor with two half permanent magnet synchronous motors (BM) and an active thrust magnetic bearing (AMB).

The proposed drive is composed of two half-motors (BM in Fig. 1), which generate torque and radial levitation forces, and one thrust magnetic bearing part (AMB in Fig. 1), which produces an axial levitation force. To prevent rotor damage in case of levitation control failure, an emergency bearing is present at each rotor end. A play between rotor and bearing inner-ring prevents any mechanical contact during normal operation. Five position sensors and a rotor angle sensor are present to measure the rotor position. Two parallel magnetized two-pole magnets are surface mounted on the rotor. In the stator slots of each half motor two asymmetrical three-phase windings are wound, as shown in Fig. 2. The windings are here represented with a number of slots per pole and phase of $q = 1$ for clarity. Due to coil short pitching ($W/\tau_p = 1/2$) and an asymmetrical winding arrangement (Fig. 2), the two windings produce not only a fundamental field for the torque, but also a space harmonic of order two ($\nu = -2$) for the radial forces. The expression of the torque (resp. of the radial forces), generated by a differential-mode counter-clockwise rotating current space vector $i_{ccw} = i_{\alpha,1} + j i_{\beta,1}$ (resp. a common-mode clockwise rotating current space vector $i_{cw} = i_{\alpha,-2} + j i_{\beta,-2}$), is detailed in [8]. Additionally, the star points N_A and N_B of the proposed windings (Fig. 2) are interconnected, so it is possible to feed a zero-sequence current $i_{d,0}$ between the two three-phase windings (Fig. 3). This current component is used to generate an axial attraction force. The axial active magnetic bearing is a conventional thrust bearing with differential windings. It

is composed of two ring electromagnets with two coils, which are fed according to the differential feeding principle. The outer electromagnet is removable in axial direction to enable the rotor insertion. The two star points N_A and N_B of the two three-phase systems from one half-motor (Fig. 2) are connected to the terminals of one of the two coils (AMB Fig. 1) of the magnetic thrust bearing. The two other star points from the second half-motor winding are connected to the second coil of the magnetic bearing. Two zero-sequence currents $i_{d,0,DE}$ and $i_{d,0,NDE}$ are flowing through the two coils of the magnetic bearing. The amplitudes of the currents $i_{d,0,DE}$ and $i_{d,0,NDE}$ follow the differential feeding Equation (1):

$$\begin{cases} i_{d,0,DE} = i_{0,bias} + \Delta i_0 \\ i_{d,0,NDE} = i_{0,bias} - \Delta i_0 \end{cases} \quad (1)$$

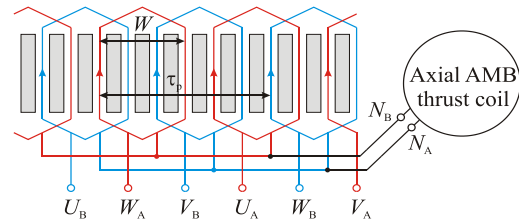


Fig. 2. Winding disposition in one half-motor (e.g., DE BM), connected to a single coil of the thrust bearing (AMB). The thrust coil (on the right) is fed through the interconnected star points N_A, N_B . The winding disposition is identical for the second half-motor.

Whereas the electromagnetic forces, resulting on the thrust disk and generated by the common mode bias current $i_{0,bias}$, are cancelling each other, the differential current Δi_0 produces a net axial force Δf_z . This principle is identical to the principle of differential feeding in active magnetic bearings. The expressions of the phase currents in U_A, V_A, W_A and U_B, V_B, W_B in stationary conditions are shown in (2) and are valid for the drive end (DE) and the non-drive end (NDE) separately. Φ_1 and Φ_2 are the phase angles of the current space vectors i_{ccw} and i_{cw} at the time $t = 0$. The current space vector i_{ccw} rotates with electrical frequency ω in the positive direction (counter-clockwise), whereas the current space vector i_{cw} rotates with the same electrical frequency ω in the negative direction (clockwise);

$$\mathbf{i}_A(t) = (i_{U,A}(t), i_{V,A}(t), i_{W,A}(t))^T = \begin{pmatrix} i_{ccw} \cdot \cos(\omega t + \phi_1) + i_{cw} \cdot \cos(-\omega t + \phi_2) + i_{d,0}/3 \\ i_{ccw} \cdot \cos(\omega t - 2\pi/3 + \phi_1) + i_{cw} \cdot \cos(-\omega t - 2\pi/3 + \phi_2) + i_{d,0}/3 \\ i_{ccw} \cdot \cos(\omega t - 4\pi/3 + \phi_1) + i_{cw} \cdot \cos(-\omega t - 4\pi/3 + \phi_2) + i_{d,0}/3 \end{pmatrix} \quad (2)$$

$$\mathbf{i}_B(t) = (i_{U,B}(t), i_{V,B}(t), i_{W,B}(t))^T = \begin{pmatrix} i_{ccw} \cdot \cos(\omega t - \pi + \phi_1) + i_{cw} \cdot \cos(-\omega t + \phi_2) - i_{d,0}/3 \\ i_{ccw} \cdot \cos(\omega t + \pi/3 + \phi_1) + i_{cw} \cdot \cos(-\omega t - 2\pi/3 + \phi_2) - i_{d,0}/3 \\ i_{ccw} \cdot \cos(\omega t - \pi/3 + \phi_1) + i_{cw} \cdot \cos(-\omega t - 4\pi/3 + \phi_2) - i_{d,0}/3 \end{pmatrix}$$

The levitation control is identical to the one for drive

with active magnetic bearings [1]. It can be realized for example with simple PID controllers that take the displacement position signals as input and calculate the required radial and axial forces to suspend the rotor at the center of the stator.

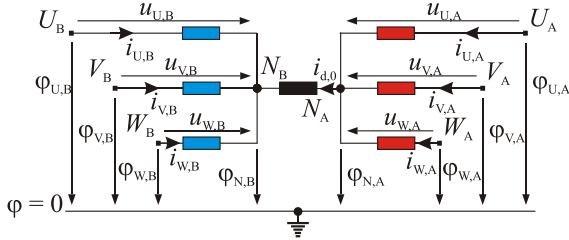


Fig. 3. Schematic representation of the six-phase winding in one half motor (Fig. 2) and definition of the currents and voltage potentials. The second winding in the second half motor is identical.

III. CONTROL STRUCTURE EXTENSION

For independent control of the torque and levitations forces, the six phase currents are transformed into two sets (DE & NDE) of three orthogonal sub-spaces $K_{S,0}$, $K_{dq,1}$, $K_{dq,-2}$. The decomposition is done as follows: The six phase currents are projected on a first stator-based subspace $K_{S,1}$ via (3) to get the differential counter-clockwise components $i_{\alpha,1}$ and $i_{\beta,1}$. It is demonstrated in [8] that these components generate a two-pole magnetic air-gap field. These components are transformed into the synchronous coordinate system $K_{dq,1}$ to control the field weakening and the torque independently. The projection of the phase currents on a second sub-space $K_{S,-2}$ via (3) gives the common-mode clockwise components $i_{\alpha,-2}$ and $i_{\beta,-2}$, which are necessary to produce radial forces. These components are exciting a four-pole air-gap field (harmonic order $\nu = -2$), which interacts with the two-pole rotor permanent magnet field to generate the radial forces [8]. To obtain an independent control of the horizontal and vertical radial forces, these components are transformed into a clockwise rotating coordinate system $K_{dq,-2}$, rotating with the electrical frequency ω . Since the number of pole-pairs of the levitation field ($p_2 = 2$) is different from the one of the rotor field ($p_1 = 1$), the levitation field harmonic $\nu = -2$ rotates in stationary condition at a slip $s = 0.5$ (4). Finally, the projection of the six phase currents on $K_{S,0}$ via (3) gives a single differential zero-sequence current component $i_{d,0}$. Whereas the radial suspension forces and the torque in each half motor are independent from each other, the net axial force results from the difference of the axial forces, generated by the two currents $i_{d,0,DE}$ and $i_{d,0,NDE}$. When these two components are controlled according to (1), the resulting net force Δf_z is directly proportional to Δi_0 . The described current projections are factorized according to (3). The control of each current component

is done in the sub-spaces $K_{S,0}$, $K_{dq,1}$, $K_{dq,-2}$, for each half motor (DE and NDE in Fig. 1) with simple PI controllers. The voltage outputs are then transformed back to the set of stator coordinate systems $\{K_{S,0}, K_{S,1}, K_{S,-2}\}$ before being sent to the modulators. The speed and position control scheme as well as the linearized model of the proposed drive is identical to the one with active magnetic bearing suspension and is therefore not explained here. An overview of the considered sub-spaces is given in Table 1, with the corresponding space dimension:

$$\begin{pmatrix} i_{\alpha,1} \\ i_{\beta,1} \\ i_{\alpha,-2} \\ i_{\beta,-2} \\ i_{d,0} \end{pmatrix} = \frac{1}{6} \begin{pmatrix} 2 & -1 & -1 & -2 & 1 & 1 \\ 0 & \sqrt{3} & -\sqrt{3} & 0 & -\sqrt{3} & \sqrt{3} \\ 2 & -1 & -1 & 2 & -1 & -1 \\ 0 & \sqrt{3} & -\sqrt{3} & 0 & \sqrt{3} & -\sqrt{3} \\ 3 & 3 & 3 & -3 & -3 & -3 \end{pmatrix} \begin{pmatrix} i_{U,A} \\ i_{V,A} \\ i_{W,A} \\ i_{U,B} \\ i_{V,B} \\ i_{W,B} \end{pmatrix}, \quad (3)$$

$$s = [n_{syn} - (-(n_{syn} / -2))] / n_{syn} = 0.5. \quad (4)$$

Table 1: List of the defined sub-spaces

| Name | Description | Dim. |
|-------------|--|------|
| $K_{S,0}$ | Stator zero-sequence sub-space | 1 |
| $K_{dq,1}$ | Counter-clockwise synchronous differential component sub-space | 2 |
| $K_{dq,-2}$ | Clockwise synchronous common-mode component sub-space | 2 |
| $K_{S,1}$ | Stator counter-clockwise differential component sub-space | 2 |
| $K_{S,-2}$ | Stator clockwise common-mode component sub-space | 2 |
| $K_{S,A}$ | $(\alpha\beta\gamma)$ stator sub-space of winding A | 3 |
| $K_{S,B}$ | $(\alpha\beta\gamma)$ stator sub-space of winding B | 3 |

IV. SPACE VECTOR MODULATION EXTENSION

The proposed winding has six phases and five degrees of freedom (DOF). The six phase terminal potentials $\varphi_{U,A}$, $\varphi_{V,A}$, $\varphi_{W,A}$, $\varphi_{U,B}$, $\varphi_{V,B}$, $\varphi_{W,B}$ are impressed by a six phase inverter. It is shown in Fig. 3 that the star-point potentials $\varphi_{N,A}$ and $\varphi_{N,B}$ are not impressed by the inverter, so the 3D SVM is not suitable for this problem. Indeed, the two modulators, necessary to calculate the proper firing instants of the power switches, require a novel pulse width modulation to impress a zero-sequence voltage $u_{d,0}$. Here, a solution is proposed, based on the space vector modulation principle. The pulse pattern of a single six-phase system (Fig. 4) is described by six pulse widths ($t_{0,A}$, $t_{1,A}$, $t_{2,A}$, $t_{0,B}$, $t_{1,B}$ and $t_{2,B}$). The voltage space, covered by this 5D SVM, forms a 5D polytope. In contrast to the common 2D SVM, projections of the reference voltage vectors in 5D voltage spaces are difficult to apprehend. In Fig. 3, the phase voltages $u_{U,A}$, $u_{V,A}$, $u_{W,A}$, can be determined as a function of the phase potentials $\varphi_{U,A}$, $\varphi_{V,A}$, $\varphi_{W,A}$ and the star point

potential $\varphi_{N,A}$. Obviously, the two star point potentials $\varphi_{N,A}$ and $\varphi_{N,B}$ are functions of all the six phase potentials $\varphi_{U,A}, \dots, \varphi_{W,B}$. After projection of the phase voltage vector $\mathbf{u}_A = (u_{U,A}, u_{V,A}, u_{W,A})^T$ into the coordinate system $K_{S,A}$ with the Clarke transformation (5), it can be noticed that the components $u_{\alpha,A}$ and $u_{\beta,A}$ of \mathbf{u}_A , in $K_{S,A}$, are independent of $\varphi_{U,B}, \varphi_{V,B}$ and $\varphi_{W,B}$. Doing the same transformation in $K_{S,B}$ with $\mathbf{u}_B = (u_{U,B}, u_{V,B}, u_{W,B})^T$, it is possible to split the 5 DOF problem into smaller problems by projection of the stator voltage vector $\mathbf{u}_S = (u_{\alpha,1}, u_{\beta,1}, u_{\alpha,2}, u_{\beta,2}, u_{d,0})^T$ in $K_{S,A}$ and $K_{S,B}$. The zero-voltage components $u_{0,A}$ and $u_{0,B}$ depend however on all the phase potentials $\varphi_{U,A}, \dots, \varphi_{W,B}$. While the actual values of $u_{0,A}$ and $u_{0,B}$ are not of interest, the zero-sequence voltage $u_{d,0}$, which drives the zero-sequence current component $i_{d,0}$ in $K_{S,0}$, is given by $u_{d,0} = \varphi_{N,A} - \varphi_{N,B}$. To take advantage of the orthogonality mentioned above, a two-step calculation of the pulse pattern is introduced. First the four pulse widths $t_{1,A}, t_{2,A}, t_{1,B}$ and $t_{2,B}$ of the active voltage switching states $V_{1,A}, V_{2,A}, V_{1,B}$ and $V_{2,B}$ are determined to generate solely the counter-clockwise differential voltage space vector components ($u_{\alpha,1}, u_{\beta,1}$) and the clockwise common-mode voltage space vector components ($u_{\alpha,2}, u_{\beta,2}$). To do so, relation (6) is used, followed by two inverse Clarke transformations in A and B. In a second step, the pulse widths $t_{0,A}, t_{0,B}, t_{7,A}$ and $t_{7,B}$ of the zero-voltage switching states $V_{0,A}, V_{0,B}, V_{7,A}$ and $V_{7,B}$ are determined to get the required zero-sequence differential voltage component $u_{d,0}$. The general determination of the zero-voltage pulse widths is an underdetermined problem, so that symmetry considerations and polytope boundaries are exploited to find a unique solution. Despite its simplicity, this algorithm is only suited to this particular problem and is not a general solution of the 5D SVM:

$$\begin{pmatrix} u_{\alpha,A} \\ u_{\beta,A} \\ u_{0,A} \end{pmatrix} = \frac{1}{3} \begin{pmatrix} 2 & -1 & -1 \\ 0 & \sqrt{3} & -\sqrt{3} \\ 1 & 1 & 1 \end{pmatrix} \begin{pmatrix} u_{U,A} \\ u_{V,A} \\ u_{W,A} \end{pmatrix} \\ = \frac{1}{3} \begin{pmatrix} 2\varphi_{U,A} - \varphi_{V,A} - \varphi_{W,A} \\ \sqrt{3}(\varphi_{V,A} - \varphi_{W,A}) \\ \varphi_{U,A} + \varphi_{V,A} + \varphi_{W,A} - 3\varphi_{N,A} \end{pmatrix}, \quad (5)$$

$$\begin{pmatrix} u_{\alpha,A} \\ u_{\beta,A} \\ u_{\alpha,B} \\ u_{\beta,B} \end{pmatrix} = \frac{1}{2} \begin{pmatrix} 1 & 0 & 1 & 0 \\ 0 & 1 & 0 & 1 \\ -1 & 0 & 1 & 0 \\ 0 & -1 & 0 & 1 \end{pmatrix} \begin{pmatrix} u_{\alpha,1} \\ u_{\beta,1} \\ u_{\alpha,2} \\ u_{\beta,2} \end{pmatrix}. \quad (6)$$

V. CONTROL OF THE ZERO-SEQUENCE CURRENT

In the proposed scheme, the zero-sequence voltage $u_{d,0}$ is modulated with the difference of pulse width of the zero-voltage switching states $V_{0,A}, V_{0,B}, V_{7,A}$ and $V_{7,B}$. In order to produce a positive zero-voltage component $u_{d,0}$, the pulse width $t_{7,A}$, of the positive zero-voltage

switching state $V_{7,A}$ (“ppp”, where all three phase terminals are switched to U_{dc}) in the three-phase system A is increased, while the pulse width $t_{7,B}$ of the positive zero-voltage switching state $V_{7,B}$ in the three-phase system B is reduced (Fig. 4). The variation of the zero-of $u_{d,0}$ over a switching period T_{sw} , becomes positive. An illustration of asymmetrical pulse patterns is given in Fig. 4. The determination of the four zero-voltage pulse widths $t_{0,A}, t_{0,B}, t_{7,A}$ and $t_{7,B}$ is formulated as (7), (8) and (9):

$$(t_{0,A}, t_{7,A}, t_{0,B}, t_{7,B}) \in \mathbb{R}_{\geq 0}^4, \quad (7)$$

$$t_{z,i} = t_{0,i} + t_{7,i} = T_{sw} - t_{1,i} - t_{2,i} \geq 0 \quad i = A, B, \quad (8)$$

$$\frac{k_{eq}}{T_{sw}} \cdot \int_0^{T_{sw}} \sum_{i=U,V,W} (\varphi_{i,A}(t) - \varphi_{i,B}(t)) \cdot dt = u_{d,0}(t). \quad (9)$$

Whereas the two first conditions (7) and (8) are very simple to compute, the third condition (9) requires those machine parameters, which are relevant for the zero-sequence components. A simplified equivalent circuit of the zero-sequence system is proposed in Fig. 5, which considers due to the high switching frequency only the inductances, which are limiting the zero-sequence current $i_{d,0}$. The zero-sequence current $i_{d,0}$ magnetizes the air-gap of the two half-motors BM (Fig. 1) with a field space harmonic of order three ($\nu = 3$). It magnetizes additional regions in the slots and winding overhangs as well. The equivalent leakage inductance is named $L_{\sigma,0,BM}$ for A and B. It also magnetizes the leakage inductance of the magnetic bearing AMB (Fig. 1) itself, which is called $L_{\sigma,AMB}$. Finally it magnetizes the magnet bearing air-gap region of interest with a magnetizing inductance $L_{h,AMB}$. Integrating the left side of (9), it can be shown that the third condition is equivalent to (10), where the coefficient k_{eq} characterizes the equivalent voltage divider of the circuit (Fig. 5) according to (11):

$$\frac{k_{eq}}{T_{sw}} \cdot \int_0^{T_{sw}} \sum_{i=U,V,W} (\varphi_{i,A}(t) - \varphi_{i,B}(t)) \cdot dt = u_{d,0}(t), \quad (10)$$

$$k_{eq} = \frac{L_{h,AMB} + L_{\sigma,AMB}}{3 \cdot (L_{h,AMB} + L_{\sigma,AMB}) + 2L_{0,BM}}. \quad (11)$$

In order to obtain a single formulation of the solution, the pulse width t_1 is defined so that t_1 corresponds to the first active voltage state “pnn”, where one of the three phases is at the DC link voltage U_{dc} , while the two others are switched to ground potential. The pulse width t_2 corresponds to the second active voltage state “ppn”, where two of the three phases are switched to U_{dc} , while the remaining one is switched to ground potential. Following this convention, the third condition is reformulated as (12). Finally the solution ($t_{0,A}, t_{0,B}, t_{7,A}, t_{7,B}$) of the problem is given by the intersection of three hyper-surfaces in $\mathbb{R}_{\geq 0}^4$, defined by (8) and (12). As a consequence, the solution can be underdetermined, or a single point, or there can be

no solution at all. The underdetermined case occurs, when the reference zero-sequence voltage $u_{d,0}$ is small enough, and the inverter has enough voltage reserve, (i.e., when the modulated active voltage vectors $(u_{\alpha,A}, u_{\beta,A})^T$ and $(u_{\alpha,B}, u_{\beta,B})^T$ in windings A and B are below the maximal admissible voltage vector amplitude). In the underdetermined case, the additional constraint (13) is proposed where the pulse widths $t_{Z,A}$ and $t_{Z,B}$ are defined in (8) and the pulse width $t_{Z,MB}$ is defined in (12):

$$t_{Z,MB} = t_{7,A} - t_{0,A} - t_{7,B} + t_{0,B} = \frac{2T_{sw} u_{d,0}}{3k_{eq} U_{dc}} \left[\frac{t_{2,A} - t_{1,A}}{3} - \frac{t_{2,B} - t_{1,B}}{3} \right], \quad (12)$$

$$t_{7,A} - t_{0,A} = \frac{t_{Z,A} t_{Z,MB}}{t_{Z,A} + t_{Z,B}} \Leftrightarrow t_{7,B} - t_{0,B} = -\frac{t_{Z,B} t_{Z,MB}}{t_{Z,A} + t_{Z,B}}, \quad (13)$$

$$(t_{0,i}, t_{7,i}) = (0, t_{z,i}) \text{ or } (t_{z,i}, 0), i = A, B, \quad (14)$$

$$\left. \begin{aligned} t_{0,A} &= \frac{1}{2} \left(t_{Z,A} - \frac{t_{Z,B}}{t_{Z,A} + t_{Z,B}} t_{Z,MB} \right), \\ t_{0,B} &= \frac{1}{2} \left(t_{Z,B} - \frac{t_{Z,A}}{t_{Z,A} + t_{Z,B}} t_{Z,MB} \right), \\ t_{7,A} &= \frac{1}{2} \left(t_{Z,A} + \frac{t_{Z,B}}{t_{Z,A} + t_{Z,B}} t_{Z,MB} \right), \\ t_{7,B} &= \frac{1}{2} \left(t_{Z,B} + \frac{t_{Z,A}}{t_{Z,A} + t_{Z,B}} t_{Z,MB} \right). \end{aligned} \right\} \quad (15)$$

This condition (13) is chosen to get a continuous transition of the solutions $(t_{0,A}, t_{0,B}, t_{7,A}, t_{7,B})$ when $t_{Z,A} = 0$ or $t_{Z,B} = 0$ in (8) (i.e., when one modulated active vector $(u_{\alpha,A}, u_{\beta,A})^T$ or $(u_{\alpha,B}, u_{\beta,B})^T$ reaches the maximal admissible voltage vector amplitude). The Equations (8), (12) and (13) are reformulated in a matrix form and the explicit solution (15) is obtained by inversion of the matrix. When no solution is possible (i.e., when $t_{Z,A} < 0$ or $t_{Z,B} < 0$ or $t_{Z,A} + t_{Z,B} = 0$), the reference voltage amplitude is too high, and/or the inverter has not enough voltage reserve. In this case, the modulator algorithm provides the maximum voltage amplitude available by following the over-modulation (14). For proper operation of the levitated drive however, field weakening operation should be considered. The expression of k_{eq} (11) shows that the magnetizing inductance of the magnetic bearing $L_{h,AMB}$ should be intentionally designed to be big, and the other leakage inductances should be low, to prevent an inverter over-sizing. The two-step calculation is done as follows: During a control period T_{sw} , after all the current control calculations are completed, the reference voltage vector $\mathbf{u} = (u_{d,1}, u_{q,1}, u_{d,-2}, u_{q,-2}, u_{d,0})^T$ in $\{K_{S,0}, K_{dq,1}, K_{dq,-2}\}$ is transformed into the stator sub-spaces $\{K_{S,0}, K_{S,1}, K_{S,-2}\}$ to obtain $\mathbf{u}_S = (u_{\alpha,1}, u_{\beta,1}, u_{\alpha,-2}, u_{\beta,-2}, u_{d,0})^T$. The vector components $u_{\alpha,1}$, $u_{\beta,1}$, $u_{\alpha,-2}$ and $u_{\beta,-2}$ are then projected

on the α - β planes A and B with (6). Thanks to the orthogonality properties explained above, the calculation of the pulse widths $t_{1,A}$ and $t_{2,A}$ (resp. $t_{1,B}$ and $t_{2,B}$, Fig. 4) to modulate solely the voltage components $u_{\alpha,A}$, $u_{\beta,A}$ (resp. $u_{\alpha,B}$, $u_{\beta,B}$) is the same as for the conventional 2 DOF SVM. In a second step, the pulse widths $t_{0,A}$ and $t_{7,A}$ (resp. $t_{0,B}$ and $t_{7,B}$, Fig. 4) of the two zero-voltage switching states $V_{0,A}$ and $V_{7,A}$ (resp. $V_{0,B}$ and $V_{7,B}$) are determined with (15). When there is no solution, (14) is used instead to insure maximum amplitude of the zero-sequence voltage $u_{d,0}$.

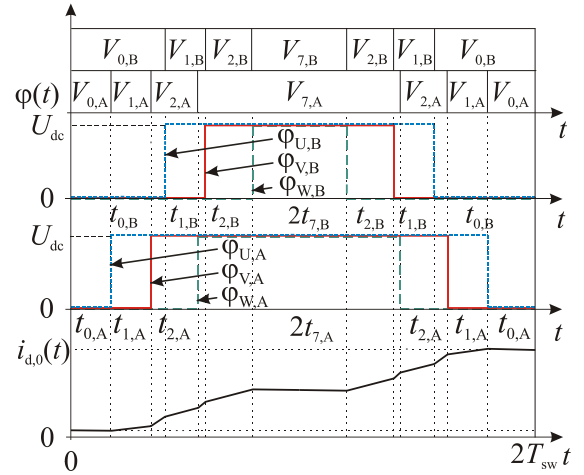


Fig. 4. Example of an asymmetrical pulse pattern for a six-phase system $U_A, V_A, W_A, U_B, V_B, W_B$ (e.g., DE BM) to produce a positive zero-voltage component and two equal active voltage space vectors $(u_{\alpha,A}, u_{\beta,A})^T = (u_{\alpha,B}, u_{\beta,B})^T$. The pulse width of the positive zero-voltage switching state V_7 is larger in the winding A than in the winding B. Hence, the resulting zero-sequence current $i_{d,0}$ increases.

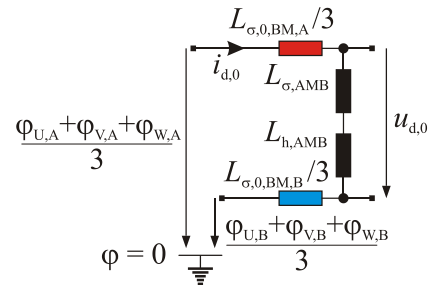


Fig. 5. Simplified inductive equivalent circuit of the zero-sequence component. The two half motors (BM: DE & NDE) are described by the two zero-sequence winding leakage inductances $L_{\sigma,0,BM}$. The axial magnetic bearing is described by a winding leakage inductance $L_{\sigma,AMB}$ and a magnetizing inductance $L_{h,AMB}$.

VI. CONCLUSION

A new six degree of freedom magnetic suspension system is presented. It consists of sets of antisymmetric three phase windings interconnected at the star points. The control of such windings requires an extension of the field orientation control to transform the phase currents into three independent sub-spaces $K_{S,0}$, $K_{dq,1}$, $K_{dq,2}$. A two-step calculation is presented to determine the SVM pulse pattern, which is necessary for the control of the zero-sequence current component $i_{d,0}$.

REFERENCES

- [1] A. Chiba, T. Fukao, O. Ichikawa, M. Oshima, M. Takemoto, and D. G. Dorrell, *Magnetic Bearings and Bearingless Drives*. Oxford: Elsevier Linacre House, 2005.
- [2] P. E. Kascak, "Fully levitated rotor magnetically suspended by two pole-pair separated conical motors," Ph.D. Thesis, Case Western Reserve University, Cleveland (OH, USA), 2010.
- [3] G. Munteanu, A. Binder, and S. Dewenter, "Five-axis magnetic suspension with two conical air gap bearingless PM synchronous half-motors," in *Proceedings of the International Symposium on Power Electronics, Electrical Drives, Automation and Motion (SPEEDAM), 2012*, pp. 1246-1251, Sorrento, Italy, 20-22 June 2012.
- [4] J. Asama, Y. Hamasaki, T. Oiwa, and A. Chiba, "Proposal and analysis of a novel single-drive bearingless motor," in *IEEE Transactions on Industrial Electronics*, vol. 60, no. 1, pp. 129-138, Jan. 2013.
- [5] Q. D. Nguyen and S. Ueno, "Analysis and control of non-salient permanent magnet axial gap self-bearing motor," in *IEEE Transactions on Industrial Electronics*, vol. 58, no. 7, pp. 2644-2652, July 2011.
- [6] J. Abrahamsson, J. Ogren, and M. Hedlund, "A fully levitated cone-shaped Lorentz-type self-bearing machine with skewed windings," in *IEEE Transactions on Magnetics*, vol. 50, no. 9, pp. 1-9, Sept. 2014.
- [7] G. Wu, X. Wang, Q. Ding, and T. Ni, "Design and analysis of a novel axial actively regulated slotless skew winding bearingless motor," in *IEEE International Conference on Mechatronics and Automation (ICMA), 2015*, Beijing, China, pp. 1864-1869, 2-5 Aug. 2015.
- [8] G. Messenger and A. Binder, "Analytical comparison of conventional and modified winding for high speed bearingless permanent magnet synchronous motor applications", in *International Conference on Optimization of Electrical and Electronic Equipment (OPTIM), 2014*, Brasov, Romania, pp. 330-337, 22-24 May 2014.



Gael Messenger was born in Cannes La Bocca in France. He received the M. degree in Electrical Engineering from the Technical University of Darmstadt, Darmstadt, Germany, in 2012 where he is currently working toward the Ph.D. degree. His current research interests include design and control of high speed bearingless motors.



Andreas Binder Senior Member IEEE, Member VDE, IET, VDI, EPE, received the degrees Dipl.-Ing. (diploma) and Dr. Techn. (Ph.D.) for Electrical Engineering from the University of Technology, Vienna/Austria, in 1981 and 1988, respectively. From 1981 to 1983 he worked at ELIN-Union AG, Vienna, on large synchronous generator design. From 1983 to 1989 he joined the Institute of Electrical Machines and Drives, Technical University, Vienna, as Researcher. From 1989 to 1997 he rejoined industry, leading groups for developing DC and inverter-fed AC motors and drives, at Siemens AG, Bad Neustadt and Erlangen, Germany. Since 1994 he is Lecturer (habilitation) at University of Technology, Vienna/Austria, and received in 1997 the ETG-Literature Award of the German Assoc. of Electrical Engineers, VDE. Since October 1997, he is Head of the Institute of Electrical Energy Conversion, Darmstadt University of Technology, as a Full Professor, being responsible for teaching and research for electrical machines, drives and railway systems. He is the author or co-author of more than 280 scientific publications and two books and holds several patents. He received Dr. h.c. from University of Technology Bucharest in 2007 and is the recipient of the Medal of Honour of the ETG/VDE 2009 for outstanding contributions at VDE.

Magnetic Propulsion Force Calculation of a 2-DoF Large Stroke Actuator for High-Precision Magnetic Levitation System

Mousa Lahdo^{1,2}, Tom Ströhla², and Sergej Kovalev¹

¹Department of Informatics, Electrical Engineering and Mechatronics
University of Applied Sciences Mittelhessen, Friedberg, 61169, Germany
mousa.lahdo@iem.thm.de, sergej.kovalev@iem.thm.de

²Department of Mechatronics
Ilmenau University of Technology, Ilmenau, 98693, Germany
tom.stroehla@tu-ilmenau.de

Abstract — The design of high-precision magnetic levitation positioning systems requires fast electromagnetic models. Since three-dimensional finite element method (3D-FEM) is very time-consuming, in order to calculate magnetic forces, an interesting alternative is to determine the forces semi-analytically due to the high accuracy with a short calculation time. In this paper, a new compact semi-analytical equation for determining the magnetic propulsion forces of a new ironless two degrees of freedom (2-DoF) actuator for a high-precision magnetic levitation system is presented. The derived equation is based on the magnetic scalar potential and the Lorentz force law. An important result is that this new expression takes also the position dependence of the propulsion forces over the whole planar stroke into account. The calculated propulsion forces from the derived equations and the verification by 3D-FEM (Maxwell 3D) are presented in this paper as well.

Index Terms — Analytical calculation, ironless actuator, Lorentz force, magnetic levitation, magnetic scalar potential, Maxwell 3D.

I. INTRODUCTION

Due to the ongoing miniaturization of electronic components, many modern applications, such as the semiconductor manufacturing or nanotechnology, requires vacuum compatible planar positioning systems with long planar strokes and precisions up to the nanometer (nm) range [1]. One promising solution to achieve these requirements is the combination of multiple electrodynamic linear actuators with active magnetic guidances in a triangular or rectangular configuration [2].

These high-precision 6-DoF magnetic levitation positioning systems can position objects precisely up to the nm range without any contact in multiple degrees of

freedom with only one moving element [3]. In order to eliminate hysteresis effects, flux saturation and eddy-currents, obtained from ferromagnetic materials, currently most of the high-precision magnetic levitation positioning systems known in the literature are realized with ironless actuators [3]. These ironless actuators consist usually of a stator with air-core coils and a mover with either a Halbach array [4] or a single permanent magnet [5]. The main advantage of the iron-free structure of these systems are the linear relationship between the currents and forces and the fast current changes in the air-core coils, which allows the realization of simple and highly dynamic control algorithms.

For the purpose of designing, analyzing and optimizing of such systems, often 3D-FEM are required and used because the geometry of such positioning systems is a complex 3D problem [6-7]. However, the main problem of 3D-FEM is that it requires partly several hours to obtain a solution, since it needs extremely fine meshing within the air gap as well as the surrounding medium in order to obtain accurate results of the forces and magnetic fields. Consequently, alternative solutions are required in order to calculate magnetic forces and fields very fast [8].

One interesting alternative is the calculation of the magnetic forces and fields analytically, because it combines high accuracy with a very low computational time compared to 3D-FEM [9-11]. Therefore, many scientists calculate forces in planar positioning systems and in ironless systems analytically instead using 3D-FEM [12-14]. Mostly, they focus on the calculation of the repulsive levitation forces of magnetic guidances. However, because of the inherently unstable behavior of repulsive magnetic guidances, the moving magnet experiences, in addition to the levitation force, also a destabilizing force, that intends to push the permanent magnet laterally away from the center position. Thus, the determination of these undesired propulsion forces

are a crucial task, since they must compensate from propulsion actuators in order to restore the lateral stability and to move and position the mover simultaneously.

In this paper, attention is given to the semi-analytical calculation of the planar propulsion forces of a novel 2-DoF actuator presented in [3]. The main contributions are new expressions, which consider the position dependence of the desired propulsion force and the planar destabilizing propulsion forces over the whole planar stroke.

II. 2-DOF ACTUATOR

The actuator under investigation is shown in Fig. 1. This novel 2-DoF actuator for 6-DoF high-precision magnetic levitation systems is proposed in order to overcome the limitations of Halbach arrays and reluctance actuators [3]. It consists of air-core propulsion and guiding coils generating two perpendicular forces (levitation and propulsion) on a single moving magnet. This actuator configuration reduces the mover mass significantly and consequently the power consumption of the guiding coil. A 6-axis motion can be realized with only three or four of such actuators in a triangular or rectangular configuration [3]. As mentioned, the magnetic guiding coil generates not only a desired repulsive levitation force, but also an undesired destabilizing propulsion force. Figure 2 shows a more detailed illustration of this unstable behavior.

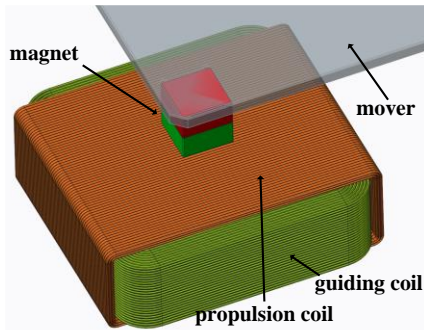


Fig. 1. Ironless 2-DoF actuator.

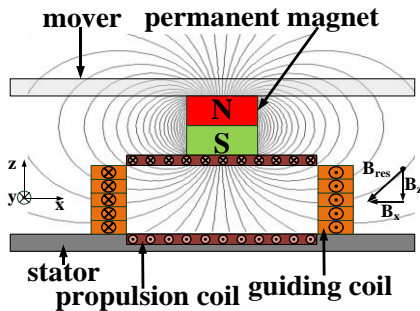


Fig. 2. Generation of the propulsion and levitation force.

As can be seen, the magnetic field generated by the permanent magnet creates flux density components in the x - and z -direction. The x -component of the magnetic flux density creates the desired levitation force, i.e., the motion of the mover along the z -direction is stable. This is because as the air gap increases, the repulsive levitation force decreases and thus, the gravitational force restores the mover in the equilibrium position. Nevertheless, the z -component of the magnetic flux density is responsible for a destabilizing propulsion force that intends to push the permanent magnet away from the equilibrium position. This instability is consistent with Earnshaw's theorem, which states that a stable levitation based only on static magnetic forces between dc coils and permanent magnets is never stable in all directions simultaneously [15]. Consequently, a stable levitation can only be achieved by an additional propulsion actuator in combination with a control system.

However, the total force acting on the permanent magnet is generated according to the electrodynamic principle (Lorentz force) and can be calculated using the Lorentz force formula:

$$\mathbf{F} = \int_{V_{coil}} \mathbf{J} \times \mathbf{B} dV_{coil}, \quad (1)$$

where \mathbf{J} is the current density in the coil, \mathbf{B} the magnetic flux density generated by the neodym-iron-boron ($NdFeB$) permanent magnet and dV_{coil} represents the small volume element in the coils.

A. Analytical calculation of the magnetic flux density

In order to evaluate the Lorentz force according to (1), the first important step is the calculation of the magnetic flux density of the $NdFeB$ permanent magnet inside the coil volume. One possible calculation approach known in the literature is based on the magnetic scalar potential, which results in a reduction of the magnet to a distribution of fictive magnetic charges (magnetic surface charge model) (Fig. 3) [13]. The magnetic surface charge model is derived from the magnetic scalar potential φ . The starting point is Ampere's law for current-free region:

$$\nabla \times \mathbf{H} = 0, \quad (2)$$

where ∇ is the Nabla-Operator and \mathbf{H} is the magnetic field strength.

Since (2) is rotation-free, from a mathematical point of view, the magnetic field strength can be described by introducing a magnetic scalar potential φ [16]:

$$\mathbf{H} = -\nabla \cdot \varphi. \quad (3)$$

Inserting the constitutive relation,

$$\mathbf{B} = \mu_0 \cdot (\mathbf{H} + \mathbf{M}), \quad (4)$$

where μ_0 is the vacuum permeability and \mathbf{M} the magnetization of the permanent magnet into Gauss's law for magnetism:

$$\nabla \cdot \mathbf{B} = 0, \quad (5)$$

yields,

$$\nabla \cdot \mathbf{H} = -\nabla \cdot \mathbf{M}. \quad (6)$$

By introducing a fictive magnetic charge density $\rho = -\nabla \cdot \mathbf{M}$ and using the magnetic scalar potential φ , this results in:

$$\nabla^2 \cdot \varphi_m = -\rho. \quad (7)$$

Under the condition that there are no boundary surfaces in the whole volume, that is $\mu = const.$, and under the assumption of ideal magnets, which are characterized by a fixed and uniform magnetization in the volume of the magnets, the solution for the magnetic scalar potential φ is as follows [13]:

$$\varphi = \frac{1}{4\pi} \oint_{S_{mag}} \frac{\mathbf{M}(\mathbf{r}_Q) \cdot \mathbf{n}}{|\mathbf{r} - \mathbf{r}_Q|} dS_{mag}, \quad (8)$$

where dS_{mag} is the surface that bounds the volume V of the magnet, $\mathbf{r} = \{x, y, z\}$ describes the point of evaluation and $\mathbf{r}_Q = \{x_Q, y_Q, z_Q\}$ describes the position of the source. In free-space, the magnetic flux density can be expressed as:

$$\mathbf{B} = \mu_0 \mathbf{H}, \quad (9)$$

and finally with (8) substitute into (3), (9) becomes:

$$\mathbf{B} = \frac{\mu_0}{4\pi} \oint_{S_{mag}} \mathbf{M}(\mathbf{r}_Q) \cdot \mathbf{n} \cdot \frac{(\mathbf{r} - \mathbf{r}_Q)}{|\mathbf{r} - \mathbf{r}_Q|^3} dS_{mag}. \quad (10)$$

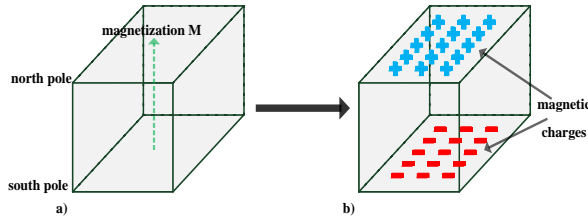


Fig. 3. *NdFeB* permanent magnet (a) and magnetic surface charge model (b).

B. Destabilizing force calculation of the guiding coil

Using (10) and inserting into (1), the total Lorentz force can be generally written as:

$$\mathbf{F} = \int_{V_{coil}} \mathbf{J} \times \left(\frac{\mu_0}{4\pi} \oint_{S_{mag}} \mathbf{M}(\mathbf{r}_Q) \cdot \mathbf{n} \cdot \frac{(\mathbf{r} - \mathbf{r}_Q)}{|\mathbf{r} - \mathbf{r}_Q|^3} dS_{mag} \right) dV_{coil}. \quad (11)$$

In order to calculate the destabilizing propulsion force, we split the whole guiding coil in four identical coil sections according to Fig. 4, where two of the coil sections generate a force in the x -direction (CS1 and CS3), and the remaining coil sections (CS2 and CS4) in the y -direction, respectively. For calculation of the propulsion force in x -direction generated by CS1 and CS3, we determine the z -component of the magnetic flux density B_z :

$$B_z = \mathbf{B} \cdot \mathbf{e}_z = \frac{\mu_0}{4\pi} \oint_{S_{mag}} \mathbf{M}(\mathbf{r}_Q) \cdot \mathbf{n} \cdot \frac{(\mathbf{r} - \mathbf{r}_Q)}{|\mathbf{r} - \mathbf{r}_Q|^3} \cdot \mathbf{e}_z dS_{mag}, \quad (12)$$

and assume also a constant and uniform volume current density in the y -direction (see Fig. 4 (b)):

$$\mathbf{J} = \frac{N \cdot I}{b_{ai} \cdot h} \cdot \mathbf{e}_y, \quad (13)$$

where N is the number of coil turns, I the current through the coil, $b_{ai} \cdot h$ the cross sectional area and \mathbf{e}_y is the unit vector in the y -direction. Under consideration of the parameters, shown also in Fig. 4, the destabilizing propulsion force in x -direction as a function of the current mover position over the whole planar stroke can be calculated according to (14), shown at the bottom of the next page.

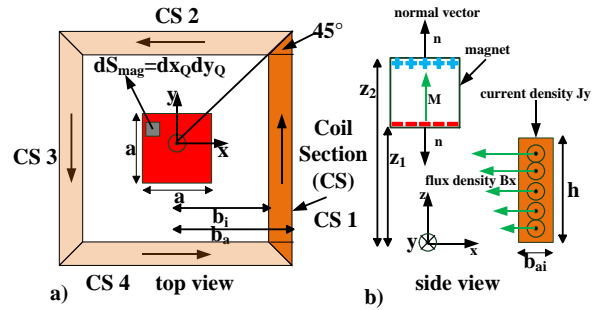


Fig. 4. Geometry of the magnetic guiding coil.

This derived equation is semi-analytical, because this equation requires besides an analytical integration, also a numerical integration.

In the exact manner, we derive (15) in order to calculate the destabilizing propulsion force along the y -direction. Since the undesired destabilizing propulsion forces along the x - and y -direction acts simultaneously on the permanent magnet, the superposition of both forces must be applied in order to determine the total destabilizing force:

$$F_{xy} = \sqrt{F_x^2 + F_y^2}. \quad (16)$$

C. Force calculation of the propulsion coil

The propulsion coil in the 2-DOF actuator contributes towards the desired motion in the planar stroke. The magnitude of the propulsion force component must be bigger than the magnitude of the destabilizing propulsion force components generated by the guiding coil, in order to counteract these destabilizing forces and to move and position the mover precisely within the planar stroke. Similar to the guiding coil, we divide the propulsion coil into four sections as shown in Fig. 5. Only CS2 generates the propulsion force in the desired

direction, whereas the other coil sections generate a force in the opposite direction. To determine the desired propulsion force acting in the x -direction as a function of the current mover position, we calculate the force components of the coil sections using (17–19) with the parameters also shown in Fig. 5. The actual propulsion force on the magnet can be calculated using (20):

$$F_{x,prop} = F_{CS_2} - F_{CS_4} - F_{CS_{13}}. \quad (20)$$

$$F_x = \frac{\mu_0 M N \cdot I}{4\pi b_{ai} h} \left(\sum_{\alpha=0}^1 \sum_{\beta=1}^2 \int_{-\frac{a}{2}+yp}^{\frac{a}{2}+yp} \int_{-\frac{a}{2}+xp}^{\frac{a}{2}+xp} \int_{-\frac{h}{2}}^{\frac{h}{2}} \int_{(1-\alpha) \cdot b_i - \alpha \cdot b_a}^{(1-\alpha) \cdot b_a - \alpha \cdot b_i} \int_{-x}^x \frac{-(-1)^\beta (z - z_\beta)}{\left(\sqrt{(x - x_Q)^2 + (y - y_Q)^2 + (z - z_\beta)^2}\right)^3} dy dx dz dx_Q dy_Q, \quad (14)$$

$$F_y = \frac{\mu_0 M N \cdot I}{4\pi b_{ai} h} \left(\sum_{\alpha=0}^1 \sum_{\beta=1}^2 \int_{-\frac{a}{2}+yp}^{\frac{a}{2}+yp} \int_{-\frac{a}{2}+xp}^{\frac{a}{2}+xp} \int_{-\frac{h}{2}}^{\frac{h}{2}} \int_{(1-\alpha) \cdot b_i - \alpha \cdot b_a}^{(1-\alpha) \cdot b_a - \alpha \cdot b_i} \int_{-y}^y \frac{-(-1)^\beta (z - z_\beta)}{\left(\sqrt{(x - x_Q)^2 + (y - y_Q)^2 + (z - z_\beta)^2}\right)^3} dx dy dz dx_Q dy_Q, \quad (15)$$

$$F_{CS_2} = \frac{\mu_0 M N_p \cdot I_p}{4\pi b_c h_{c1}} \left(\int_{-\frac{a}{2}+yp}^{\frac{a}{2}+yp} \int_{-\frac{a}{2}+xp}^{\frac{a}{2}+xp} \int_{\frac{h_c}{2}}^{\frac{h_c}{2}+h_{c1}} \int_{-\frac{b_c}{2}}^{\frac{b_c}{2}} \int_{-\frac{b_d}{2}}^{\frac{b_d}{2}} \sum_{\beta=1}^2 \frac{-(-1)^\beta (z - z_{\beta p})}{\left(\sqrt{(x - x_Q)^2 + (y - y_Q)^2 + (z - z_{\beta p})^2}\right)^3} dy dx dz dx_Q dy_Q, \quad (17)$$

$$F_{CS_4} = \frac{\mu_0 M N_p \cdot I_p}{4\pi b_c h_{c1}} \left(\int_{-\frac{a}{2}+yp}^{\frac{a}{2}+yp} \int_{-\frac{a}{2}+xp}^{\frac{a}{2}+xp} \int_{-\frac{h_c}{2}}^{\frac{h_c}{2}} \int_{-\frac{b_c}{2}}^{\frac{b_c}{2}} \int_{-\frac{b_d}{2}}^{\frac{b_d}{2}} \sum_{\beta=1}^2 \frac{-(-1)^\beta (z - z_{\beta p})}{\left(\sqrt{(x - x_Q)^2 + (y - y_Q)^2 + (z - z_{\beta p})^2}\right)^3} dy dx dz dx_Q dy_Q, \quad (18)$$

$$F_{CS_{13}} = \frac{\mu_0 M N_p \cdot I_p}{4\pi b_c h_{c1}} \left(\sum_{\alpha=0}^1 \sum_{\beta=1}^2 \int_{-\frac{a}{2}+yp}^{\frac{a}{2}+yp} \int_{-\frac{a}{2}+xp}^{\frac{a}{2}+xp} \int_{-\frac{h_c}{2}}^{\frac{h_c}{2}} \int_{(1-\alpha) \cdot (\frac{b_d}{2} - k) - \alpha \cdot \frac{b_d}{2}}^{(1-\alpha) \cdot \frac{b_d}{2} - \alpha (\frac{b_d}{2} - k)} \int_{-\frac{b_c}{2}}^{\frac{b_c}{2}} \frac{-(-1)^\beta (y - y_Q)}{\left(\sqrt{(x - x_Q)^2 + (y - y_Q)^2 + (z - z_{\beta p})^2}\right)^3} \right. \quad (19)$$

$\cdot dx dy dz dx_Q dy_Q.$

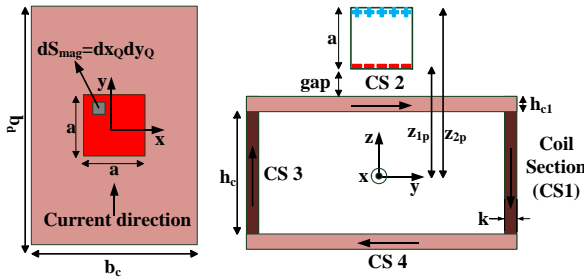


Fig. 5. Geometry of the magnetic propulsion coil.

III. RESULTS AND DISCUSSION

As already mentioned, the quintuple equations are semi-analytical, i.e., after two consecutive analytical integrations with the Symbolic Math Toolbox of MATLAB, it is difficult to express the remaining

The results based on our proposed equations can be used to design the control system. One possible approach is to store the Lorentz force values acting on the permanent magnet as a function of the current mover position in a look up table. Another approach is to use a polynomial function to fit the forces versus x and y . Anyway, both approaches can greatly help in the design of the control system.

expression in an analytical form. Thus, after the analytical integration, we convert the remaining expression in a function handle using *matlabFunction* and used the intern numerical integration function *integral3* to evaluate the remaining triple integral. The function of the numerical integration is used with the default settings. In order to simplify the calculation procedure, a MATLAB program is written which contains the analytical and numerical integration. Based on our MATLAB program, the destabilizing propulsion forces are calculated in millimeters in the horizontal plane from -20 mm to $+20$ mm (Fig. 6).

In order to validate the semi-analytical equations, the Lorentz forces acting on the coils were also predicted using 3D-FEM (Fig. 7). The parameters and dimensions required for the numerical and semi-analytical calculation are given in Table 1.

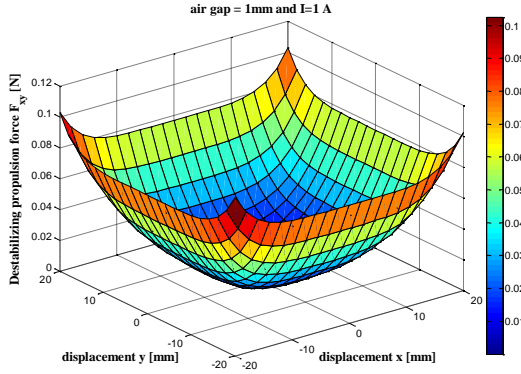


Fig. 6. Calculated destabilizing force.

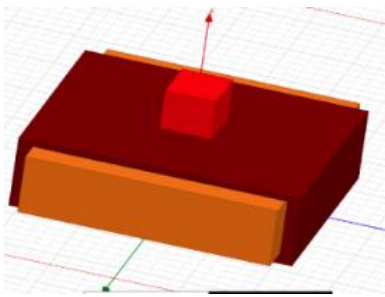


Fig. 7. 3D-FEM model (Maxwell 3D).

Table 1: Parameters for the force calculation

| Parameter | Symbol | Value | Unit |
|------------------------------|---------------|-----------------|-------------------|
| Number of turns | N/N_p | 250 / 200 | |
| Current | I/I_p | 1 / 1 | A |
| Remanence of PM | $\mu_0 M$ | 1.44 | Vs/m ² |
| Coil thickness | b_{ai}/b_c | 10 / 80 | mm |
| Coil height | $h/h_c/k/h_c$ | 30 / 30 / 5 / 3 | mm |
| Coil length | b_d | 110 | mm |
| Magnet length | a | 20 | mm |
| Coil inner side | b_i | 40 | mm |
| Coil outer side | b_a | 50 | mm |
| Neg. magnetic charges height | z_1/z_{1p} | 34 / 19 | mm |
| Pos. magnetic charges height | z_2/z_{2p} | 54 / 39 | mm |

The comparison of the destabilizing force-displacement curves using the derived equations and 3D-FEM is shown in Fig. 8, and the comparison of the propulsion force generated by the propulsion coil can be seen in Fig. 9, respectively. It can be observed in both figures, that the numerical and semi-analytical computation shows a very good agreement. The max. error between the solutions of our equation and the numerical ones in all investigated curves is below 1%. In order to determine the forces over the whole planar stroke, the calculation time of the 3D-FEM takes several hours, whereas the semi-analytical approach with MATLAB

takes only a few seconds. Consequently, our proposed method is a very fast alternative to the time-consuming 3D-FEM and can be used for designing and optimizing the 2-DoF actuator. Moreover, the presented theory in this paper can be easily adopted for other ironless PM-actuators.

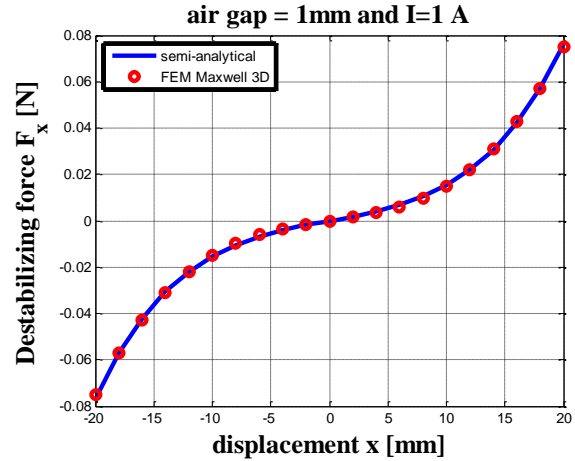


Fig. 8. Force-displacement curve of the guiding coil.

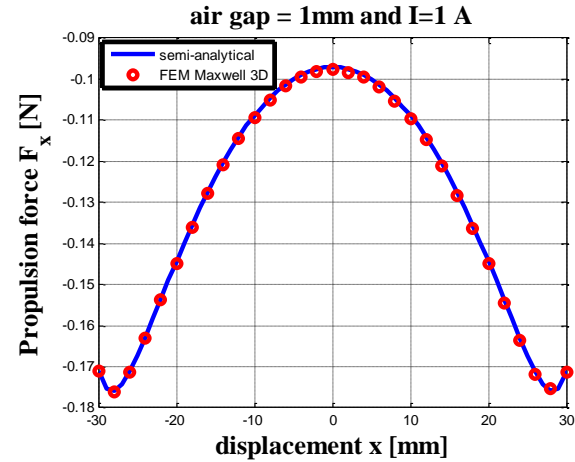


Fig. 9. Force-displacement curve of the propulsion coil.

IV. CONCLUSION

The new equation in this paper for determining the propulsion forces can help to evaluate the performance of our proposed 2-DoF actuator. It allows a very short calculation time compared to 3D-FEM and can be implemented very easy in MATLAB.

The results obtained by our new equation have been compared with 3D-FEM results. Both show a very good agreement with a maximum error of 1%.

The presented theory in this paper can also be used to derive similar semi-analytical equations for analysis, optimization and design issues of other ironless PM-actuators.

REFERENCES

- [1] H. Butler, "Position control in lithographic equipment," *IEEE Control System Magazine*, vol. 31, iss. 5, pp. 28-47, 2011.
- [2] L. Guang, Z. Yu, Z. Ming, D. Guanghong, and M. Tomizuka, "Six-DOF maglev nano precision microstage development," *IEEE International Conference on Mechanic Automation and Control Engineering (MACE)*, Wuhan, China, 2010.
- [3] M. Lahdo and S. Kovalev, "A novel high-precision magnetic levitation system," *Innovative Small Drives and Micro-Motor Systems*, Cologne, Germany, 2015.
- [4] H. Zhu, T. J. Teo, and C. K. Pang, "Conceptual design and modeling of a six degrees-of-freedom unlimited stroke magnetically levitated positioner," *IEEE/ASME International Conference on Advanced Intelligent Mechatronics (AIM)*, Besancon, France, pp. 1569-1574, 2014.
- [5] S. Verma, H. Shakir, and W.-J. Kim, "Novel electromagnetic actuation scheme for multi-axis nanopositioning," *IEEE Trans. on Magnetics*, vol. 42, no. 8, pp. 2052-2062, 2006.
- [6] A. V. Lebedev, E. A. Lomonova, P. G. Van Leuven, and J. Steinberg, "Analysis and initial synthesis of a novel linear actuator with active magnetic suspension," *Industry Applications Conference*, vol. 3, pp. 2111-2118, 2004.
- [7] Y. C. Lai, Y. L. Lee, and J. Y. Yen, "Design and servo control of a single-deck planar maglev stage," *IEEE Trans. on Magnetics*, vol. 43, iss. 6, pp. 2600-2602, 2007.
- [8] S. Mendaci, H. Allag, and M. R. Mekideche, "Multi-objective optimal design of surface-mounted permanent magnet motor using NSGA-II," *Applied Computational Electromagnets Society (ACES) Journal*, vol. 30, no. 5, May 2015.
- [9] J. W. Jansen, J. L. G. Janssen, J. M. M. Rovers, J. J. H. Paulides, and E. A. Lomonova, "(Semi-) analytical models for the design of high-precision permanent magnet actuators," *International Compu-mag Society Newsletter*, vol. 16, no. 2, pp. 4-17, 2009.
- [10] S. Wu, S. Zuo, X. Wu, F. Lin, and J. Shen, "Magnet modification to reduce pulsating torque for axial flux permanent magnet synchronous machines," *Applied Computational Electromagnets Society (ACES) Journal*, vol. 31, no. 3, Mar. 2016.
- [11] A. Shiri and A. Shoulaie, "Calculation of the magnetic forces between planar spiral coils using concentric rings," *Applied Computational Electromagnets Society (ACES) Journal*, vol. 25, no. 5, May 2010.
- [12] H. Jiang, X. Huang, G. Zhou, Y. Wang, and Z. Wang, "Analytical force calculation for high-precision planar actuator with Halbach magnet array," *IEEE Trans. on Magnetics*, vol. 45, no. 10, pp. 4543-4546, 2009.
- [13] J. W. Jansen, J. P. C. Smeets, T. T. Overboom, J. M. M. Rovers, and E. A. Lomonova, "Overview of analytical models for the design of linear and planar motors," *IEEE Trans. on Magnetics*, vol. 50, no. 11, 2014.
- [14] E. P. Furlani, "A formula for the levitation force between magnetic disks," *IEEE Trans. on Magnetics*, vol. 29, iss. 6, pp. 4165-4169, 1993.
- [15] S. Earnshaw, "On the nature of the molecular forces which regulate the constitution of the lumeniferous ether," *Trans. Cambridge Philos. Soc.*, vol. 7, pp. 97-112, Mar. 1839.



Mousa Lahdo received the diploma degree in Electrical Engineering from the University of Applied Sciences Mittelhessen in Friedberg, Germany, in 2012. Since then, he is a Research Associate and Ph.D. student at the Department of Mechatronics, Ilmenau University of Technology. His current research interests include magnetic bearings and magnetic levitation systems and novel integrated electro-mechanical actuators and motors for precision engineering systems.



Tom Ströhl researches at the Department of Mechatronics, Ilmenau University of Technology. He teaches Electrical Drive Systems as well as Mechanical and Fluid Actuators. He completed his Ph.D. on the subject of Model-Based Design of Electromagnets and he was involved in the development of the draft for the software SESAM. In numerous research and industrial projects, he gained experience in the design of electromagnetic drives and the magnetic measurement technology. He is co-author of several books on electromagnets and theoretical electrical engineering.



Sergej Kovalev is Professor for Electrical Drives, Electrical Engineering and Measurement Systems at the University of Applied Sciences in Friedberg, Germany, since 2012. He enrolled as a Ph.D. candidate in the Mechatronics Department at Technical University Ilmenau, Germany, in 1995 and received his Ph.D. degree in 2001. He has 14 years industrial experience in the R&D

departments at different firms in Germany. His research interest is the mechatronics of precision engineering, especially direct drives.

Magneto-Mechanical Model of Passive Magnetic Axial Bearings versus the Eccentricity Error, Part I: Physical Mathematical Model

Roberto Muscia

Department of Engineering and Architecture
University of Trieste, Trieste, Italy
muscia@units.it

Abstract — In this paper we illustrate a particular analytical numerical model of passive magnetic bearings with axial magnetization. The approach is based on the magnetic charges method. This method avoids the utilization of the finite element analysis. In relation to the system geometry, we find explicit formulations for computing magnetic fields by simple numerical integrations. A detailed magnetostatic model is developed and the nonlinearity of the magnetization vector \mathbf{M} of the ring magnets can be considered by a very simple modification of the equations illustrated. The equations can be immediately implemented in a mathematical software and only few minutes are sufficient to obtain the results.

Index Terms — Levitation, magnetic bearings, magnetostatic field, natural frequencies, stiffnesses.

I. INTRODUCTION

The magnetic levitation allows the suspension of one object above another without the two coming into contact. There are several studies and applications of this phenomenon [1], [2] and one of the best known is represented by passive magnetic bearings [3-6]. Generally these bearings can be of two types depending on the direction of polarization of the rings: axial or radial. In both cases, the forces that keep the rings separate are repulsive. Therefore, the rings of these bearings are arranged with the same poles facing each other. The value of these repulsive forces depends on the air gap between the facing surfaces. The air gap changes as a function of the applied forces. Consequently, it is possible to define a bearing stiffness which varies depending on the magnitude of the load applied and/or by the mutual position of the rings. Since the rotating rings of the magnetic bearings are always keyed to a shaft on which other elements are also fixed, an elastic system characterized by a certain stiffness and mass is defined. Therefore, we can evaluate the natural vibration frequencies of this mechanical system. These frequencies depend on the stiffness and mass suspended by the magnetic levitation. Since the stiffness changes with the

mutual position of each pair of facing rings, the stiffness and the natural frequency of the system vary versus the applied load. Thus, in general, with regard to each stationary working condition of the magnetic bearings, a natural frequency of the system is fixed. In this respect, we have developed a model based on magnetic charges to evaluate stiffnesses and natural frequencies of a magnetic levitation system with a passive axial magnetic bearing. We note that the same procedure can be easily extended to calculate the above mentioned stiffness and frequencies also for passive radial magnetic bearing.

II. CONFIGURATION OF THE SYSTEM

Figure 1 shows the case study. The polarized ring A is fixed. The moving ring of the bearing is denoted by B. The two rings have the facing surfaces polarized with the same pole. The polarized ring B can rotate around its own axis with a certain angular velocity ω and is positioned at a distance t from ring A. Therefore t is the air gap of the bearing. This air gap can also be considered as a translation degree of freedom of the system. The axes of the two rings are parallel but, in general not coaxial. An eccentricity e is defined: e represents a coaxiality error. The ring B supports a mass m whose value is equal to the sum of all the masses rigidly integral with the same ring B. The vertical force \mathbf{F} is the axial force applied to the bearing. The dashed segments a and b represent the two circumferences that pass through the section centers of gravity of the polarized rings. The sections of these rings have been considered to be identical for both rings A and B. The shape of the sections is rectangular. Figure 2 illustrates the magnetization vector \mathbf{M} of A and B. The \mathbf{M} direction is defined by different values of the angle α . Three cases have been considered: $\alpha = 90, 60, 30$ degrees. The discrete variability of the angle α has only been considered for illustrating a general procedure to obtain the equations of the field and the forces when the magnetization \mathbf{M} depends on the same α and possibly on the radius. For simplicity, such procedure is illustrated by fixing the module of \mathbf{M} to a constant value. Moreover, its direction does not change when the planes π_1 and π_2 ,

to which \mathbf{M} belongs, radially move towards or away from the respective axes of the magnets A and B (see Fig. 2). If \mathbf{M} depends on α and the radius r (the distance from the axes of the magnets), in all the integrals indicated in the following Section III, \mathbf{M} and the other quantities versus α and r must remain under the integral sign (in this case the magnetization model is not linear). Moreover, also the volume charge density $\rho_M(\mathbf{P})$ defined in the generic point P (end of the vector \mathbf{P}) of the permanent magnets has to be considered. In the case study (\mathbf{M} and α are constants), since the magnetization model is linear, the inclined magnetization can be decomposed in an axial and a circular component independent of α and r . The circular component defines a flux inside the magnet and does not generate any external magnetic field outside the same magnet. Therefore, the circular components of \mathbf{M} of the two polarized rings cannot interact since they produce no field and force outside the magnets. This consideration will be also illustrated by the numerical examples.

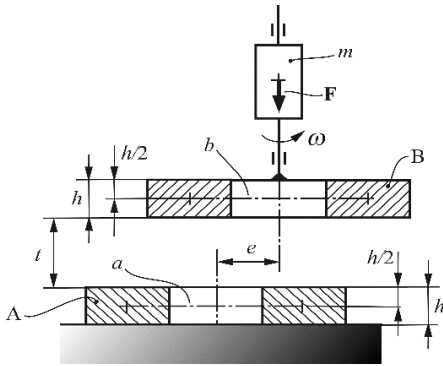


Fig. 1. Axially polarized rings with eccentricity e .

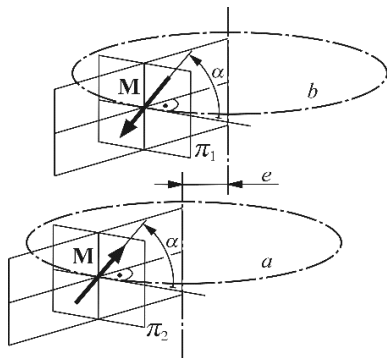


Fig. 2. Direction of the magnetization vectors \mathbf{M} in the two polarized rings.

III. EVALUATION OF THE MAGNETIC FIELD

The calculation of the levitation forces has been performed by using the magnetostatic model and the

magnetic charge method [7-9]. The surface charge density $\sigma_M(\mathbf{P})$ and the volume charge density $\rho_M(\mathbf{P})$:

$$\sigma_M(\mathbf{P}) \equiv \mathbf{M}(\mathbf{P}) \cdot \hat{\mathbf{n}}, \quad (1)$$

$$\rho_M(\mathbf{P}) \equiv -\nabla \cdot \mathbf{M}(\mathbf{P}), \quad (2)$$

were considered. This method can be considered a valid alternative to the finite element method that is often utilized [10], [11]. As a matter of fact, the time computation and the accuracy of the results can improve, even though an analytical formulation is necessary.

A. Surface charge density $\sigma_M(\mathbf{P})$ for the polarized rings A and B

In Fig. 3 an infinitesimal element of the magnet A is illustrated. The point P represents the center of the element. The element shows six infinitesimal faces denoted by dS_1, dS_2, \dots , and dS_6 . The correspondent normal versors are $\hat{\mathbf{n}}_1, \hat{\mathbf{n}}_2, \dots$, and $\hat{\mathbf{n}}_6$. The expressions of the versors can be suitably expressed versus the angle θ . The magnetization vector $\mathbf{M}(M_x, M_y, M_z)$ is applied to the point P of the infinitesimal magnet illustrated in Fig. 3. The moduli with the signs M_x, M_y , and M_z of the components of \mathbf{M} can be expressed versus the angles θ and α (see Fig. 4). By using Eq. (11), we obtain the six surface charge densities σ_{MAi} relative to the surfaces dS_i ($i=1, 2, \dots, 6$) of the infinitesimal magnet A:

$$\sigma_{MA1} = M \sin \alpha, \quad (3)$$

$$\sigma_{MA2} = -M \sin \alpha, \quad (4)$$

$$\sigma_{MA3} = -M \cos \alpha, \quad (5)$$

$$\sigma_{MA4} = M \cos \alpha. \quad (6)$$

For the surfaces dS_5 and dS_6 , σ_{MA5} and σ_{MA6} are equal to zero (\mathbf{M} is always perpendicular to the normal straight line of the surfaces dS_5 and dS_6). The surface charge densities σ_{MBi} of the polarized ring B are obtained by changing the sign of the σ_{MAi} .

B. Volume charge density $\rho_M(\mathbf{P})$ for the polarized rings A and B

By observing Figs. 3 and 4 we obtain:

$$M_x = -M \cos \alpha \frac{p_y}{\sqrt{p_x^2 + p_y^2}}, \quad (7)$$

and

$$M_y = M \cos \alpha \frac{p_x}{\sqrt{p_x^2 + p_y^2}}, \quad (8)$$

where p_x, p_y , and p_z are the components of the vector \mathbf{P} that identifies the point P. By using Eq. (2) and by deriving

Eqs. (7) and (8) with respect to p_x , and p_y , respectively, we obtain:

$$\frac{\partial M_x}{\partial p_x} = M \cos \alpha \frac{p_x p_y}{(p_x^2 + p_y^2)^{3/2}}, \quad (9)$$

and

$$\frac{\partial M_y}{\partial p_y} = -M \cos \alpha \frac{p_x p_y}{(p_x^2 + p_y^2)^{3/2}}. \quad (10)$$

The partial derivative $\partial M_z / \partial p_z$ is equal to zero. By substituting Eqs. (9), (10), and $\partial M_z / \partial p_z = 0$ in Eq. (2), we note that volume charge density $\rho_{MA}(\mathbf{P})$ is always equal to zero. For the magnet B we obtain the same result, i.e., $\rho_{MB}(\mathbf{P}) = 0$, whatever the value of α is.

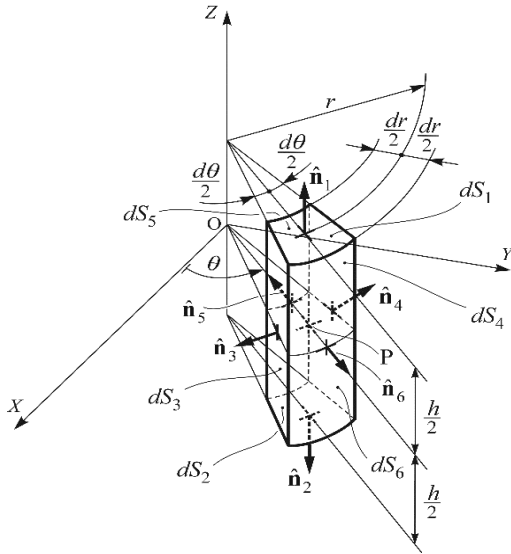


Fig. 3. Infinitesimal element of the polarized ring A with versors outgoing from the surfaces.

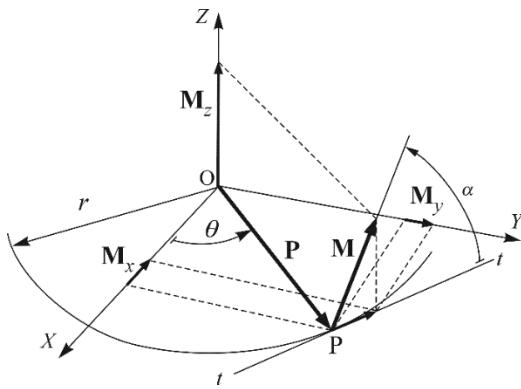


Fig. 4. Magnetization vectors components \mathbf{M}_x , \mathbf{M}_y , and \mathbf{M}_z , in the generic point P of the magnet A (see Fig. 3). $t-t$ is the tangent to the circumference of radius r in P (\mathbf{P} is always perpendicular to $t-t$).

C. Surfaces dS_1, dS_2, \dots , and dS_4

In order to evaluate the magnetic induction generated by the magnet A and the forces/moments applied to the magnet B, since σ_{MA5} , σ_{MB5} , σ_{MA6} , and σ_{MB6} are equal to zero, we evaluate the only expressions of the surfaces dS_1, dS_2, \dots , and dS_4 . By observing Fig. 5, we can define the expressions of the infinitesimal surfaces dS_i with $i=1, 2, \dots, 4$ versus $d\theta$, dr and h . Denoting by $\mathbf{P}_i(p_{xi}, p_{yi}, p_{zi})$ the vectors that identify the centers P_i of the above-mentioned surfaces dS_i , we obtain the expression of the components p_{xi} , p_{yi} , and p_{zi} in function of θ , r and h .

D. Evaluation of the magnetic induction $\mathbf{B}(\mathbf{P}')$

In order to evaluate forces and moments applied to the magnet B, four contributions $\mathbf{B}_1(\mathbf{P}')$, $\mathbf{B}_2(\mathbf{P}')$, \dots , $\mathbf{B}_4(\mathbf{P}')$ of the magnetic induction have to be considered. \mathbf{P}' is the vector that identifies the point where the magnetic induction will be computed is given by [4]:

$$\mathbf{B}_i(\mathbf{P}') = \frac{\mu_0}{4\pi} \int_{S_i} \frac{\sigma_{MA_i}(\mathbf{P})(\mathbf{P}' - \mathbf{P})}{|\mathbf{P}' - \mathbf{P}|^3} dS_i, \quad (11)$$

with $i=1, 2, \dots, 4$. μ_0 is the free space permeability. The volume contribution to $\mathbf{B}_i(\mathbf{P}')$ is always equal to zero because $\rho_{AM}(\mathbf{P}) = 0$. By substituting Eqs. (3)-(6) and the expressions of p_{xi} , p_{yi} , and p_{zi} versus θ , r and h in Eq. (11), we achieve the components $B_{xi}(\mathbf{P}')$, $B_{yi}(\mathbf{P}')$, and $B_{zi}(\mathbf{P}')$ of $\mathbf{B}_i(\mathbf{P}')$. For example, the components $B_{xi}(\mathbf{P}')$ is the following:

$$B_{xi}(\mathbf{P}') = \frac{\mu_0 M \sin \alpha}{4\pi} \int_0^{2\pi} \int_{r_i}^{r_e} \frac{(p'_x - r \cos \theta) r}{\left[(p'_x - r \cos \theta)^2 + (p'_y - r \sin \theta)^2 + (p'_z - h/2)^2 \right]^{3/2}} d\theta dr. \quad (12)$$

The other components have a similar formulation. The components $B_x(\mathbf{P}')$, $B_y(\mathbf{P}')$ and $B_z(\mathbf{P}')$ of the resultant magnetic induction $\mathbf{B}(\mathbf{P}')$ in the generic point \mathbf{P}' of the B magnet surfaces are obtained by adding the correspondent components $B_{xi}(\mathbf{P}')$, $B_{yi}(\mathbf{P}')$, and $B_{zi}(\mathbf{P}')$ with $i=1, 2, \dots, 4$. Since the sign of $B_{xi}(\mathbf{P}')$, $B_{yi}(\mathbf{P}')$, and $B_{zi}(\mathbf{P}')$ is opposite to the sign of $B_{xi+1}(\mathbf{P}')$, $B_{yi+1}(\mathbf{P}')$, and $B_{zi+1}(\mathbf{P}')$, respectively, when i is equal to 3 and 4 and the corresponding moduli are equal to each other, we have:

$$B_x(\mathbf{P}') = B_{x1}(\mathbf{P}') + B_{x2}(\mathbf{P}'), \quad (13)$$

and analogous expressions of $B_y(\mathbf{P}')$ and $B_z(\mathbf{P}')$.

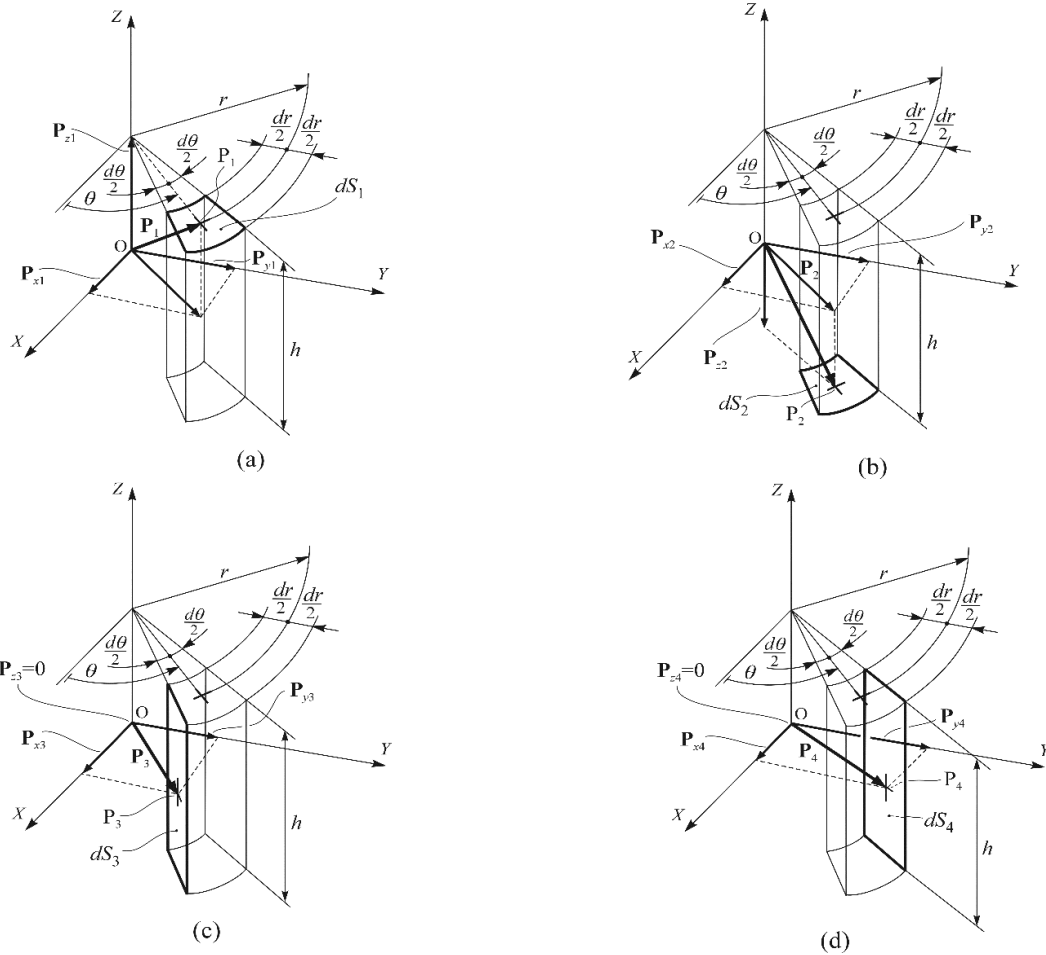


Fig. 5. Evaluation of: (a) dS_1 , (b) dS_2 , (c) dS_3 , and (d) dS_4 with the relative P_1 , P_2 , P_3 , and P_4 centres (see also Fig. 3) in the magnet A.

IV. EVALUATION OF FORCES AND MOMENTS APPLIED TO THE POLARIZED RING B

With reference to Fig. 6, the infinitesimal resultant force $d\mathbf{F}$ applied from the magnet A to a generic infinitesimal element of the magnet B is obtained by adding four force $d\mathbf{F}_i$ ($i=1, 2, \dots, 4$):

$$d\mathbf{F} = d\mathbf{F}_1 + d\mathbf{F}_2 + d\mathbf{F}_3 + d\mathbf{F}_4. \quad (14)$$

Each of them is applied to the correspondent surfaces dS_i that define the infinitesimal element of the polarized ring B (see Fig. 6). We observe that these surfaces have the same expressions of the correspondent surfaces defined for the magnet A. Since the surfaces charges densities σ_{MB5} and σ_{MB6} are equal to zero, the surfaces dS_5 and dS_6 relative to the ring B do not give any contribution to $d\mathbf{F}$. By denoting $\mathbf{P}'_i(p'_{xi}, p'_{yi}, p'_{zi})$ the vectors that identify the centers P'_i of the above-mentioned surfaces dS_i ($i=1, 2, \dots, 4$), we can define the expressions of p'_{xi} ,

p'_{yi} , and p'_{zi} versus p_{xi} , p_{yi} , p_{zi} , e , and t (see Fig. 6). The forces $d\mathbf{F}_i$ are applied to the points P'_i . The evaluation of $d\mathbf{F}_i$ is performed by the following relation:

$$d\mathbf{F}_i = \sigma_{Bi}(\mathbf{P}'_i)\mathbf{B}(\mathbf{P}'_i) dS_i, \quad (15)$$

where $i=1, 2, \dots, 4$. By using Eq. (13) and the analogous expressions of $B_y(\mathbf{P}')$ and $B_z(\mathbf{P}')$, integrating Eq. (15), we compute the moduli with the signs F_{xi} , F_{yi} , and F_{zi} of the \mathbf{F}_i components. For example, the components F_{x1} and F_{x3} are the following:

$$F_{x1} = -M \sin \alpha \int_0^{2\pi} \int_{r_i}^{r_e} B_x(\mathbf{P}'_1) r d\theta dr, \quad (16)$$

$$F_{x3} = M \sin \alpha \int_{r_i}^{r_e} B_x(\mathbf{P}'_3) h dr. \quad (17)$$

The other components have an analogous formulation. Therefore, by adding the four forces \mathbf{F}_i (F_{xi} , F_{yi} , F_{zi}) we obtain the resultant force applied to the ring B.

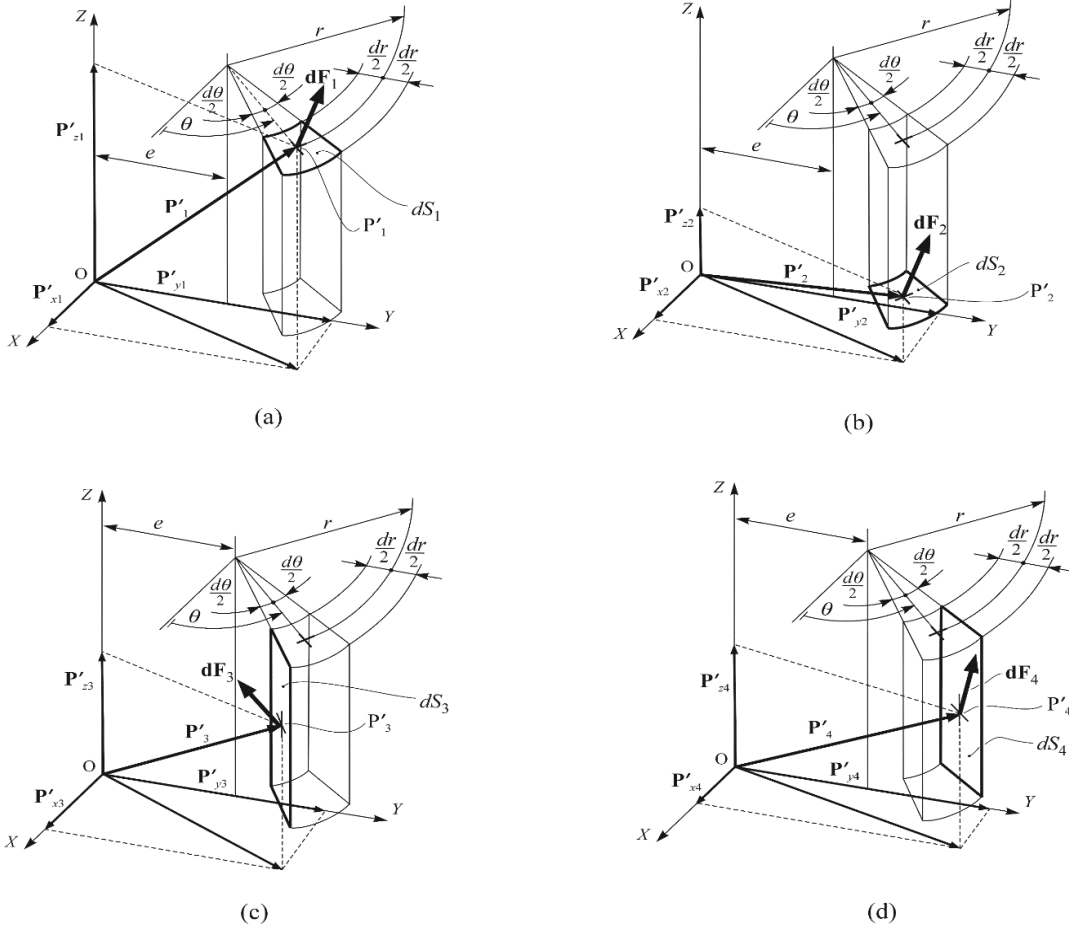


Fig. 6. Infinitesimal forces: (a) $d\mathbf{F}_1$, (b) $d\mathbf{F}_2$, (c) $d\mathbf{F}_3$, and (d) $d\mathbf{F}_4$ applied to the corresponding centres P_1 , P_2 , P_3 , and P_4 of the surfaces dS_1 , dS_2 , dS_3 , and dS_4 of the infinitesimal element of the magnet B.

V. EVALUATION OF THE TORQUE APPLIED TO THE POLARIZED RING B

In order to check the correctness of the physical mathematical model, it is suitable to verify the law of energy conservation. This check can be performed by computing the moment component τ_z along the axis Z applied from the ring A to the ring B. τ_z must always be equal to zero, whatever the values of α and e are. If this condition is not met, the law of energy conservation is not verified and the model is wrong (the ring B spontaneously rotates). The computation of τ_z is performed by integrating the following relation:

$$d\tau_z = d\tau_{z1} + d\tau_{z2} + d\tau_{z3} + d\tau_{z4}, \quad (18)$$

where

$$d\tau_{zi} = d\mathbf{F}_i \times \mathbf{P}'_i, \quad (19)$$

and $i=1, 2, \dots, 4$. $d\tau_{zi}$ represents the moment around the axis Z generated from the force $d\mathbf{F}_i$ applied to the

corresponding surface dS_i of the infinitesimal element of the ring B. Therefore, by Eqs. (18) and (19) we obtain the following modulus with sign of τ_z :

$$\begin{aligned} \tau_z = M \sin \alpha \int_0^{2\pi} \int_{r_i}^{r_e} r [B_x(r \cos \theta, r \sin \theta + e, \frac{h}{2} + h + t)(r + e) \sin \theta - \\ B_y(r \cos \theta, r \sin \theta + e, \frac{h}{2} + h + t) r \cos \theta] - \\ r [B_x(r \cos \theta, r \sin \theta + e, \frac{h}{2} + t)(r + e) \sin \theta - \\ B_y(r \cos \theta, r \sin \theta + e, \frac{h}{2} + t) r \cos \theta] d\theta dr. \end{aligned} \quad (20)$$

In relation to the law of energy conservation the value of τ_z computed by Eq. (20) must be equal to zero, whatever the angle α of the magnetization \mathbf{M} is (see Fig. 2). Eq. (20) has been numerically evaluated and in Part II we briefly discuss this aspect. The values of τ_z versus α and e obtained are very small and confirm the

previous statement.

VI. AXIAL/RADIAL STIFFNESSES AND NATURAL FREQUENCIES

A. Stiffnesses

In general, the computation of the stiffness K is based on the following relation:

$$K = \frac{\partial F(p)}{\partial p}, \quad (21)$$

where $F(p)$ is the force versus the parameter p that defines the degree of freedom (DOF) along which the stiffness is computed. In the present study we evaluate the axial stiffness K_t along the axis Z versus the air gap t :

$$K_t = \frac{\partial F_z(t)}{\partial t}, \quad (22)$$

and the radial stiffness K_e along the axis Y where the eccentricity e is defined:

$$K_e = \frac{\partial F_y(e)}{\partial e}. \quad (23)$$

The evaluation of K_e can be interesting also when we study an axial magnetic bearing. As a matter of fact, K_e has to be considered together with the other radial stiffnesses of the two radial bearings keyed on the shaft. The dynamic behaviour of the system also depends on K_e .

B. Natural frequencies

The natural frequencies of a system depend on its mass and stiffness. From the modelization point of view, the number of these frequencies is equal to the number of degrees of freedom of the model. In relation to the device schematized in Fig. 1, we can consider various models. The choice of the model is strictly connected to the dynamic behaviour of the real system that we want study. If a rigid body schematization of the real system is acceptable and the radial bearings of the vertical shaft have a very high radial stiffness, we can modelize the structure by one degree of freedom (DOF) model (the DOF along the axis Z). If the flexural stiffness of the shaft is not high and there are radial excitation forces, it is necessary to introduce new DOFs. Moreover, also if the radial stiffness of the radial bearing is not high, other radial DOFs associated with these bearing have to be considered. We observe that the system can become very complex. The vibrational behavior will depend on nonlinear magnetic stiffnesses and also small chaotic precessional motions can rise. In a demanding practical application, this kind of motions can be due to the alignment errors of the shaft (concentricity, circularity, perpendicularity, plumb, straightness, see Fig. 7 [12]). In the present study we can limit ourselves to two simple cases. The first one considers a model with a DOF only along the axis Z . In the second case the model has a DOF

only along the axis Y . The two models are illustrated in Figs. 8 (a) and 8 (b), respectively. The model of Fig. 8 (a) can be used to study the dynamical behaviour of a device where all the stiffnesses are much higher than the stiffness K_t defined by Eq. (22). In Fig. 8 (a) m_{tot} represents the total suspended mass. Conversely, Fig. 8 (b) shows a model to study a system with a shaft that can only horizontally translate. By this schematization we again assume that the stiffness of all parts of the device are very high with respect to the radial stiffness K_e furnished by Eq. (23). In this case the translation DOF could be due to the radial clearances of the radial bearings. These clearances would allow a small horizontal translation of the rigid shaft. Therefore, the shaft horizontally translates during its rotation. Small rotations around the centres of the bearing could also occur. Nevertheless, if the flexural stiffness of the shaft is high, in general the influence of the corresponding rotational DOFs on the vibration behavior is negligible. With reference to this hypothesis and overall for simplicity, we can consider the simplified model illustrated in Fig. 8 (b). The system would normally be studied by using complex modelizations based on rotor dynamics (see, for example, [13]). The four masses indicated in Fig. 8 (b) represent the point masses to modelize, for example, the rotating mass of a hydrounit for electric generation (see Fig. 9 [12]). If we assume to substitute the oleodynamic thrust bearing (see particular C in Fig. 9) with a passive magnetic axial bearing (see Fig. 1), we can suitably fix the values of m_1, m_2, \dots , and m_4 versus the masses of the various rotating parts of the hydrounit [mass of the thrust bearing, shafts, rotor, turbine (not illustrated), etc.]. Therefore, the mass of the polarized ring B indicated in Fig. 1 contributes to defining the mass m_2 shown in Fig. 8 (b). With reference to the two models illustrated in Fig. 8 we evaluate the corresponding natural angular frequencies ω_{em_h} , $\omega_{em_{tot}}$, ω_{tm_h} , and $\omega_{tm_{tot}}$ of the system by the following relations:

$$\omega_{em_h} = \sqrt{\frac{K_e(e)}{m_1 + m_2 + m_3 + m_4}}, \quad (24)$$

$$\omega_{em_{tot}} = \sqrt{\frac{K_e(e)}{m_{tot}}}, \quad (25)$$

$$\omega_{tm_h} = \sqrt{\frac{K_t(t)}{m_1 + m_2 + m_3 + m_4}}, \quad (26)$$

$$\omega_{tm_{tot}} = \sqrt{\frac{K_t(t)}{m_{tot}}}. \quad (27)$$

As soon as m_{tot}, m_1, m_2, \dots , and m_4 have been fixed and the stiffnesses K_t and K_e are known [see Eqs. (22) and (23)], we can compute the natural angular frequencies

versus the air gap t and the eccentricity e [when we evaluate $K(t)$ we fix a certain value of e and vice versa].

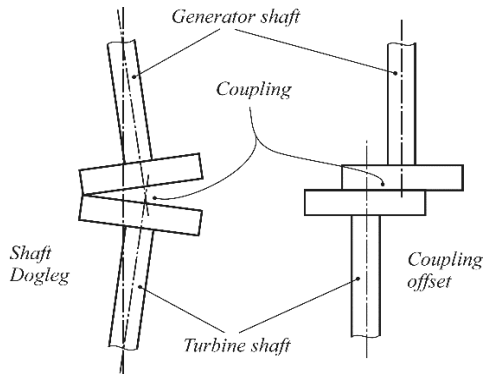


Fig. 7. Alignment errors of a turbine and generator shafts of a hydrounit [12].

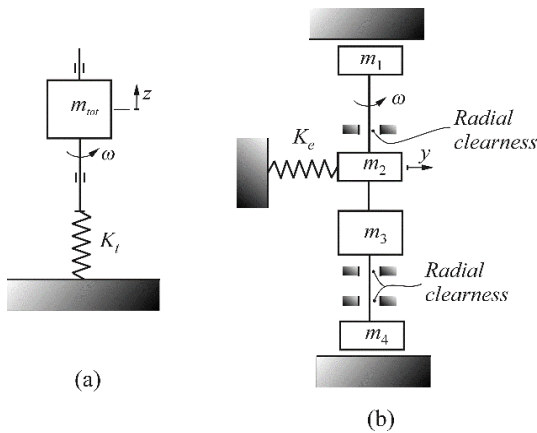


Fig. 8. Simplified physical model of the system with one (a) vertical and (b) horizontal DOF.

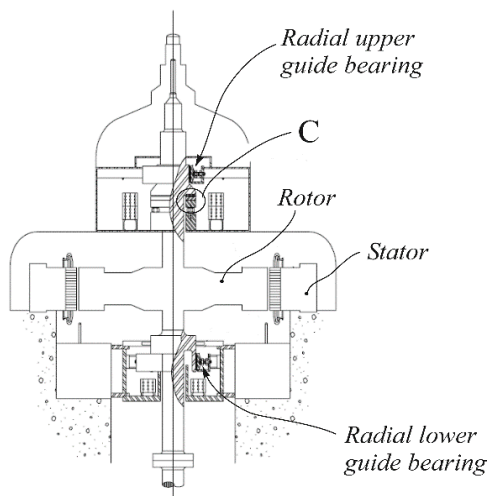


Fig. 9. A typical vertical disposition rotor/stator with thrust bearing C of a hydrounit for electric generation [12].

VII. CONCLUSION

A detailed formulation for evaluating forces, moments, stiffnesses and natural frequencies of a thrust magnetic bearing has been presented. Equations for checking the correctness of the analysis based on the magnetic charges method was considered. A mechanical model referred to a vertical disposition of a hydrounit for electric generation for performing the numerical calculations illustrated in Part II has been developed.

REFERENCES

- [1] H. Li, S. Wang, H. He, Y. Huangfu, and J. Zhu, "Electromagnetic – thermal – deformed – fluid – coupled simulation for levitation melting of titanium," *IEEE Transactions on Magnetics*, vol. 52, no. 3, 7402104, 2016.
- [2] Z. J. Sun, B. Ye, Y. Qiu, X. G. Cheng, H. H. Zhang, and S. Liu, "Preliminary study of a legged capsule robot actuated wirelessly by magnetic torque," *IEEE Transactions on Magnetics*, vol. 50, no. 8, 5100706, 2014.
- [3] J. P. Yonnet, "Passive magnetic bearings and couplings", *IEEE Transactions on Magnetics*, vol. 17, pp. 1169-1173, 1981.
- [4] E. P. Furlani, "A formula for the levitation force between magnetic disks," *IEEE Transactions on Magnetics*, vol. 29, pp. 4165-4169, 1993.
- [5] E. Tripodi, A. Musolino, A. R. Rizzo, and D. Casini, "Stability analysis of a new passive PMS bearing," *Proceedings of ISMB14*, Linz, Austria, August 11-14, 2014.
- [6] E. Rodriguez, J. Santiago, J. Pérez-Loya, F. S. Costa, G. Guilherme, J. G. Oliveira, and R. M. Stephan, "Analysis of passive magnetic bearings for kinetic energy storage systems," *Proceedings of ISMB14*, Linz, Austria, August 11-14, 2014.
- [7] W. F. Brown, Jr., "Electric and magnetic forces: A direct calculation I," *Am. J. Phys.*, vol. 19, pp. 290-304, 1951.
- [8] W. F. Brown, Jr., "Electric and magnetic forces: A direct calculation II," *Am. J. Phys.*, 19, pp. 333-350, 1951.
- [9] E. Furlani, *Permanent Magnets and Electromechanical Devices*. Academic Press, New York, 2001.
- [10] S. Wu, S. Zuo, X. Wu, F. Lin, and J. Shen, "Magnet modification to reduce pulsating torque for axial flux permanent magnet synchronous machines," *ACES Journal*, vol. 31, no. 3, pp. 294-303, March 2016.
- [11] Y. Chen and K. Zhang, "Electromagnetic force calculation of conductor plate double Halbach permanent magnet electrodynamic suspension," *ACES Journal*, vol. 29, no. 11, pp. 916-922, November 2014.
- [12] D. Temple, W. Duncan, and R. Cline, "Alignment of vertical shaft hydrounits," *Hydroelectric Re-*

search and Technical Service Group, Facilities Instructions, Standards and Technique, vol. 2-1, United States Department of the Interior Bureau of Reclamation, Denver, Colorado, 2000.

- [13] S. Y. Yoon, Z. Lin, and P. E. Allaire, *Chapter 2 – Introduction to Rotor Dynamics, in Control of Surge in Centrifugal Compressors by Active Magnetic Bearings*. Springer, London, pp. 17-55, 2013.

Supplementary materials

All the details of the analytical formulations can be requested to the author at muscia@units.it.



Roberto Muscia Professor at the University of Trieste, Trieste, Italy. He received his Master's degree in Mechanical Engineering from the University of Trieste in 1981. From 1983 to 1998 he was Researcher with the same university. From 1998 he is Associate Professor. At the present time his research interests focus on the study of mechanical problems in magnetic devices to improve their design.

Magneto-Mechanical Model of Passive Magnetic Axial Bearings versus the Eccentricity Error, Part II: Application and Results

Roberto Muscia

Department of Engineering and Architecture
University of Trieste, Trieste, Italy
muscia@units.it

Abstract — In this paper we apply the physical mathematical model described in Part I [1]. The study shows: i) the influence of the eccentricity of two polarized rings of the bearing on the stiffness; ii) the numerical efficiency of the response surfaces for evaluating the magnetic field in any point of the domain fixed; iii), in relation to a demanding application example (possible replacement of a big axial oleodynamic bearing with a thrust magnetic passive bearing), the danger arising from possible resonances (the natural frequencies of the device are near to the excitation frequencies).

Index Terms — Levitation, magnetic bearings, magnetostatic field, natural frequencies, stiffnesses.

I. INTRODUCTION

With reference to the formulations illustrated in Part I, some numerical computations to evaluate forces/moments, stiffnesses, and natural frequencies relative to an application example have been performed. The calculation of the magnetic induction was executed first thing. This computation is based on the response surfaces [2]. The components $B_x(\mathbf{P}')$, $B_y(\mathbf{P}')$, and $B_z(\mathbf{P}')$ have been evaluated in a certain number of points suitably arranged on the surface where we compute $\mathbf{B}(\mathbf{P}')$. Subsequently, a surface that interpolates the values of $B_x(\mathbf{P}')$, $B_y(\mathbf{P}')$, and $B_z(\mathbf{P}')$ is defined. The two dimensional domain of the surface is represented by the integration parameters that define the polar coordinates of the generic point \mathbf{P}' (in general these coordinates are r and θ). In Fig. 1, an example of response surface is illustrated. For example, the points \mathbf{P}' where $B_x(\mathbf{P}')$ is computed are indicated by a small circle. In this way we can virtually have infinite points \mathbf{P}' where the magnetic induction is known without performing other integrations: as soon as we fix r and θ we can immediately interpolate the corresponding value of $\mathbf{B}(\mathbf{P}')$. The interpolation is so fast that it is possible to perform the integration to compute forces and moments

in a few seconds. Moreover, as illustrated in Fig. 1, by plotting $B_x(r,\theta)$, $B_y(r,\theta)$, and $B_z(r,\theta)$ a check of the interpolation fitness can be easily performed: the response surface must not show anomalous peaks, it has to be a continuous function of r and θ . All these computations have been performed by using *Mathematica* [3]. These computations can surely be performed by using the finite elements methods [4], [5] but, the computing time can be much longer. In relation to the influence of the inclination angle α of the magnetization \mathbf{M} (see Fig. 2 in Part I [1]), we observe that it has always a constant value. Consequently, the quantity $\sin\alpha$ has always been put out from all the integral signs defined in Part I [1] for computing the magnetic inductions, forces and moments. This fact enables us to compute at once the previous quantities relative to each angle α lower than 90 degrees as soon as the same quantities have been computed with $\alpha=90$ degrees. As a matter of fact, to perform the magnetic inductions computation, we have only to multiply each value obtained with $\alpha=90$ degrees by the sine of the new angle $\alpha < 90$ degrees. In the case of forces, moments, and stiffnesses, the values evaluated with $\alpha=90$ degrees have to be multiplied for the square of the sine of the new angle $\alpha < 90$ degrees.

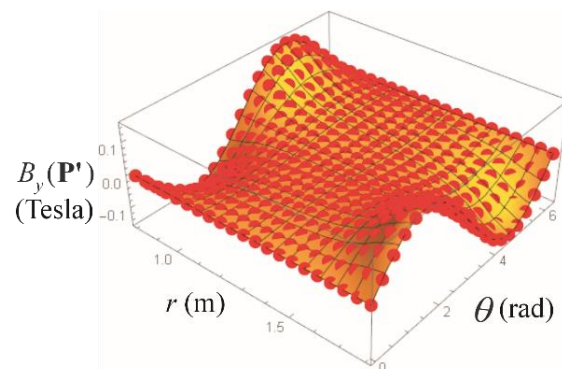


Fig. 1. Response surface for magnetic induction computation relative to 441 points (r,θ) .

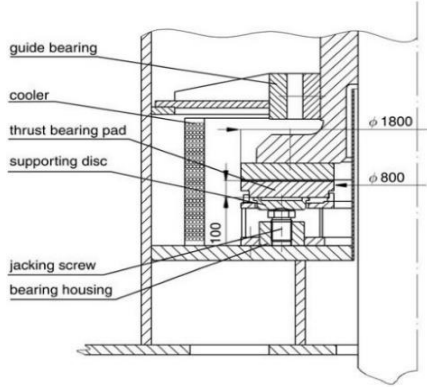


Fig. 2. Some real dimensions of a hydrounit thrust bearing with Kaplan turbine [8].

II. A DEMANDING APPLICATION EXAMPLE

The physical mathematical model previously described in Part I [1] has been applied to define a possible initial step in dimensioning of a thrust magnetic passive bearing. This bearing should be able to generate the same thrust of a big axial oleodynamic bearing assembled in a hydrounit for electrical generation. With reference to an axial passive magnetic bearing that can generate a thrust equal about to 30 KN, some researchers [6], [7] are experimentally testing such kind of solution. In relation to a real hydrounit for electrical generation, in Fig. 2 [8] the inner and outer diameters of the relative oleodynamic bearing are reported in mm. Figure 3 [8] shows the thrust bearing pads of the bearing. The positioning of the bearing is indicated in Fig. 9 in Part I [1] (see the particular C) and the axial dimension of the bearing pads is equal to 100 mm (see Fig. 2). Over the bearing pads, the upper ring integral to the vertical shaft has a thickness also equal about to 100 mm. Unlike the bearing pads, the upper ring rotates together with the shaft. Therefore, in relation to our application example, for the polarized rings illustrated in Fig. 1 in Part I [1] we can fix the following dimensions: $h=100$ mm, $r_i=400$ mm, and $r_e=900$ mm. The bearing pads and the upper ring would be substituted by the polarized rings A and B, respectively. Polarized rings of the previous size could be practically manufactured by superimposing many smaller polarized angular sectors. The thrust that the hydrodynamic bearing generates during a stationary working is very high and is equal to 5.5×10^6 N (with a rotational speed equal to 187.5 rpm). In order to obtain magnetic levitation forces so high, it is necessary to fix a very high value of the magnetization vector \mathbf{M} . Nowadays, with reference to available neodymium magnets, the maximum value of the corresponding module $|\mathbf{M}|$ is equal to 11.38×10^5 A/m [9]. However, as we will discuss in the following Section III, also if we use

this high value of $|\mathbf{M}|$, by considering an air gap ranging from 20 to 30 mm, we obtain about one-fifteenth of the thrust generated by the hydrodynamic bearing illustrated in Figs. 2 and 3. Therefore, in order to achieve the above-mentioned thrust by passive magnetic levitation, it would be necessary to utilize at least sixteen polarized rings B (see Fig. 2 in Part I [1]) integral to the shaft and sixteen rings A integral to the base. From an engineering point of view, this number of rings is certainly too high. However, if we consider a Halbach configuration [10] of each polarized ring as illustrated in Fig. 4 [11], we could reduce the number of the rings magnets in such a way that a feasibility study could be considered. With reference to our demanding application example, since a Halbach magnets configuration could increase the attractive force of about fifty percent, assuming that the increase is true also when the facing magnets that generate repulsive forces, we could utilize only eight pairs of polarized rings. With reference to this configuration we observe that eight rings A (see Fig. 1 in Part I [1]) have to be fixed to the non-rotating frame. The other eight rings B will be fixed to the shaft of the rotor-generator system. For example, four pairs A, B of rings could be arranged to define the upper axial bearing (see the area C in Fig. 9 in Part I [1]). The other four pairs of polarized rings A, B could be put under the rotor. Consequently, the axial height of each upper and lower magnetic passive bearing would be a bit greater than $(100+100+20) \times 4 = 880$ mm [20 mm represents a mean air gap t between each pair of rings and 100 mm is h (see Fig. 1 in Part I [1])]. The values of the air gap have been fixed from a possible engineering point of view in relation to a hypothetic stationary working condition of the device. The natural angular frequencies $\omega_{em_{tot}}$ and $\omega_{tm_{tot}}$ were evaluated with reference to Eqs. (25) and (26) in Part I [1], respectively, by considering the total mass m_{tot} equal to 5.775×10^5 Kg plus 31200 Kg of 16 polarized rings: $m_{tot} = 6.087 \times 10^5$ Kg. The value of 5.775×10^5 Kg is greater than 5% with respect to the value of 5.5×10^5 Kg. The 5.5×10^5 Kg has been simply obtained by computing the mass that corresponds to the load of 5.5×10^6 N due to the gravity acceleration. This load is applied to the oleodynamic bearing. Moreover, in order to compute the frequencies ω_{em_i} and $\omega_{em_{tot}}$ by Eqs. (24) and (25) in Part I [1], respectively, in relation to all the simplifications considered, we can also assume,

$$m_1 + m_2 + m_3 + m_4 = m_{tot}. \quad (1)$$

Consequently, we obtain:

$$\omega_e = \omega_{em_h} = \omega_{em_{tot}}, \quad (2)$$

$$\omega_t = \omega_{tm_h} = \omega_{tm_{tot}}. \quad (3)$$

Moreover, if we consider eight pairs of polarized rings with eight Halbach rings B keyed on the shaft and

eight Halbach rings A fixed to the base of the structure, the stiffnesses K_t and K_e relative to each pair of rings A, B non Halbach must be multiplied by 16 (the magnetic “springs” work in a parallel way). Consequently, the new equations for computing ω_e and ω_t relative to the two uncoupled vertical and horizontal DOFs (Degrees of Freedom) are the following [see Eqs. (22), (23), (25), and (27) in Part I]:

$$K_{tze}(t) = \frac{\partial F_z(t)}{\partial t}, \quad (4)$$

$$\omega_{tze}(t) = \sqrt{\frac{16K_{tze}(t)}{m_{tot}}}, \quad (5)$$

$$K_{ezt}(e) = \frac{\partial F_z(e)}{\partial e}, \quad (6)$$

$$\omega_{ezt}(e) = \sqrt{\frac{16K_{ezt}(e)}{m_{tot}}}, \quad (7)$$

$$K_{eyt}(e) = \frac{\partial F_y(e)}{\partial e}, \quad (8)$$

$$\omega_{eyt}(e) = \sqrt{\frac{16K_{eyt}(e)}{m_{tot}}}. \quad (9)$$

The maximum value of the eccentricity e considered in the numerical simulations was put equal to 0.01 m. However, in relation to a correct working of the hydrounit, $e=0.01$ m certainly is not an acceptable value (it is too high). Maximum values of e about equal or lower than 0.0001 m should be considered. Nevertheless, from the simulation point of view, the previous maximum value $e=0.01$ m has been fixed to test the fitness of the modelization. In this respect, we observe that the forces, stiffnesses, and natural angular frequencies must be always continuous functions of e . Always in order to check the correctness of the model, the air gap t range has been fixed from 0.003 m to 0.5000 m. From a possible practical point of view, when the device works under a stationary condition, the real value of t could reasonably change from 0.01 to 0.05 m.



Fig. 3. Tilting-pads thrust bearing [8].

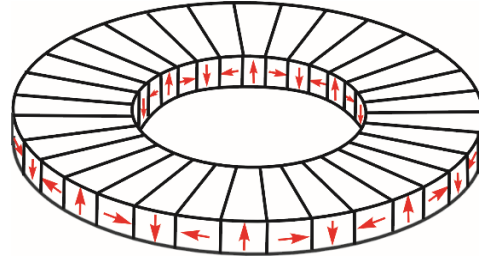


Fig. 4. A Halbach configuration [10] of a polarized ring [11].

III. RESULTS

The results that have been obtained versus the air gap t and the eccentricity e are: i) the magnetic induction \mathbf{B} on the ring horizontal surfaces of the upper magnet; ii) the levitation force; iii) the axial and radial stiffnesses of the bearing; iv) the natural frequencies in correspondence with certain values of the mass m_{tot} . Table 1 summarizes the main data utilized to perform some simulations. The computation of the magnetic induction was executed in the points \mathbf{P}'_1 and \mathbf{P}'_2 of the upper and lower surfaces, respectively, of the polarized ring B. 441 points on each surface have been fixed. The polar coordinates of these points are defined by a radius r and an angle θ (see Fig. 6 in Part I [1]). The values of r and the correspondent angle θ have been fixed by the following relations:

$$r = r_i + \frac{(r_e - r_i)}{k_r} i, \quad (10)$$

$$\theta = \frac{2\pi}{k_\theta} j, \quad (11)$$

where $i=0, 1, \dots, k_r$ and $j=0, 1, \dots, k_\theta$. This kind of discretization of the surfaces allows us to obtain good response surfaces and limit the computation time to few tens of seconds (by using a computer with an Intel I5 and 4 GB of RAM). An example of these results is illustrated in the previously cited Fig. 1. Another example concerning the magnetization induction vectors relative to the upper surface of the ring B with $t=0.050$ m, $e=0.000$ m, and $\alpha=90$ degrees is illustrated in Fig. 5. We observe the complete axial symmetry of the field. The same symmetry characterizes all the magnetic field configurations computed by using any value of the eccentricity e and α (see Table 1). This fact confirms that the law of energy conservation is respected because such a symmetry implies that the moment τ_z around the axis Z [see Eq. (20) in Part I [1]] is always equal to zero. As a matter of fact, the numerical evaluations performed have always given values of τ_z almost equal to zero or relatively small. In this regard, we observe that the component F_x of the resultant force \mathbf{F} applied to the polarized ring B should be equal to zero. Therefore, it

is sufficient that the difference between F_{x1} and F_{x2} (components of the forces applied to the lower and upper surfaces of the ring B, $F_x = F_{x1} + F_{x2}$) is equal to a few newtons and τ_z at once reaches a value higher than zero, for example 3 Nm. Nevertheless, in relation to the precision of the numerical simulations, it is necessary to consider the orders of magnitude of the quantities evaluated. In the case study we observe that F_z and also F_y (when e is greater than zero) are equal to hundred thousands of newtons. Moreover, overall they were computed by a kind of formulation similar to that used to evaluate F_x . Therefore, with reference to the approximations that affect the numerical integration in the study context, we can consider the numerical results obtained for F_x and τ_z very good, i.e., a good approximation of zero. In this respect, a typical trend of F_x versus $0.003 \leq t \leq 0.015$ m (with $e=0$ and $\alpha=90$ degrees) is illustrated in Fig. 6. When different values of the parameter e is fixed, similar trends have been obtained. In relation to the values obtained for F_z versus the air gap t , Fig. 7 shows some curves examples. The curves have been achieved by fixing $\alpha=90, 70,$ and 30 degrees, eccentricity $e=0.000$ m and the values of t reported in Table 1. With reference to a non-operative working condition of the magnetic bearing for the hydrounit application example, we also have performed some calculations with an air gap $t=0.003$ m. In order to assure a non-dangerous working condition of the system, this value is certainly too small. This air gap could be easily set to zero as a consequence of a small axial overload together with planarity, perpendicularity, etc. errors. In this case, to avoid the destruction of the device, mechanical “catcher” bearings could be suitably integrated around and outside the rings of the magnetic bearings. In Fig. 8 the axial stiffnesses $K_{ze}(t)$ corresponding to the previous F_z (see Fig. 7) are reported. These stiffnesses have been evaluated by Eq. (4). Figure 9 shows the relative angular natural frequencies $\omega_{tze}(t)$ computed by Eq. (5). In Fig. 10 a comparison among three functions $F_z(e)$ is presented. Three values of the air gap t have been considered: $t=0.003, 0.010, 0.020$ m. We note that the vertical levitation force changes enough versus the value of t . In relation to the scale of the representation of the graphs, as soon as t is fixed, it could seem that $F_z(e)$ is almost independent of e . Nevertheless, by using Eq. (6) we note that the axial stiffness $K_{ezt}(e)$ shows significantly different trends versus the three values of t (see Fig. 11). If, by Eq. (7) we compute the correspondent axial natural angular frequency $\omega_{ezt}(e)$, we obtain the various resonance conditions of the system along the vertical DOF versus the correspondent values of the eccentricity e . Figure 12 shows $\omega_{ezt}(e)$: it can

change from about 2 to 24 rpm. With reference to the component F_y applied to the polarized ring B, in Fig. 13 the corresponding trend versus e is reported. The curves are relative to the three values of air gap t previously considered. We note that the radial force F_y is sufficiently independent of t and increases almost linearly versus e . By deriving $F_y(e)$ with respect to e , we obtain the radial stiffness K_{eyt} of the levitation system [see Eq. (8)]. Figure 14 shows the functions $K_{eyt}(e)$ versus t . By observing these curves, the nonlinearity of $F_y(e)$ is pointed out. By using Eq. (9) we obtain the correspondent radial natural angular frequencies $\omega_{eyt}(e)$. These frequencies vary from about 64.5 to 68.7 rpm (see Fig. 15). As noted in Section I, the values of forces and stiffnesses relative to an angle α of inclination of the magnetization \mathbf{M} lower than 90 degrees, can be simply obtained by multiplying the corresponding values computed with $\alpha=90$ degrees by $\sin^2 \alpha$. For the correspondent natural angular frequency the multiplicative factor is equal to $\sin \alpha$. Consequently, when α decreases, also the stiffnesses and natural frequencies become lower.

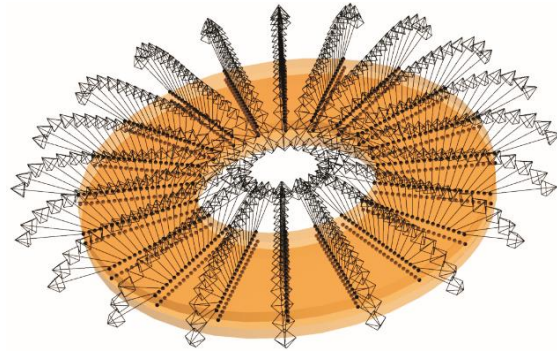


Fig. 5. Magnetization induction vectors in 441 points of the upper surface of the upper polarized ring B (see Fig. 1 in Part I).

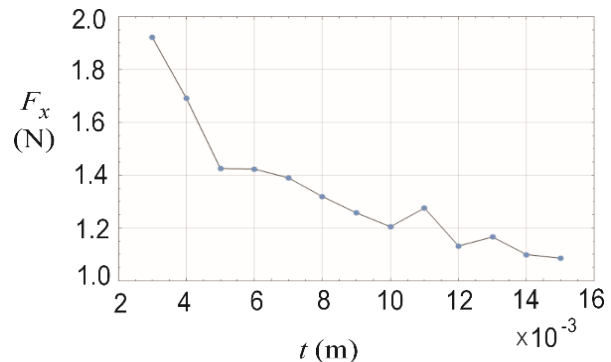


Fig. 6. A typical trend of the radial force F_x when $e=0$ and $\alpha=90$ degrees versus the air gap t .

Table 1: Parameters used for the numerical simulations

| | |
|---|---|
| Module of the Uniform Magnetization $ \mathbf{M} $ | 11.38×10^5 A/m |
| Inner radius of the magnets r_i | 0.4 m |
| Outer radius of the magnets r_e | 0.9 m |
| Free space permeability μ_0 | $4\pi \times 10^{-7}$ Wb/Am |
| α | 90, 70, 30 degrees |
| e | 0.000, 0.001, 0.002, ..., 0.010 m |
| t | 0.003, 0.004, ..., 0.012, 0.015, 0.017, 0.020, 0.025, 0.030, 0.035, 0.040, 0.050, 0.075, 0.100, 0.150, 0.200, 0.300, 0.400, 0.500 m |
| h | 0.1 m |
| m_{tot} | 6.087×10^5 Kg |
| Number k_r of subdivision intervals of $r_e - r_i$ | 20 |
| Number k_θ of subdivision intervals of 2π | 20 |
| Number $(k_r + 1) \times (k_\theta + 1)$ of points where the magnetic induction has been computed | 441 |

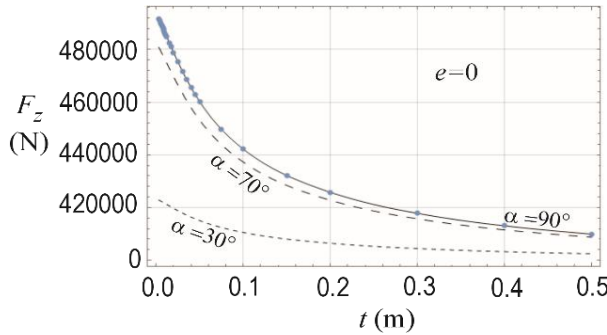


Fig. 7. Vertical levitation force F_z when $e=0$ versus the air gap t and the angle α .

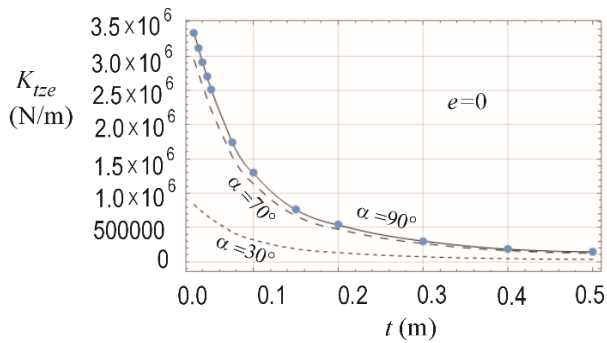


Fig. 8. Stiffnesses K_{tze} versus the air gap t when $e=0$ versus the air gap t and the angle α .

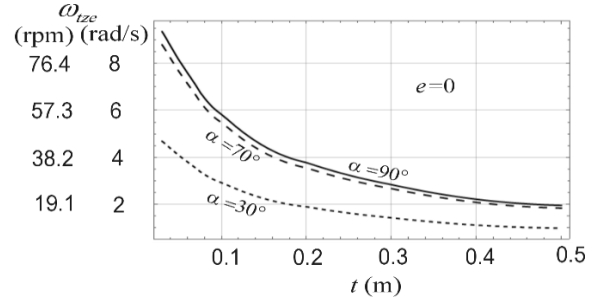


Fig. 9. Axial angular natural frequency ω_{tze} versus the air gap t and the angle α when the eccentricity $e=0$.

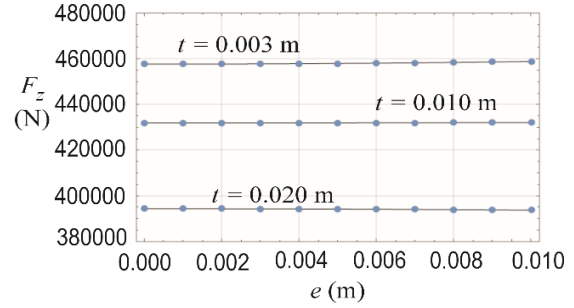


Fig. 10. Interpolation of the force F_z relative to three air gap values t versus the eccentricity e , with $\alpha=90$ degrees.

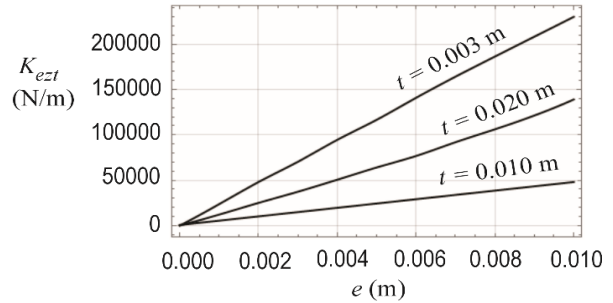


Fig. 11. Axial stiffness K_{ezt} relative to three air gap t values versus the eccentricity e , with $\alpha=90$ degrees.

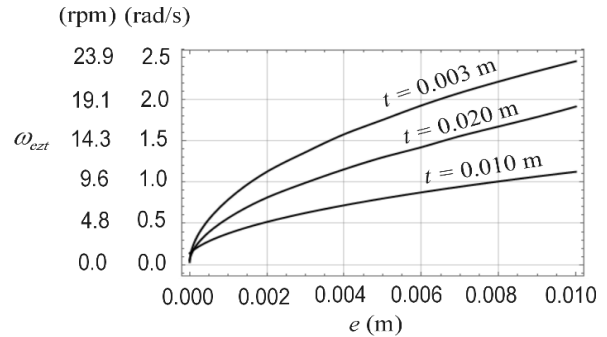


Fig. 12. Axial angular natural frequency ω_{ezt} relative to three air gap t values versus the eccentricity e , with $\alpha=90$ degrees.

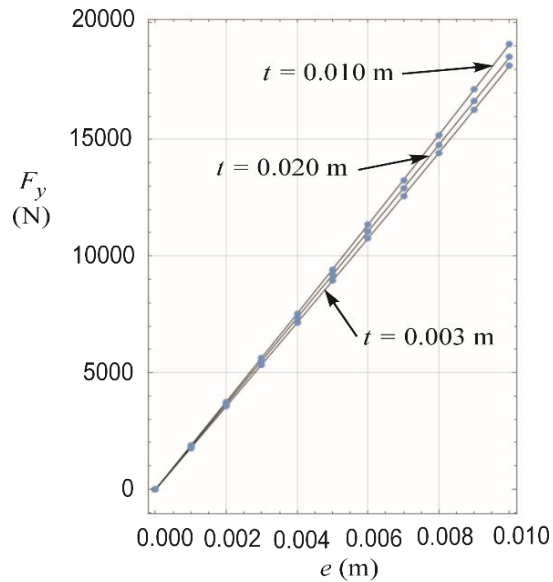


Fig. 13. Force F_y relative to three air gap values t versus the eccentricity e , with $\alpha=90$ degrees.

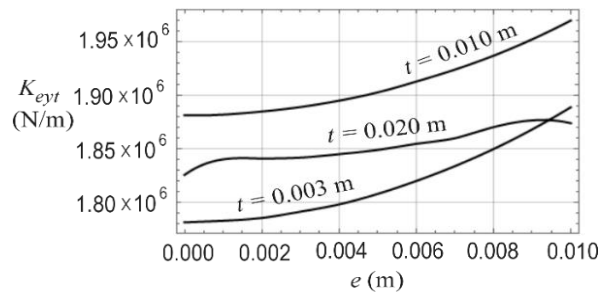


Fig. 14. Radial stiffness K_{eyt} relative to three air gap t values versus the eccentricity e , with $\alpha=90$ degrees.

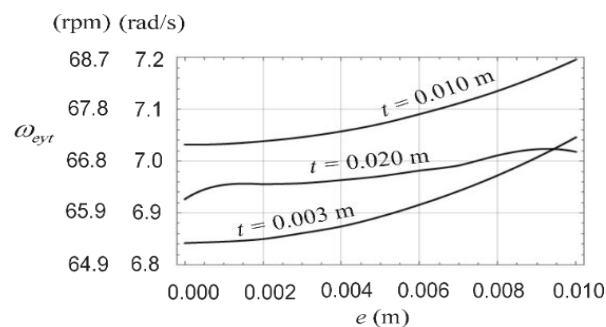


Fig. 15. Radial angular natural frequency ω_{eyt} relative to three air gap t values versus the eccentricity e , with $\alpha=90$ degrees.

IV. SOME CONSIDERATIONS ON THE RESULTS OBTAINED

With reference to the vertical levitation force we note that in the domain $0.000 \leq e \leq 0.010$ m F_z varies very

little (see Fig. 10). Conversely, the corresponding curve of $F_y(e)$ shows an almost linear variation, from 0 to about 20000 N (see Fig. 13). The component $F_x(e)$, in general is several orders of magnitude lower than $F_y(e)$ and, overall, $F_z(e)$. As previously mentioned, $F_x(e)$ should be equal to zero, whatever the value of e is. The irregular trend of $F_x(e)$ depends on the number of effective digits fixed to perform the integrations. In this respect, we note that all the integrations have been performed by setting a precision for the computation with five effective digits of accuracy [3]. If a greater number of effective digits is fixed (for example 15), the computation time becomes very high and, in general, significant improvements of the results are not obtained (only small differences affect the results achieved with 5 and 15 effective digits). From an engineering point of view, we observe that a high value of stiffness (axial and radial) as much as possible independent of the air gap and the eccentricity would be suitable. In the case of the passive magnetic levitation this condition is partially met. Moreover, the angular natural frequencies are lower than the stationary rotation speed of the hydrounit (187.5 rpm). Therefore, during periods of start-ups and shutdowns the system passes more or less quickly through its resonant frequencies. If this passage is not quite fast, dangerous vibrations can arise. With reference to the simplified model illustrated in Fig. 8 (a) in Part I [1], we observe that it can reflect reality better than the one reported in Fig. 8 (b), also in Part I. However, the lateral instability of the magnetic levitation [12] is also confirmed by observing the trend of the force F_y (see Fig. 13): it quickly increases versus the eccentricity. Finally, we observe that in spite of the simplifications, the results obtained and the relative considerations suggest which basic problems can arise if we consider substituting a classic hydrodynamic thrust bearing with passive magnetic bearings. We can note that also the hydrodynamic bearings have their drawbacks [13]. Therefore, possible preliminary studies of alternative solutions could be acceptable.

V. CONCLUSION

The knowledge of the natural vibration frequencies of a system is important to avoid an operating condition where the frequencies of the excitation forces are near or equal to the above-mentioned natural frequencies. The passive bearings are parts of a mechanical system and determine the corresponding natural frequencies versus the applied load and the oscillating masses. In order to avoid dangerous resonances or beats it is convenient to evaluate how these frequencies change in function of different operating conditions. In the case study it was found that a reduction of the air gap beyond certain limits causes a significant increase of the stiffness of the axial bearing. Consequently, we obtain an increase of the natural frequency of the system. Therefore, the larger the load applied the higher the aforesaid frequency. This

behavior is similar to that which was found in another study concerning the passive radial bearings [14]. With reference to the demanding application example, this fact can surely be advantageous if we were able to increase the natural frequencies to a speed higher than the stationary rotational speed of the device (187.5 rpm). Unfortunately, higher natural frequencies correspond to too small air gaps that, from an engineering point of view, cannot be accepted. This problem could be studied and, perhaps, solved, by considering additional permanent magnets. The position of these magnets should be controlled by a feedback system versus the instantaneous values of air gaps and natural frequencies. Finally, if we consider a nonlinear magnetization \mathbf{M} of the ring magnets, the details of the mathematical model illustrated in Part I [1] enable a very fast and easy modification to compute the field and the forces due to the surface charge density $\sigma_M(\mathbf{P})$.

REFERENCES

- [1] R. Muscia, "Magneto-mechanical model of passive magnetic axial bearings versus the eccentricity error, Part I: Physical mathematical model," *ACES Journal*, 2017.
- [2] G. E. P. Box and D. Norman, *Response Surfaces, Mixtures, and Ridge Analyses*, Second edition, Wiley, 2007.
- [3] *Mathematica* 10.3 (2016), <http://www.wolfram.com/mathematica>
- [4] S. Wu, S. Zuo, X. Wu, F. Lin, and J. Shen, "Magnet modification to reduce pulsating torque for axial flux permanent magnet synchronous machines," *ACES Journal*, vol. 31, no. 3, pp. 294-303, March 2016.
- [5] Y. Chen and K. Zhang, "Electromagnetic force calculation of conductor plate double Halbach permanent magnet electrodynamic suspension," *ACES Journal*, vol. 29, no. 11, pp. 916-922, November 2014.
- [6] J. J. Pérez-Loya, C. J. D. Abrahamsson, F. Evestedt, and U. Lundin, "Initial performance tests of a permanent magnet thrust bearing for a hydropower synchronous generator test-rig," *AIM2016*, Bormio, Italy, March 14-16, 2016.
- [7] J. J. Pérez-Loya, J. De Santiago, and U. Lundin, "Construction of a permanent magnet thrust bearing for a hydropower generator test setup," *1st Brazilian Workshop on Magnetic Bearings – BWMB*, Rio de Janeiro, Brazil, October 2013.
- [8] L. Dabrowski and M. Wasilczuk, "Evaluation of water turbine hydrodynamic thrust bearing performance on the basis of thermoelastohydrodynamic calculations and operational data," *Proceedings of the Institution of Mechanical Engineers, Part J: Journal of Engineering Tribology*, vol. 218, pp. 413-421, 2004.
- [9] Neodymium Magnets-An Expert Information Source, E-magnets, UK, Northbridge Road, Berkhamsted, Hertfordshire, HP4 1EH, 2016. <http://www.ndfeb.info.com>
- [10] K. Halbach, "Design of permanent multipole magnets with oriented rare earth cobalt material," *Nucl. Instrum. Methods*, vol. 169, pp. 1-10, 1981.
- [11] D. J. Eichenberg, C. A. Gallo, and W. K. Thompson, "Development and Testing of an Axial Halbach Magnetic Bearing," Report *NASA Center for Aerospace Information*, Hanover, MD 21076-1320, 2006.
- [12] R. J. Duffin, "Free suspension and Earnshaw's theorem," *Archive for Rational Mechanics and Analysis*, vol. 14, iss. 1, pp. 261-263, January, 1963.
- [13] M. Wasilczuk, "Friction and lubrication of large tilting-pad thrust bearings," *Lubricants*, vol. 3, pp. 164-180, 2015.
- [14] L. Zidarič, "Studio delle Configurazioni di Equilibrio di Cuscinetti Magnetici Passivi," *Dissertation* (in Italian), University of Trieste, Department of Engineering and Architecture, Trieste, Italy, 2012.

Supplementary Materials

For further information concerning the *Mathematica* programming, you can contact the author at muscia@units.it.



Roberto Muscia Professor at the University of Trieste, Trieste, Italy. He received his Master's degree in Mechanical Engineering from the University of Trieste in 1981. From 1983 to 1998 he was Researcher with the same university. From 1998 he is Associate Professor. At the present time his research interests focus on the study of mechanical problems in magnetic devices to improve their design.

Performance of Yokeless Heteropolar Electrodynamic Bearings

C. Dumont, V. Kluykens, and B. Dehez

Department of Mechatronic, Electrical Energy, and Dynamic Systems (MEED)
 Université catholique de Louvain, Louvain-la-Neuve, 1348, Belgium
 corentin.dumont@uclouvain.be, virginie.kluykens@uclouvain.be, bruno.dehez@uclouvain.be

Abstract — Electrodynamic bearings (EDBs) are a promising way to support rotors passively with no friction. In particular, heteropolar EDBs could allow for combining the motor and guiding functions, thereby optimizing the use of permanent magnets. Despite this advantage, few efforts have been dedicated to the evaluation and optimization of the performance of heteropolar EDBs. In this paper, the performance of a yokeless topology of heteropolar EDB is evaluated and optimized. This is done by evaluating the parameters of a parametric dynamical model of the EDB using a two-dimensional analytical model of the field distribution in the bearing. Compared to existing EDBs, the present one is shown to achieve a reasonable stiffness to permanent magnet volume ratio at high speeds.

Index Terms — Bearing, electrodynamic, heteropolar, magnetic, optimization, passive, performance.

I. INTRODUCTION

Passive electrodynamic bearings (EDBs) allow to support a rotating object without contact. They are based on the electromagnetic interaction forces between permanent magnets (PMs) and the currents flowing in conductors. These currents are induced by the relative speed between the PMs and the conductors.

For efficiency purposes, EDBs are designed in such a way that there is no variation in the PM flux linked by the winding when the rotor spins in a centered position. As a result, there are no induced currents, no forces, and above all no losses in the bearing when the rotor spins in a centered position. This property is referred to as “null-flux”. It is found in all the designs of EDBs that are studied nowadays [1].

However, when the rotor spins in an off-centered position, currents are induced in the winding. This creates a force on the rotor that tends to restore its centered position. In this case, the energy dissipated in the windings comes from the drive torque on the rotor to keep the spin speed constant. On the one hand, this prevents the operation at zero spin speed. On the other hand, it eliminates the need for an additional electrical power supply to feed the EDBs, as is the case for the

existing active magnetic bearings (AMBs). Furthermore, the absence of control system induces gains in compactness, simplicity, costs and reliability. As a result, EDBs could be well suited for applications where these aspects are critical.

Nevertheless, the stiffness associated with the centering force of EDBs is low compared with AMBs. Moreover, some external damping must be added to the system to allow a stable operation above a given spin speed [2]. In this paper, only non-rotational damping between the rotor and the stator is considered. This damping should be added in a passive way in order to keep the advantages of passive bearings, which can be an issue [2]. Consequently, the bearing radial stiffness and the amount of damping required for stabilization are the main quality indices of an EDB.

For the last 15 years, the research on EDBs has focused on homopolar topologies, which constitute most of the implementations of EDBs nowadays [3-5]. This resulted in significant progress in their modeling, allowing for accurate predictions of their behavior and performance.

As opposed to their heteropolar counterparts, homopolar EDBs can be built using bulk conductors [3] [5], resulting in simple and robust bearing designs. They also allow for filtering the force excitations that are synchronous with the spin speed [6]. Therefore, in case of rotor unbalance, the rotor can spin around its axis of inertia without transmitting forces to the housing. However, the homopolar field source could hardly be coupled to a winding to create a torque, which is the case in heteropolar EDBs. Despite this advantage, the actual potential of heteropolar EDBs still needs to be evaluated.

In this context, the paper presents an optimization of the performance of the heteropolar EDB introduced in [7]. Although the chosen bearing topology can perform the motor function, the present optimization concerns only the guiding function in the aim of providing an upper limit for the performance of this kind of bearing.

The paper is organized as follows. In Section II, the bearing topology and model are presented, as well as the model parameters identification process. In Section III, the EDB optimization is described and the results are

analyzed. Finally, the performance of the optimal bearings are compared to the performance of existing homopolar EDBs in Section IV.

II. MODELING AND PERFORMANCE EVALUATION

The EDB topology studied in this paper is shown in Fig. 1.

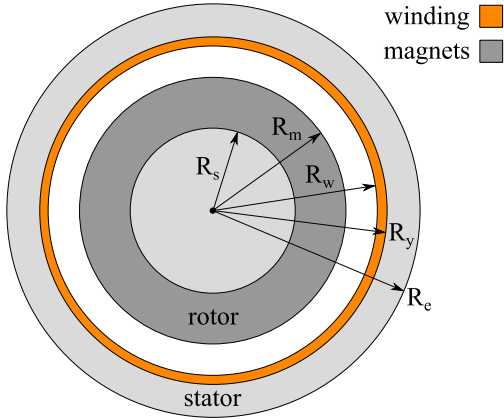


Fig. 1. Bearing topology and design parameters.

The rotor PMs have one pole pair. The winding has three phases (Fig. 2) and two pole pairs in order to have the null-flux characteristic [8].

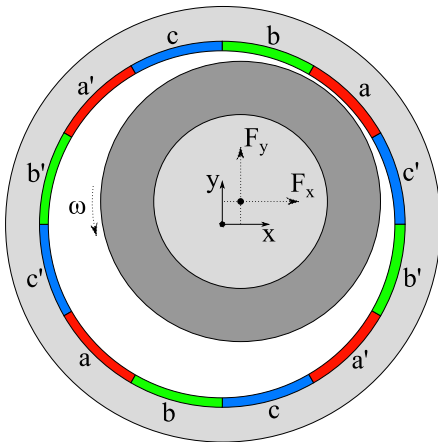


Fig. 2. Rotor position, electrodynamic forces and winding phases.

The properties of the bearing materials are given in Table 1. As regards the modeling assumptions, the magnetic permeability of the shaft iron is infinite and the materials have linear magnetic characteristics, i.e., magnetic hysteresis and saturation are neglected. The eddy currents in bulk materials and the impact of the rotor off-centering on the winding inductances are also neglected.

Table 1: Bearing material properties

| Parameters | Units | Definition |
|---------------------|-------------------|---|
| $\rho_m = 7500$ | kg/m^3 | Specific mass of the NdFeB magnets |
| $B_r = 1.2$ | T | PM remanent magnetization |
| $\rho_s = 7800$ | kg/m^3 | Specific mass of the shaft iron |
| $\sigma_{cu} = 6e7$ | $(\Omega m)^{-1}$ | Copper conductivity |
| $\mu_s = \infty$ | / | Relative magnetic permeability of the shaft iron |
| $\mu_r = 1$ | / | Relative magnetic permeability of the winding, magnets, and stator yoke |

The dynamics of the rotor is studied using the Jeffcott rotor model. Therefore, the rotor is assumed to move in the radial plane only. Using complex coordinates, the position of the rotor and the electrodynamic forces are:

$$z = x + jy, \quad (1)$$

$$F = F_x + jF_y. \quad (2)$$

They are linked with the external input force F_e through the state-space model [9]:

$$\begin{bmatrix} \dot{F} \\ \dot{z} \end{bmatrix} = A \begin{bmatrix} F \\ z \end{bmatrix} + BF_e, \quad (3)$$

where the dynamic and input gain matrices are:

$$A = \begin{bmatrix} -\frac{R}{L_c} - j\omega & -\frac{3K_\Phi^2}{2L_c} & -j\omega \frac{3K_\Phi^2}{2L_c} \\ \frac{1}{M} & -\frac{C}{M} & 0 \\ 0 & 1 & 0 \end{bmatrix}, \quad (4)$$

$$B = \frac{1}{M} [0 \quad 1 \quad 0]^T. \quad (5)$$

The parameters in (4)-(5) are given in Table 2. As the bearing is studied in 2D, all the parameters and performance indices are evaluated per unit of active bearing length. The parameters R , L_c , and K_Φ are identified using the 2D analytical model presented in [7] with the material properties listed in Table 1. In particular, K_Φ is the ratio of the peak PM magnetic flux in a winding phase to the amplitude of the rotor off-centering $|z|$. The rotor is assumed to weigh three times the weight of its active length, which yields:

$$M = 3[\rho_m \pi (R_m^2 - R_s^2) + \rho_s \pi R_s^2], \quad (6)$$

where ρ_m and ρ_s are given in Table 1. Lastly, the spin speed ω and the damping C are set arbitrarily.

Table 2: Parameters of the dynamical model

| Parameters | Units | Definition |
|------------|--|-------------------------------|
| R | Ω/m | Winding phase resistance |
| L_c | H/m | Winding cyclic inductance |
| M | kg/m | Rotor mass |
| K_Φ | $\left(\frac{N\Omega s}{m^3}\right)^{0.5}$ | Flux constant |
| C | Ns/m^2 | External non rotating damping |
| ω | rad/s | Rotor spin speed |

From these parameters, the two bearing performance indices can be calculated. The bearing quasi-static radial stiffness is derived from (3):

$$K = \Re e \left\{ \frac{F}{z} \right\} \Big|_{z=0, \dot{z}=0, \ddot{z}=0} = \frac{3\omega^2 L_c K_\Phi^2}{2(R^2 + (\omega L_c)^2)}. \quad (7)$$

Lastly, the damping required for stabilization C_s is obtained by increasing the value of C until the three eigenvalues of (4) cross the imaginary axis.

III. OPTIMIZATION

The bearing is optimized using a NSGA-II genetic algorithm with 100 individuals and 100 iterations. The mutation probability is 0.3, and the crossover rate is 0.9. From this, a Pareto front of optimal solutions that defines the area of achievable performance is obtained. The two objective functions K and C_s are optimized at a given spin speed ω rad/s. Defining the variables of the optimization problem:

$$x_1, x_2 \in [0,1], \quad (8)$$

the constraints on the geometric parameters can be formulated as:

$$R_m = x_1 R_{m,max}, \quad (9)$$

$$R_s = 0.2 R_m, \quad (10)$$

$$R_w = R_m + 1.5 \text{ mm}, \quad (11)$$

$$R_y = R_w + x_2 (\beta R_{m,max}). \quad (12)$$

In (9)-(12), the arbitrary parameters are set in order to get the best possible results, and thus an upper bound for the bearing performance. In (9), the maximum rotor radius $R_{m,max}$ is constrained by the maximum rotor peripheral speed $v_{max} = 250$ m/s:

$$R_{m,max} = \max(R_m) = \frac{v_{max}}{2\pi\omega}. \quad (13)$$

This is a realistic value for PM rotors with a retaining sleeve [10, 11]. In (10), the ratio of the rotor shaft radius to magnet radius is 0.2. This low value yields better results as the amount of magnet, and thus the bearing performance are maximized. In (11), the air gap width is set at 1.5 mm, which includes the width of a potential sleeve and allows for rotor eccentricities. In (12), the maximum winding thickness is related to the maximum rotor thickness $R_{m,max}$ through the factor $\beta = 1$. This allows the algorithm to explore a large yet realistic range of winding thicknesses.

Let us analyze the results for $\omega = 2\pi 1000$ rad/s and $\beta = 1$. The Pareto front in Fig. 3 shows that the damping required for stabilization increases with the bearing stiffness. The graph was limited to values of $C_s < 500$ Ns/m², which can be considered as very large for damping added in a passive, contactless way. Damping values of an order of magnitude of 10 Ns/m are reported in the literature [4].

Regarding thermal limitations, the winding current densities for each individual on the Pareto front are presented in Fig. 4. The losses are calculated assuming a static eccentricity of the rotor with an off-centering

$z = 0.5(R_w - R_m)$. In this case, the current density always lies below the maximum value of 5 A/mm² that is typical of enclosed PM machines [12]. In Fig. 4, the individuals are arranged in the same order as in Fig. 3, the individuals with lower stiffnesses on the left-hand side and the individuals with higher stiffnesses on the right hand side. This will be the case for all the figures in the following sections.

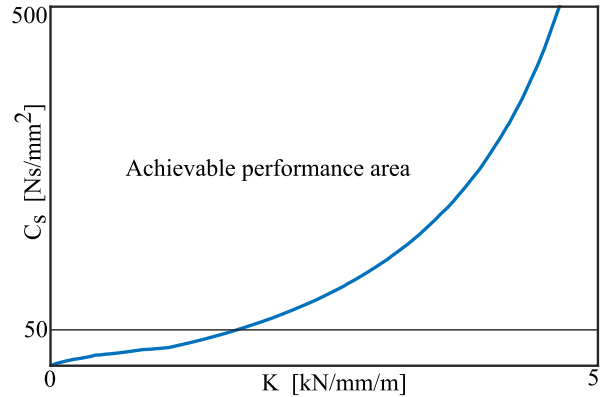


Fig. 3. Pareto front of the bearing performance at $\omega = 2\pi 1000$ rad/s.

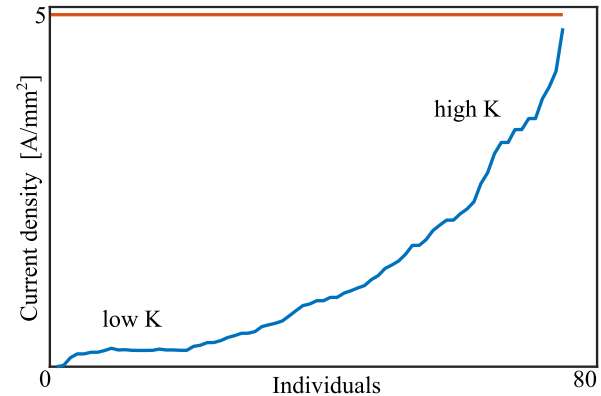


Fig. 4. Current densities associated with the individuals on the Pareto front, and maximum value of 5 A/mm².

Figures 5 and 6 show that bearings with a thicker winding require less damping for stabilization. This is the case for the individuals 1-20 with winding thicknesses nearing the maximum value. It corresponds to expectations as a lower winding resistance yields a more inductive behavior of the bearing that is known to have a positive effect on the stability [4, 7].

On the contrary, the individuals 20-80 have a greater PM thickness and the winding is closer to the PM on average. As a result, the magnetic field strength and the bearing stiffness are higher. However, the winding is more resistive as $(R_y - R_w)$ decreases, which affects the stability.

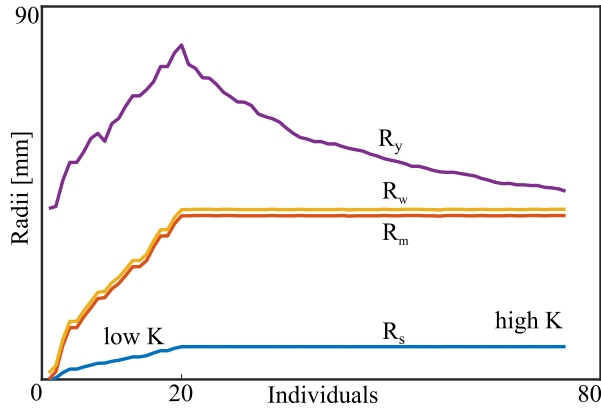


Fig. 5. Geometrical parameters of the individuals on the Pareto front for $\omega = 2\pi 1000$ rad/s.

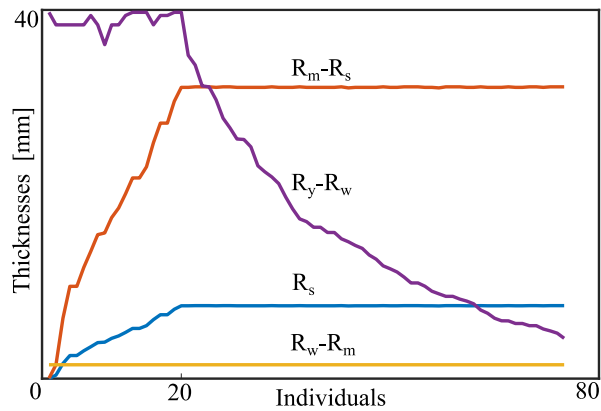


Fig. 6. Width of the shaft (R_s), PMs ($R_m - R_s$), air gap ($R_w - R_m$) and winding ($R_y - R_w$).

The Pareto fronts corresponding to the spin speeds $\omega = 2\pi\{50,100,500,1000\}$ rad/s are shown in Fig. 7. For a given value of K , more damping is required to stabilize the bearings running at higher speeds. This is due to the mechanical constraint on the peripheral speed. The value of $R_{m,max}$ is lower for the individuals running at higher speeds, which lowers the volume of PMs. An absence of the constraint on the peripheral speed would yield opposite results, as a given winding is more inductive while running at higher speeds.

Finally, the graphs of the bearing geometrical parameters in the cases $\omega = 2\pi\{50,100,500\}$ rad/s have a shape similar to that of the $\omega = 2\pi 1000$ rad/s case. In each case, the crosses in Fig. 7 and in the zoomed view in Fig. 8 indicate the individuals that have PMs and winding widths close to their maximum values. For instance, it is the 20th individual in the case of $\omega = 2\pi 1000$ rad/s (Fig. 6). For individuals lying further to the left on the Pareto front, the winding thickness reaches its maximum value, whatever the spin speed. In this area,

the Pareto fronts for all the speeds are almost superimposed, as shown in Fig. 8 ($\beta = 1$). Furthermore, the values of damping lie in the range $C_s \in [0,50]$ Ns/m in this figure, which is more realistic. As a result, a bearing optimized under the constraints (9)-(13) requires a same amount of damping for a given stiffness, whatever the spin speed.

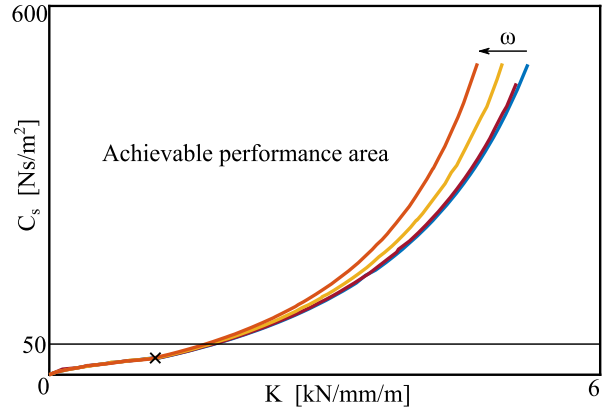


Fig. 7. Pareto fronts for $\omega = 2\pi\{50,100,500,1000\}$ rad/s.

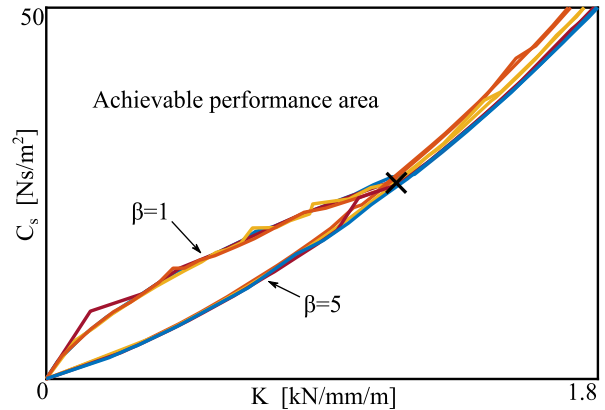


Fig. 8. Zoom on the area of interest where $C_s < 50$ Ns/m.

For $\omega = 2\pi\{50,100,500\}$ rad/s, the winding current densities lie far below the limit of 5 A/mm^2 .

Lastly, Fig. 8 shows the Pareto fronts corresponding to $\beta = 5$ in (12). As expected, the corresponding area of achievable performance is larger, because increasing β allows the algorithm to explore a wider range of winding thicknesses, although they may be unrealistic. These fronts constitute an absolute performance limit, as further increasing β has no impact on their positions.

Finally yet importantly, the Pareto fronts in Figs. 7-8 constitute an upper performance bound as considering additional constraints and/or the end-effects may reduce the performance of the bearing under study.

IV. PERFORMANCE COMPARISON

The performance of existing EDBs were summarized in [1]. The stiffness to PM volume ratios were calculated, yielding the black triangles in Fig. 9. The ranges given by the vertical bars correspond to the EDBs lying on the Pareto front in Fig. 7.

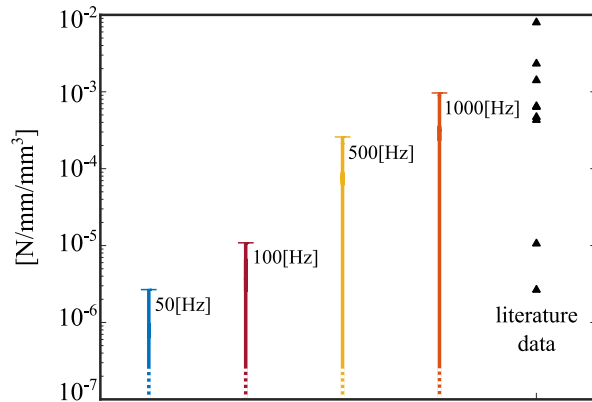


Fig. 9. Stiffness to volume ratio of the existing EDBs (triangles) and of the individuals on the Pareto fronts of Fig. 7 (solid lines).

The overall shape of the graph shows that bearings operating at higher spin speeds can achieve higher ratios. Compared with existing EDBs, the present topology provides a reasonable ratio at high speed, although it was not optimized considering this specific criterion.

V. CONCLUSION

In this paper, the domain of achievable performance of a heteropolar EDB was obtained by generating a Pareto front using an optimization algorithm. The two performance indices, namely the stiffness and the damping required for stabilization, were evaluated by combining two analytical models predicting the field distribution in the EDB and its dynamic behavior. The domain of achievable performance was obtained for different spin speeds. This highlighted a clear trade-off between stiffness and stability.

Then, the bearings lying on the Pareto front were compared to existing EDBs in terms of stiffness to volume ratio. It was shown that ratios similar to that of existing EDBs can be achieved at high speeds with the present EDB topology. This ratio could be further optimized as it was not an objective function of the present optimization.

Future work should include a study of both motor and bearing functions to take their respective constraints into account, and more especially thermal constraints.

REFERENCES

[1] J. G. Detoni, "Progress on electrodynamic passive magnetic bearings for rotor levitation," *Proc. Inst.*,

Mech., Eng., Part C: J. Mech. Eng. Sci., vol. 228, pp. 1829-1844, 2014.

- [2] A. Tonoli, N. Amati, F. Impinna, and J. G. Detoni, "A solution for the stabilization of electrodynamic bearings: Modeling and experimental validation," *J. Vib. Acoust.*, vol. 133, no. 2, 2011.
- [3] T. A. Lembke, "Design and analysis of a novel low loss homopolar electrodynamic bearing," *Ph.D. Dissertation*, Royal Inst. Tech., Sweden, 2005.
- [4] A. V. Filatov and E. H. Maslen, "Passive magnetic bearing for flywheel energy storage systems," *IEEE Trans. Magn.*, vol. 37, no. 6, pp. 3913-3924, 2001.
- [5] J. G. Detoni, "Developments on electrodynamic levitation of rotors," *Ph.D. Dissertation*, Politecnico di Torino, Turin, Italy, 2012.
- [6] J. G. Detoni, F. Impinna, A. Tonoli, and N. Amati, "Unified modelling of passive homopolar and heteropolar electrodynamic bearings," *J. Sound and Vibrations*, vol. 331, no. 19, pp. 4219-4234, 2012.
- [7] C. Dumont, V. Kluyskens, and B. Dehez, "Yokeless radial electrodynamic bearing," *Mathematics and Computers in Simulation*, vol. 130, pp. 57-69, 2016.
- [8] C. Dumont, V. Kluyskens, and B. Dehez, "Null-flux radial electrodynamic bearings," *IEEE Trans. Magn.*, vol. 50, no. 10, pp. 1-12, 2014.
- [9] C. Dumont, V. Kluyskens, and B. Dehez, "Linear state-space representation of heteropolar electrodynamic bearings with radial magnetic field," *IEEE Trans. Magn.*, vol. 52, no. 1, pp. 1-9, 2016.
- [10] A. Binder and T. Schneider, "High-speed inverter-fed AC drives," *2007 International Aegean Conference on Electrical Machines and Power Electronics*, Bodrum, pp. 9-16, 2007.
- [11] A. Borisavljevic, *Limits, Modeling and Design of High-Speed Permanent Magnet Machines*, Springer-Verlag Berlin Herdelberg, 2013.
- [12] D. G. Dorrell, M.-F. Hsieh, M. Popescu, L. Evans, D. A. Staton, and V. Grout, "A review of the design issues and techniques for radial-flux brushless surface and internal rare-earth permanent-magnet motors," *IEEE Trans. Magn.*, vol. 58, no. 8, pp. 3741-3757.



Corentin Dumont was born in Belgium in 1989. He received the Electromechanical Engineering degree in 2012 and the Ph.D. degree in 2017 from the Université catholique de Louvain (UCL), Belgium. He is currently a Researcher at the Department of Mechatronics, Elect-

rical Energy, and Dynamic Systems (MEED) of the Université catholique de Louvain (UCL). His research focuses on magnetic bearings.



Virginie Kluyskens was born in Belgium, in 1980. She received the Electromechanical Engineering degree in 2004 and the Ph.D. degree in 2011 from the Université catholique de Louvain (UCL), Louvain-la-Neuve, Belgium. She is currently Senior Researcher at the MEED Department of the UCL. Her research interests are in the field of passive magnetic bearings.



Bruno Dehez was born in Belgium, in 1975. He received the degree in Electromechanical Engineering and the Ph.D. degree from the Université catholique de Louvain (UCL), Louvain-la-Neuve, Belgium, in 1998 and in 2004, respectively. He is currently a Professor at the Ecole Polytechnique de Louvain (EPL), and is Head of the MEED Department of the UCL. His research interests are in the field of design and optimization of electromagnetic devices, and particularly of electrical machines and actuators.

Modeling and Discussing an Interconnected Flux Magnetic Bearing

Domingos F. B. David¹, José A. Santisteban¹, and Afonso C. Del Nero Gomes²

¹Departments of Mechanical and Electrical Engineering
Universidade Federal Fluminense, Niteroi, Rua Passo da Pátria 156, CEP 20420-40, Brazil
domingos@vm.uff.br, jasantisteban@vm.uff.br

²Department of Electrical Engineering
Universidade Federal do Rio de Janeiro - CT, Rio de Janeiro, CEP 21945-970, Brazil
nero@coep.ufrj.br

Abstract — An alternative idea for the construction of active magnetic bearings, adapted from a successful structure used in split-winding self-bearing motors, has been recently discussed in the literature. A mathematical model for this bearing configuration is developed in this paper. Preliminary theoretical results predict a greater equivalent stiffness for this model, when compared with traditional active magnetic bearings. The use of recently built prototypes for testing if these expectations hold true is also discussed.

Index Terms — Active magnetic bearings, interconnected magnetic flux, modeling.

I. INTRODUCTION

Conventional active magnetic bearings (AMBs) [1], [2], [3], here called Type A, are based on the structure shown in Fig. 1. There are four “U-shaped electromagnets”, two for the x or horizontal direction and two in the y direction, resulting in four independent magnetic flux loops.

The windings in the x and y direction are fed with currents $i_0 \pm i_x(t)$ and $i_0 \pm i_y(t)$; the constant current i_0 is the base, or bias, and the differential currents i_x and i_y will control the rotor position. Using basic reluctance concepts, the resultant forces f_x and f_y can be expressed in terms of these currents, the air magnetic permeability μ_0 , the total number of coils n_a , the cross section area in the stator ferromagnetic material A_a and the nominal length h of the air gaps. After a standard linearization procedure [1] around the operating point $x = y = i_x = i_y$, the forces generated by the Type A structure are shown in (1). Notice that the non connected nature of the magnetic fluxes leads to uncoupled forces:

$$\begin{cases} f_x = k_p^a x + k_i^a i_x \\ f_y = k_p^a y + k_i^a i_y \end{cases} \text{ where } \begin{cases} k_p^a = \mu_0 A_a n_a^2 i_0^2 / h^3 \\ k_i^a = \mu_0 A_a n_a^2 i_0^2 / h^2 \end{cases} \quad (1)$$

A different structure for magnetic bearings,

here named Type B, with four windings that cause interconnected magnetic loops, is depicted in Fig. 2.

This structure is found in the split-windings self-bearing motors researched in Brazil [4], [5]. In that approach, to provide spinning torques and radial restoring forces at the same time, alternate currents are injected in the windings; for the simpler case of AMBs, DC currents are considered.

Although other results are known with the Type B bearing concept [6], the authors of this article did not identify, up to now, the association of the interconnected flux structure with uncoupled equations for radial restoring forces or with higher values of the magnetic constants.

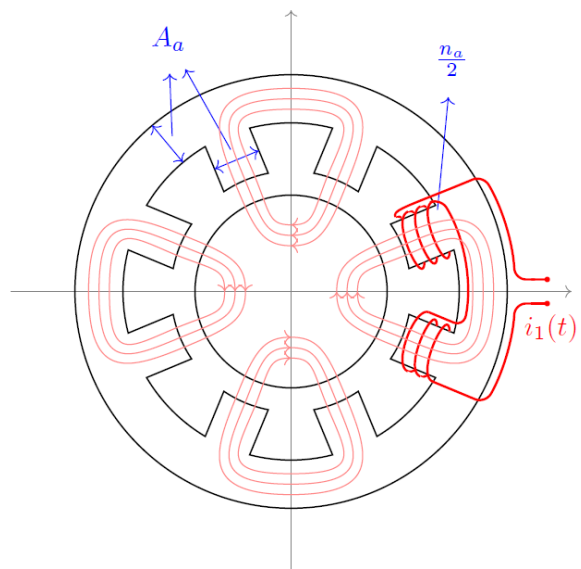


Fig. 1. Type A, or traditional, configuration for AMBs; windings are shown for the positive x (y) direction control the horizontal (vertical) position.

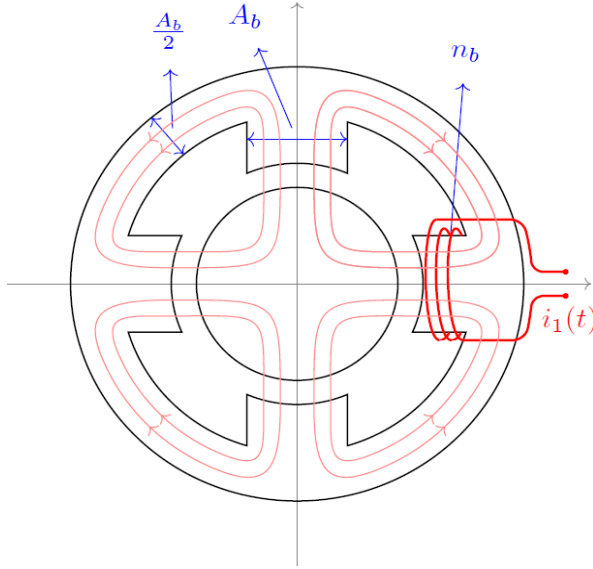


Fig. 2. Type B, the proposed configuration for AMBs; windings are shown for the positive x direction only; the flux paths are interconnected. Opposing pairs of windings along the x (y) direction control the horizontal (vertical) position.

The generation of reluctance forces f_x and f_y in Type B bearings is detailed in Section II, which follows closely [7] and [8]. The linearized final expressions for these forces also show a decoupled nature, and the position and current constants, k_p^b and k_i^b , have higher values than in case A. Section III presents analytic results and simulations on how increasing $k_{p,i}$ affects dynamic and control aspects of AMBs [8]. Details of the prototypes built to allow real comparisons between Types A and B, together with discussions about real tests, final comments and considerations on what remains to be done are made in Sections IV and V.

II. FORCE GENERATION IN TYPE B BEARING

A detailed study of the force generation in the flux interconnected structure was presented in [4], [7] and [8]; the main points are repeated below. The x and y components of a radial displacement of the rotor change the nominal gap width h as shown in Fig. 3.

To compensate the displacements, it is usual to apply differential currents [1] to the pairs of windings: the differential, or control, currents $i_x(t)$, for the x or horizontal direction, and $i_y(t)$, for the vertical direction, are added and subtracted to a base, or bias, current i_0 , a constant DC level. The total current, imposed at each

winding are:

$$i_1(t) = i_0 + i_x(t), i_3(t) = i_0 - i_x(t), \text{ at the } x \text{ axis, (2)}$$

$$i_2(t) = i_0 + i_y(t), i_4(t) = i_0 - i_y(t), \text{ at the } y \text{ axis. (3)}$$

Light pink lines in Fig. 2 represent the magnetic flux distribution caused by these currents. The reluctance forces depend on the total magnetic fluxes Φ_k , $k = 1, 2, 3, 4$, in the four air gaps with cross section area A_b :

$$f_x = \frac{\Phi_1^2 - \Phi_3^2}{2\mu_0 A_b} \quad \text{and} \quad f_y = \frac{\Phi_2^2 - \Phi_4^2}{2\mu_0 A_b}. \quad (4)$$

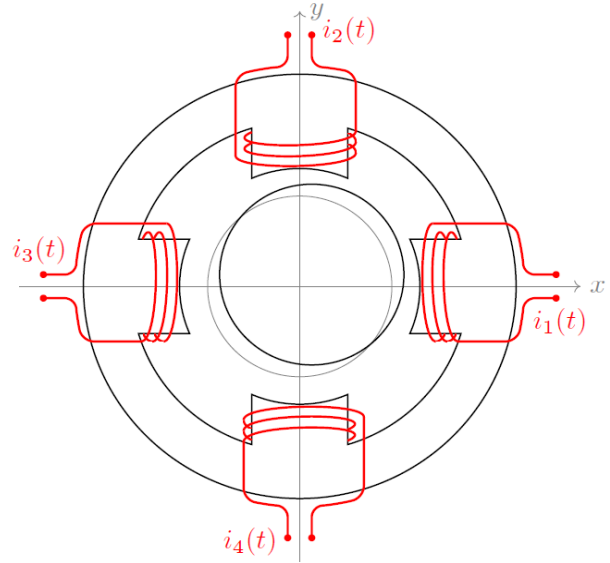


Fig. 3. When the rotor moves x and y in the horizontal and vertical positions, the air gap widths change to $h - x$ in the right pole, $h + x$ (left pole), $h - y$ (upper pole) and $h + y$ (lower pole); the fluxes are not shown.

The ferromagnetic connections in Type B allow a current injected in any winding to cause fluxes in all four air gaps; Fig. 4 illustrates the effects of i_1 in all four “poles”. If Φ_{jk} denotes the flux in air gap j caused by a current in winding k , the total magnetic flux Φ_1 in “pole” 1 depends on Φ_{11} , Φ_{12} , Φ_{13} , Φ_{14} . Assuming no air or ferromagnetic losses, and positive signs for fluxes headed to the rotating center, the total magnetic fluxes in the poles are:

$$\Phi_1 = \Phi_{11} + \Phi_{12} - \Phi_{13} + \Phi_{14}, \quad (5)$$

$$\Phi_2 = -\Phi_{21} - \Phi_{22} - \Phi_{23} + \Phi_{24}, \quad (6)$$

$$\Phi_3 = -\Phi_{31} + \Phi_{32} + \Phi_{33} + \Phi_{34}, \quad (7)$$

$$\Phi_4 = -\Phi_{41} + \Phi_{42} - \Phi_{43} - \Phi_{44}. \quad (8)$$

For the determination of the sixteen values of Φ_{jk} , let the magneto-motive generated by current i_1 be denoted by F_1 and the reluctances of the air gaps in the four poles in Fig. 3 by R_1 , R_2 , R_3 and R_4 . Figure 5 shows the equivalent circuit.

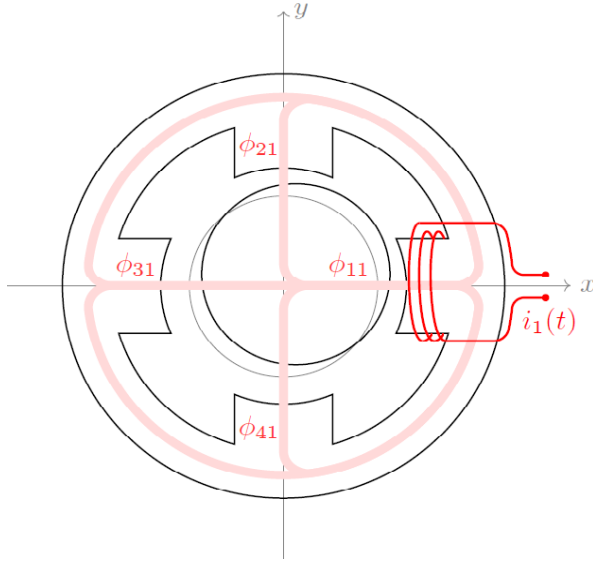


Fig. 4. Magnetic flux distribution associated to i_1 in type B magnetic bearing; current injected only in winding 1 causes fluxes in all air gaps.

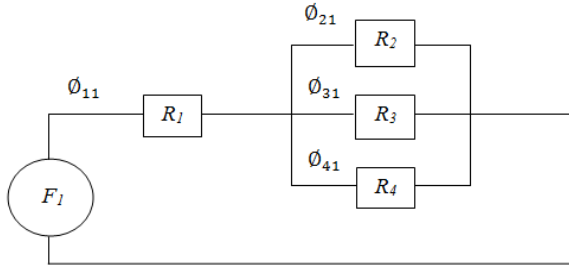


Fig. 5. Magnetic flux equivalent circuit associated to current only in winding 1 of type B magnetic bearing.

In the following development, A_b is the cross section area of the poles in Fig. 2. Considering that the reluctances are:

$$R_1 = \frac{h-x}{\mu_0 A_b}; R_2 = \frac{h-y}{\mu_0 A_b}; R_3 = \frac{h+x}{\mu_0 A_b}; R_4 = \frac{h+y}{\mu_0 A_b}; \quad (9)$$

the equivalent reluctance R_1^e can be found to be:

$$R_1^e = \frac{R_1 R_2 R_3 + R_1 R_2 R_4 + R_1 R_3 R_4 + R_2 R_3 R_4}{R_2 R_3 + R_2 R_4 + R_3 R_4}. \quad (10)$$

To avoid cumbersome formulas, the following auxiliary variables are defined:

$$N = R_1 R_2 R_3 + R_1 R_2 R_4 + R_1 R_3 R_4 + R_2 R_3 R_4, \quad (11)$$

$$D_1 = R_2 R_3 + R_2 R_4 + R_3 R_4, \quad (12)$$

$$D_2 = R_1 R_3 + R_1 R_4 + R_3 R_4, \quad (13)$$

$$D_3 = R_1 R_2 + R_1 R_4 + R_2 R_4, \quad (14)$$

$$D_4 = R_1 R_2 + R_1 R_3 + R_2 R_3. \quad (15)$$

Since $F_1 = n_b i_1$, algebraic operations lead to expressions for the fluxes associated to $i_1 = i_0 + i_x$ imposed to the winding in pole 1 of Fig. 3:

$$\Phi_{11} = \frac{F_1}{R_1^e} = n_b (i_0 + i_x) \frac{D_1}{N}, \quad (16)$$

$$\Phi_{21} = n_b (i_0 + i_x) \frac{R_3 R_4}{N}, \quad (17)$$

$$\Phi_{31} = n_b (i_0 + i_x) \frac{R_2 R_4}{N}, \quad (18)$$

$$\Phi_{41} = n_b (i_0 + i_x) \frac{R_2 R_3}{N}. \quad (19)$$

The same procedure, repeated for currents i_2, i_3, i_4 imposed at the windings in poles 2, 3 and 4, in Fig. 3, results in:

$$\Phi_{12} = n_b (i_0 + i_y) \frac{R_3 R_4}{N}; \quad \Phi_{22} = n_b (i_0 + i_y) \frac{D_2}{N};$$

$$\Phi_{32} = n_b (i_0 + i_y) \frac{R_1 R_4}{N}; \quad \Phi_{42} = n_b (i_0 + i_y) \frac{R_1 R_3}{N};$$

$$\Phi_{13} = n_b (i_0 - i_x) \frac{R_2 R_4}{N}; \quad \Phi_{23} = n_b (i_0 - i_x) \frac{R_1 R_4}{N};$$

$$\Phi_{33} = n_b (i_0 - i_x) \frac{D_3}{N}; \quad \Phi_{43} = n_b (i_0 - i_x) \frac{R_1 R_2}{N};$$

$$\Phi_{14} = n_b (i_0 - i_y) \frac{R_2 R_3}{N}; \quad \Phi_{24} = n_b (i_0 - i_y) \frac{R_1 R_3}{N};$$

$$\Phi_{34} = n_b (i_0 - i_y) \frac{R_1 R_2}{N}; \quad \Phi_{44} = n_b (i_0 - i_y) \frac{D_4}{N}.$$

The total fluxes Φ_k for $k = 1, 2, 3, 4$ can be determined by substituting the previous values of the partial fluxes Φ_{jk} in Equations (5) to (8). Then, with the help of (4), the total reluctance forces generated in Type B magnetic bearing can be expressed as:

$$f_x = \frac{\mu_0 A_b n_b^2}{2} q_x(h, x, y, i_0, i_x, i_y), \quad \text{and} \quad (20)$$

$$f_y = \frac{\mu_0 A_b n_b^2}{2} q_y(h, x, y, i_0, i_x, i_y), \quad (21)$$

where $q_{x,y}$ are the following functions:

$$q_x(h, x, y, i_0, i_x, i_y) = \frac{N_1^2 - N_2^2}{\Delta^2}, \quad \text{and} \quad (22)$$

$$q_y(h, x, y, i_0, i_x, i_y) = \frac{N_3^2 - N_4^2}{\Delta^2}, \quad (23)$$

with:

$$N_1 = (i_1 + i_2)\Delta_1 + (i_1 - i_3)\Delta_2 + (i_1 + i_4)\Delta_3,$$

$$N_2 = (i_3 - i_1)\Delta_2 + (i_2 + i_3)\Delta_4 + (i_3 + i_4)\Delta_5,$$

$$N_3 = (i_1 + i_2)\Delta_1 + (i_2 + i_3)\Delta_4 + (i_2 - i_4)\Delta_6,$$

$$N_4 = (i_1 + i_4)\Delta_3 + (i_3 + i_4)\Delta_5 + (i_4 - i_2)\Delta_6.$$

The currents i_k are defined in equations (2) and (3). If the distances $h \pm x$ and $h \pm y$ are denoted by δ_x^\pm and δ_y^\pm , the "Δs" values above are:

$$\Delta_1 = \delta_x^+ \delta_y^+, \quad \Delta_2 = \delta_y^+ \delta_x^-, \quad \Delta_3 = \delta_x^+ \delta_y^-,$$

$$\Delta_4 = \delta_x^- \delta_y^+, \quad \Delta_5 = \delta_x^- \delta_y^-, \quad \Delta_6 = \delta_x^+ \delta_x^-, \quad \text{and}$$

$$\Delta = \delta_x^- \delta_y^- \delta_x^+ + \delta_x^- \delta_y^- \delta_y^+ + \delta_x^- \delta_x^+ \delta_y^+ + \delta_y^- \delta_x^+ \delta_y^+.$$

In order to make the linearization of Equations (20) and (21), it should be considered that AMB's operate around a point $P_0 = (x, y, i_x, i_y)_0 \cong (0, 0, 0, 0)$. The partial derivatives in the vicinity of this point are:

$$\left. \frac{\partial q_x}{\partial x} \right|_{P_0} = \frac{4i_0^2}{h^3}, \quad \left. \frac{\partial q_x}{\partial y} \right|_{P_0} = 0, \quad (24)$$

$$\left. \frac{\partial q_x}{\partial i_x} \right|_{P_0} = \frac{4i_0^2}{h^2}, \quad \left. \frac{\partial q_x}{\partial i_y} \right|_{P_0} = 0. \quad (25)$$

If a similar procedure is made for q_y , the combined results lead to the linear expressions for the Type B structure forces:

$$\begin{cases} f_x = k_p^b x + k_i^b i_x \\ f_y = k_p^b y + k_i^b i_y \end{cases} \quad \text{where} \quad \begin{cases} k_p^b = 2\mu_0 A_b n_b^2 i_0^2 / h^3 \\ k_i^b = 2\mu_0 A_b n_b^2 i_0^2 / h^2 \end{cases}. \quad (26)$$

Two remarkable aspects are to be observed in Equation (26):

- (a) The complex interconnected fluxes in the Type B structure also lead to decoupled forces, in a similar way to Equation (1), derived for the Type A AMB's;
- (b) there is a factor 2 in Equation (26), when compared to Equation (1), derived for the Type A structure.

III. THEORETICAL COMPARISONS

Assuming the same outside diameter of the stator, the following advantages can be identified for the Type B active magnetic bearing when it is compared with Type A:

- 1) The position and current constants k_p^b and k_i^b in Equation (26) are two times bigger than their counterparts k_p^a and k_i^a in Equation (1);
- 2) the cross section area A_b can be chosen greater than A_a ; it is reasonable to have $A_b \approx 2A_a$;
- 3) the number of coils n_b can, possibly, be larger than n_a .

In conclusion the position (k_p) and current (k_i) constants for Type B AMBs have values at least 2 times higher than in case A. Depending on design aspects (A_b and n_b), even higher rates can be achieved. How much can be these constants increased? The magnetic saturation seems to be the limit.

In order to evaluate the effects of k_p and k_i in an AMB performance, a theoretical analysis was applied in [8] to a simple control problem summarized in Fig. 6: a particle moving without friction in a horizontal and rectilinear path is to be positioned.

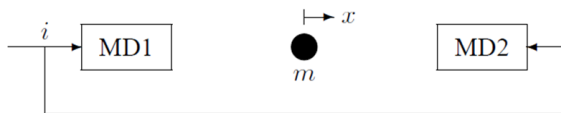


Fig. 6. The particle position $x(t)$ is to be controlled by injecting currents in the magnetic devices MD1 and MD2.

The magnetic devices apply a horizontal force $f(t) = k_p x(t) + k_i i(t)$ on the sphere, where i is a control current and x measures the displacement with respect to the reference position. A controller is desired, capable of driving the sphere position to 0 for all possible initial conditions $x(0)$, and in the eventual presence of constant, horizontal disturbance forces v . This is a simple, but meaningful, problem: many aspects of the real life operation and control of AMBs are present in it.

A stabilizing PD controller $C(s) = as + \beta$ was designed; it ensured, as expected, that non zero initial displacements $x(0)$ were corrected, when $v = 0$. When

a constant v was present, the controller effect lacked efficiency: the steady state offset error caused by such disturbances was found to be:

$$\rho = \frac{v_0}{\beta k_i - k_p}, \quad (27)$$

where v_0 is the disturbance magnitude. The well known fact that PD controllers do not completely reject ($\rho = 0$) constant disturbances becomes apparent. But Equation (27) tells more: for a fixed, stabilizing controller, ρ decreases when k_p and k_i increase by the same factor. In other words, if the position and current coefficients in a magnetic force generation law are both increased by the same amount, the resulting PD control is less sensitive to constant disturbances, and this characterizes a better, stiffer suspension.

In addition, it was simple to verify that a PID controller caused complete rejection of step disturbances, as expected, and that high or low values for the magnetic constants were not crucial in the stabilizing stage. But when constant disturbance rejection was needed, better transient behaviors were a direct consequence of higher k_p and k_i values.

The conclusions of the simple example in reference [8] are valid in much more general situations, involving real world applications of practical interest. And these conclusions are: increasing the values of the magnetic force constants k_p and k_i is a highly desirable goal in the AMB field.

IV. PROTOTYPE BUILDING AND SIMULATIONS

The final conclusions of Sections II and III are that the interconnected fluxes in the Type B structure increase the values of the magnetic force constants k_p and k_i . How can one be sure about the theoretical tools used in those developments? The idea of the Type B structure has already been tested. In the prototype used at UFRJ [4], a vertical rotor is positioned in the radial directions by a self-bearing motor based on the interconnected fluxes of the Type B structure. This situation is more complicated, because the windings are fed with AC currents, to achieve the dual capabilities: torque generation and radial positioning. The device has worked!

The best possible way to give definite answers to the seminal questions posed above is by constructing prototypes and testing them in an exhaustive way. Only after this important stage, will the ideas proposed here be validated or not. Two prototypes, one for Type A and the other for Type B, have been constructed. Figure 7 shows a top view of them. A vertical rotor with a large, perforated upper disk will fill the above pieces; the same Fig. 7, in the center, shows a view of a mounted kit, with the rotor inserted in the casing with the stators.



Fig. 7. Top view of prototypes A, in the left and B in the right; notice the 8 “poles” in Type A, and only 4 “poles” in Type B. A mounted kit is shown in the center, with a vertical rotor inserted in one of the casings.

A finite element simulation of the magnetic characteristics of Type A and Type B structures [8] was done, and some results are shown below.

Figure 8 confirms the assumption that the flux generated at a particular winding is localized and does not interact with the other fluxes. Figure 9 shows clearly that a differential current in one direction does not affect the flux distribution in the other direction, thus confirming Equation (25).

The geometry of the flux lines, how they interconnect in Type B or remain isolated in Type A, confirms the basic assumptions used in Section II and on which this work relies.

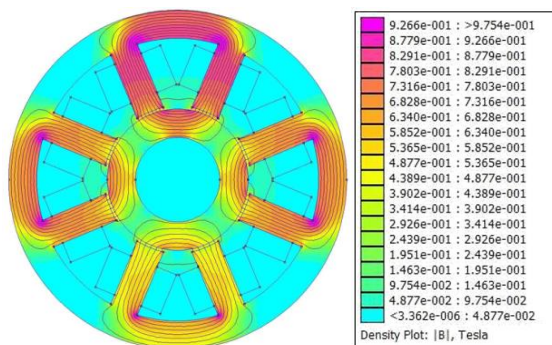


Fig. 8. Flux distribution in a Type A structure with balanced currents in the x axis and a differential current in the y direction.

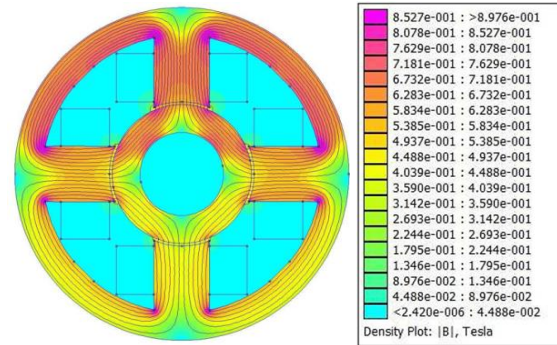


Fig. 9. Flux distribution in a Type B structure with balanced currents in the x axis and a differential current in the y direction.

A detailed mathematical model was built to describe the dynamic aspects of the prototypes. For evaluating their disturbance behavior, simulations were made when an extra mass was fixed in the upper disk. The rotor will be unbalanced by this and harmonic forces will be generated at the x and y axes. The resulting torques will disturb the centering capabilities of the most basic control laws used, imposing orbital movements to the rotor. This means that using the same initial conditions as before, the radial displacements will not tend to zero anymore. As expected, Type B behaves better than Type A in these extreme conditions; more details can be found in [9].

V. COMMENTS AND CONCLUSIONS

The results in the previous section confirm the basic assumptions of Type B superiority on which this work relies. These are good news, but sound statements cannot be made yet: the prototypes are already finished but have not reached an operational stage yet. The laboratory tests are in a very primitive stage and no solid measurements has been made up to now. The authors have great expectations that the here called Type B concept will be a valid contribution for the active magnetic bearings field, because of the possibility of increasing their equivalent mechanical stiffness.

REFERENCES

- [1] G. Schweitzer, H. Bleuler, and A. Traxler, *Active Magnetic Bearings*. Hochschulverlag AG an der ETH Zürich, 1994.
- [2] A. Chiba, T. Fukao, O. Ichikawa, M. Oshima, M. Takemoto, and D. Dorrel, *Magnetic Bearings and Bearingless Drives*. Newnes-Elsevier, 2005.
- [3] G. Schweitzer, E. Maslen, H. Bleuler, M. Cole, P. Keogh, R. Larsonneur, R. Nordmann, and Y. Ogada, *Magnetic Bearings: Theory Design and Applications to Rotating Machinery*. Springer-Verlag, 2009.
- [4] D. F. B. David, “Levitação de rotor por mancais-

motores radiais magnéticos e mancal axial sc auto-estável,” *D. Sc. Thesis*, COPPE-UFRJ, 2000.

- [5] E. F. Rodriguez and J. A. Santisteban, “An improved control system for a split winding bearingless induction motor,” *IEEE Transactions on Industrial Electronics*, vol. 58, no. 8, pp. 3401-3408, 2011.
- [6] L. Santos and K. Kjolhed, “Experimental contribution to high-precision characterization of magnetic forces in active magnetic bearings,” *Journal of Engineering for Gas Turbines and Power*, vol. 129, pp. 503, 2007.
- [7] D. F. B. David, J. A. Santisteban, and A. C. D. N. Gomes, “Interconnected four poles magnetic bearings,” in *Proceedings of the 1st Brazilian Workshop on Magnetic Bearings*, 2013. www.magneticbearings2013.com.br
- [8] “Interconnected four poles magnetic bearings simulations and testing,” *Proceedings of ISMB14, 14th International Symposium on Magnetic Bearings*, pp. 30-35, 2014. <http://ismb14.magneticbearings.org>
- [9] “Laboratory tests on an interconnected four poles magnetic bearing,” in *Proceedings of ISMB15, 15th International Symposium on Magnetic Bearings*, 2016.



Domingos F. B. David: B.Sc. in Naval Engineering by the Federal University of Rio de Janeiro, in 1976; M.Sc. (1978) and D.Sc. (2000) in Mechanical Engineering from COPPE, at the same University. He has worked, until 1995, as Project Engineer dealing with equipments for the nuclear and chemical industries. Since then, he has been researching and teaching at the Mechanical Engineering Dept. of the Fluminense Federal University, Rio de Janeiro, Brazil.



José A. Santisteban: B.Sc. and Engineer degrees in Electronic Engineering from Universidad Nacional de Ingeniería (UNI), Lima, Perú, in 1986 and 1988, respectively, and the M.Sc. and D.Sc. degrees in Electrical Engineering from Universidade Federal do Rio de Janeiro (COPPE/UFRJ), Rio de Janeiro, Brazil, in 1993 and 1999, respectively. From 1988 to 1991, he was a Researcher and an Assistant Professor with UNI. From 1993 to 1995, he was a Researcher with UFRJ. In 1999, he joined the Fluminense Federal University, Niterói, Brazil, where he is currently an Associate Professor in

the Electrical Engineering Department acting in the Graduate Programs of Mechanical Engineering and the Electrical and Telecommunications Engineering. His current research activities include bearingless machines, power electronics, and electrical drives. He is a Member of the Brazilian Society of Power Electronics (SOBRAEP) and the Brazilian Society of Mechanical Engineering (ABCM). He is a co-author of the first Brazilian book on magnetic bearings.



Afonso C. Del Nero Gomes: B.Sc. in Aeronautical Engineering by ITA, the Aeronautical Technology Institute; M.Sc. and D.Sc. in Systems Engineering by COPPE in the Federal University of Rio de Janeiro, where he has been researching and teaching for undergraduate and graduate levels, for all his academic career.

Crucial Parameters and Optimization of High-Speed Bearingless Drives

Hubert Mitterhofer and Siegfried Silber

Linz Center of Mechatronics GmbH
Altenbergerstrasse, 69 - 4040 Linz, Austria
hubert.mitterhofer@lcm.at, siegfried.silber@lcm.at

Abstract — Bearingless drives integrate the functionality of magnetic bearings and an electric machine into a single device. While this integration allows very compact drives offering all advantages of magnetic levitation, the design process becomes significantly more complex. This work deals with the numerous topological and geometric design decisions which need to be taken for such a bearingless drive. Additionally, the definition of suitable optimization targets for the electromagnetic simulation process is outlined. The proposed guidelines generate a complex relationship of different dependencies which is then fed into the *MagOpt* optimizer for the design of a high speed bearingless disk drive, which allows verifying the optimization results through measurement results from two prototype drives.

Index Terms — Bearingless drive, force and torque evaluation, *MagOpt*, optimization.

I. INTRODUCTION

Magnetic bearings dispose of several characteristics which have allowed them to conquer certain fields of applications requiring, e.g., high-purity, long lifetime, or high rotational speeds. By integrating magnetic bearings and electric drives in a bearingless drive, the mechanical dimensions become more compact while the complexity in design, optimization, and control increases.

The design process of a high-speed bearingless drive demands several topological decisions. Section 0 presents the most stringent choices and discusses their respective influence on the drive performance. Section 0 first deals with the remaining geometric parameters and selects the actual optimization parameters. Before the optimization, not only the parameters but also the targets need to be defined. Other than in the design of conventional electrical machines, literature presents no widely used performance parameters since both, the torque and the bearing performance including their cross-coupling and their angle dependency are relevant. Therefore, this work proposes suitable optimization targets, characterizing different aspects of the performance of a bearingless disk drive. Their use as target values allows applying optimization tools, in this case, the general purpose

optimizer *MagOpt*.

Eventually, the optimization results for two certain designs are given in section 0. The comparison with the measurements at two actually constructed prototypes shows the benefits of the optimization.

II. TOPOLOGICAL DECISIONS

A. Machine topology

Bearingless drives have been constructed using different machine topologies, from classic permanent magnet synchronous machines (PMSMs) to induction machines or reluctance based types. A good overview about the early developments is given in [1]. However, for achieving full levitation with a mechanically compact design, the PMSM topology with a permanent magnet rotor is the preferable solution. Additionally, high energy density and good efficiency, even for small drives, speak in favor of this motor topology. Therefore, as for most recent developments, the PMSM topology is chosen for the targeted high-speed drive.

B. Rotor

A disk-shaped rotor can be chosen over an elongated rotor because of its passive stability in axial and tilt directions [2]. Supplemented with the active stabilization in radial direction by the bearingless unit, stable levitation can be achieved with one bearing point.

For high rotational speeds, an inner rotor with two-pole magnetization has been used in the drives presented in [3], [4] or [5]. The inner rotor with its smaller diameter is subject to lower centrifugal forces. The low pole number results in the highest mechanical frequency for a given electrical frequency. However, the two-pole diametrical magnetization also adds anisotropic stiffness characteristic to the drive. Viewed in the stationary coordinate system, the effect can, e.g., be written for the destabilizing radial reluctance force as:

$$F_{r,rel} = \begin{bmatrix} \bar{c}_r(1 + \hat{c}_r \cos(2\Omega t)) & \bar{c}_r \hat{c}_r \sin(2\Omega t) \\ \bar{c}_r \hat{c}_r \sin(2\Omega t) & \bar{c}_r(1 - \hat{c}_r \cos(2\Omega t)) \end{bmatrix} \begin{bmatrix} \Delta x \\ \Delta y \end{bmatrix}, \quad (1)$$

with Δx and Δy , being the stator-bound radial deflections. Ω gives the angular frequency of rotation and \bar{c}_r and \hat{c}_r

stand for the mean stiffness value and its variation ratio, respectively. An equal formulation is possible for the stabilizing tilt reluctance torque. More details on this matter can be found in [6].

Despite this complexity increase for the system, the effect on a rotor is negligible when we can assume operation at high rotational speeds since Equation (1) clearly shows that the principal frequency of the anisotropic force on a deflected rotor is twice as high as the frequency of rotation and, therefore, quickly surpasses the radial rigid body mode, given as:

$$\omega_r = \sqrt{\frac{\bar{c}_r}{m_{rotor}}}, \quad (2)$$

with m_{rotor} standing for the rotor mass.

C. Stator core

One of the main topological decisions concerns the used stator material. While laminated electrical steel with low hysteresis losses is surely preferable for low speed applications, high frequencies of the rotating magnetic field provoke high eddy current losses which may call for the use of soft magnetic composite (SMC) material. These sintered materials feature very low electric conductivity and thus, low eddy current losses which scale according to:

$$p_{Fe,ed} \sim f^2, B^2, \quad (3)$$

where f and B denote the principal frequency of the magnetic field and the flux density, respectively. Due to the hysteresis losses which dominate in SMC materials, scaling according to:

$$p_{Fe,h} \sim f, B^2, \quad (4)$$

there is a break-even point for a certain field frequency above which SMC is beneficial. In literature (e.g., in [7]), this point is typically found to be between 1 kHz and 2 kHz, depending on the quality of the compared SMC and laminated steel materials, which makes the use of SMC interesting in high-speed drives. Due to the potential advantage concerning the core loss and the additional simplicity in prototyping (the SMC can be milled from a block form), the SMC material *Somaloy 700 5P* is selected for the current analysis.

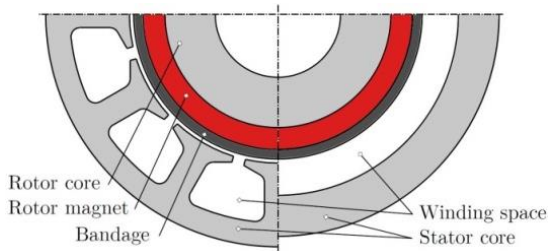


Fig. 1. Slotted (left) and slotless (right) stator topology.

A second principal decision for the stator design

concerns the question if a slotted or a slotless core shall be applied (cf. Fig. 1). While the former provides small magnetic air gaps and, thus, high air gap flux density, the latter offers low stator losses due to the sinusoidal flux density distribution, the absence of higher slot harmonics, and the wider air gap. For very high speed machines, it has been shown in literature, e.g., in [4] or [8] and [9], that the slotless core is the better choice.

D. Winding system

The proposed slotless stator form directly triggers the decision between air gap winding or toroid winding. Both are depicted in Fig. 2. While electromagnetically equal, the toroid winding has the more compact mechanical form with reduced copper volume when a flat rotor shape is used [10]. Additionally, it offers simple prototype manufacturing and good cooling properties. Manufacturing in an automated process may be more complex than for the air gap winding but overall, the toroid winding seems advantageous.

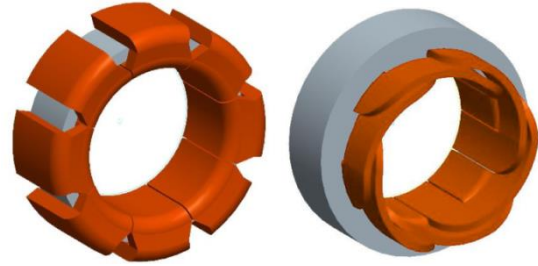


Fig. 2. Toroid winding (left) and air gap winding (right).

Concerning the winding connection topology, it is possible to differ between the following configurations.

1) Separated windings

When multiple sets of windings are used, i.e., one for torque and another one for bearing force creation, the term *separate winding system* is applied. In this case, the necessary currents and voltages for the motor and bearing function are calculated, applied, and controlled separately. This poses a very intuitive approach to the problem of parallel torque and force creation which is frequently used and well documented in numerous publications, e.g., [11], [12].

2) Combined windings

For additional mechanical simplification, the reduction to a single back iron core with one single set of windings is possible. The current components for torque and forces now have to be superposed before being applied to the drive. In this so-called *combined winding system*, the simplification of the mechanical setup increases the control complexity. Many studies have dealt with this winding type, e.g., [13], [14], or [5].

3) Dual-purpose no-voltage windings

A third winding topology has appeared recently ([15], [16], [18]), partly mixing the properties of separated and the combined windings. It provides combined windings with different coil terminals for torque and force current connections by tapping the respective coils. This is termed *parallel motor winding* or *bridge winding* and can, more generally be found in literature as *dual-purpose no-voltage (DPNV)* windings. However, this topology can increase the amount of necessary power switches and current sensors significantly as shown in [16]. Additionally, a full description of the multiple DPNV connection possibilities would go beyond the scope of this work but can be found in the cited publications.

The authors of [17] have compared separated and combined winding systems for a disk shaped bearingless radial pump. Another work [18] discusses the differences between two DPNV winding types and eventually compares them to a separated winding system. All these considerations have come to the conclusion that the correct winding choice is highly dependent on the available power electronics. One of the most stringent differences, however, is the sensitivity to the rotor-field induced back-EMF which must be analyzed in order to allow a topology decision.

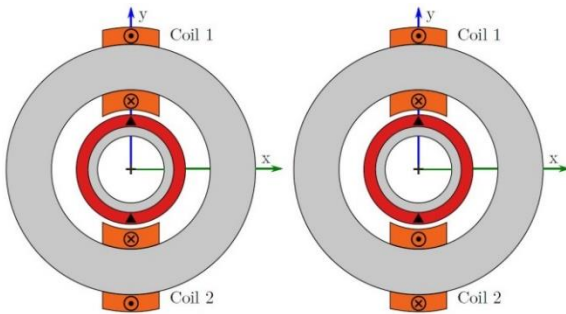


Fig. 3. Separated winding example for bearing forces (left) or torque creation (right) with a two-pole rotor.

The separated winding example in Fig. 3 shows two configurations of coils, each wound around a slotless stator core in a toroid winding manner. They can be connected in order to produce bearing forces (identical winding sense) and torque (opposing winding sense), respectively. Coil 1 and Coil 2 have an identical number of winding turns and, thus, identical values for resistance $R = R_1 = R_2$, inductance $L = L_1 = L_2$, and linked rotor flux amplitude $\hat{\psi} = \hat{\psi}_1 = \hat{\psi}_2$. Due to the winding sense, it becomes clear that the back-EMF V_{BEMF} in the two coils adds up for the torque winding while it cancels out in the force winding setup. Figure 4 shows this relationship in an equivalent circuit. When the voltage drops in L_1 and L_2 cancel out in the torque winding due to the opposing winding sense, the voltage at the clamps

of a connected full bridge inverter is:

$$V_{bridge,T} = i_T 2R + 2\hat{\psi} \cos(\omega t) \omega, \quad (5)$$

where i_T gives the torque current and ω specifies the electrical angular frequency. With a DC-link voltage of V_{DC} , the maximum rotational frequency is limited to:

$$\omega_{max} = \frac{V_{DC} - i_T 2R}{2\hat{\psi}}. \quad (6)$$

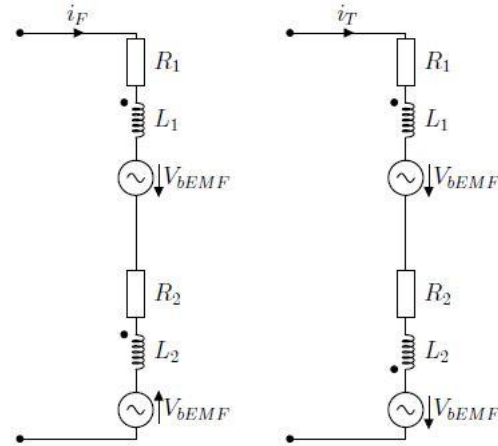


Fig. 4. Equivalent circuit for force (left) and torque creation (right) in the separated winding shown in Fig. .

In a combined winding scheme, each of the coils needs to be controlled individually which results in the corresponding circuit diagram shown in Fig. 5.

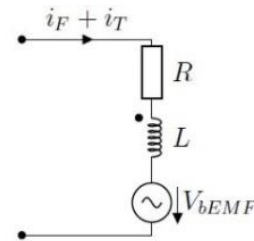


Fig. 5. Equivalent circuit for a combined winding system.

In analogy to the separated winding described above, the clamp voltage at a full bridge is expressed as:

$$V_{bridge} = (i_F + i_T)R + L \frac{d(i_F + i_T)}{dt} + \hat{\psi} \cos(\omega t) \omega, \quad (7)$$

since neither the inductive voltage drop nor the back-EMF cancels out. This limits the maximum rotational frequency to:

$$\omega_{max} = \frac{V_{DC} - (i_F + i_T)R - L \frac{d(i_F + i_T)}{dt}}{\hat{\psi}}. \quad (8)$$

As the back-EMF component is relevant for both, torque and force creation, a voltage reserve needs to be respected in order to guarantee that even at maximum speed, the system can react sufficiently to a radial

disturbance by injecting the necessary force currents.

At a first glance, the combined winding topology seems disadvantageous due to the independence of the force creation from V_{BEMF} . However, this apparent flaw can be resolved by respecting the said voltage reserve. Also, the combined winding always uses the entire conductor cross section which increases efficiency. Lower part count and maximum mechanical compactness add to the advantages of the combined winding which is why it is chosen here.

At the beginning of Section 0, the toroid winding form is presented as an alternative to the air gap winding which in turn was deducted from the winding in a slotted motor. Therefore, each phase shown in the left image in Fig. 6 consists of two coil halves which, together, are electrically equivalent to the air gap winding. This is called *double coil* arrangement. It is, however, also possible, to use only one half per phase (right part in Fig. 6) forming a *single coil* arrangement. Both forms are used for the optimization process below.

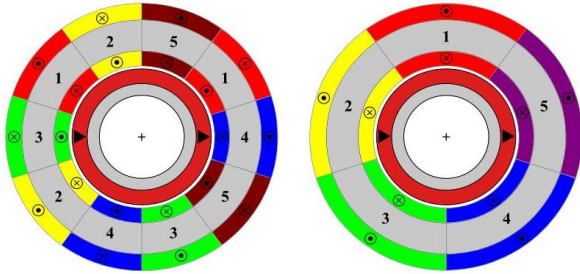


Fig. 6. Exemplary double coil (left) or single coil (right) arrangement for a drive with eight phases.

III. OPTIMIZATION

With a chosen stator (slotless SMC core), a certain winding structure (toroid) with a selected connection (combined winding), the most influential remaining topological choices are the coil number per phase (single or double coil) and the number of phases. The different features of the resulting options have been discussed in [5], leaving the single coil scenarios with 6 or 8 phases as the most beneficial ones. However, for the sake of comparability with preceding studies, only the 5-phase double coil (5pd) and the promising 6-phase single coil (6ps) and 8-phase single coil (8ps) arrangements are selected for optimization.

A. Geometric parameters

Different geometric parameters characterize the drive. In the present case, the rotor diameter d_{ro} and the rotor magnet height h_{PM} are set to a fixed value (cf. Table 1), making the further radial parameters, the rotor back iron (yoke) height h_Y , the height of the rotor bandage h_B , the air gap width δ , the height of the coils

h_{coil} , and the stator height h_{Fe} relevant for the design. Furthermore, the axial stator length l_{Fe} and the phase number m are varied in order to find the best choice.

The parameters h_B and δ are determined by the mechanical safety demands, the necessary touchdown bearing dimensions, and the manufacturing tolerances and will not be used as optimization parameters. The remaining optimization parameters are listed in Table 2.

Table 1: Optimization data – fixed parameters

| Fixed Parameter | Value |
|-----------------|---------------|
| d_{ro} | 30 mm |
| h_{PM} | 4.5 mm |
| δ | 1.5 mm |
| Coil topology | 5pd, 6ps, 8ps |

Table 2: Optimization data – variables and targets

| Variable Parameter | Range | Target | Limit Value |
|--------------------|------------|---------------|------------------------|
| h_Y | 2.5 – 3 mm | c_z | $> 2 \frac{N}{mm}$ |
| h_{coil} | 2 – 3.5 mm | c_τ | $> 0.8 \frac{Nm}{rad}$ |
| h_{Fe} | 9 – 13 mm | $k_{startup}$ | < 2 |
| l_{Fe} | 10 – 14 mm | \bar{T}_z | $> 45 mNm$ |

B. Optimization targets

The passive stiffness coefficients and the active bearing performance are the most important properties besides the torque capacity. Unfortunately, high passive stiffness calls for small magnetic air gaps while active forces and torque require the exact opposite in order to provide a large copper cross section for the stator coils. This conflict can be solved by defining the necessary conditions for the drive in order to function properly and leave the remaining parameters to optimization. In [5], multiple criteria have been defined of which are briefly explained below.

1) Radial force

The active radial force F_r must overcome the passive radial reluctance force, defined in Equation (1). This allows setting a necessary criterion:

$$F_r(\varphi, -\vartheta) > F_{r,rel}(\vartheta - \varphi)\delta \quad \forall \varphi, \vartheta \in [0, 2\pi], \quad (9)$$

for guaranteeing the rotor lift-off for every possible initial rotor deflection angle ϑ , determining the necessary force direction as $-\vartheta$, and every rotor orientation angle φ . The achievable radial force is maximized for the nominal current density J_{max} while zero drive motor torque T_z is produced:

$$F_{r,max}(\varphi, -\vartheta) = \max F_r(\varphi, -\vartheta) |_{J_{1..m} \leq J_{max}, T_z = 0}. \quad (10)$$

For a practical and meaningful value, the radial reluctance force can be substituted by the radial stiffness value and then be put into relation with the maximized

radial force. For a worst-case startup current coefficient, this ratio needs to be maximized, yielding:

$$k_{startup} = \max_{\forall \varphi, \vartheta \in [0, 2\pi]} \frac{\bar{c}_r (1 + \hat{c}_r \cos(2(\vartheta - \varphi))) \delta}{F_{r,max}(\varphi, -\vartheta)}, \quad (11)$$

which, multiplied with J_{max} , must not exceed the short-time tolerable overload current density $J_{startup}$.

2) Axial stiffness

For guaranteeing a limited axial deflection $\delta_{z,max}$ of the rotor due to gravitational acceleration g , the axial stiffness constant must satisfy:

$$c_z > \frac{m_{rotor} g}{\delta_{z,max}}. \quad (12)$$

3) Torque and tilt stiffness

When the necessary criteria in Sections 1) and 2) are met, the drive torque T_z and the tilt stiffness c_τ can be maximized as remaining optimization targets. As the drive torque value also needs to be evaluated under the maximum current density constraint and the independency from the radial forces, a similar criterion as for the forces can be written for the mean torque as:

$$\bar{T}_z = \frac{1}{2\pi} \int_0^{2\pi} \max(T_z(\varphi) |_{J_{1..m} \leq J_{max}, F_x=F_y=0}) d\varphi. \quad (13)$$

C. Optimization setup

Before optimization, the simulation setup is verified by comparing simulation and measurement for two available prototypes. These have different geometric parameters and dispose of a 5pd and a 6ps winding, respectively. All target parameters obtained in simulation except for the tilt stiffness have been measured and the values given in Table 3 show good agreement with an acceptable error of $\leq 10\%$.

Table 3: Comparison of simulated and measured data

| | 5pd Design | | 6ps Design | |
|------------------------------|-------------|--------------|-------------|--------------|
| | <i>Sim.</i> | <i>Meas.</i> | <i>Sim.</i> | <i>Meas.</i> |
| c_z in $\frac{N}{mm}$ | 2.31 | 2.21 | 1.782 | 1.84 |
| c_τ in $\frac{Nm}{rad}$ | 0.749 | n.a. | 0.565 | n.a. |
| $k_{startup}$ | 2.19 | 2.29 | 2.605 | 2.81 |
| \bar{T}_z in <i>mNm</i> | 24.0 | 22.92 | 38.97 | 37.39 |

For the actual optimization, *MagOpt*, developed at LCM GmbH, was used. *MagOpt* provides an interface to several commercial and open-source programs such as CAD and finite element tools via the respective APIs. After configuring a simulation chain with starting

parameters and result targets, the built-in genetic optimizer is used to automatically run the simulations. An initial generation of parameter sets is created, sent to the parametric model in a 3D FE solver, in this case, *Ansoft Maxwell*, and the results are obtained from the simulation output. After processing the results, the next generation of data sets is created, sent to the solver, etc. As the numerical simulation itself can be considered a standard procedure for the design of electric drives and magnetic bearings, the automated optimization is the key feature for this parameter-heavy design process. Within a matter of days, several thousand parameter sets are numerically evaluated, converging to the specified targets, forming the resulting Pareto fronts.

IV. ANALYSIS AND CONCLUSION

A. Analysis of the result

The automated optimization process is stopped when the Pareto front shown in Fig. 7 converges and no longer produces new individuals in the graph. The top left and the bottom right graphs which display the two passive stiffnesses and the two active torque or force targets, respectively, are not useful for finding the optimal individuals. In these two images, both displayed targets benefit from and are weakened by the same geometrical changes. The remaining four graphs compare targets which show opposed reactions to a geometry variation. It is these graphs that the optimum needs to be selected from. It quickly becomes clear that the 5-phase, 6-phase, and 8-phase designs do not differ in the passive stiffness targets as these results do not depend on the winding characteristics. The most prominent difference appears in the torque capacity where the 6ps and 8ps designs dominate. This is the only feature where the topology choice is significantly more important than the geometric choice.

After filtering the solutions according to the target limits given in Table 2, the ones marked with red circles in Fig. 7 remain. For each phase number, one individual is selected and shown in Table 4. While all three meet the targets, the 6ps and 8ps designs are clearly favorable.

Table 4: Selected individuals

| Parameter | 5pd | 6ps | 8ps | Target | 5pd | 6ps | 8ps |
|-------------------------|------|------|-------|------------------------------|------|------|------|
| h_V in <i>mm</i> | 2.91 | 2.94 | 2.96 | c_z in $\frac{N}{mm}$ | 2.03 | 2.14 | 2.17 |
| h_{coil} in <i>mm</i> | 3.3 | 3.21 | 3.27 | c_τ in $\frac{Nm}{rad}$ | 0.84 | 0.82 | 0.85 |
| h_{Fe} in <i>mm</i> | 9.63 | 9.82 | 10.51 | $k_{startup}$ | 1.63 | 1.68 | 1.73 |
| l_{Fe} in <i>mm</i> | 13.4 | 12.7 | 13.95 | \bar{T}_z in <i>mNm</i> | 47.6 | 69.2 | 76.4 |

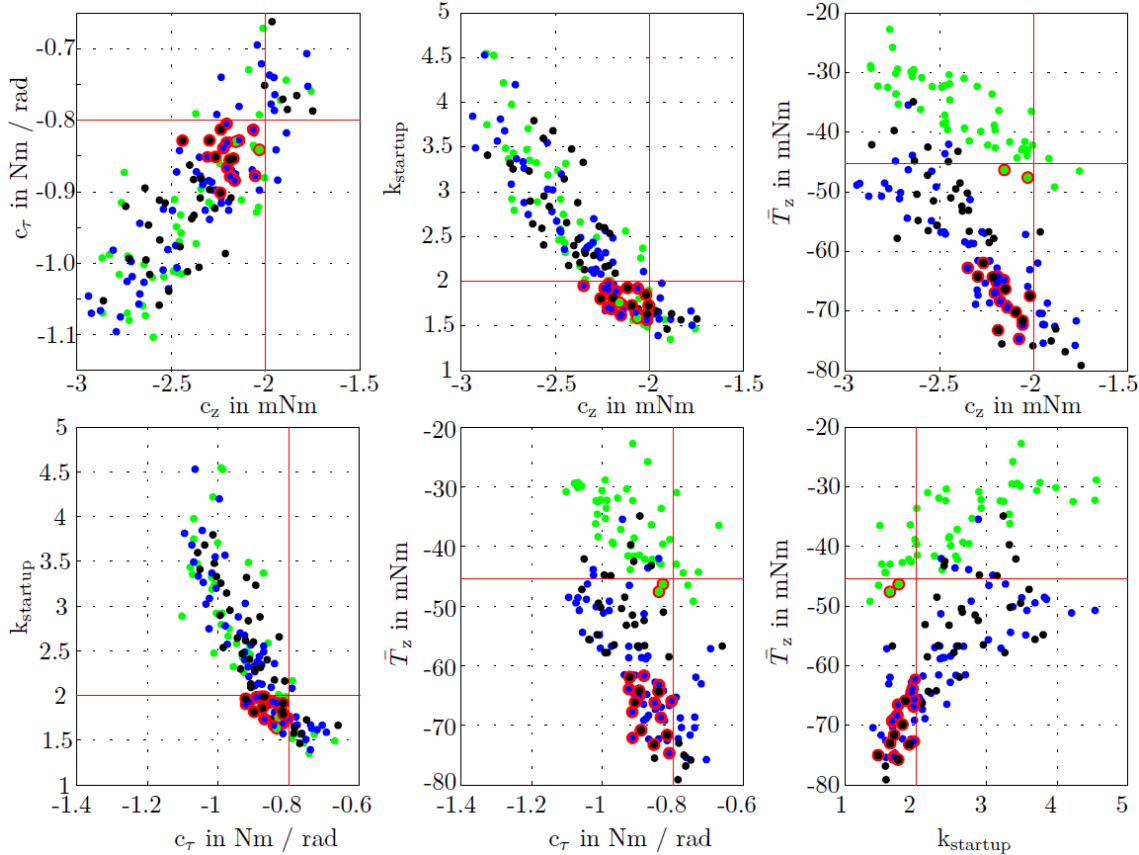


Fig. 7. Optimization output: Pareto fronts with 5pd variants (green) and 6ps variants (blue). Individuals marked red fulfill all targets indicated as red lines.

V. CONCLUSIONS

The design of bearingless drives is a complex undertaking which is expressed by the plurality of topological decisions to take and the numerous geometric parameters influencing the drive performance. Several interesting conclusions can be drawn from the design process.

Characteristic requirements such as high speed, high torque or high efficiency need to be respected in every design step and cannot be left to optimization alone. This is especially true for the selection of the winding topology and the phase number which heavily influence the necessary power electronics circuit.

However, even if certain topological decisions are taken in advance, a multi-criteria optimization based on numerical electromagnetic simulation is necessary due to the large number of influential parameters. Also, the definition of optimization targets is significantly more complex than with a conventional electric machine and their number is higher since active and passive magnetic forces need to be considered.

Even if MagOpt does not restrict the number of variable parameters or targets, a large number of either one will make the optimization process lengthy and the

results hard to interpret. Therefore, it is important to stick to realistic parameter ranges and necessary targets.

ACKNOWLEDGEMENT

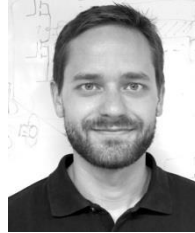
This work was conducted within the COMET-K2 program of the Linz Center of Mechatronics (LCM), and was funded by the Austrian Federal Government and the Federal State of Upper Austria. The authors thank all involved partners for their support.

REFERENCES

- [1] A. Salazar, A. Chiba, and T. Fukao, "A review of developments in bearingless motors," *Proc. 7th Int. Symp. on Magnetic Bearings*, 2000.
- [2] R. Schoeb and N. Barletta, "Principle and application of a bearingless slice motor," *Proc. 5th Int. Symp. on Magnetic Bearings*, 1996.
- [3] H. Mitterhofer, W. Gruber, and W. Amrhein, "On the high speed capacity of bearingless drives," *IEEE Trans. on Ind. Electronics*, vol. 61, no. 6, pp. 3119-3126, 2014.
- [4] D. Steinert, T. Nussbaumer, and J. W. Kolar, "Slotless bearingless disk drive for high-speed and high-purity applications," *IEEE Trans. on Ind.*

- Electronics*, vol. 61, 2014.
- [5] H. Mitterhofer, B. Mrak, and W. Gruber, "Comparison of high-speed bearingless drive topologies with combined windings," *IEEE Trans. on Ind. Applications*, vol. 51, no. 3, pp. 2116-2122, 2015.
 - [6] H. Grabner, H. Bremer, W. Amrhein, and S. Silber, "Radial vibration analysis of bearingless slice motors," *Proc. 9th Int. Symp. on Magnetic Bearings*, 2004.
 - [7] A. Schoppa, P. Delarbre, E. Holzmann, and M. Sigl, "Magnetic properties of soft magnetic powder composites at higher frequencies in comparison with electrical steels," *Proc. 3rd Int. Electric Drives Production Conference*, 2013.
 - [8] A. Chebak, P. Viarouge, and J. Cros, "Analytical computation of the full load magnetic losses in the soft magnetic composite stator of high-speed slotless permanent magnet machines," *IEEE Trans. on Magnetics*, vol. 45, pp. 952-955, 2009.
 - [9] T. Baumgartner, A. Looser, C. Zwysig, and J. W. Kolar, "Novel high-speed, Lorentz-type, slotless self-bearing motor," *Proc. Energy Conversion Congress and Exposition*, 2010.
 - [10] H. Mitterhofer, H. Grabner, and W. Amrhein, "Comparison of two and four pole rotors for a high speed bearingless drive," *Proc. 13th Int. Symp. on Magnetic Bearings*, 2012.
 - [11] A. Chiba, D. T. Power, and M. A. Rahman, "Characteristics of a bearingless induction motor," *IEEE Trans. on Magnetics*, 1991.
 - [12] P. Karutz, T. Nussbaumer, W. Gruber, and J. W. Kolar, "The bearingless 2-level motor," *Proc. 7th Int. Conf. on Power Electronics and Drive Systems*, 2007.
 - [13] W. Gruber, T. Nussbaumer, H. Grabner, and W. Amrhein, "Wide air gap and large-scale bearingless segment motor with six stator elements," *IEEE Trans. on Magnetics*, 2010.
 - [14] T. Reichert, T. Nussbaumer, and J. W. Kolar, "Bearingless 300-W PMSM for bioreactor mixing," *IEEE Trans. on Ind. Electronics*, 2012.
 - [15] A. Chiba, S. Horima, and H. Sugimoto, "A principle and test result of a novel bearingless motor with motor parallel winding structure," *Proc. Energy Conversion Congress and Exposition*, 2013.
 - [16] E. Severson, S. Gandikota, and N. Mohan, "Practical Implementation of dual purpose no voltage drives for bearingless motors," *Proc. IEEE Applied Power Electronics Conference and Exposition*, 2015.
 - [17] K. Raggl, T. Nussbaumer, and J. W. Kolar, "Comparison of winding concepts for bearingless pumps," *Proc. Int. Conf. on Power Electronics*, 2007.
 - [18] E. Severson, R. Nilssen, T. Undeland, and N. Mohan, "Dual-purpose no-voltage winding design for the bearingless AC homopolar and consequent

pole motors," *IEEE Trans. on Ind. Applications*, vol. 51, no. 4, pp. 2884-2895, 2015.



Hubert Mitterhofer studied Mechatronics at Johannes Kepler University (JKU), Austria and Université de Pierre et Marie Curie, France and received his diploma in 2008 and his Ph.D. degree in 2017. Since 2013, he is working as a Researcher at the Linz Center of Mechatronics GmbH (LCM), dealing with electrical drive development, bearingless high speed drives and magnetic bearings. Mitterhofer is involved in the development of MagOpt and is maintaining the web portal magneticbearings.org. His personal technical interests also cover agriculture technology and renewable energies.



Siegfried Silber studied Electrical Engineering at the University of Technology Graz and obtained his Dr.Techn. degree from JKU Linz, Austria, in 1995 and 2000, respectively. He was with the Institute for Electrical Drives and Power Electronics at the JKU from 1995 to 2014 and joined LCM in 2014 where he is Technical Area Manager for Electrical Drives. His research interests include electrical drives, power electronics, magnetic bearings and bearingless motors. Silber is leading the development of the mechatronic component optimizer MagOpt and the open source tool X2C for model-based development and code generation of real-time control algorithms for microprocessor units.

Performance Tests of a Permanent Magnet Thrust Bearing for a Hydropower Synchronous Generator Test-Rig

J. José Pérez-Loya, C. Johan D. Abrahamsson, Fredrik Evestedt, and Urban Lundin

Division of Electricity, Department of Engineering Sciences
Uppsala University, Uppsala, SE75121, Sweden

Jose@Angstrom.uu.se, Johan.Abrahamsson@Angstrom.uu.se, Fredrik.Evestedt@Angstrom.uu.se,
Urban.Lundin@Angstrom.uu.se

Abstract — Permanent magnets are an attractive material to be utilized in thrust bearings as they offer relatively low losses. If utilized properly, they have a long service lifetime and are virtually maintenance free. In this contribution, we communicate the results of the tests performed on a permanent magnet thrust bearing that was custom built and installed in a hydropower synchronous generator test-rig. Tridimensional finite element simulations were performed and compared with measurements of axial force. Spin down times and axial force ripple have also been measured. We found good correspondence between the measurements and the simulations.

Index Terms — Axial bearing, Halbach array, hydropower, magnetic bearing, permanent magnet, thrust bearing.

I. INTRODUCTION

A. Background

Large electromagnetic actuators have been used successfully since the 1950's to partly bear the load of vertical hydropower units [1]. This places hydropower among the oldest applications of magnetic thrust bearings. Even though, the technology improves the reliability and efficiency of the thrust system, their utilization is not widespread. They have been mostly utilized in pump storage stations. Notably, as a problem solver in Europe's largest installation of this type at Dinorwig in the United Kingdom [2]. In general, as often happens with industrial components, thrust bearings for hydropower are required to be technically superior compared to the past. They are required to have a higher degree of efficiency, to operate with a higher level of reliability, to be more sustainable and to bear larger loads, both static and transient. They also need to operate in tougher conditions, the generation patterns required by energy markets and the introduction of intermittent solar and wind power results in an increased number of start and stop operations. Moreover, in some occasions, the generators are required to operate at a peak level, or on the contrary at low capacity. This operational patterns cause extra wear and tear in the

thrust bearing pads. When it comes to reliability, a high percentage of the generator failures in large machines are due to bearing failures [3, 4, 5]. According to an analysis performed in 1980, more than half of the operational failures of equipment in hydropower stations is due to unreliable operation of the thrust bearing [6]. The economic implications of such failures are large. Not only due to the expenses required to repair the machine, but also due to production loss. On top of this, some utilities are looking for strategies to eliminate oil in the hydropower stations in order to eliminate the risk of pollution in the rivers. To achieve this objective relatively small hydropower generators have been fully levitated [7]. When it comes to large installations, thrust bearings are at its limit. Increasing their size to increase their capacity is not an easy task as the losses depend on the diameter of the bearing. With mechanical solutions, installing more than one bearing in order to increase the load capacity is not an option for machines in hydropower sizes. One way to cope with these challenges is to use magnetic forces either from electromagnets, permanent magnets or a combination of both [8], bearing the force only by magnetic means or in combination with mechanical bearings in a similar fashion as it has been done since the 1950's, but with 65 years of advances in crucial technology in relevant areas, such as control, electronics and magnetic materials. At Uppsala University a synchronous generator hydropower test-rig with magnetic bearings has been designed and constructed. The test-rig is flexible enough to allow the study of the behavior of the machine while operating on a permanent magnet thrust bearing, an electromagnetic thrust bearing, a roller thrust bearing or any combination of them. With these new tools, the advantages of utilizing magnetic forces in the thrust system can be further investigated.

The focus of this paper is on the performance and finite element simulations of a permanent magnet thrust bearing constructed with 2532 N48 Nd-Fe-B permanent magnets in a Halbach array. The permanent magnet thrust bearing, is the preferred bearing for the test-rig as it does not require external power or control to function

and it offers lower losses compared to its mechanical counterpart.

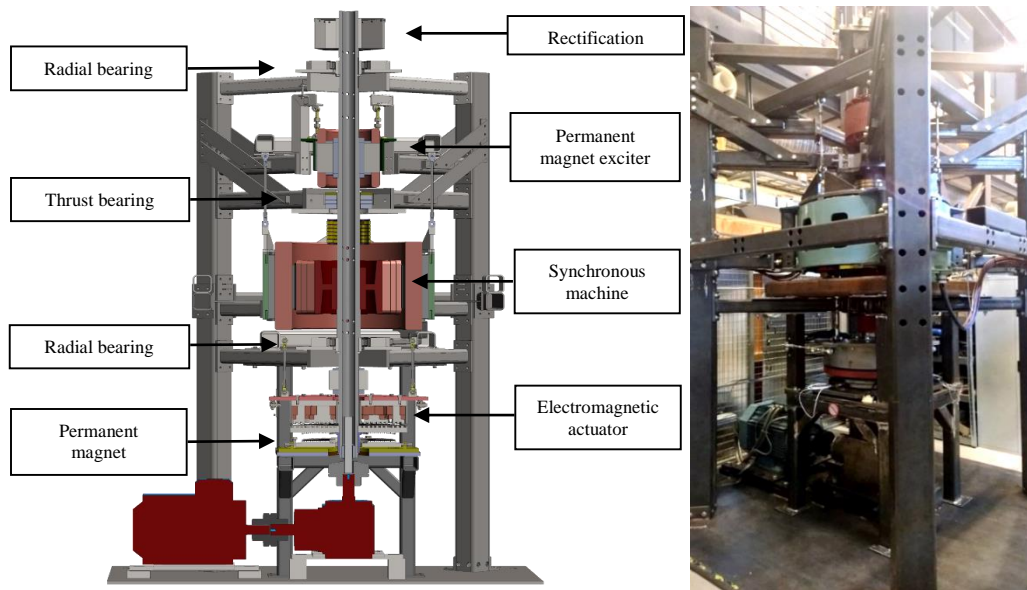


Fig. 1. (Left) Cross sectional view of the 3D CAD model of the vertical synchronous generator test-rig built and designed at Uppsala University. (Right) Actual test rig.

B. Brief description of the experimental test-rig

The vertical synchronous generator test-rig built and designed by the hydropower group at Uppsala University as described by Wallin, [9] has been upgraded to accommodate a range of features. As shown in Fig. 1, from bottom to top, some of them are: a permanent magnet thrust bearing, an electromagnetic actuator and a brushless excitation system with permanent magnets [10]. The machine was also equipped with a roller thrust bearing that was mounted between the generator and the brushless exciter. After the upgrades, the shaft resulted in a weight of 12.56 kN. The rotational speed needed to synchronize the machine with the grid is 500 rpm. To mimic the power exerted by water on a turbine, an induction motor and a gearbox were utilized, they can be seen in Fig. 1 (left) in dark red. The torque was transferred from the gearbox to the shaft of the test rig through a flexible coupling and a ball spline, these components can be seen in Fig. 2 (top). This construction allowed us to adjust the axial position of the shaft in relation to the static parts without affecting the torque transfer. The idea was to be able to use the machine while resting on the permanent magnet thrust bearing, the roller bearing, while utilizing the electromagnet actuator or as well as any possible combination between them. The actual adjustment of the axial position of the shaft was realized by moving the permanent magnet thrust bearing up and down. When the permanent magnet thrust bearing sat at its lowest position, the shaft descended to rest on the mechanical bearing. In this position, the

airgap of the permanent magnet thrust bearing was so large that there was virtually no force exerted on the shaft by the permanent magnets. On the contrary, as the permanent magnet thrust bearing was moved up, the magnetic forces started to push on the shaft. If raised enough, the shaft could be released from the mechanical bearing and rest only on the permanent magnets, all the experiments reported in this paper were performed with the test-rig in this position, except the spin down test on the mechanical bearing. When resting on the magnetic thrust bearing, the shaft is stable in the axial direction but unstable in the radial direction. This phenomena can be described by extension of Earnshaw's theorem for electrostatic charges [11]. For this reason, the shaft was held in the radial direction by two radial roller bearings. They sit under the control and rectification box and under the generator respectively. To allow them to function properly regardless of the axial position chosen, the shaft was provisioned with oversized inner races. In this way contact between the rollers and a proper inner race was always achieved. The designation of both radial bearings selected is NU 326 ECP, the inner races belong to NU 2326 ECMA, all from SKF.

C. Permanent magnet thrust bearing

The device was designed and custom built as part of a major upgrade to the test rig. The estimated weight of the rotating parts at the design stage was around 15 kN. The bearing was to be built by hand. Magnets that could be easily and safely handled by a person with no special

equipment were needed. For this practical reasons, it was decided to utilize cubic 12 mm N48 Nd-Fe-B permanent magnets. In order to accommodate as much magnetic material as possible in a given volume, a Hallbach array arranged in the radial direction was selected, 13 rows of magnets with alternating polarity were mounted to create a homo polar array in the angular direction. For practical and economic reasons it was convenient to utilize cubic magnets. However, the segmentation of the array carried its own drawbacks. One of them was that it could generate axial force ripple as the shaft rotates. There is at least one technique to prevent, or at least reduce this inconvenience. It involves covering the magnets with a thin piece of ferromagnetic material to smoothen out the field across the segmentation [12]. For this bearing, we decided to install a different number of magnets in the rotor than in the stator. Each of the rows of magnets have one pair of magnets difference than its counterpart in the other plate. By doing this, a constant overlap of magnetic material was achieved even when the shaft was rotated. Another measure taken to prevent force oscillations was to randomly position the rows of magnets in the angular direction in relation to each other. The resulting pattern of this efforts in the rotor plate is shown in Fig. 2. The details of the construction of the bearing can be found in [13]. Another drawback of this construction was that in order to evaluate the force capabilities of the bearing including the effect of the segmentation full 3D Finite element simulations were needed. The existent analytical formulas [8] or 2D simulations were not capable of evaluating the axial force ripple caused by the segmentation.



Fig. 2. (Top) Flexible coupling and driving end of the shaft. (Bottom) Permanent magnet thrust bearing rotor prior assembly. The details of the segmentation of the magnetic material can be appreciated.

II. METHOD

To be able to assess the performance of the bearing, we performed finite element simulations, axial force and axial force ripple measurements, and spin down tests.

A. Three dimensional finite element simulations

In order to take into account the segmentation in the bearing, we have simulated it using 3D FEM static simulations. For all of them, we used 2535 volumes. One for each magnet, one for a cylindrical portion of air between the permanent magnet surfaces that was basically the airgap, and two more for the air surrounding the magnets in the radial direction. Since a Hallbach array was utilized, we decided not to model the steel plates in which the magnets were mounted as the field in this region was expected to be relatively low. We started the simulation routine by importing the geometry from a dedicated CAD software (Solid Works 2015) into a commercial finite element program (Comsol 5.1). After the geometry was processed, we proceeded to mesh the cylindrical volume that represented the airgap. In this part of the procedure, we required 5 tetrahedral elements in the axial direction as it is the main region of interest. Afterwards, the mesh that resulted in the interface between the airgap and the magnet assembly was swept to discretize the remaining bodies, for each of them we utilized two elements in the axial direction, thus it resulted in pentahedral elements. With this meshing procedure, it was possible to take into account the segmentation of magnetic material in the permanent magnet thrust bearing assembly. One of the resulting meshes is shown in Fig. 3.

The resulting number of degrees of freedom solved for each mesh are shown in Table 1. As it can be seen, the number of degrees of freedom increases when the airgap is reduced. The reason is that we decided to utilize 5 elements in the axial direction to model the airgap. Therefore, the resulting number of elements varied with the airgap length. For a smaller airgap, the maximum size of the element was reduced, resulting in a larger number of mesh elements.

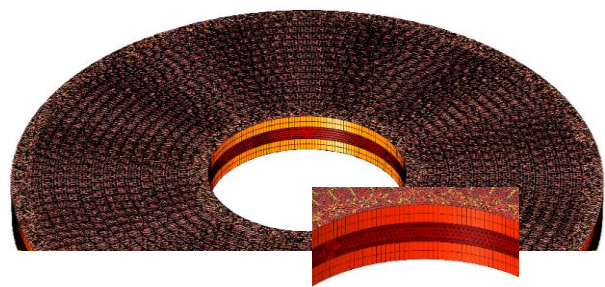


Fig. 3. One of the meshes utilized to calculate the force in the permanent magnet thrust bearing with the finite element method.

Table 1: Number of degrees of freedom solved for each simulation depending on the airgap length

| Airgap (mm) | Number of Degrees of Freedom Solved |
|-------------|-------------------------------------|
| 10 | 2.7756e7 |
| 11 | 2.5157e7 |
| 12 | 1.9514e7 |
| 13 | 1.7788e7 |
| 14 | 1.6306e7 |
| 15 | 1.4765e7 |
| 16 | 1.1542e7 |

After the meshing was performed, we proceeded to set the finite element formulation. We utilized the following constitutive relation for all the simulated volumes:

$$\mathbf{B} = \mu_0 \mu_r \mathbf{H} + \mathbf{B}_r. \quad (1)$$

For the two volumes surrounding the magnets and the volume that represented the airgap, the relative permeability was set to $\mu_r = 1$. Since the grade of Nd-Fe-B permanent magnet material selected had a relatively high coercivity and the height to width aspect ratio of the magnets selected was high [14], we considered that implementing the \mathbf{BH} curve of the magnets was not needed. Therefore, we set the relative permeability of the permanent magnet material to $\mu_r = 1.037$ and the remanence to $\mathbf{B}_r = 1.35\text{T}$. The typical remanence for this batch of magnets was obtained directly from the manufacturer (Sura magnets), and the permeability from the datasheet of a typical N48 permanent magnet from Arnold magnetics [15]. The direction of magnetization of the permanent magnets was set according to the schematic shown in Fig. 4.

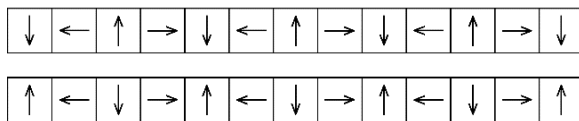


Fig. 4. Direction of magnetization utilized in the Hallbach arrays of the permanent magnet thrust bearing.

Afterwards, we solved for the magnetic vector potential using the following equation form:

$$\nabla \times (\mu_0^{-1} \mu_r^{-1} (\mathbf{B} - \mathbf{B}_r)) = \mathbf{0}, \quad (2)$$

where:

$$\mathbf{B} = \nabla \times \mathbf{A}. \quad (3)$$

In all the studies, the forces between the volumes that represented the stator and the rotor of the permanent magnet thrust bearing were calculated using the Maxwell stress tensor. In total, we performed 7 simulations at different airgaps to evaluate the force as the plates approached each other and 38 simulations at 16 mm airgap for different rotational positions between the

plates. 5 simulations in steps of 1 degree, 18 simulations in steps of 2 degrees, and 15 in steps of 5 degrees. With this amount of simulations we were able to cover one third a revolution. This was done to evaluate the axial force ripple as the bearing rotated.

B. Thrust vs. distance measurements

The measurements of thrust and distance between the bearing plates were taken in situ, with the bearing installed in the machine. We started by measuring the load exerted by the weight of the shaft on the bearing and the distance between the rotor and the stator. Afterwards, we artificially increased the load in the bearing as described in Fig. 5. To evaluate the axial force, three load cells were inserted in parallel under the bearing. The load cells used are of the doughnut type, model LTH350 from the company Futek. They were previously calibrated and the signals were properly amplified. We measured the airgap between the plates manually with a caliper at different points around the circumference of the bearing and then calculated the average.

C. Spin down tests

The test rig was provisioned with speed sensors that made it possible to evaluate the rotational speed of the machine over time during spin-down. The machine was accelerated to one third of the rated speed, afterwards the driving power was disconnected, the rotational speed was recorded when the machine was resting on the permanent magnet thrust bearing as well as when it was resting on the roller bearings.

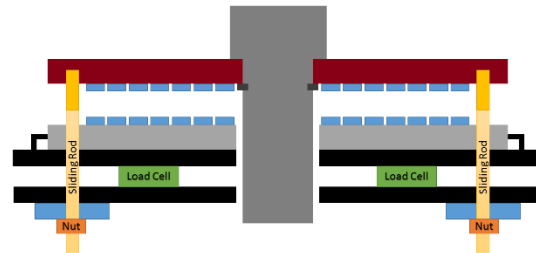


Fig. 5. Schematic of the axial force test set-up. Sliding rods (yellow) were attached to the rotor plate (red). Torque was applied to the nuts (orange), through washers (blue) that pressed on the static foundation that holds the bearing (black). By reaction, the rotor plate (red) was pulled downwards. The sliding rods were used to maintain the radial placement of the plates. To reduce their influence on the measurements, they were properly greased. The distance measurements between the plates were taken manually with a caliper, the force measurements were recorded with load cells (green).

D. Axial force ripple measurements

In order to evaluate the movement of the shaft in the axial direction, we measured the relative position

between the rotor and the stator with a high accuracy Eddy-current sensor from MICRO-EPSILON model eddyNCDT3010,S2. We did it at 500 rpm, the rated speed. At the same, we recorded the force measured in the three load cells that were described in Section II-B.

III. RESULTS AND DISCUSSIONS

The results arising from the methods presented are summarized in this section. The finite element method calculations are compared with the measurements performed for the thrust vs. distance and the axial force ripple.

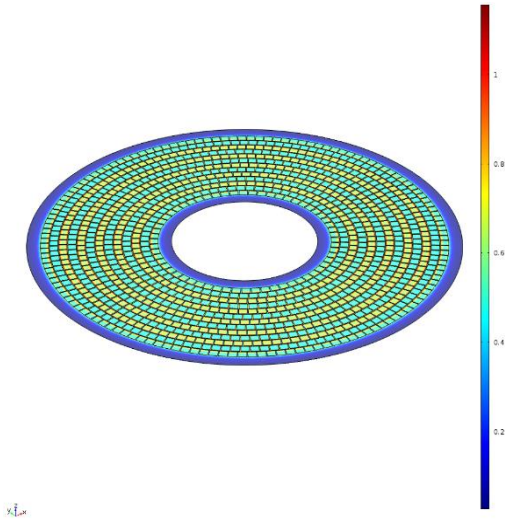


Fig. 6. Simulated flux density in the surface of one the permanent magnet bearing plates at an airgap of 16 mm. In order to be able to simulate the effects of the segmentation of the magnetic material, three-dimensional simulations were performed. In the figure, the flux density distribution pattern of the Hallbach array can be appreciated.

A. Thrust vs. distance measurements and finite element calculations

As described in the previous section, the permanent magnet thrust bearing was loaded from its usual load (shaft weight), to a value just under the maximum that the load cells could take. We also simulated the bearing in the same range. The resulting simulated magnetic flux density at the surface of one of the plates of the magnetic bearing is shown in Fig. 6. The calculated force between the plates at different airgaps with the three dimensional simulations and its corresponding measurements are shown in Fig. 7. We found good correspondence between them. In all the cases, the simulations showed a slight overestimation of the force. The discrepancy increased as the airgap was reduced. This is most likely due to the effects that we had chosen to neglect in order to simplify

the simulations, mainly the full magnetic characteristics of the permanent magnets and the steel plates in which the magnets were assembled. If both were implemented, it is expected that the force calculated would be lower as the plates approach each other. This is due to the fact that the leakage field on the plates will result in a small attractive force. On the other hand, the magnetic domains would deviate from ideal as the magnets are pushed closer. Both effects act in detriment of the repulsive force. Nevertheless, as we suspected, the influence of this simplifications were small. On the practical side, during the measurements, the assembly was constrained radially not only by the sliding rods utilized to exert and extra force on the bearing, but also by the radial bearings and the spline. They certainly had an effect on the measured forces, but as it can be appreciated from the comparison this effect was small as well.

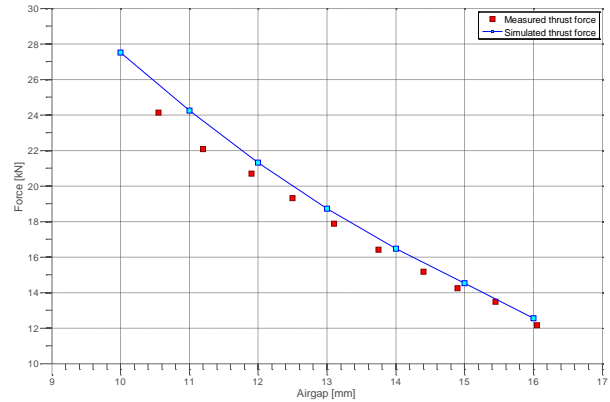


Fig. 7. Simulated and measured thrust forces as a function of airgap length.

B. Spin down tests

After the installation of the permanent magnet thrust bearing into the hydropower test-rig, a number of spin-down tests were made. These tests were performed with the rotor resting axially only on the permanent magnet thrust bearing, and also when it was supported only by the mechanical roller bearing. The rotor was accelerated to a rotational speed of 166.7 rpm, one third of the rated speed of the test-rig. The drive was thereafter turned off, and the rotor allowed to spin-down. The measured rotational speed over time for the two cases can be found in Fig. 8. From the figure it can be concluded that the losses in the machine when it is supported by the permanent magnet thrust bearing are lower than when it is supported by its mechanical counterpart. It is hard to isolate the losses of each thrust bearing from the losses in the other parts of the system, but if it is assumed that windage and radial bearing losses are the same for both tests, the difference presented in Fig. 8 corresponds to the difference in losses between both bearings.

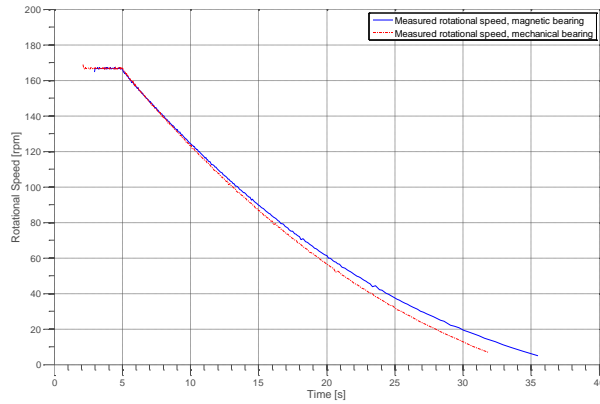


Fig. 8. Measured rotational speed as function of time during a spin-down test from a rotational speed of 166.7 rpm when the shaft was supported by the permanent magnet thrust bearing and the corresponding set of measurements when it was carried by a roller bearing.

C. Axial ripple measurements and finite element calculations

In order to estimate the influence that the segmentation of the magnetic material utilized to build the Hallbach arrays for the magnetic bearing as it rotates, we performed a large number of static simulations along one third of a revolution at an airgap of 16 mm which is the operational distance between the bearing plates. We did the simulations in different increments, the idea was to map the influence of the segmentation at different levels. The simulations with a small step (1 degree) were performed to try to map the influence within the width of a magnet. We found from the simulations that the influence of the segmentation on the axial force as the bearing rotates is very small. The average force obtained in all the 38 simulations was 12.5589 kN, the maximum force simulated was 12.55974 kN and the corresponding minimum was 12.53914 kN. We found that maximum variation from the average was a bit more than 30 N. The results of the simulations are shown in Fig. 9.

In order to be able to compare the results from the finite element simulations, we also measured the relative movement between the shaft at rated speed and the force through the load cells, the results of these measurements are shown in Fig. 10. From the measurements of force we can see that the obtained thrust force peak oscillations were roughly double than the simulated values. Still, the figures were quite low compared to the operational thrust. In the distance measurements, sharp peaks can be appreciated, they corresponded to four equidistant holes in the measured surface. They were useful to measure the rotational position. From this measurements a pattern can be appreciated, the distance between the plates varied periodically with the rotational frequency. The measured variation was small, the measured peak was less than a fifth of a millimeter.

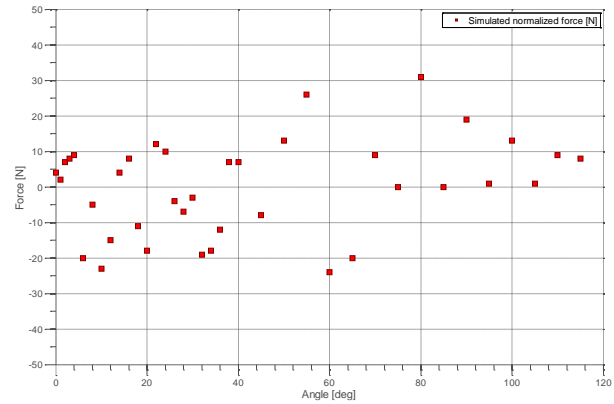


Fig. 9. Simulated normalized force obtained from static three dimensional simulations. As it can be seen in the figure, the expected variation in the force as the bearing rotates is very low compared to the actual carried force of 12.55 kN.

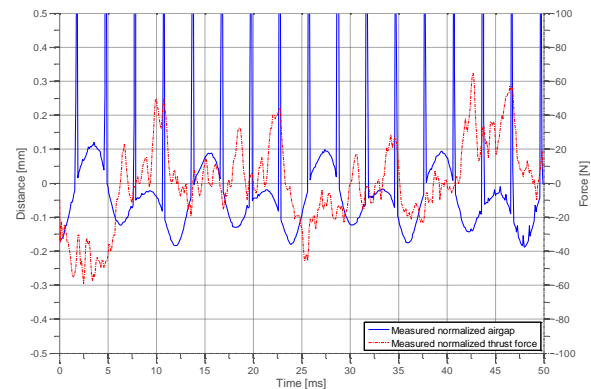


Fig. 10. Normalized measurements of airgap and thrust force at rated speed.

IV. CONCLUSIONS

The results presented in this paper showed that the design, construction and installation of a permanent magnet thrust bearing useable for rotor weights up to a couple of tons is technically feasible. For practical reasons, we decided to build a segmented structure. For the weight required, there were practically no constraints in terms of space, this allowed us to have a comfortable design that resulted in a bearing with a large airgap. Nevertheless, we took provisions to reduce the axial force ripple as much as possible in spite of the segmentation of the magnetic material utilized. The efforts resulted in relatively low axial oscillations. The expected thrust force and the expected ripple due to the segmentation of the magnetic material were simulated utilizing three dimensional finite element calculations. The calculated values had good correspondence with measured ones. The bearing presented in this paper will allow the further investigation magnetic bearings. The simulation tools

verified in this work, will allow us to design larger bearings.

ACKNOWLEDGMENT

This work was supported by the Swedish Centre for Smart Grids and Energy Storage (SweGRIDS) and StandUP for Energy.

REFERENCES

- [1] T. Nakata, "Magnetic thrust bearings," *Fuji Denki Review*, vol. 4, no. 2, 1958.
- [2] Voith, "Modernization of Europe's largest solution," *HyPower*, no. 2, pp. 38-41, 2002.
- [3] M. Nässelqvist, R. Gustavsson, and J. Aidanpää, "Resonance problems in vertical hydropower unit after turbine upgrade," *IAHR 24th Symposium on Hydraulic Machinery and Systems*, Foz do Iguaçu, Brazil, Oct. 2008.
- [4] R. Ong, J. H. Dymond, R. D. Findlay, and B. Szabados, "Shaft current in AC induction machine – An online monitoring system and prediction rules," *IEEE Transaction on Industry Applications*, vol. 37, no. 4, 2001.
- [5] A. Bonett and G. C. Soupkup, "Cause and analysis of stator and rotor failures in three-phase squirrel-cage induction motors," *IEEE Trans. Ind. Applicat.*, vol. 28, pp. 921-936, 1992.
- [6] Y. I. Baiborodov, A. V. Tereshchenko, A. E. Aleksandrov, V. S. Shchetkin, I. B. Pokrovskii, V. P. Tukmakov, and I. S. Gurbanov, "Results of full-scale tests of the thrust bearing with elastic metal-plastic segments for the turbine-generator unit at the Bratsk hydroelectric station," *Hydrotechnical Construction*, 16: 348, 1982. doi:10.1007/BF02116888
- [7] K. Yamaishi, "Applications and performance of magnetic bearing for water turbine generator," *Proceedings of MAG '97, Industrial Conference and Exhibition on Magnetic Bearings*, Virginia, USA, Aug. 1997.
- [8] H. Ma, Q. Wang, and P. Ju, "Study of the load reduction for hydrogenerator bearing by hybrid magnetic levitation," *International Journal of Applied Electromagnetics and Mechanics*, no. 43, pp. 215-226, 2013.
- [9] M. Wallin, M. Ranlöf, and U. Lundin, "Design and construction of a synchronous generator test setup," *XIX International Conference on Electrical Machines – ICEM*, Rome, Italy, Sep. 2010.
- [10] J. K. Nøland, F. Evstedt, J. J. Pérez-Loya, J. Abrahamsson, and U. Lundin, "Design and characterization of a rotating brushless PM exciter for a synchronous generator test setup," *International Conference on Electrical Machines 2016 (ICEM'16)*, 2016.
- [11] J. Abrahamsson, "Kinetic Energy Storage and Magnetic Bearings for Vehicular Applications," Ph.D. Dissertation, Uppsala, 2014.
- [12] J. Kumbernuss, C. Jian, J. Wang, H. X. Yang, and W. N. Fu, "A novel magnetic levitated bearing system for vertical axis wind turbines (VAWT)," *Applied Energy*, vol. 90, pp. 148-153, 2012.
- [13] J. J. Pérez-Loya, J. de Santiago, and U. Lundin, "Construction of a permanent magnet thrust bearing for a hydropower generator test setup," *1st Brazilian Workshop on Magnetic Bearings – BWMB*, Rio de Janeiro, Brazil, Oct. 2013.
- [14] J. J. Pérez-Loya and U. Lundin, "Optimization of force between cylindrical permanent magnets," *Magnetics Letters, IEEE*, vol. 5, pp. 1-4, 2014.
- [15] Arnold Magnetic Technologies, "Neodymium-Iron-Boron Magnet Grades Summary Product List & Reference Guide," Arnold Magnetic Technologies Corp., 2015. [Online]. Available: <http://www.arnoldmagnetics.com/Portals/0/Files/Catalogs%20and%20Lit/Neo/151021/Catalog%20-%20151021.pdf?ver=2015-12-07-103821-497>

J. J. Pérez-Loya received the B.Sc. degree in Mechanical and Electrical Engineering from ITESM, Monterrey, Mexico, in 2006, and the M.Sc. degree in Electric Power Engineering from the Chalmers University of Technology, Gothenburg, Sweden, in 2010. Since 2011, he has been working towards the Ph.D. degree in Engineering Physics at Uppsala University, Uppsala, Sweden. He spent 3 years at Ingeniería de Control y Potencia (ICP), Mexico, where he gained industrial experience in water and electricity distribution. His research interest includes the utilization of magnetic forces in electrical machines.

C. J. D. Abrahamsson received the Ph.D. degree in Engineering Physics from Uppsala University, Uppsala, Sweden, in 2014. From 2002 to 2008, he held different positions at ABB, Ludvika, Sweden and Baden, Switzerland, with tasks ranging from research to management. His research interests include scientific simulation, field theory, magnetic bearings, and electric drivelines. Since 2014, he is a Researcher at the Division of Electricity at Uppsala University.

F. Evstedt received the M.Sc. degree in Renewable Electricity Production from Uppsala University, Uppsala, Sweden, in 2015. He is currently working towards the Ph.D. degree in Engineering Physics at Uppsala University, Uppsala, Sweden. His research interest include electronics, power electronics, measurement circuits and PCB design.

U. Lundin received the Ph.D. degree in Condensed Matter Theory from Uppsala University, Uppsala, Sweden, in 2000. From 2001 to 2004, he was a Postdoctoral at the University of Queensland, Brisbane, Australia. In 2004, he joined the Division for Electricity at Uppsala University where he is currently Professor in Electricity with specialization towards Hydropower Systems. His

research focuses on synchronous generators and their interaction with mechanical components and the power system. He leads the Hydropower Group and has been involved in the industrial implementation of research projects. His current research interests include excitation systems and magnetic bearings.

Vibration Isolation of Magnetic Suspended Platform with Double Closed-loop PID Control

Mao Tang¹, Jin Zhou¹, Chaowu Jin¹, and Yuanping Xu^{1,2}

¹College of Mechanical and Electrical Engineering
Nanjing University of Aeronautics and Astronautics, Nanjing 210016, China
tangm@nuaa.edu.cn, zhj@nuaa.edu.cn, jinchaowu@nuaa.edu.cn, ypxu@nuaa.edu.cn

²Laboratory of Robotic Systems
Ecole Polytechnique Federale Lausanne (EPFL), Lausanne 1015, Switzerland

Abstract — In magnetic vibration isolation field, magnetic force is used for the isolation, while the whole isolation system is always supported passively, which have non-control shortcomings. Aimed at this problem, a novel active control strategy with a double closed-loop PID algorithm was designed in this paper. The double closed-loop strategy includes an internal and external loop control, which was designed to fulfill the magnetic levitation and isolation, respectively. Firstly, the vibration isolation strategy proposed in this paper was simulated in both time and frequency domain. The simulation results showed that this method possesses good performance of vibration isolation. Then, an active levitation and vibration isolation control experiment was designed. The experimental results showed that the control algorithm has a good vibration control effect under periodic vibration and random vibration conditions.

Index Terms — Double closed-loop PID, magnetic levitation, vibration isolation.

I. INTRODUCTION

With the development of precise and ultraprecise manufacturing technology, the vibration control in the process of mechanical equipment operation is getting more and more attention. The research on the vibration isolation control has developed from passive isolation control to active isolation control [1-2], and from single degree-of-freedom (DOF) vibration [3-4] to multi degrees-of-freedom vibration [5-6].

The magnetic levitation technology possesses the advantages of no contact, no friction, free of lubricating oil pollution, adjustable bearing stiffness and levitation position [7]. Thus, the application of vibration control combining with the magnetic levitation technology has good prospects.

For most of the magnetic vibration isolation system, the whole system is supported by the traditional methods

such as spring, rubber pad and air bag [3, 6, 8]. Although traditional passive support can bear more weight, the bearing characteristics like height and stiffness are not easy to adjust. And traditional passive support is unable to achieve active control to the external disturbance. Therefore, the magnetic technology can be utilized to support and isolate vibration using the electromagnetic force without any additional vibration isolation equipment, which is very promising for the optical instruments, or those light load equipment sensitive to vibration. This method can simplify the vibration isolation system structure, reduce cost, and increase the vibration isolation frequency range combining the passive and active vibration isolation. So the magnetic suspension platform realizing both stable suspension and broadband vibration isolation has great research value.

In this paper, a new double closed-loop control based on the PID control [9] was proposed and applied to a one DOF magnetic levitation platform with the combined functions of active levitation and the active vibration isolation. The controller using the relative displacement and absolute acceleration as feedback signal adopted the inner loop to control the magnetic levitation support and the outer one to control the vibration isolation.

The remainder of this paper is organized as follows: Section 2 analyzes the vibrating transmissibility of the passive vibration isolation system and the passive-active vibration isolation system. Section 3 presents the vibrating transmissibility of magnetic levitation system with inner PID loop controlling the magnetic levitation support. Section 4 is the simulation of the system with double closed-loop PID. Section 5 shows the experimental results of the magnetic levitation system with double closed-loop PID control, and conclusion are drawn in Section 6.

II. ACTIVE AND PASSIVE VIBRATION ISOLATION

According to whether the controller is needed or not,

vibration isolation system can be divided into active and passive vibration isolation system. Passive vibration isolation system can be simplified as one DOF mass-spring-damping vibration isolation model, as shown in Fig. 1.

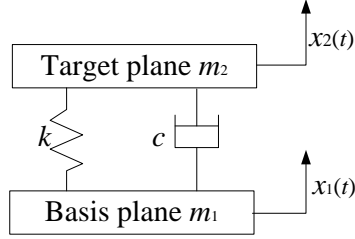


Fig. 1. Principle for passive isolation.

For the Fig. 1, the equation of motion can be written as:

$$m_2 \ddot{x}_2(t) + k(x_2(t) - x_1(t)) + c(\dot{x}_2(t) - \dot{x}_1(t)) = 0, \quad (1)$$

where m_2 is the mass of the target plane, k is the supporting stiffness, c is the damping coefficient, $x_1(t)$ is vibration displacement of the basis plane, and $x_2(t)$ is the vibration displacement of the target plane. The main purpose of the vibration isolation is to reduce the vibration transmitted from the basic object to the target plane.

The transmissibility of vibration acceleration amplitude is:

$$\frac{\ddot{X}_2}{\ddot{X}_1} = \frac{X_2}{X_1} = \sqrt{\frac{k^2 + (c\omega)^2}{(k - m_2\omega^2) + (c\omega)^2}}, \quad (2)$$

where X_1 and X_2 are amplitude of the basis plane and the amplitude of the of the target plane, respectively. ω is the frequency of vibration. Therefore, the relationship between the vibration frequency and the vibration transmissibility can be obtained:

$$\begin{cases} \frac{\ddot{X}_2}{\ddot{X}_1} \geq 1, \omega \leq \sqrt{\frac{2k}{m_2}} = \sqrt{2}\omega_n \\ \frac{\ddot{X}_2}{\ddot{X}_1} < 1, \omega > \sqrt{\frac{2k}{m_2}} = \sqrt{2}\omega_n \end{cases}, \quad (3)$$

where ω_n is the natural frequency of vibration without damping. According to Equation (3), the passive vibration isolation is effective only when the vibration frequency ω is larger than $\sqrt{2}\omega_n$. This limitation restricts the application of passive vibration isolation in low frequency vibration.

With the development of control technology, active vibration isolation becomes more and more important and relatively has better performance in theory comparing to the passive isolation. In order to combine the advantages of passive vibration isolation with the advantages of active vibration isolation, active isolator can be series connected with the passive vibration

isolation, which is shown in Fig. 2.

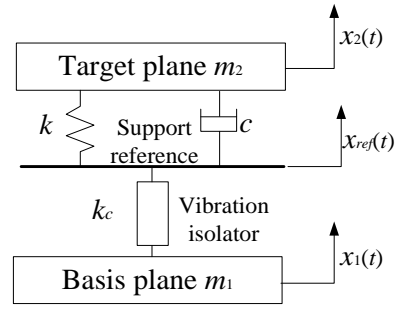


Fig. 2. Principle for series connection of passive isolation and active isolation.

The active vibration isolation uses the acceleration signal of the target plane as the feedback signal. Then, the vibration isolation controller outputs the control signal to change relative position between x_1 and the support reference position x_{ref} . The control function is:

$$x_{ref} - x_1 = K_c \ddot{x}_2, \quad (4)$$

where K_c is the active controller transfer function. The motion equation of the whole system is:

$$\begin{cases} m_2 \ddot{x}_2 + k(x_2 - x_{ref}) + c(\dot{x}_2 - \dot{x}_{ref}) = 0 \\ x_{ref} - x_1 = K_c \ddot{x}_2 \end{cases}. \quad (5)$$

In order to simplify the analysis, we assume that the control transfer function K_c is the constant gain k_c . The vibration acceleration amplitude transmissibility with the active vibration isolator is:

$$\frac{\ddot{x}_2}{\ddot{x}_1} = \frac{x_2}{x_1} \quad (6)$$

$$= \sqrt{\frac{k^2 + (c\omega)^2}{[-(m_2 - kk_c)\omega^2 + k] + (c\omega + ck_c\omega^3)^2}}.$$

The effect of vibration isolation is expressed by the logarithm of the transmissibility:

$$\lambda = 20 \log_{10} \frac{\ddot{X}_2}{\ddot{X}_1}. \quad (7)$$

Figure 3 draws the vibration transmissibility for passive isolation with and without active isolation series connected.

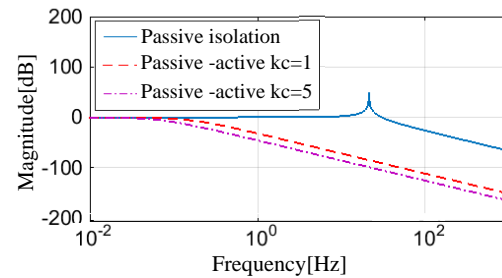


Fig. 3. Comparison of vibration transmissibility between the passive isolation with and without active isolation series connected.

In Fig. 3, compared to passive vibration isolation, resonance frequency and resonance peak decrease with vibration active isolator series connected. Logarithmic transmissibility of vibration acceleration is less than 0 at low frequency. And when k_c is larger, the vibration transmissibility is lower.

III. MAGNETIC LEVITATION PLATFORM

Magnetic levitation system is composed of controller, power amplifier, displacement sensors, acceleration sensor, soft magnetic material and coil, as shown in Fig. 4. The displacement signal of target plane measured by the displacement sensor is used as a feedback signal to be input to the controller. The control signal is converted into the control current i through a power amplifier, which is superimposed with the bias current I , and input to the coil. Then the electromagnet generates electromagnetic force to the suspended target plane, in order to control movement of the target plane.

The mathematical model of 1-DOF magnetic levitation platform is:

$$m\ddot{x} + mg = F(x, i), \quad (8)$$

where m is the total mass of suspended target which contains target plane and thrust disc and shaft between them as shown in Fig. 4, \ddot{x} is the acceleration of the levitation target, F is electromagnetic force resultant from the upper and lower magnetic poles, and x is the displacement compared to the middle position.

At the equilibrium position, the linearized electromagnetic force $F(x, i)$ can be written as [10]:

$$\hat{F}(x, i) = k_i \cdot i + k_x \cdot x, \quad (9)$$

where k_i and k_x are the open loop current gain and the actuator stiffness, respectively.

The control block diagram of the magnetic levitation supporting system is shown in Fig. 5.

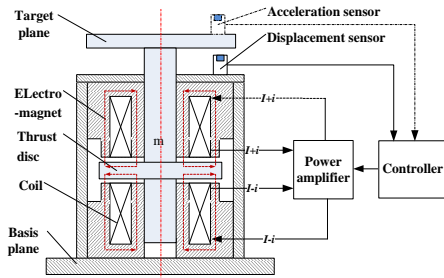


Fig. 4. 1-DOF magnetic levitation platform.

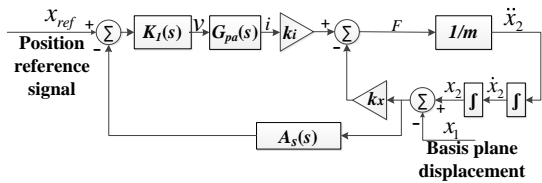


Fig. 5. Diagram of magnetic levitation supporting system.

Figure 5 presents the magnetic levitation supporting system based on PID control. $K_1(s)$ is the support controller with PID control, $G_{pa}(s)$ is the transfer function of the power amplifier, $A_s(s)$ is the displacement sensor, x_{ref} is position reference signal. x_2 is absolute displacement of the target plane. x_1 is the basis plane absolute displacement. The input of magnetic support system is the acceleration signal of basis plane. And the output of magnetic support system is the acceleration signal of target plane. The transfer function is:

$$\frac{\ddot{x}_2(s)}{\ddot{x}_1(s)} = \frac{A_s(s)K_1(s)G_{pa}(s)k_i + k_x}{ms^2 + A_s(s)K_1(s)G_{pa}(s)k_i + k_x}. \quad (10)$$

$G_1(s) = A_s(s)K_1(s)G_{pa}(s)k_i + k_x$, $s = j\omega$, so the vibration transmissibility is:

$$\frac{\ddot{X}_2}{\ddot{X}_1} = \sqrt{\frac{\text{Re}^2(G_1(j\omega)) + \text{Im}^2(G_1(j\omega))}{[\text{Re}(G_1(j\omega)) - m_2\omega^2]^2 + \text{Im}^2(G_1(j\omega))}}. \quad (11)$$

The transfer function of the PID control can be written as:

$$K_j(s) = K_{p,j} \left(1 + \frac{1}{T_{i,j}s} + \frac{T_{d,j}}{1+T_{f,j}s} s \right) \quad (12)$$

$$= P_j + I_j \frac{1}{s} + \frac{D_j}{1+T_{f,j}s} s,$$

where $j = 1, 2$, $P_j = K_{p,j}$ is proportion coefficient, $I_j = K_{p,j}/T_{i,j}$ is integral coefficient, and $D_j = K_{p,j}T_{d,j}$ is differential coefficient, and $T_{f,j}$ is the time constant of the low-pass filter.

Using three different PID control parameter groups, the vibration acceleration transmissibility of magnetic support system is simulated without vibration isolator. The simulation results show in Fig. 6.

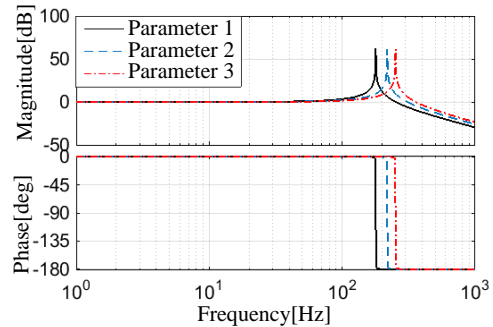


Fig. 6. Simulated vibration transmissibility of levitation supporting loop with different control parameters.

The three PID parameter groups (parameter 1, parameter 2 and parameter 3) have different value of proportion coefficient and integral coefficient and differential coefficient respectively. According to the simulation results, the levitation support system has the effect of vibration isolation only in the high frequencies, while the vibration that transmitted to the target plane

will be amplified in the lower frequencies. The vibration transmission characteristics are similar to the passive vibration isolation system.

IV. NUMERICAL SIMULATIONS FOR DOUBLE CLOSED-LOOP PID

To realize active supporting and active vibration isolation at the same time with only one magnetic levitation actuator, the controller needs new control strategy. The control system contains the active vibration isolation loop and the levitation support loop. For the vibration isolation, in order to facilitate the installation of sensors and vibration signal measurement, the acceleration sensor is used to measure the target plane vibration. For the levitation support, displacement sensor is used to measure the relative displacement of the target plane relative to the basis plane.

Figure 7 is the control system block diagram in which the inner loop is nested in the outer loop. In the outer loop, \ddot{x}_2 is the acceleration signal of the target plane measured by acceleration sensor, $A_a(s)$ is the transfer function of acceleration sensor. $K_2(s)$ is the isolation controller. The output signal of $K_2(s)$ which is the position reference signal x_{ref} of the inner levitation support loop, is input to the levitation support controller $K_1(s)$. The control signal from $K_1(s)$ is transformed into control current by power amplifier to control the target plane.

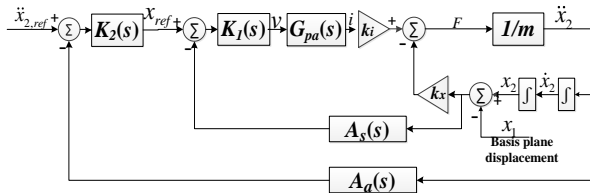


Fig. 7. Diagram for internal-and-external loop control system.

Vibration isolation controller $K_2(s)$ also uses the PID control. The structure of the system can be equivalent to the system shown in the Fig. 2.

After adding the isolation loop, transfer function from the basis acceleration \ddot{x}_1 to the target acceleration \ddot{x}_2 is:

$$\frac{\ddot{x}_2(s)}{\ddot{x}_1(s)} = \frac{A_a(s)K_1(s)G_{pa}(s)k_i + k_x}{ms^2 + A_s(s)K_1(s)G_{pa}(s)k_i + k_x + A_a(s)K_1(s)K_2(s)G_{pa}(s)k_i s^2} \quad (13)$$

$G_2(s) = A_a(s)K_1(s)G_{pa}(s)k_i s^2$, $s = j\omega$, so the vibration transmissibility is:

$$\frac{\ddot{X}_2}{\ddot{X}_1} = \sqrt{\frac{\text{Re}^2(G_1(j\omega)) + \text{Im}^2(G_1(j\omega))}{[\text{Re}(G_1(j\omega)) + \text{Re}(G_2(j\omega)) - m_2\omega^2]^2 + [\text{Im}(G_1(j\omega)) + \text{Im}(G_2(j\omega))]^2}} \quad (14)$$

The acceleration sensor transfer function is:

$$A_a = A_g \times 0.0078, \quad (15)$$

where A_g is the acceleration signal gain. The vibration transmissibility at different A_g shows in Fig. 8.

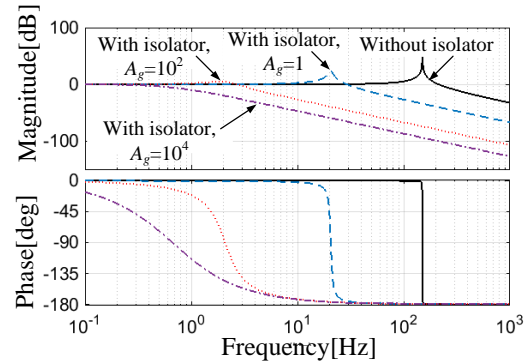


Fig. 8. Comparison among the simulated vibration transmissibility with different A_g .

As Fig. 8 shows, the addition of active vibration isolation loop can effectively reduce the vibration transmissibility and the resonance frequency.

After adding the active vibration isolation loop, the dynamic characteristics of new system is obtained through the step response simulation. The result shows in Fig. 9.

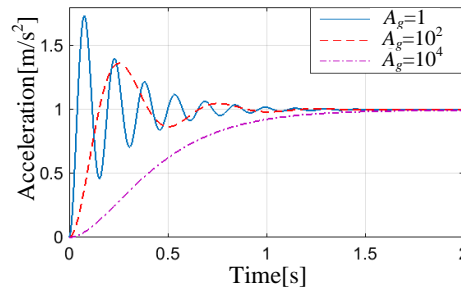


Fig. 9. Step response of double closed-loop PID control system with different A_g .

Figure 9 is the system step response at different A_g , when adding vibration isolation loop. It can be seen from the figure, with the increase of A_g , the overshoot decreases and the settling time increases. So when A_g ranging from 100 to 300, the system can get better performance.

The vibration isolation effect of the system is simulated in time domain, taking $A_g=10$, with the vibration acceleration amplitude of basis plane is 1.0m/s^2 and vibration frequency is 25 Hz. Amplitude of target plane with and without the isolation shows in Fig. 10. Without the vibration isolation, the vibration amplitude of the target plane is 1.0m/s^2 , while with the vibration isolation, the amplitude becomes 0.08m/s^2 . So the amplitude transmissibility is -21.9dB .

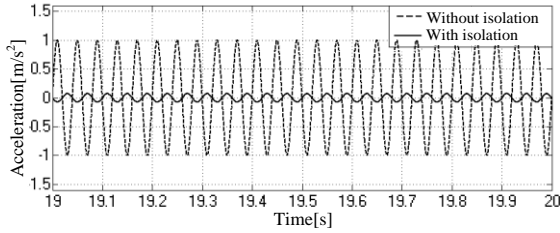


Fig. 10. Simulated result in time domain, 25 Hz.

When the basis plane vibrates randomly with maximum amplitude of 1.0m/s^2 , it can be seen from the Fig. 11 that, without vibration isolation loop, maximum amplitude of levitation target is magnified and about 5.5m/s^2 . With the vibration isolation loop, the maximum amplitude of target plane is 0.6m/s^2 , so isolation effect to the random vibration is equally obvious.

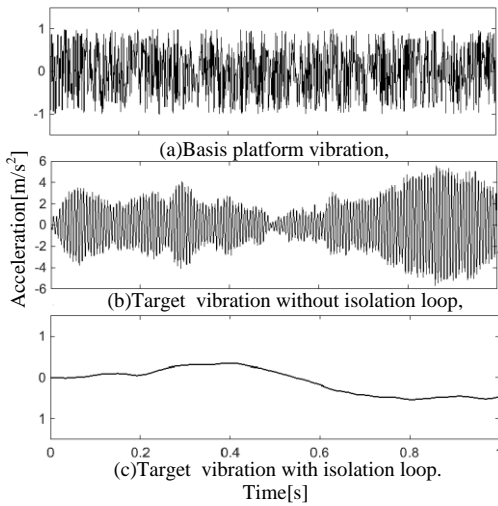


Fig. 11. Simulated results in time domain of random vibration isolation.

V. VIBRATION ISOLATION EXPERIMENT

The principle diagram of the experimental magnetic levitation platform with active vibration isolation and levitation support is shown in Fig. 12. And the real experimental system built according to principle diagram consisting of seven main parts is shown in Fig. 13.

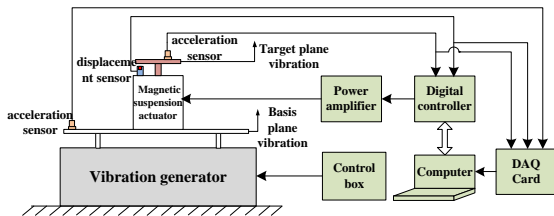


Fig. 12. Vibration isolation with double closed-loop PID control.

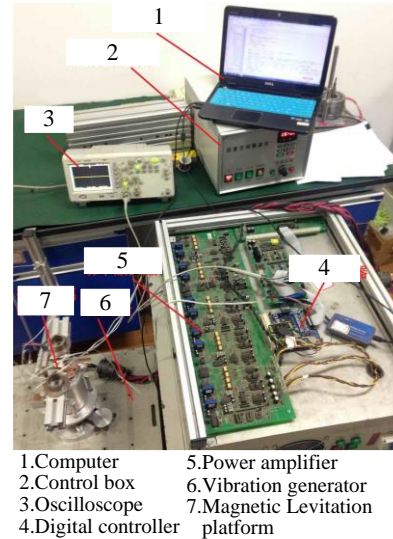


Fig. 13. Real experimental equipment.

Setting vibration frequency of the basis plane to 25 Hz, for the convenience of observation, using acceleration sensor to detect the vibration signal, the vibration acceleration with and without vibration isolation loop is compared in Fig. 14 and Fig. 15. The vibration acceleration amplitude of the basis plane is 10.1m/s^2 . Without the vibration isolation loop, the target vibration acceleration is amplified to 13.2m/s^2 . After adding vibration isolation loop, the amplitude of acceleration is 3.33m/s^2 . The vibration acceleration transmissibility from the basis to the target plane before and after adding the vibration isolation loop is respectively 2.33 dB and -9.46 dB.

As shown in the Fig. 16, after the vibration isolation, the power density of the basic frequency 24.9 Hz and the double frequency 49.8 Hz of the target plane respectively reduce 71.4% and 93.3%.

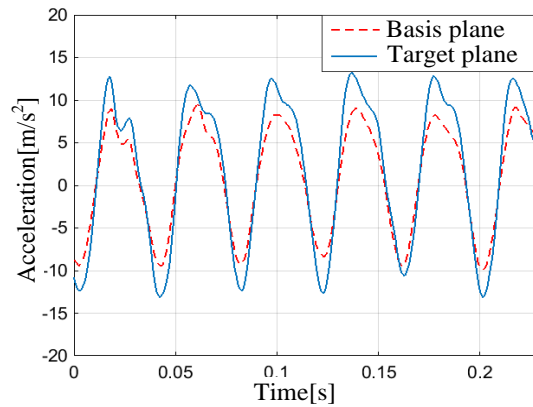


Fig. 14. Experimental comparison between base plane and target plane vibration without vibration isolation loop, 25 Hz.

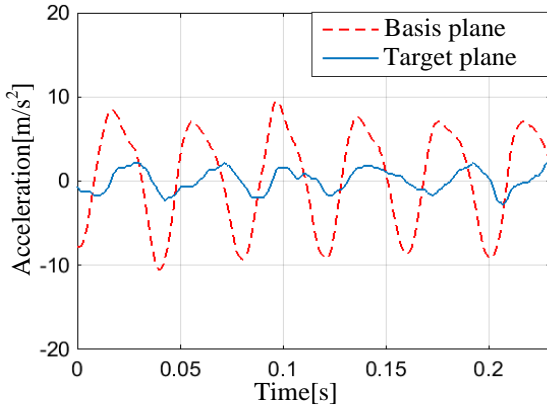


Fig. 15. Experimental comparison between base plane and target plane vibration with vibration isolation loop, 25 Hz.

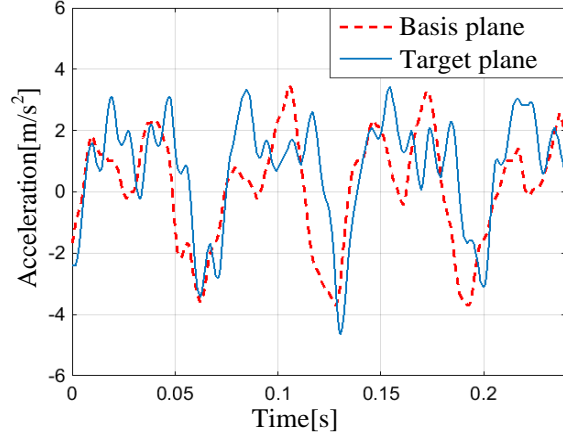


Fig. 17. Experimental comparison between base plane and target plane vibration without vibration isolation loop, random vibration.

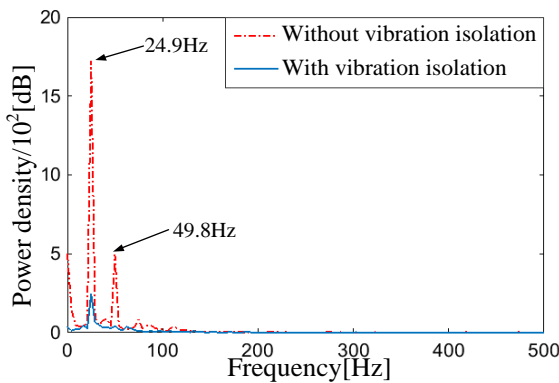


Fig. 16. Experimental spectrogram of frequency domain.

Setting the basis plane vibration to random vibration which has lower frequency components, the comparison between the acceleration without and with the vibration isolation is shown as Figs. 17 and 18. Without the isolation loop, vibration amplitude of the basis plane acceleration is 3.59m/s^2 and the amplitude of the target acceleration is 4.10m/s^2 . And after adding isolation loop, vibration amplitude of the basis plane acceleration is 4.15m/s^2 and the amplitude of the target acceleration is 1.84m/s^2 . The vibration acceleration transmissibility from the basis plane to the target plane without and with the vibration isolation is respectively 1.15 dB and -7.06 dB. So the target vibration acceleration is obviously reduced relative to acceleration without the isolation.

From Fig. 19, in the power density of random vibration, the main frequency components after the vibration isolation have a significant reduction in. Such as in 14.8 Hz frequency, the power density decreases by 55.1% and in 29.1 Hz frequency, the power density decreases by 75.9%.

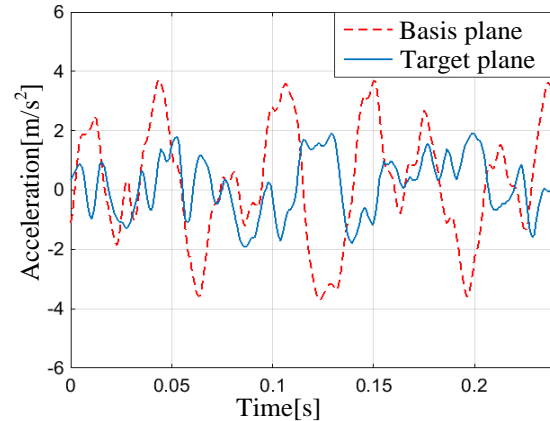


Fig. 18. Experimental comparison between base plane and target plane vibration with vibration isolation loop, random vibration.

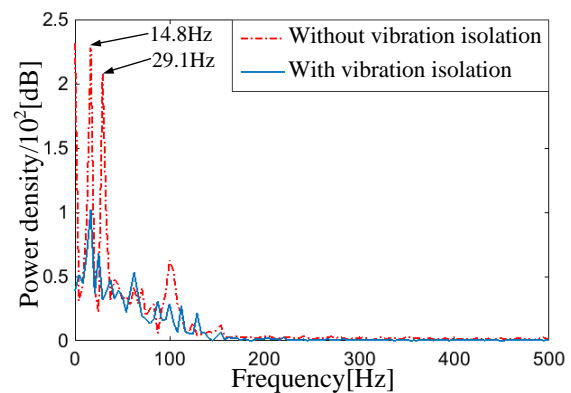


Fig. 19. Experimental spectrogram of frequency domain of random vibration.

VI. CONCLUSION

This paper proposed a new double closed-loop vibration isolation strategy which contained inner loop for levitation support and outer loop for vibration isolation. The double closed-loop control system was designed for the magnetic levitation platform. The simulation result shows the good vibration isolation effect of this method. And the bigger the acceleration sensor gain A_g is, the better the vibration isolation effect is. The vibration isolation experiment of magnetic levitation vibration isolation system with double closed-loop PID control under periodic and random vibration conditions was designed to prove the effectiveness of vibration isolation. After adding the vibration isolation loop, vibration acceleration transmissibility of 25 Hz periodic vibration decreased from 2.33 dB to -9.46 dB. And the maximum acceleration transmissibility of low frequency random vibration decreased from 1.15 dB to -7.06 dB.

ACKNOWLEDGMENT

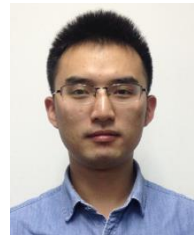
This work was supported by the National Natural Science Foundation of China (51675261), and the Fundamental Research Funds for the Central Universities (NS2016053), and the Open Project Program of Jiangsu Key Laboratory of Large Engineering Equipment Detection and Control (JSKLEDC201502).

REFERENCES

- [1] D. L. Margolis, "A procedure for comparing passive, active, and semi-active approaches to vibration isolation," *Journal of the Franklin Institute*, vol. 315, no. 4, pp. 225-238, 1983.
- [2] L. L. Sun, C. H. Hansen, and C. Doolan, "Evaluation of the performance of a passive-active vibration isolation system," *Mechanical Systems & Signal Processing*, vol. 50-51, pp. 480-497, 2015.
- [3] Y. B. Kim, W. G. Hwang, C. D. Kee, and H. B. Yi, "Active vibration control of a levitation system using an electromagnetic damper," *Proceedings of the Institution of Mechanical Engineers Part D Journal of Automobile Engineering*, vol. 215, pp. 865-873, 2001.
- [4] F. An, H. Sun, and X. Li, "Adaptive active control of periodic vibration using maglev actuators," *Journal of Sound and Vibration*, vol. 331, no. 9, pp. 1971-1984, 2012.
- [5] B. de Marneffe, M. Avraam, A. Deraemaeker, M. Horodinca, and A. Preumont, "Vibration isolation of precision payloads: a six-axis electromagnetic relaxation isolator," *Journal of Guidance Control and Dynamics*, vol. 32, no. 2, pp. 395-401, 2009.
- [6] Y. Kim, S. Kim, and K. Park, "Magnetic force driven six degree-of-freedom active vibration isolation system using a phase compensated velocity

sensor," *Review of Scientific Instruments*, vol. 80, no. 11, pp. 1347-1352, 2009.

- [7] Y. Xu, J. Zhou, C. Jin, and Q. Guo, "Identification of the dynamic parameters of active magnetic bearings based on the transfer matrix model updating method," *Journal of Mechanical Science & Technology*, vol. 30, no. 7, pp. 2971-2979, 2016.
- [8] C. Song, Y. Hu, and Z. Zhou, "Control mechanism of a differential magnetic levitation active vibration isolation system," *Journal of Vibration and Shock*, vol. 29, no. 7, pp. 24-27, 2010.
- [9] J. H. Wu, J. W. Lei, J. H. Shi, and D. Liu, "The design and simulation of missile internal and external loops with dual PID control," *Applied Mechanics & Materials*, vol. 644-650, pp. 146-149, 2014.
- [10] G. Schweitzer and E. H. Maslen, *Magnetic Bearings: Theory, Design, and Application to Rotating Machinery*. Springer, New York, USA, 2009.



bearings.

Mao Tang was born in 1991. He received B.S. degrees in Mechanical Engineering and Automation from Nanjing University of Aeronautics and Astronautics (NUAA) in 2014. He is currently pursuing a M.S. in NUAA. His research focuses on vibration control and magnetic



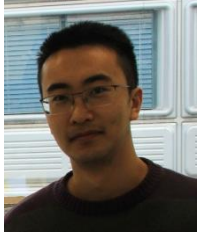
currently a Full Professor in the College of Mechanical and Electrical Engineering, Nanjing University of Aeronautics and Astronautics (NUAA). Her research focuses on magnetic bearings and vibration control.

Jin Zhou received the Ph.D. degree in Mechanical Engineering from China University of Mining and Technology (CUMT) in 2001. From 2011 to 2012, she was a Visiting Scholar in the Rotating Machinery and Control Laboratory (ROMAC) of the University of Virginia. She is



research focuses on magnetic bearings.

Chaowu Jin obtained B.S., M.S. and Ph.D. degrees in Mechanical Engineering from Nanjing University of Aeronautics and Astronautics (NUAA) from 2002 to 2011. He is currently an Associate Professor in the College of Mechanical and Electrical Engineering, NUAA. His



Yuanping Xu was born in 1989. He received B.S. degrees in Mechanical Engineering and Automation from Nanjing University of Aeronautics and Astronautics (NUAA) in 2012. He is currently pursuing a Ph.D. in NUAA and is a guest Ph.D. student in EPFL. His research focuses on magnetic levitation technology.

Sensorless Control for a Three-pole Active Magnetic Bearing System

Shyh-Leh Chen¹ and Kang-Yu Liu²

¹Department of Mechanical Engineering and Advanced Institute of Manufacturing with High-tech Innovations
National Chung Cheng University, Chiayi 621, Taiwan
imeslc@ccu.edu.tw

²Motor Drive Solution BU
Delta Electronics Inc., Taoyuan 330, Taiwan
ken.yu.liu@deltaww.com

Abstract — This study proposes a novel sensorless control of a current-controlled three-pole active magnetic bearing (AMB) system. It is based on the smooth current controller incorporated with the estimated rotor displacements. The rotor position information is extracted from additional sensing coil currents. The sensing coil currents are generated from three phase voltages injected to the additional coils on each magnetic pole. The dynamic model of the 3-pole AMB with the additional high frequency input is derived for levitation control and for position estimation. The results are verified through simulation analysis.

Index Terms — Active magnetic bearing, sensorless control, smooth current control.

I. INTRODUCTION

High speed and high accuracy are the major trends for machines in the 21st century. In this regard, active magnetic bearing (AMB) is an important element since it can provide noncontact suspension. This brings several important advantages, including a significant increase of the maximum rotation speed, friction-loss reduction, etc. However, the potential of its industrial applications has not been fully explored yet. One of the main reasons is its high cost. Therefore, cost reduction has always been an important research direction for the development of AMB system. Hardware accounts for the major part of the overall cost of an AMB. The elimination of some hardware requirements can substantially cut down the overall cost. The three-pole AMB was proposed for this particular purpose [1-4]. It has been shown that the three-pole AMB system requires less power amplifiers, possesses less copper and iron losses and provides more space for heat dissipation, coil winding and sensor installation.

To further reduce the overall cost, one may note that position sensors are in general more expensive than electrical sensors. It has been found that electrical signals

may be used to estimate the mechanical information [5], leading to the so-called self-sensing technique. Thus, sensor cost can be reduced.

In AMB system, the rotor displacement is the controlled variable, and thus, it must be measured or estimated. The rotor displacement is often measured using eddy-current sensors, which are the most widely used one for the magnetic bearing application [6]. It has the characteristics of small physical size with high resolution, excellent temperature stability, small phase shift and high dc stability. However, eddy current sensor has some drawbacks, including relatively high cost, as well as periodic calibration and maintenance requirements.

There have been a large number of self-sensing studies in the literature [7]. The nonlinear high-gain observer method was presented in [8], but the observer design is quite complex. The approach of pulse width modulation (PWM) switching power amplifiers was proposed in [9], [10], but this method requires good performance of PWM. Another approach is to inject a high frequency signal to the electromagnet wires [11], [12]. This signal is modulated by the varying air gap through the inductance of the coil. By demodulating the output signal with the frequency component of the injection signal, the air gap and thus the rotor displacements can be obtained. Some of the techniques have been well known in the field of motor control [13], but has been applied to AMB only recently.

This paper presents a new sensorless control technique for the three-pole AMB system. An additional coil on each magnetic pole is implemented for sensorless control. A three phase high frequency voltage is provided for the additional 3 coils. The current measurement of the additional coils and the original coils makes it possible to obtain the position of rotor.

This paper is organized as follows. After the introduction, the mathematical model of three-pole AMB system with additional coils is described and a smooth current controller is proposed in Section II. In

Section III, the rotor position estimation is proposed. Numerical simulations are carried out in Section IV to verify the design of additional coil three-pole AMB system. Finally, conclusions are drawn in Section V.

II. SYSTEM MODELING AND SMOOTH CURRENT CONTROL

A. Three-pole magnetic bearing model

The three-pole AMB considered here has been studied previously in [1-4, 14]. The three poles are arranged in a radially symmetric Y-shaped structure to produce a uniform force distribution in the 2-D configuration space. The upper two poles are wired together in a differential way so that only two independent coil currents and hence two power amplifiers are required. It has been shown in [1] that this configuration is the optimal design in the sense of minimum heat dissipation. In this section, in order to achieve sensorless control of the three-pole AMB, there will be an additional coil on each pole to provide three phase voltage source, as shown in Fig. 1. In other words, there are two sets of coils: control coils and sensing coils. The control coils for the upper two poles are wound in a differential way. In other words, the two poles share the same control current i_2 , but with opposite winding directions (i.e., $i_3 = -i_2$). The magnetic circuit for the three-pole AMB is given by Fig. 2, assuming that the reluctances exist only on the air gaps. By simple circuit analysis, the magnetic flux passing through each pole, denoted by ϕ_{is} , can be obtained as:

$$\phi_{1s} = \frac{(R_2 + R_3)N_1 I_1 - R_3 N_2 I_2 - R_2 N_3 I_3}{R_1 R_2 + R_2 R_3 + R_3 R_1}, \quad (1)$$

$$\phi_{2s} = \frac{-R_3 N_1 I_1 + (R_1 + R_3)N_2 I_2 - R_1 N_3 I_3}{R_1 R_2 + R_2 R_3 + R_3 R_1}, \quad (2)$$

$$\phi_{3s} = \frac{-R_2 N_1 I_1 - R_1 N_2 I_2 + (R_1 + R_2)N_3 I_3}{R_1 R_2 + R_2 R_3 + R_3 R_1}, \quad (3)$$

where $N_1 I_1 = N_i + N_s i_{1s}$, $N_2 I_2 = N_i + N_s i_{2s}$, $N_3 I_3 = N_i + N_s i_{3s}$, N is the number of control coil turns on each pole, N_s is the number of sensing coil turns on each pole, i_1 to i_3 are the control coil currents, i_{1s} to i_{3s} are the sensing coil currents and R_1 to R_3 are the reluctances of the air gaps between the rotor and the three magnetic poles. The reluctance can be expressed by:

$$R_j = \frac{l_j}{\mu A}, \quad (4)$$

where l_1 to l_3 represent the air gaps, μ is the magnetic permeability of the air and A is the face area of each pole.

The magnetic force of the three-pole AMB can be easily obtained. Assume that the magnetic characteristic is linear (i.e., linear B-H relationship) and fringing effects and flux leakage are neglected. Then, by

Ampere's law and principle of virtual work, the magnetic force is related to the magnetic flux by:

$$F_i = \frac{\phi_{is}^2}{2\mu A}, \quad i = 1 \sim 3. \quad (5)$$

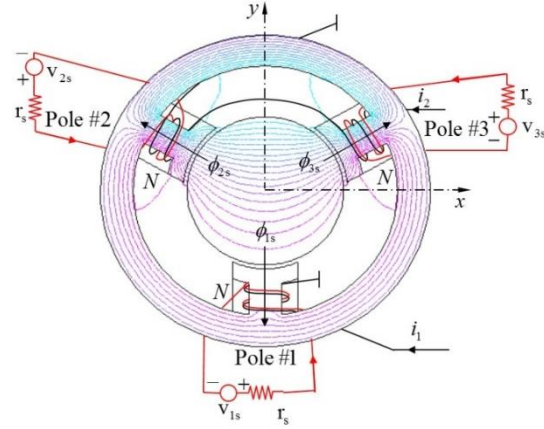


Fig. 1. The current-controlled three-pole AMB system with sensing coils.

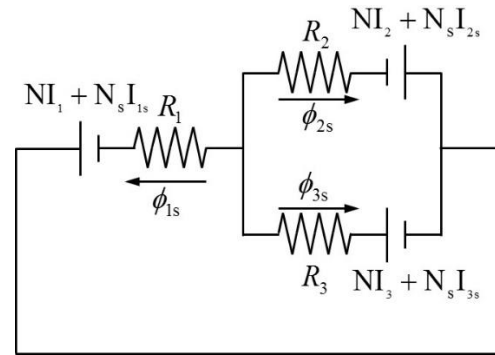


Fig. 2. Magnetic circuit for the additional coil three-pole AMB.

Using Newton's second law of motion, the magnetic force generated by the three poles in the X and Y directions are:

$$\ddot{x}_r = \frac{1}{m}(F_3 - F_2)\cos(30^\circ) = c_0 \Phi_{1s} \Phi_{2s}, \quad (6)$$

$$\ddot{y}_r = \frac{1}{m}[(F_3 + F_2)\sin(30^\circ) - F_1] - g = \frac{c_0}{2}(\Phi_{2s}^2 - \Phi_{1s}^2) - g, \quad (7)$$

where $c_0 = \frac{4\mu A}{3m}$, m is rotor mass, Φ_{1s} and Φ_{2s} are defined by:

$$\Phi_{1s} = \frac{3}{4\mu A}(\phi_{3s} + \phi_{2s}), \quad (8)$$

$$\Phi_{2s} = \frac{\sqrt{3}}{4\mu A}(\phi_{3s} - \phi_{2s}). \quad (9)$$

B. Coordinate transformations

Note that the magnetic fluxes ϕ_{is} contain the contribution from both control and coil currents. Due to the differential winding configuration, there are only two independent control currents since $i_3 = -i_2$. On the other hand, the sensing coil currents i_{is} will be generated by the three phase voltages as shown in Fig. 1. That is, they need to satisfy the Faraday's induction law as:

$$\begin{bmatrix} v_{1s} \\ v_{2s} \\ v_{3s} \end{bmatrix} = r_s \begin{bmatrix} i_{1s} \\ i_{2s} \\ i_{3s} \end{bmatrix} + N_s \begin{bmatrix} \dot{\phi}_{1s} \\ \dot{\phi}_{2s} \\ \dot{\phi}_{3s} \end{bmatrix}, \quad (10)$$

where v_{1s} to v_{3s} are three phase voltage, r_s is coil resistance. Equation (10) can be transformed into the Cartesian coordinate through the inverse Clarke transformation:

$$\begin{bmatrix} f_a \\ f_b \\ f_c \end{bmatrix} = \begin{bmatrix} 0 & -1 \\ -\frac{\sqrt{3}}{2} & \frac{1}{2} \\ \frac{\sqrt{3}}{2} & \frac{1}{2} \end{bmatrix} \begin{bmatrix} f_x \\ f_y \end{bmatrix}, \quad (11)$$

to yield,

$$\begin{bmatrix} v_x \\ v_y \end{bmatrix} = r_s \begin{bmatrix} i_x \\ i_y \end{bmatrix} + N_s \begin{bmatrix} \dot{\phi}_x \\ \dot{\phi}_y \end{bmatrix}. \quad (12)$$

In other words, v_x, v_y are the transformed three phase voltages; i_x, i_y are the transformed sensing currents; ϕ_x, ϕ_y are the transformed magnetic fluxes on the three poles. It can be shown that Equations (8) and (9) will become:

$$\Phi_{1s} = \frac{3}{4\mu A} (\phi_{3s} + \phi_{2s}) = \frac{3}{4\mu A} \phi_y, \quad (13)$$

$$\Phi_{2s} = \frac{\sqrt{3}}{4\mu A} (\phi_{3s} - \phi_{2s}) = \frac{3}{4\mu A} \phi_x. \quad (14)$$

Thus, Equation (12) can be re-written as:

$$\begin{bmatrix} v_x \\ v_y \end{bmatrix} = r_s \begin{bmatrix} i_x \\ i_y \end{bmatrix} + \frac{4\mu AN_s}{3} \begin{bmatrix} \dot{\Phi}_{2s} \\ \dot{\Phi}_{1s} \end{bmatrix}. \quad (15)$$

Also, in terms of rotor displacements and coil currents, Equations (13) and (14) become:

$$\begin{bmatrix} \Phi_{1s} \\ \Phi_{2s} \end{bmatrix} = -\frac{N}{L} \begin{bmatrix} 2l_0 - y_r & \sqrt{3}x_r \\ x_r & \sqrt{3}(2l_0 + y_r) \end{bmatrix} \begin{bmatrix} i_1 \\ i_2 \end{bmatrix} - \frac{N_s}{L} \begin{bmatrix} -\frac{3}{2}x_r & -3l_0 + \frac{3}{2}y_r \\ -3l_0 - \frac{3}{2}y_r & -\frac{3}{2}x_r \end{bmatrix} \begin{bmatrix} i_x \\ i_y \end{bmatrix}, \quad (16)$$

where x_r and y_r are the rotor displacements, l_0 is the nominal air gap and $L = 4l_0^2 - (x_r^2 + y_r^2)$ is always

positive in the operation rang because that the rotor displacement is always smaller than the nominal air gap, i.e., $(x_r^2 + y_r^2) \leq l_0^2$. Finally, let us define the system states as $x_{1s} = x_r$, $x_{2s} = \dot{x}_r$, $x_{3s} = y_r$, $x_{4s} = \dot{y}_r$, $x_{5s} = \Phi_{1s}$, $x_{6s} = \Phi_{2s}$. That is,

$$x_s = [x_{1s} \ x_{2s} \ x_{3s} \ x_{4s} \ x_{5s} \ x_{6s}]^T.$$

Then, the system dynamics can be obtained as:

$$\dot{x}_s = \begin{bmatrix} x_{2s} \\ c_0 x_{5s} x_{6s} \\ x_{4s} \\ \frac{c_0}{2} (x_{6s}^2 - x_{5s}^2) - g \\ \frac{3}{4\mu AN_s} (v_y - r_s i_y) \\ \frac{3}{4\mu AN_s} (v_x - r_s i_x) \end{bmatrix}, \quad (17)$$

where $v_x = V \cos \omega t$, $v_y = V \sin \omega t$, V is the amplitude of the three phase voltage. The sensing currents depend on the rotor displacements and control currents, and can be obtained from Equation (16) as:

$$\begin{bmatrix} i_x \\ i_y \end{bmatrix} = \frac{2}{3N_s} \begin{bmatrix} -x_{1s} & 2l_0 - x_{3s} \\ 2l_0 + x_{3s} & -x_{1s} \end{bmatrix} \begin{bmatrix} x_{5s} \\ x_{6s} \end{bmatrix} + \frac{2N}{3N_s} \begin{bmatrix} 0 & \sqrt{3} \\ 1 & 0 \end{bmatrix} \begin{bmatrix} i_1 \\ i_2 \end{bmatrix}. \quad (18)$$

C. Smooth current control

It is well known that the AMB system is unstable and nonlinear. As a result, it is necessary to design a stabilizing feedback controller for stable suspension. Following the smooth current controller proposed in [3], we will design a controller for this system. For more details on smooth current control, please refer to [3]. Let us first consider the rotor dynamics part in the overall state Equation (17), i.e.,

$$\dot{x}_s = \begin{bmatrix} x_{2s} \\ c_0 \Phi_{1s} \Phi_{2s} \\ x_{4s} \\ \frac{c_0}{2} (\Phi_{2s}^2 - \Phi_{1s}^2) - g \end{bmatrix}. \quad (19)$$

Regarding Φ_{1s} and Φ_{2s} as virtual control inputs, we can design a control law as:

$$\Phi_{1s} = \psi_1(x), \quad \Phi_{2s} = \sqrt{\frac{2g}{c_0}} + \psi_2(x), \quad (20)$$

$$\psi_1(x) = k_{11}x_{1s} + k_{12}x_{2s} + k_{13}z_1, \quad (21)$$

$$\psi_2(x) = k_{24}x_{3s} + k_{25}x_{4s} + k_{26}z_2, \quad (22)$$

where $z_1 = \int x_{1s} dt$, $z_2 = \int x_{3s} dt$, and k_{ij} 's are the PID feedback gains. Therefore, from Equation (16), the overall control law for the control currents is given by:

$$\begin{bmatrix} i_1 \\ i_2 \end{bmatrix} = -\frac{1}{\sqrt{3}N} \begin{bmatrix} \sqrt{3}(2l_0 + x_{3s}) & -\sqrt{3}x_{1s} \\ -x_{1s} & 2l_0 - x_{3s} \end{bmatrix} \begin{bmatrix} \psi_1(x) \\ \sqrt{\frac{2g}{c_0}} + \psi_2(x) \end{bmatrix} \\ + \frac{N_s}{N} \begin{bmatrix} 0 & \frac{3}{2} \\ \frac{\sqrt{3}}{2} & 0 \end{bmatrix} \begin{bmatrix} i_x \\ i_y \end{bmatrix}. \quad (23)$$

Note that unlike the standard smooth current control [3], here the control currents need to compensate the disturbance from the sensing currents.

Comments on the computational issues of the feedback control law (23) are made here. An important parameter in the control law is c_0 . It is related to the magnetic force model. In order to get accurate value, it is better to use finite element method for the model of magnetic forces [15]. It can also be obtained by experimental calibration of magnetic force model, as presented in [2].

III. THE ROTOR DISPLACEMENT ESTIMATION

The estimation of rotor displacements will be based on Equation (16), or equivalently, Equation (18). It is the relationship between the rotor displacements and the electrical and magnetic quantities: the control currents i_1, i_2 , the sensing currents i_x, i_y , and the equivalent magnetic fluxes Φ_{1s}, Φ_{2s} . Equation (18) can be re-written as:

$$i_x = \frac{(-2x_r\Phi_{1s} + 4l_0\Phi_{2s} - 2y_r\Phi_{2s} + 2\sqrt{3}Ni_2)}{3N_s}, \quad (24)$$

$$i_y = \frac{(4l_0\Phi_{1s} + 2y_r\Phi_{1s} - 2x_r\Phi_{2s} + 2Ni_1)}{3N_s}, \quad (25)$$

which is equivalent to:

$$x_r\Phi_{1s} + y_r\Phi_{2s} = 2l_0\Phi_{2s} + \alpha, \quad (26)$$

$$x_r\Phi_{2s} - y_r\Phi_{1s} = 2l_0\Phi_{1s} + \beta, \quad (27)$$

where $\alpha = \sqrt{3}Ni_2 - \frac{3}{2}N_s i_x$ and $\beta = Ni_1 - \frac{3}{2}N_s i_y$. From

Equations (26) and (27), one can obtain the rotor displacements as:

$$x_r = \frac{1}{\Phi_{1s}^2 + \Phi_{2s}^2} (4l_0\Phi_{1s}\Phi_{2s} + \alpha\Phi_{1s} + \beta\Phi_{2s}), \quad (28)$$

$$y_r = \frac{1}{\Phi_{1s}^2 + \Phi_{2s}^2} (2l_0(\Phi_{2s}^2 - \Phi_{1s}^2) - \beta\Phi_{1s} + \alpha\Phi_{2s}). \quad (29)$$

In (28) and (29), the control currents i_1, i_2 and sensing currents i_x, i_y can be measured by the current sensors.

Also, the equivalent magnetic fluxes Φ_{1s}, Φ_{2s} can be obtained by integrating Equation (15), i.e.,

$$\begin{bmatrix} \Phi_{1s} \\ \Phi_{2s} \end{bmatrix} = \frac{3}{4\mu AN_s} \int \left(\begin{bmatrix} v_y \\ v_x \end{bmatrix} - r_s \begin{bmatrix} i_y \\ i_x \end{bmatrix} \right) dt. \quad (30)$$

Therefore, Equations (28) and (29) can be used for the estimation of rotor displacements, and can be used for the feedback control in the smooth current controller (23).

Comments on the computational issues of position estimation algorithm (28) and (29) are made here. Note that the equivalent magnetic fluxes Φ_{1s}, Φ_{2s} are important quantities for the position estimation, as can be easily seen from (18) and (29). The computation of Φ_{1s}, Φ_{2s} using (30) could lead to large error if the transformed three-phase voltages v_x, v_y and the sensing currents i_x, i_y are contaminated with large noise. Therefore, a key point to obtain good estimation is to use filters to handle v_x, v_y and i_x, i_y before computing (30). An alternative way to get Φ_{1s}, Φ_{2s} is to use finite element method [15] to compute magnetic fluxes ϕ_{is} and then use (13) and (14). This approach will yield more accurate Φ_{1s}, Φ_{2s} , but it is time-consuming and not feasible for real-time sensorless control.

IV. SIMULATION RESULTS

To verify the effectiveness of the proposed sensorless control, numerical simulation will be carried out in this section. The nominal values of the system parameters are shown in Table 1. Note that the frequency of the sensing voltage is 100 Hz with amplitude of 1V. The control gains k_{ij} 's in (21) and (22) are designed using the method of pole placement. The closed-loop poles are chosen at:

$$\lambda_{11} = -28, \lambda_{12} = -25.5, \lambda_{13} = -13;$$

$$\lambda_{21} = -25.5, \lambda_{22} = -23, \lambda_{23} = -23.5;$$

where λ_{1i} represents the poles for the closed-loop linearized dynamics in the X-direction, and λ_{2i} for the Y-direction. The initial conditions for the system state $x_s(0)$ is taken to be:

$$x_s(0) = \begin{bmatrix} 0 & 0 & -5 \times 10^{-4} m & 0 & 0 & 1 \times 10^{-2} \end{bmatrix}.$$

Note that there is a backup bearing placed on half way between the stator and the rotor. In other words, the practical allowable operation range for the rotor is a circle with radius of $5 \times 10^{-4} m$, which is marked by dashed lines in the following figure. Hence, the initial condition represents the situation that rotor is initially at rest on the backup bearing. The simulation results are shown in Fig. 3 and Fig. 4. Figure 3 shows the performance of the smooth current controller with the proposed rotor estimation scheme. Figures 3 (a) and 3 (b) indicate that the rotor can be levitated to the bearing center within 0.3 seconds. In Fig. 3 (c), the control

currents exhibit periodic oscillation to compensate for the sensing currents. Figure 4 shows the response of rotor displacement estimation and the estimation error. It indicates that both X and Y displacements can be estimated with good accuracy. The simulation results clearly verify the effectiveness of the proposed method.

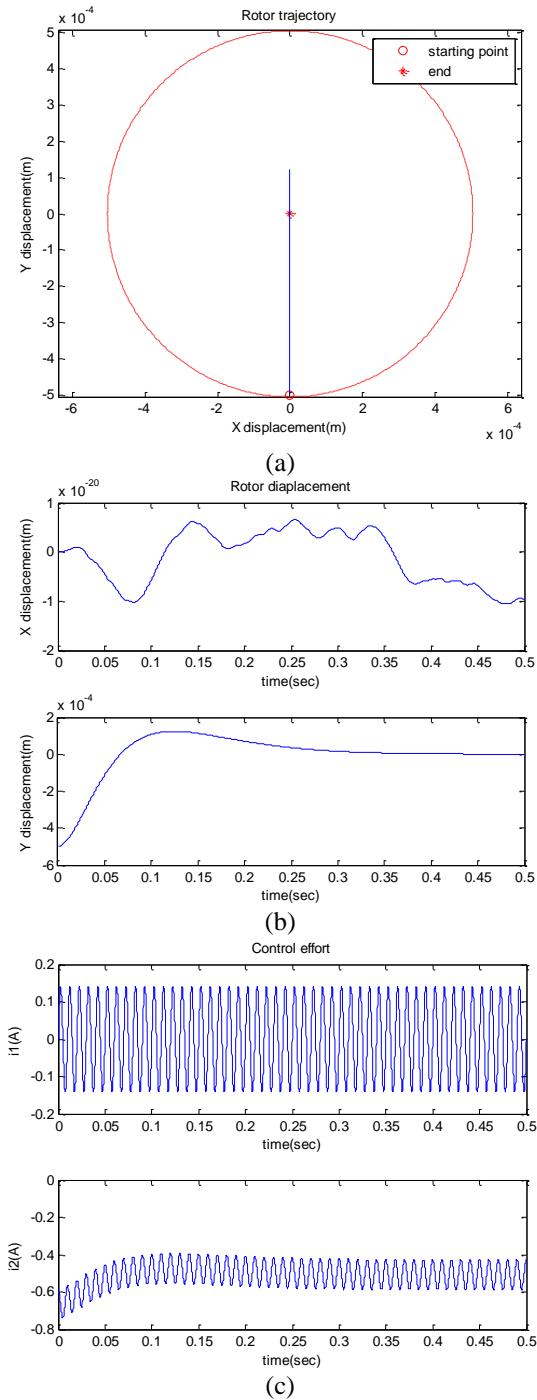


Fig. 3. Numerical simulations: (a) rotor trajectory with smooth current controller; (b) rotor displacements with smooth current controller; (c) control currents.

Table 1: Parameters of the AMB system

| | |
|-------------------------------------|---------------------------|
| Rotor mass | 0.6595kg |
| Nominal air gap | $0.95 \times 10^{-3} m$ |
| Permeability | $4\pi \times 10^{-7} H/m$ |
| Number of coil turns | 300 |
| Number of additional coil turns | 20 |
| Cross sectional area of the air gap | $4 \times 10^{-4} m^2$ |
| Amplitude of sensing voltage | 1V |
| Frequency of sensing voltage | 100Hz |
| Resistance of additional coil turns | 0.7056 Ω |

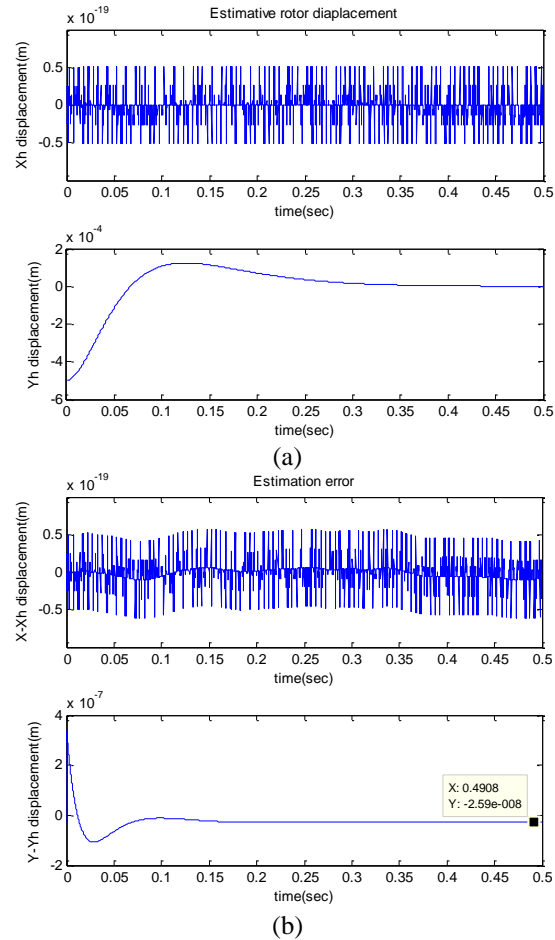


Fig. 4. Numerical simulations: (a) estimated rotor displacements; (b) estimation error.

V. CONCLUSIONS AND FUTURE WORKS

A sensorless controller for a three-pole AMB system has been proposed in this study. It is based on the smooth current controller with additional three-phase sensing coil currents to estimate the rotor displacements. Numerical simulations verify the effectiveness of the proposed method. In the future, the stability of the closed-loop system will be analyzed and the experimental validation will be performed.

ACKNOWLEDGMENT

This work was supported in part by the Ministry of Science and Technology, Taiwan, ROC, under Grants MOST 105-2218-E-194-003.

REFERENCES

- [1] S. L. Chen and C. T. Hsu, "Optimal design of a three - pole active magnetic bearing," *IEEE Transactions on Magnetics*, vol. 38, no. 5, pp. 3458-3466, 2002.
- [2] S. L. Chen, S. H. Chen, and S. T. Yan, "Experimental validation of a current-controlled three-pole magnetic rotor-bearing system," *IEEE Transactions on Magnetics*, vol. 41, no. 1, pp. 99-112, 2005.
- [3] C. T. Hsu and S. L. Chen, "Exact linearization of a voltage-controlled 3-pole active magnetic bearing system," *IEEE Transactions on Control Systems Technology*, vol. 10, no. 4, pp. 618-625, 2002.
- [4] S. L. Chen, "Nonlinear smooth feedback control of a three-pole active magnetic bearing system," *IEEE Transactions on Control Systems Technology*, vol. 19, no. 3, pp. 615-621, 2011.
- [5] T. Mizuno, T. Ishii, and K. Araki, "Self-sensing magnetic suspension using hysteresis amplifiers," *Control Engineering Practice*, vol. 6, pp. 1133-1140, 1998.
- [6] J. Boehm, R. Gerber, and N. R. C. Kiley, "Sensors for magnetic bearings," *IEEE Transactions on Magnetics*, vol. 29, no. 6, pp. 2962-2964, 1993.
- [7] S. C. Mukhopadhyay, "Do we really need sensors? A sensorless magnetic bearing perspective," *1st International Conference on Sensing Technology*, Palmerston North, New Zealand, pp. 425-431, November 21-23, 2005.
- [8] S. L. Chen and Y. H. Hsiao, "Nonlinear high-gain observer for a three-pole active magnetic bearing system," in *Proc. ASCC*, pp. 155-159, 2011.
- [9] L. Lichuan, T. Shinshi, and A. Shimokohbe, "State feedback control for active magnetic bearings based on current change rate alone," *IEEE Transactions on Magnetics*, vol. 40, no. 6, pp. 3512-3517, 2004.
- [10] J. Wang and A. Binder, "Self-sensing magnetic bearings using multiple sampling of currents alone," in *Proc. IEEE EPE*, pp. 1-10, 2013.
- [11] J. S. Yim, J. H. Kim, S. K. Sul, H. J. Ahn, and D. C. Han, "Sensorless position control of active magnetic bearing based on high frequency signal injection method," in *Proc. IEEE APEC*, pp. 83-88, 2003.
- [12] P. Garcia, J. M. Guerrero, F. Briz, and D. Reigosa, "Sensorless control of three-pole active magnetic bearings using saliency-tracking-based methods," *IEEE Transactions on Industry Applications*, vol. 46, no. 4, pp. 1476-1484, 2010.
- [13] T. Yuvaraja and K. Ramya, "Vector control of PMSM take over by photovoltaic source," *ACES Express Journal*, vol. 1, no. 6, pp. 193-196, June 2016.
- [14] E. Schmidt and M. Hofer, "Application of the sliding surface method with 3D finite element analyses of a hybrid magnetic bearing," *25th Annual Review of Progress in Applied Computational Electromagnetics (ACES)*, Monterey, California, pp. 440-445, March 2009.
- [15] G. Liu, Y. Zhou, R. Zhou, W. Ming, and L. Huo, "Analysis and optimization of a 2-D magnet array with hexagon magnet," *Applied Computational Electromagnetics Society Journal*, vol. 28, no. 10, pp. 976-983, October 2013.



Shyh-Leh Chen was born on October 25, 1964, in Keelung, Taiwan. He received B.S and M.S. degrees from National Tsing-Hua University, Hsin-Chu, Taiwan, in 1987 and 1989, respectively, both in Power Mechanical Engineering. He received a Ph.D. degree in Mechanical Engineering from Michigan State University, East Lansing, Michigan, USA, in 1996.

Since 1996, he has been with National Chung Cheng University, Chiayi, Taiwan, where he is currently a Professor in the Department of Mechanical Engineering and a Deputy Director of Advanced Institute of Manufacturing with High-tech Innovations (AIM-HI). He also served as the Director of Advanced Machine Tools Research Center from 2010 to 2013. His research interests include nonlinear dynamics and control, wavelet analysis, with application to motion control of multi-axis systems, active magnetic bearings, and ship stabilization.



Kang-Yu Liu received the M.S. degree in Mechanical Engineering from National Chung Cheng University, Chiayi, Taiwan, R.O.C., in 2014. Currently, he is an R&D Engineer at Delta Electronics. His research interests include modeling, design, control and applications of

active magnetic bearing systems.

Algorithm for Accounting for Inner Damping in a Computer Model of Dynamics of a Flexible Rotor on Active Magnetic Bearings

Viktor F. Ovchinnikov, Mikhail Y. Nikolaev, and Vasily N. Litvinov

Research Institute of Mechanics
Lobachevsky State University of Nizhny Novgorod, Russia
minick@mech.unn.ru

Abstract — An algorithm for accounting for inner damping in an actively developed computer model of dynamics of a flexible rotor on active magnetic bearings is presented. The algorithm is illustrated by applying it for analyzing the effects of amplitude-independent inner damping on rotor dynamics when residual imbalance is present.

Index Terms — Active magnetic bearing, dynamics influenced by inner damping, flexible rotor, inner damping.

I. INTRODUCTION

One of popular applications of suspension systems based on active magnetic bearings (AMB) is supporting big size and weight flexible rotors of complex design (as in [1, 2]). Such multi-ton flexible heterogeneous rotors meet the criteria formulated in [3] that define complex unique systems. Such rotors comprise dissimilar machines: turbines, power generators, compressors, etc. Each AMB has its own control system interacting with the systems for other bearings via the rotor itself. Numerous forces influencing rotor behaviour [4] – such as weight, imbalance, gyroscopic, thermomechanical, gas-dynamic and electromagnetic effects – excite several simultaneous mode shapes in a flexible rotor, a combination of which can result in substantially different movement patterns for different rotor parts.

For the studies required both during design and operation phases of such systems, a computer model of dynamics of a flexible heterogeneous rotor on AMB is being actively developed. One of interests of development is extending the list of available forces that influence the system by adding new, yet unaccounted, forces that have considerable effect on the rotor dynamics.

Paper [5] presents formulas for generalized forces which influence dynamics of a flexible rotor on AMB: imbalance force, gyroscopic force, gravity, magnetic and circulation forces caused by electromagnetic interaction in the generator, exciter and motor as well as gas-dynamic forces in turbines, compressors and labyrinth seals of their shafts.

Inner damping can have substantial effects on rotor dynamics [6, 7], especially in transitional modes of starting and stopping the rotation when frequency passes critical values. This paper aims at designing an algorithm for accounting for inner damping in an actively developed computer model of dynamics of a flexible rotor on AMB. The introduced algorithm is illustrated by computations demonstrating the effect of inner damping on dynamics of a flexible rotor on AMB when residual imbalance is present.

II. DISCRETE MATHEMATICAL MODEL OF ROTOR DYNAMICS

The actively developed computer model of dynamics of a flexible rotor on AMB is a discrete mathematical model of rotor expressed in a computer code [5]. The model includes a mechanical model, a control system model and models of forces affecting the behaviour of the rotor on AMB.

The implementation of the aforementioned model is oriented on performing the calculations in a parallelized way, either using conventional CPU parallelization or utilizing the power of GPGPU which is now becoming more and more used in such modellings [8, 9].

Mechanical model is based on the equations and results of studying dynamics of flexible rotors [7]. A rotor is considered to be a resilient heterogeneous rod. Specific characteristics of the dynamics of the rotor on AMB are determined by flexural vibrations, which are the objective of this paper.

The model of the rotor is a series of homogeneous cylinder parts combined into one mechanical model by two types of connections: rigid coupling and flexible clutches. Flexural vibrations are described using Timoshenko beam model [10]. The solution of the initial distributed problem of determining flexural vibrations is determined by four functions describing linear and angular motions of the rotor as well as inner stresses and moments. Transition to a discrete model is based on basis functions expansion of the solution. The choice of basis functions depends on the problems being solved. The presented model proposes to generate the required laws

of variation of forces in the AMB control system, including those that are linearly dependent on rotor displacement [11, 12]. As a result, basis functions for the problem are chosen to be orthogonal eigenmodes of the oscillations of a rotor on resilient bearings with the assigned rigidity at the cross-sections where the AMBs were situated.

To obtain resulting equations of the mechanical model of a flexible rotor [13], Lagrange equations are used. Equations describing rotor dynamics in a global fixed coordinate system in the two orthogonal crosswise directions are composed for vectors of generalized coordinates C_i . The generalized coordinates are eigenmode expansion coefficients. The dimension of $C_i - n -$ is the number of generalized coordinates, i.e., the number of eigenmodes accounted for when approximating the solution. The dynamics equations in matrix form for C_i are as follows:

$$m \frac{d^2 C_i}{dt^2} + m \Omega C_i = F_i, \quad i = \overline{1, 2}, \quad (1)$$

where m is rotor mass; Ω is a diagonal $n \times n$ matrix, its elements being squares of eigenfrequencies of the rotor; F_i are vectors of generalized forces (with the dimension of n) acting in two orthogonal crosswise directions. Each F_i force is the resultant force of all the forces accounted for in the model (1) of different natures.

The control system model [5] accounts for the discrete nature of polling displacement sensors, operation of current amplifiers with dead space and relay parts, a lag in forming of control signal, the nonlinear dependence of the AMB forces on the current in the coils and a gap between the magnets and the rotor surface.

III. MODEL OF FORCES CAUSED BY INNER DAMPING

Inner damping includes both energy dissipation in the material and structural damping in the joints. It destabilizes rotor dynamics, so taking inner damping into account is essential when constructing a model of dynamics.

Numerous studies [6, 14-16] show that in a wide range of frequencies the amount of energy dissipation does not depend on the strain rate, but rather on type of the stressed state, strain level and on the temperature of material. Structural damping in the joints has similar properties. Currently there exist numerous theories of inner damping that in certain conditions are able to account for the main features of the energy dissipation process. Those theories use relations between strain and stress tensors in the process of oscillations (including nonstationary ones). In general, those relations are nonlinear and ambiguous (e.g., of a hysteresis type). Most theories and models of inner energy dissipation that are conformant to experiments are either too complex for practical application or aimed at solving the problem

with special conditions (stable oscillations, single-frequency oscillation, linear approximations) [14, 16].

The presented approach for accounting for inner damping is based on two assumptions: a) oscillation behaviour mainly depends on the amount of energy dissipated during one oscillation cycle (the area of hysteresis loop), and detailed characteristic of stress caused by deformation (the hysteresis loop shape) do not influence behaviour much; b) forces caused by inner damping are of small value, so they cannot lead to any noticeable interaction of different oscillation processes in model (1).

In the introduced model it is assumed that generalized forces caused by inner damping are independent for all generalized coordinate components ($\{q_k\}, k = \overline{1, \dots, n}$) of vector of generalized coordinates Q that describes crosswise displacement of the rotor in the coordinate system fixed to the rotor (and rotating with the rotor). For each generalized coordinate a phenomenological model of friction damping is used (model by Korchinsky, model by Leonov and Bezpalko) [15]. Keeping this in mind, generalized force caused by inner damping can be written as follows:

$$r_k = -s_k \cdot \chi \cdot |q_k|^\alpha \operatorname{sign} \frac{dq_k}{dt}, \quad k = \overline{1, n}, \quad (2)$$

where r_k is a component of generalized damping force R ; s_k is effective mechanic rigidity (as in mechanical model (1)) along the generalized axis; χ, α are parameters describing the relation of energy dissipation and rotor oscillation level.

If deformations along generalized axis q_k are cyclic and have amplitude u_k , then energy losses ΔW during one cycle are described as follows:

$$\Delta W = 4s_k \cdot \chi u_k^{\alpha+1} / (\alpha+1), \quad k = \overline{1, n}. \quad (3)$$

Total oscillation energy is $W = s_k \cdot u_k^2 / 2$, and, taking (3) into account, relative energy dissipation ψ will be:

$$\psi = \Delta W / W = 8 \cdot \chi u_k^{\alpha-1} / (\alpha+1), \quad k = \overline{1, n}. \quad (4)$$

Considering that logarithmic decrement δ is coupled with the relative energy dissipation: $\psi = 2\delta$, Equation (4) makes it possible to determine parameters χ and α experimentally from the measured logarithmic decrements.

For $\alpha = 1$, it follows from (4) that $\chi = \delta/2$, thus (2) can be transformed to:

$$r_k = -s_k \cdot \delta \cdot |q_k| \operatorname{sign} \frac{dq_k}{dt} / 2, \quad k = \overline{1, n}. \quad (5)$$

Equation (5) describes components of generalized forces caused by inner damping when damping is assumed amplitude-independent.

The dependence of inner damping on the oscillation amplitude of a flexible rotor can be taken into account by identifying the parameters of inner damping based on phenomenological model of friction damping.

To describe deformations of a flexible rotor, its motion in the coordinate system fixed to the rotor is examined. For the vectors of the generalized coordinates Q_i ($i=1,2$) characterizing rotor motion in the moving coordinates, the following equations hold:

$$\begin{aligned} Q_1 &= C_1 \cdot \cos\varphi + C_2 \cdot \sin\varphi; \\ Q_2 &= -C_1 \cdot \sin\varphi + C_2 \cdot \cos\varphi, \end{aligned} \quad (6)$$

where φ is rotor angle – the angle between axes of fixed and moving coordinate systems.

Forces R_i caused by inner damping in the moving coordinates are expressed as follows:

$$R_i = -\frac{m}{2} D \cdot \Omega \cdot H(Q_i) \quad (i=1,2), \quad (7)$$

where D is a diagonal matrix of logarithmic decrements for eigenmodes; $H(X)$ is a vector function with dimension n , with its components h_k defined as:

$$h(x_k) = |x_k| \operatorname{sign} \frac{dx_k}{dt}, \quad k = \overline{1, n},$$

where x_k are the components of n -dimensional vector X , argument of $H(X)$ function.

When expressed in a fixed coordinate system, generalized forces of inner damping N_i produce additions to the right-hand member of original Equations (1):

$$\begin{aligned} N_1 &= R_1 \cos\varphi - R_2 \sin\varphi, \\ N_2 &= R_1 \sin\varphi + R_2 \cos\varphi. \end{aligned} \quad (8)$$

Thus, accounting for inner energy dissipation and structural damping during rotor deformation could be reduced to adding generalized forces (8) to mathematical model of rotor dynamics (1). Implementation of the algorithm (1) could be summarized as following - at each integration step we sequentially execute 3 procedures:

- 1) Using known vectors of generalized coordinates and speeds in the fixed coordinate system, rotor angle and Equation (6) compute respective vectors in the coordinate system attached to the rotor.
- 2) Using forces Equation (7) compute vectors of generalized forces caused by inner damping in the coordinate system attached to the rotor.
- 3) Basing on (8) compute respective generalized forces' vectors in the fixed coordinate system.

IV. A CASE STUDY OF EFFECTS OF INNER DAMPING ON DYNAMICS OF A FLEXIBLE ROTOR

As a case study proposed algorithm was applied to a flexible vertical rotor of the generator part of the RSM (Rotor Scale Model) test bench [17] consisting of two radial AMBs with the length of 5.4 m and the mass of 640 kg. Default control law is a "linear" one that specifies AMB force to be linearly proportional to the displacements and speeds of the rotor [11]. The lowest eigenfrequencies of oscillations of rotor on AMB are 7.5 Hz, 8.2 Hz, 15.8 Hz, 39.3 Hz and 77.5 Hz.

The first two frequencies mostly correspond to rotor

oscillations as a rigid body; the others correspond mostly to flexural oscillations.

The effect of inner damping on rotor dynamics was studied for the case of residual imbalance. Inner damping is characterized with logarithmic decrement δ . Figure 1 depicts rotor displacements in the section of the upper AMB as a function of the rotation frequency in the acceleration mode with a constant angular acceleration of 0.1 Hz/sec for $\delta=0.05$ and $\delta=0.10$. Here and below the black curves correspond to logarithmic decrement $\delta=0.05$ and the gray ones correspond to $\delta=0.10$.

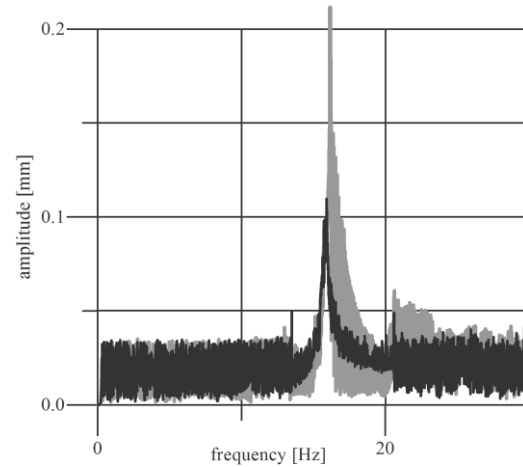


Fig. 1. Rotor displacement as a function of rotation frequency.

Figures 2-4 present rotor oscillations for the rotation frequencies of 10 Hz, 22 Hz and 25 Hz. For subcritical frequencies (under 15 Hz), rotor displacement for a given imbalance is almost constant and is determined by dead space in the current amplifiers of the AMB control system. In the presence of resonance and in the supercritical frequency region the displacement grows when internal damping increases. The main factor causing the growth is the increase of the amplitude of the first flexural eigenmode with the rotation frequency.

Figure 5 depicts oscillation spectrum for the rotation frequency of 23 Hz. The value of the peak corresponding to this frequency in the oscillation spectrum as a function of rotation frequency is shown in Fig. 6.

Rotor oscillations at the frequency of first flexural eigenmode are constantly present because of random perturbations generated in AMB control system which includes relay parts. When inner damping increases, a sharp increase of the oscillation amplitude is observed at supercritical rotation frequencies, which effectively describes the destabilization effect of inner damping. Such effects are in good agreement with known theoretical and experimental results for rotors on conventional slider bearings: the higher inner damping is, the higher is the hazard of exciting flexural oscillations of the rotor [6, 7].

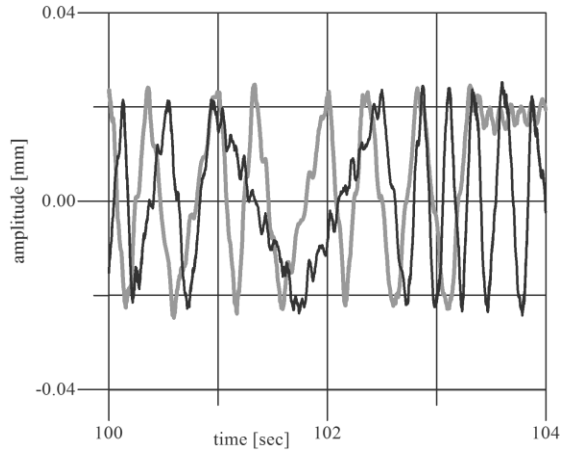


Fig. 2. Rotor oscillations for the rotation frequency of 10 Hz.

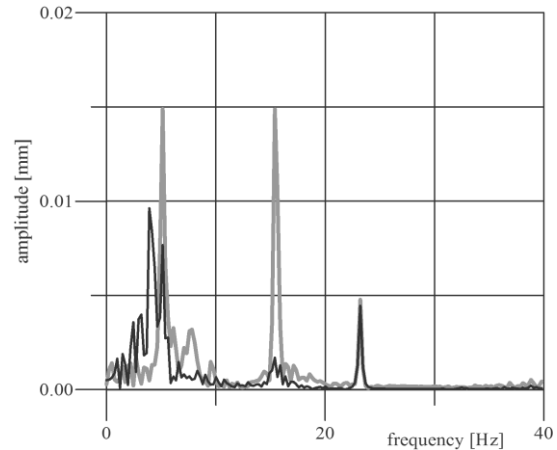


Fig. 5. Rotor oscillation spectrum at the rotation frequency of 23 Hz.

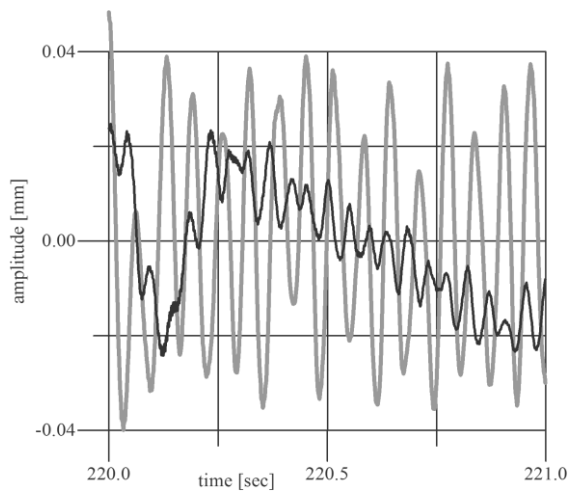


Fig. 3. Rotor oscillations for the rotation frequency of 22 Hz.

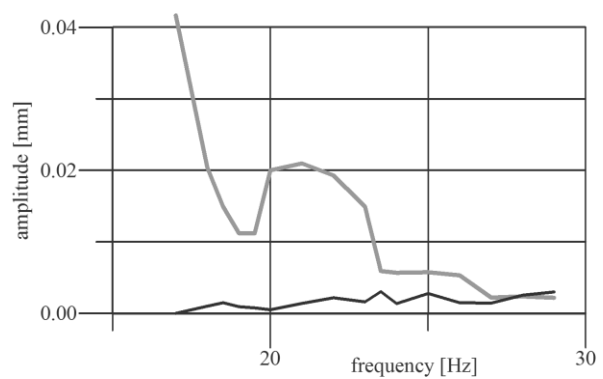


Fig. 6. The peak in the oscillation spectrum caused by the frequency of first flexural eigenmode as a function of rotation frequency.

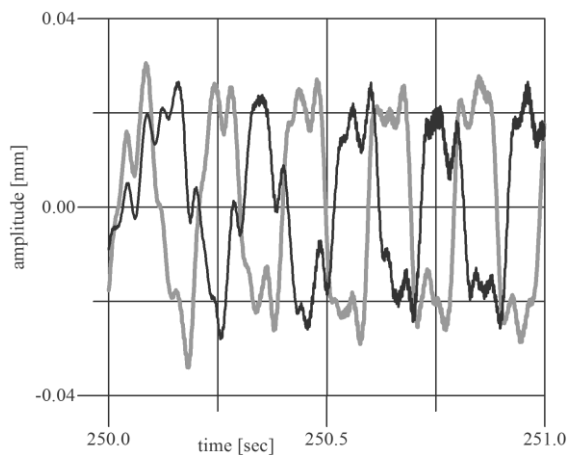


Fig. 4. Rotor oscillations for the rotation frequency of 25 Hz.

V. CONCLUSION

An algorithm for accounting for inner damping in an actively developed computer model of dynamics of a flexible rotor on AMB is presented. The model is a computer program of a discrete mathematical model of the rotor. The application of the algorithm is illustrated by analyzing the effect of amplitude-independent inner damping on dynamics of a flexible rotor in presence of residual imbalance. The results of modelling agree with known data for rotors on conventional slider bearings the higher inner damping is, the higher is the hazard of excitation of flexural rotor oscillations at supercritical rotation frequencies. The software implementation of the algorithm allows for sufficiently accurate account for inner damping effect in the computer model of dynamics of a flexible rotor on AMB. It also almost does not increase computation time which is very important for conducting multi-variant numerical experiments which are essential for design and operation of such complex rotor-based systems.

ACKNOWLEDGMENT

The research was performed with financial support from Russian Science Fund (Grant No. 16-19-10279).

REFERENCES

- [1] F. M. Mitenkov, N. G. Kodochigov, et al., "High-temperature gas-cooled reactors - energy source for industrial production of hydrogen," *Atomic Energy*, vol. 97-6, pp. 432-446, 2004.
- [2] F. Mitenkov, V. Ovchinnikov, M. Nikolaev, et al., "Modeling the dynamics of the electromagnetically suspended vertical-axis wind power plant," *Problems of Strength and Plasticity*, vol. 74, pp. 184-189, 2012.
- [3] F. M. Mitenkov, V. V. Znyshev, et al., "Problems and principles of mathematical simulation of complex unique system dynamics," *Matem. Mod.*, vol. 19-5, pp. 39-44, 2007.
- [4] G. Schweitzer, E. H. Maslin, et al., *Magnetic Bearings in Engineering*. Dordrecht, Heidelberg, London, New York, Springer, 2009.
- [5] F. M. Mitenkov, V. F. Ovchinnikov, M. Y. Nikolaev, et al., "A model of the dynamics of a flexible nonuniform electromagnetically suspended rotor," *Vestnik of Lobachevsky University of Nizhni Novgorod*, vol. 4-1, pp. 171-176, 2012.
- [6] M. Kandil, On Rotor Internal Damping Instability, *Ph.D. Thesis*, University of London, 2004.
- [7] F. M. Dimentberg, K. S. Kolesnikov, et al., *Vibrations in Engineering*. Handbook in 6 volumes. vol. 3. Oscillations of Machines, Structures and their Elements, Moscow, Mashinostroenie Publishers, 1980.
- [8] A. Capozzoli, O. Kilic, C. Curcio, and A. Liseno, "The success of GPU computing in applied electromagnetics," *ACES Express Journal*, vol. 1, no. 4, pp. 113-116, 2016.
- [9] U. Jakobus, "Benefits and challenges of GPU accelerated electromagnetic solvers from a commercial point of view," *ACES Express Journal*, vol. 1, no. 4, pp. 117-120, 2016.
- [10] S. Timoshenko, D. H. Young, and W. Weaver, Jr., *Vibration Problems in Engineering*. New York, Chichester, Brisbane, Toronto, Singapore, John Wiley & Sons, 1974.
- [11] V. Znyshev, E. V. Kiryushina, M. Y. Nikolayev, V. F. Ovchinnikov, et al., "Algorithm for generating a preassigned force of the active magnetic bearings in the control system of a rotor electromagnetic suspension," *Vestnik of Lobachevsky University of Nizhni Novgorod*, vol. 5-1, pp. 138-141, 2010.
- [12] D. V. Balandin and M. M. Kogan, "Motion control for a vertical rigid rotor rotating in electromagnetic bearings," *Journal of Computer and Systems Sciences International*, vol. 50-5, pp. 683-697, 2011.
- [13] F. R. Gantmakher, *Lectures on Analytical Mechanics*. Moscow, Nauka Publishers, 1966.
- [14] E. S. Sorokin, *About Inner Damping Theory applied for Oscillation of Flexible Systems*. Moscow, Gosstroyizdat Publishers, 1960.
- [15] Y. G. Panovko, *Inner Damping in Flexible Systems Oscillations*. Moscow, Physmatgiz Publishers, 1960.
- [16] G. S. Pisarenko, *Oscillations of Mechanical Systems Accounting for Imperfect Rigidity of Material*. Kiev, Naukova dumka Publishers, 1970.
- [17] I. V. Drumov, N. G. Kodochigov, S. E. Belov, D. S. Znamensky, et al., "Studies of the electromagnetic suspension system for the GT-MHR turbo machine rotor model," *Proceedings of HTR*, Prague, Czech Republic, no. 41, pp. 1-7, October 18-20, 2010.



Viktor Ovchinnikov graduated from Lobachevsky State University of Nizhny Novgorod. Leading Researcher of Research Institute of Mechanics of Lobachevsky State University of Nizhny Novgorod. Ph.D. (Physics and Mathematics). Field of interest: studying and modelling dynamics of flexible-body systems.



Mikhail Nikolaev graduated from Lobachevsky State University of Nizhny Novgorod. Leading Researcher at Research Institute of Mechanics of Lobachevsky State University of Nizhny Novgorod. Ph.D. (Engineering Science). Field of interest: studying and modelling dynamics of complex unique systems.



Vasily Litvinov graduated from Lobachevsky State University of Nizhny Novgorod. Junior Researcher at Research Institute of Mechanics of Lobachevsky State University of Nizhny Novgorod. Field of interest: studying and modelling dynamics of magnetic and mechanical systems.

A Stepped Magnetic Suspension System (SMSS)

Evgeni Frishman

Department of Electrical Engineering
Jerusalem College of Technology, Israel
evgeni@jct.ac.il

Abstract — In this article, the vertical and horizontal forces of interaction of permanent magnets in a magnetic support system (magnetic suspension, MS) are considered. Permanent magnets have a stepped structure and uniform magnetization \vec{M} throughout their entire volume ($\vec{M} = \text{const}$). The magnetic support system contains multi-row magnetic strips. The results of the comparison of the vertical and lateral forces for the classic horizontal magnetic system (HMS) are presented too. A stability factor index, the ratio of vertical to lateral force of interaction $\gamma = f_z/f_y$, and an effectiveness factor $\mu_{\text{eff}} = f_z/(mg)$ are defined (where mg is the weight of the magnets per unit length). A prototype of the proposed magnetic support system was built, and measurements were performed. Analysis of the obtained data indicates that the investigated magnetic suspension system performs better than the classical horizontal MS system.

Index Terms — Permanent magnets, stability, stepped suspension, suspension effectiveness factor, vertical and horizontal forces.

I. INTRODUCTION

In this work the vertical and the horizontal forces of interaction in a horizontal magnetic support (HMS) system (also referred to as magnetic levitation or suspension, MLS) are analyzed. The system contains multi-row magnetic strips (permanent magnets) and has a stepped structure as well as a classical structure.

The magnets have a rectangular cross-section and a sufficiently high stability of the magnetization \vec{M} throughout their entire volume ($\vec{M} = \text{const}$). The magnetization vector is directed vertically, along both the positive and negative directions of the z-axis.

II. MAGNETIC SUSPENSION (SUPPORT) SCHEMES

Schematic diagrams of the analyzed systems are represented in Figs. 1 to 3 (cross-section of magnetic systems). The length is in the normal direction.

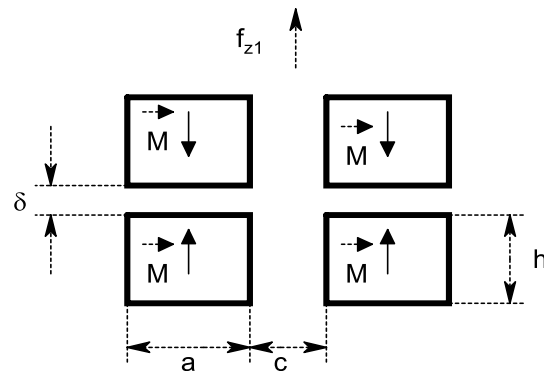


Fig. 1. Classical scheme of MLS.

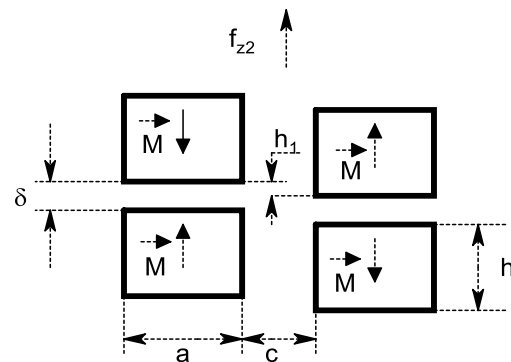


Fig. 2. Scheme with vertical displacement (stepped structure).

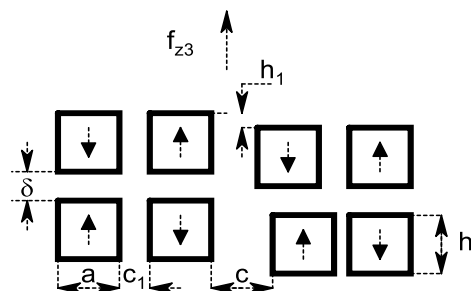


Fig. 3. Combined scheme, classical and stepped structure.

In all of the depicted schemes, the cross-sectional dimensions of the magnets are much smaller than their lengths (in the normal direction). That is, $a \ll l$ and $h \ll l$. In the system depicted in Fig. 4, the magnets $1a$ and $1b$ in the suspended section A are fixed on a the non-ferromagnetic base 2. Magnets $4a$ and $4b$ of the stationary section B are also fixed on the non-ferromagnetic base 3, like the magnets $1a$ and $1b$. The basic working gap is referred to as δ .

The distance between adjacent magnetic strips is equal to c . In the figure, arrows are used to indicate the direction of the magnetization \vec{M} of the permanent magnets 1 and 4.

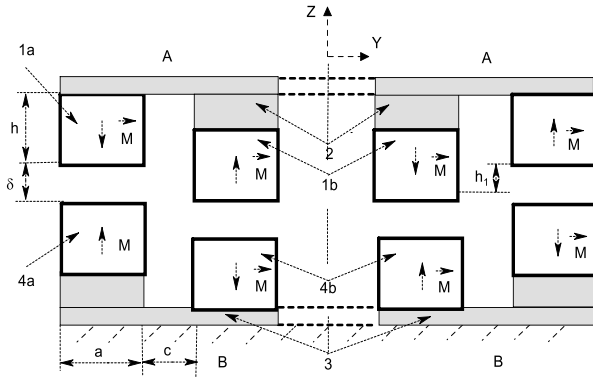


Fig. 4. The symmetrical scheme of magnetic support.

As is evident from the figure, the magnetic strips $1a$ and $1b$ (or $4a$ and $4b$) are moved in the vertical direction to h_1 . The expected effectiveness of the suspension system is based on the special features of the cross-interaction of magnets $1b$ and $4a$ (left and right pairs).

In other words, the effectiveness of the system can be explained by the distribution of the magnetic flux created by these magnets. Thus, the positive effect of the magnetic bearings (suspension) is achieved through the use of leakage flux.

The magnetic system shown in Fig. 3 differs from the system depicted in Fig. 2, in that each of the magnetic strips shown in Fig. 2 has been replaced by two strips with alternating polarities. In the plane YOX, the support system can take the form shown in Fig. 5.

III. INTERACTION ANALYSIS FOR STEPPED SYSTEM

Under certain conditions ($a \ll l$), the description of the interaction of the magnetic systems, represented with adequate accuracy in Fig. 5.1, is also valid for the case depicted in Fig. 5.2. Therefore, the interaction analysis of the magnetic systems depicted in Fig. 1 can be carried out only for the linear system (Fig. 5.1).

The forces of vertical and horizontal interaction in the magnetic systems can be determined using the

expression for the potential energy of a permanent magnet that is located in an external magnetic field:

$$E_p = \mu_0 \iiint_V \vec{M} \cdot \vec{H} \cdot dV, \quad (1)$$

In (1) $\mu_0 = 4\pi \cdot 10^{-7} \left[\frac{H}{m} \right]$, \vec{M} is the magnetization

vector (e.g., the magnet $1a$ or $1b$) and $\vec{H}(y, z)$ is the vector of magnetic field intensity (of the external magnetic field), created, for example, by the magnet $4a$ or $4b$. Integration is performed on the volumes of the magnets which possesses the magnetization \vec{M} .

Expressions for the interaction forces of permanent magnets can be obtained using the equation $\vec{F} = -\vec{\nabla} E_p$. For the vertical and horizontal components of the force, this formula gives us:

$$\vec{F}_z = -\hat{z} \frac{\partial E_p}{\partial z}, \quad \vec{F}_y = -\hat{y} \frac{\partial E_p}{\partial y}, \quad (2)$$

where \hat{y} and \hat{z} are the unit vectors of axes y and z respectively.

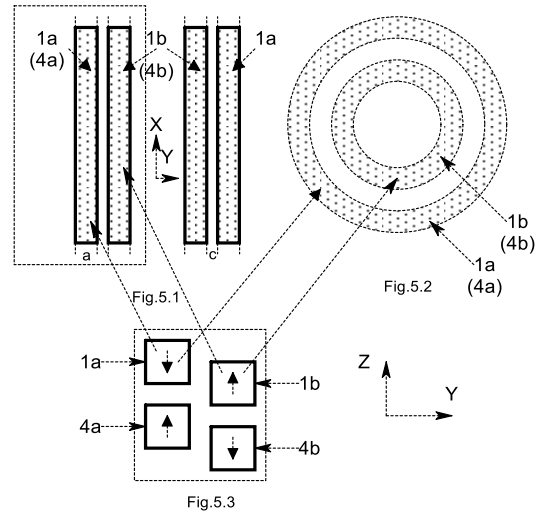


Fig. 5. Details of the stepped magnetic suspension. 5.1: Linear support. 5.2: Locked (circular) support. 5.3: Cross section. $1a$ and $1b$ – moving magnets of the support system, $4a$ and $4b$ – stationary magnets.

The efficiency μ_{eff} of the support schemes shown in Figs. 1 to 3, can be estimated using the following expression:

$$\mu_{eff} = f_z / (mg), \quad (3)$$

in which $f_z [N/m]$ is the vertical interaction force for the unit length of the system that includes magnets 1 and 4 and mg is the weight per unit length of magnets $1a$ and $1b$ (or magnets $4a$ and $4b$).

To find the interaction force of magnetic systems, we must first determine the magnetic field intensity

$\vec{H}(y, z)$ in those systems. Each magnet in Fig. 4 (e.g., $1a$ or $4a$) has a rectangular cross-section and can be represented by two faces (strips), each with a uniformly distributed fictitious magnetic charge with a surface density $\sigma = \pm\mu_0 \cdot M$ [1].

The calculation schemes for the determination of $\vec{H}(y, z)$ referred to Figs. 1 to 3 are shown in Fig. 6.

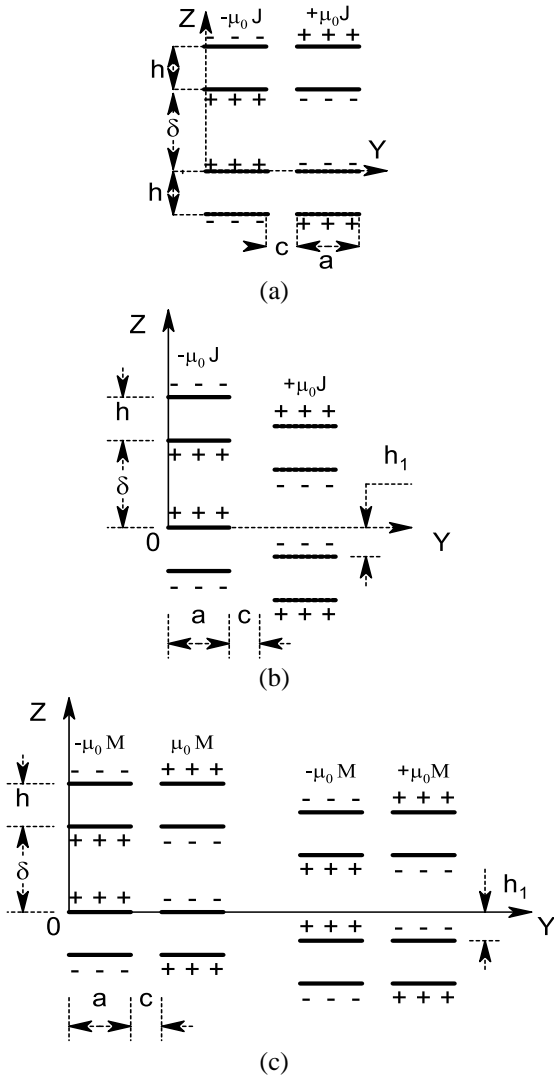


Fig. 6. Calculation schemes corresponding to Figs. 1 to 3.

In accordance with [1, 2] and as shown in Fig. 7, based on the concept of the fictitious magnetic charge, the two-dimensional potential of the magnetic field produced by the “face-charge” at any point, can be expressed as:

$$\phi(y, z) = -\frac{\sigma}{4\pi \cdot \mu_0} \int_0^a \ln \left[z^2 + (y-u)^2 \right] \cdot du. \quad (4)$$

The components of the intensity of the magnetic field are determined by the following expressions:

$$H_z(y, z) = -\frac{\partial \phi(y, z)}{\partial z}; \quad H_y(y, z) = -\frac{\partial \phi(y, z)}{\partial y}. \quad (5)$$

By substituting (4) into (5), we obtain the expressions for the intensity of the magnetic field at the point $P(y, z)$:

$$H_z(y, z) = \frac{\sigma}{2\pi \mu_0} \left(\arctg \frac{y}{z} - \arctg \frac{y-a}{z} \right), \quad (6)$$

$$H_y(y, z) = \frac{\sigma}{2\pi \mu_0} \left[\ln \left(y^2 + z^2 \right) - \ln \left((a-y)^2 + z^2 \right) \right]. \quad (7)$$

The vertical component of the force interaction of two charged surfaces with charge densities $\sigma_1 = \sigma_2 = \sigma$ can be determined using (1) and (2):

$$F_z = \sigma \int_t^{t+a} H_z(y, z) dy. \quad (8)$$

Now, using (6) after a series of transformations, the vertical force per unit length of magnetic systems can be written for the scheme in Fig. 6 (a), as:

$$f_{z1} = 2f_z(0, \delta) - 4f_z(0, \delta+h) + 2f_z(0, \delta+2h) + \\ -2f_z(a+c, \delta) - 2f_z(a+c, \delta+2h) + \\ +4f_z(a+c, \delta+h), \quad (N/m), \quad (9)$$

For the scheme in Fig. 6 (b), we can write,

$$f_{z2} = 2f_z(0, \delta) - 4f_z(0, \delta+h) + 2f_z(0, \delta+2h) + \\ f_z(a+c, \delta-h_1) + 2f_z(a+c, \delta+h-h_1) + \\ -f_z(a+c, \delta+2h-h_1) - f_z(a+c, \delta+h_1) + \\ 2f_z(a+c, \delta+h+h_1) - f_z(a+c, \delta+2h+h_1), \quad (10)$$

where the expression for $f_z(y, z)$ has the following form [2]:

$$f_z(y, z) = \frac{\mu_0 M^2}{2\pi} \left((y+a) \cdot \arctg \frac{y+a}{z} + \right. \\ \left. + (y-a) \cdot \arctg \frac{y-a}{z} - 2y \cdot \arctg \frac{y}{a} \right. \\ \left. + \frac{z}{2} \ln \frac{(z^2 + y^2)^2}{(z^2 + (y-a)^2) \cdot (z^2 + (y+a)^2)} \right). \quad (11)$$

Finally the expression of f_{z3} can be similarly derived by properly considering the interactions between the charged surfaces reported in Fig. 6 (c).

Referring to Figs. 1 to 3, the following values of the parameters have been selected for the evaluation of f_{z1} and f_{z2} : $a = 0.02m$, $h = 0.015m$, $h_1 = 0.01 \div 0.02m$ ($\Delta h_1 = 0.002m$), $\delta = 0.005 \div 0.02m$ ($\Delta \delta = 0.0025m$), $c = 0 \div 0.01m$ ($\Delta c = 0.0025m$), $c_1 = 0m$; and $c_1 = 0.005m$.

Some of the results of these calculations are presented in the Table 1 below, in which f_{z1} is the

vertical force of interaction (with $h_1 = 0$, ref. to Fig. 1, i.e., the configuration without the step).

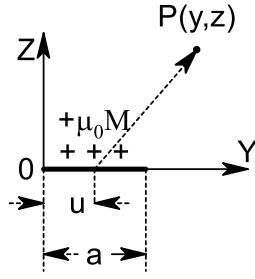


Fig. 7. The calculation scheme for a charged surface of a magnet.

Table 1: Results of the calculations for $\delta = 7.5\text{mm}$

| $\mu_{eff1} = \frac{f_{z1}}{mg}$ | h_1 [mm] | $\frac{f_{z2}}{f_{z1}}$ | $\mu_{eff2} = \frac{f_{z2}}{mg}$ |
|----------------------------------|------------|-------------------------|----------------------------------|
| 10.4 | 1.0 | 1.49 | 15.4 |
| 10.4 | 1.2 | 1.53 | 16.0 |
| 10.4 | 1.4 | 1.54 | 16.0 |
| 10.4 | 1.6 | 1.50 | 15.5 |
| 10.4 | 1.8 | 1.41 | 14.6 |
| 10.4 | 2.0 | 1.24 | 12.8 |

A graph of the dependence $f_z(\delta)$ for two cases (with the step (f_{z2}) and without the step (f_{z1})) is presented in Fig. 8.

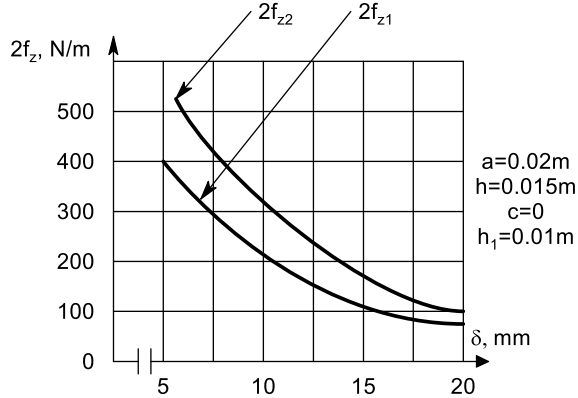


Fig. 8. Graph of the dependence $f_z(\delta)$.

IV. SIDE FORCES ANALYSIS

In the case of two magnetic strips which are offset relative to each other in the horizontal direction by the distance \tilde{y} , as shown in Fig. 9, expression (1) becomes:

$$E_p = \mu_0 M \int_0^b dx \int_{\tilde{y}}^{\tilde{y}+a} dy \int_{\delta}^{\delta+h} H_z dz. \quad (12)$$

In the case of the interaction of n magnetic strips, the potential energy of the system is determined by summing the energies Π_{ij} of each i^{th} fixed magnet ($4a$ or $4b$, Fig. 4, $h_1 = 0$) with each j^{th} magnet ($1a$, $1b$) of the moving part of the system, i.e.,

$$E_{p0} = \sum_{i=1}^n \sum_{j=1}^n \Pi_{ij}. \quad (13)$$

The dependence of side destabilizing forces (acting on a unit length of a magnetic strip) on the value of lateral displacement takes the form:

$$f_y = -\frac{1}{l \cdot n} \cdot \frac{\partial}{\partial \tilde{y}} \left(\sum_{i=1}^n \sum_{j=1}^n \Pi_{ij} \right), \quad (14)$$

where n is the number of magnetic strips on the mobile (or stationary) portion of the magnetic bearing, and l is the length of the magnetic strip.

Expression (14), which takes into account formulas (6), (7) and (13) for interacting bands (Fig. 5) with two pairs of lateral displacement \tilde{y} , allows to record a destabilizing force in the form of:

$$f_y = -\mu_0 \frac{M^2}{2\pi} \left(\int_{\delta}^{\delta+h} H_z \Big|_{y=\tilde{y}}^{y=\tilde{y}+a} dz + \frac{1}{2} \int_{\delta}^{\delta+h} H_z \Big|_{y=a+c-\tilde{y}}^{y=-\tilde{y}+2a+c} dz - \frac{1}{2} \int_{\delta}^{\delta+h} H_z \Big|_{y=\tilde{y}}^{y=\tilde{y}+2a+c} dz \right). \quad (15)$$

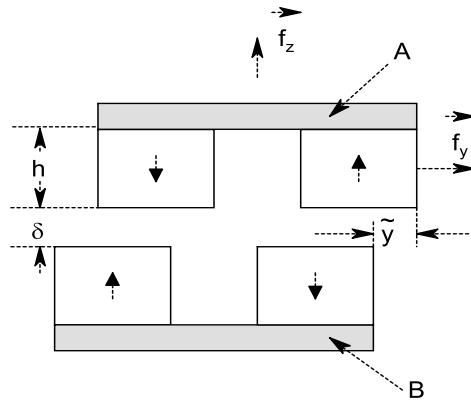


Fig. 9. The classical magnetic support scheme with lateral displacement.

Table 2 shows the results of calculations of the lateral force f_y , dependent on the distance c between the strips, with $l = 1\text{m}$, $\delta = 7.5\text{mm}$, $a = 60\text{mm}$, $h = 50\text{mm}$ and $h_1 = 0\text{mm}$, that is, the vertical offset (step) is absent. The same table shows the ratio of the vertical and lateral forces, ($\gamma = f_z/f_y$), defined as a measure of system stability (this index can essentially be defined as a destabilizing factor; the greater the value, the less resistant the support system is to tipping or sliding).

Table 3 shows the results of calculating the lateral force, dependent on the side displacement, at $l = 1m$, $\delta = 7.5mm$, $a = 60mm$, $h = 50mm$.

Table 4 shows the calculation of f_y for two and three strips with $l = 1m$, $\delta = 7.5mm$, $a = 60mm$, $h = 50mm$.

Table 2: Dependence of the side force on the distance between the strips: $\tilde{y} = 1mm$, $n = 3$, and $h_1 = 0$

| c [mm] | f_y [N/m] | $\gamma = f_z/f_y$ |
|----------|-------------|--------------------|
| 5 | 47.7 | 19.3 |
| 10 | 52.3 | 20.0 |
| 15 | 40.7 | 22.5 |

Table 3: Dependence of lateral forces on the magnitude of side displacement \tilde{y} : $n = 3$, $c = 10mm$

| \tilde{y} [mm] | f_y [N/m] | $f_y/f_{\tilde{y}=1mm}$ |
|------------------|-------------|-------------------------|
| 1 | 44.0 | 1 |
| 2 | 87.6 | 2 |
| 3 | 130.7 | 3 |
| 4 | 173.0 | 3.9 |

Table 4: Relationship of side force with number n of strips

| n | \tilde{y} [mm] | f_y [N/m] |
|-----|------------------|-------------|
| 2 | 1 | 41.0 |
| 3 | 1 | 44.0 |
| 2 | 2 | 81.0 |
| 3 | 2 | 88.0 |

Figure 10 is a plot of the clearance δ at the lateral displacement \tilde{y} , when $a = 64mm$, $h = 56mm$ and $c = 10mm$.

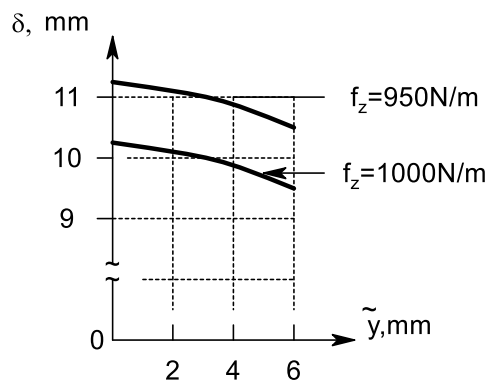


Fig. 10. Loci of the vertical force in the lateral displacement - clearance (\tilde{y} - δ) plane.

V. CONCLUSION

The vertical and horizontal forces of interaction between permanent magnets in a magnetic support system (magnetic suspension, MS) have been investigated. The main results of the investigations are here briefly summarized.

1. The analysis of the obtained data for the stepped MS indicates that the investigated magnetic suspension system (Fig. 2 and Fig. 3) outperforms the classic horizontal system (Fig. 1).

2. The ratio $\gamma = f_z/f_y$ increases with increasing width a , indicating a reduction of the instability of the support system in the horizontal plane (Fig. 9).

3. The stability factor γ grows more slowly than the width a of the magnetic strip. Doubling \tilde{y} causes $\gamma = f_z/f_y$ to double. The nonlinearity of the relationship $f_y(\tilde{y})$ becomes apparent when $\tilde{y}/a \geq 0.5$. For smaller values of \tilde{y} , the lateral force between the magnets can be approximated by $f_y(\tilde{y}) = k\tilde{y}$.

4. Increasing the number of rows of magnets leads to an increase of the lateral force f_y , as was the case for the vertical force f_z .

REFERENCES

- [1] W. Baran, "Berechnung von Anziehungs- und Haftkräften für Magnet mit Feinpolteilung," *Techn. Mitt. Krupp Forsch. - Ber.*, vol. 21, pp. 72-83, 1963.
- [2] A. E. M. Frishman and M. I. Umanov, "Analysis of vertical and horizontal interaction forces in permanent magnets maglev systems," *Vestnik Dnepropetrovskogo nazionalnogo Universiteta Zeleznodoroznogo Transporta*, vol. 2, no. 41, pp. 136-141, 2012.

Coupled Electromechanical Analysis of a Permanent-Magnet Bearing

Vincenzo Di Dio¹ and Luca Sani²

¹DEIM, Department of Energy, Engineering Information and Mathematical Model
University of Palermo, Palermo, 90128, Italy
vincenzo.didio@unipa.it

²DESTEC, Department of Energy, Systems, Territory and Constructions Engineering
University, Pisa, 56122, Italy
luca.sani@unipi.it

Abstract — In this paper we present a new Permanent Magnets (PMs) bearing, which is composed of a rotor capable to levitate at a short distance from a dedicated stator. Proper configurations of PMs arranged on both the stator and the rotor allows having the magnetic suspension. Intrinsic mechanical instability characterizes the device; a passive stabilization is attempted exploiting eddy currents on a conducting sheet that surrounds the magnets on the stator. The system has been simulated by means of a dedicated numerical code that takes into account the effects of magneto-mechanical coupling. The coupled problem has been integrated by means of a prediction-correction nested scheme. Some interesting results, extensively discussed here, has been produced by simulation activity. In particular the stability of to the center of mass with respect to the translations has been passively obtained, if the rotations are actively prevented.

Index Terms — Computational electromagnetic, coupled analysis, magnetic bearings, magnetic levitation, permanent magnets.

I. INTRODUCTION

In the late 1960s, the modern development of Magnetic Levitation systems (known as MAGLEV) started when the possibility to use magnetic forces to levitate vehicles became sustainable, mainly due to some discoveries of that time: development of low-temperature superconducting wire, transistor and chip based electronic control technology [1], [2]. MAGLEV provides high-speed motion, safety, reliability, low environmental impact and minimum maintenance [3]. There are two basic options to obtain magnetic levitation: a) electromagnetic system [4]-[6] working in attraction mode with forces generated by electromagnets; b) electrodynamic system [7], [8] working in repulsive mode with forces generated by superconductive coils. An application example is flywheel energy storage systems, which are considered to be an attractive alternative to

conventional electrochemical batteries [9], [10]. Unstable behavior is the main feature of both solutions. The first option is unstable in the levitating direction which is vertical, in general. The attractive force increases when the two parts of the system approach each other. The second option, i.e., the electrodynamic system is unstable in the transverse-to-levitation and in the motion directions. Nowadays a new class of MAGLEV systems can be conceived via the use of Rare Earth PMs (e.g., NdFeB) characterized by high values of remnant field. The suspension is then assured by the repulsion of properly shaped PMs [11], [12]. Stability of levitation systems based on PMs is prevented by Earnshaw's theorem [13]. This theorem states that a set of steady charges, magnetizations or currents cannot stay in stable equilibrium under the action of steady electric and magnetic field. As applications of MAGLEV or magnetic bearing devices must be fail-safe, severe constraints are posed on the design and operation of the stabilization systems. So a great effort is devoted to the design of passive and more reliable stabilization devices. In some cases, electric and magnetic systems can avoid the consequences of the Earnshaw's theorem: time varying fields (e.g., eddy currents, alternating gradient), ferrofluids, superconductors and diamagnetic systems. In this paper, the use of eddy current stabilization to reduce or compensate the intrinsic instability of the bearing is investigated: if some magnetized parts of a system are in motion near conductive materials, eddy currents are induced and the system is not under the action of steady magnetic fields. Since the system is now governed by the diffusion equation, the hypothesis of the Earnshaw's theorem (direct consequence of the Laplace equation) is not valid. Some preliminary results of the coupled electromechanical analysis of a PMs bearing are discussed in this paper, demonstrating how the presence of motional induced eddy currents have a positive effect on the dynamic of the bearing device. This electrodynamic effect allows to reduce the complexity of the control

system. Section 2 introduces the proposed device, Section 3 briefly describes the numerical code used for the analysis of the device, while Section 4 discusses the results.

II. PROPOSED DEVICE

The proposed system is shown in Figs. 1 and 2: it exploits the induced eddy currents to contrast the instability related to the PMs arrangement.

It is mainly composed of a toroidal stator and a segmented rotor made of at least three blocks equally spaced along the circumference. The rotor can move with 6 degrees of freedom (DOF) with respect to the fixed stator. The PMs in both the stator and the rotor are arranged in Halbach array configurations [14] focusing the field lines in the airgap between them. A sheet of conductive material surrounds the stator (black in Fig. 2). Levitation along z-direction is achieved by the repulsion of PMs with opposite magnetization. To describe the dynamics of the proposed device we assume that the moving part rotates around a vertical shaft, directed as the z-axis that is the symmetry axis of the stator. Motion-induced eddy currents flow on the stator sheet; subsequently a levitation force on the z-axis in addition with the levitation force of the PMs and a magnetic drag torque are observed. Those currents interact with the PMs of the rotor reducing the cause which produces the eddy currents themselves. This reduction is produced by a drag force on the rotor which produces a velocity reduction, and by moving away the field source (the PMs on the rotor) from the conductive region.

Since the levitation force is a decreasing function of the distance, the system is stable in the levitation direction. When the system rotates in the symmetric configuration, the radial forces are deleted. A net force in the radial direction is expected to appear if the system does not run in symmetrical conditions (e.g., a radial displacement of the rotation shaft occurs). This force is the resultant of the forces between the two PMs systems and of the interactions between the motion-induced eddy currents on the stator and the PMs on the rotor. Earnshaw's theorem states that the forces between the PMs are destabilizing. If we consider a displacement of the rotor in the x-axis (Fig. 2), currents induced on the conductive sheet are stronger on the side of the displacement, while they get weaker on the opposite side where the distance is greater. The net resulting force is then directed along the negative x-axis direction and it performs a stabilizing action. This stabilizing effect occurs in principle also in the case of angular displacement of the rotation shaft with respect to the vertical (y-axis) direction. As a result of this angular displacement, since the rotor is divided in three sectors (or more), some of these sectors are closer to the stator, while others are more distant. The induced currents on the part of the

stator corresponding to the nearest rotor sectors are more intense and the resulting forces exerted on the rotor PMs are stronger. On the contrary, the forces on the more distant rotor sectors are weaker. The final effect is a torque restoring the vertical position of the rotation shaft.

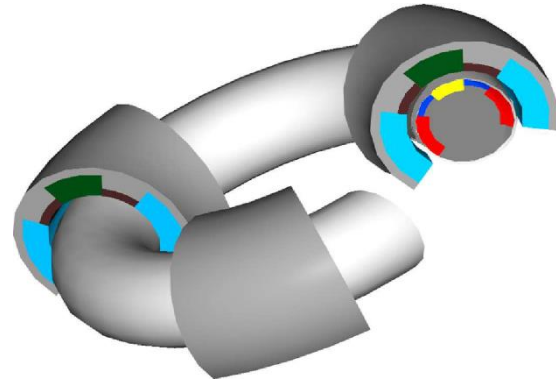


Fig. 1. A 3D view of the analysed device.

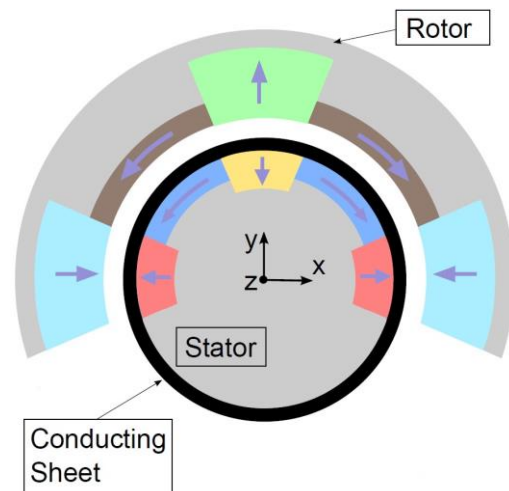


Fig. 2. Cross section of the bearing.

III. THE NUMERICAL FORMULATION

The performances of this device have been investigated by a numerical model. The equations describing the rotor dynamics with six DOFs are inherently nonlinear because of the dependence of the force on the position of the rotor itself. Moreover the problem of rigid body dynamics is coupled with the diffusion equation of the magnetic field. The solution of the electromagnetic problem has been carried out by an integral formulation that reduces the diffusion equation to an equivalent network with time varying parameters. The values of the parameters in the electrical equations are function of the position of the rotor. The details of the adopted formulation are reported in [15] - [23].

Under the hypothesis of linear magnetisable materials, the equations of the problem produced by

the equivalent network formulation coupled with the Newton-Euler equations of motion can be written as:

$$\begin{aligned} \mathbf{L}(C(t))\frac{d\mathbf{i}}{dt} + [\mathbf{R}(C(t)) + \mathbf{K}(C(t), \dot{C}(t))] \mathbf{i} &= \mathbf{e}(t) \\ \mathbf{F}(C(t)) &= m\ddot{\mathbf{q}} \\ \mathbf{M}(C(t)) &= \mathbf{I}_{\theta\theta}\dot{\omega} + \omega \times \mathbf{I}_{\theta\theta}\omega, \end{aligned} \quad (1)$$

where $\mathbf{e}(t)$ represents the vector of the applied voltage generators and \mathbf{i} is the vector of the currents in the elementary volumes, including the equivalent magnetization currents. All the coefficients matrices are function of $C(t)$ which represents the system configuration at the instant t . $C(t)$ is defined as the set of the positions and orientations of all the elementary volumes in which the device is discretized:

$$C(t) = (x(t), y(t), z(t), \phi(t), \theta(t), \psi(t)), \quad (2)$$

$\mathbf{L}(C(t))$ denotes the inductance matrix; $\mathbf{R}(C(t))$ is the resistance matrix and $\mathbf{K}(C(t), \dot{C}(t))$ takes into account the electromotive force due to the motional effects. In particular $\dot{C}(t)$, termed as the derivatives of the system configuration at the instant t , describes the velocity of every elementary volume in the hypothesis of rigid body. The $\dot{C}_i(t)$ corresponding to the i -th elementary volume is constituted by the three components of the translation velocity, the three components of the angular velocity, and the three coordinates of the center of rotation.

Equation (1) is solved by a prediction correction nested scheme. The rationale behind it is the search for an approximation inside the time step of the behaviour of the coefficients in electrical and mechanical equations. The predictor-corrector approach is used to obtain an approximate behavior of the named quantities by a linear interpolation between the known values at the previous time step and the predicted values at the next time step. Inserting this knowledge in the equations has the effect of considering updated values of the coefficients, allowing a coupling between the equations which is stronger than the one in a simply staggered scheme and comparable with a monolithic approach.

The integration algorithm can be described as follows ($\Delta t = t_{n+1} - t_n$):

- assuming $C(t)$ constant in the interval Δt an estimate of the currents at t_n is obtained by a trapezoidal rule applied on (1a);
- an estimate of $C(t_{n+1}) = C_{n+1}$ is obtained by applying forward Euler integration to (1b) and (1c);
- a piecewise linear approximation is assumed for \mathbf{L} in Δt , similarly for \mathbf{R} and \mathbf{K} :

$$\dot{\mathbf{L}}(t_n) \approx \frac{\mathbf{L}(\tilde{C}(t_{n+1})) - \mathbf{L}(\tilde{C}(t_n))}{\Delta t}, \quad (3)$$

and as a consequence,

$$\mathbf{L}(t) \approx \mathbf{L}(t_n) + \dot{\mathbf{L}}(t_n) \cdot (t - t_n) = \mathbf{L}_n + \dot{\mathbf{L}}_n \cdot (t - t_n), \quad (4)$$

similarly for the other coefficients.

- The expressions are introduced in (1a):

$$\begin{aligned} (\mathbf{L}_n + \dot{\mathbf{L}}_n \cdot (t - t_n)) \frac{d\mathbf{i}}{dt} + [(\mathbf{R}_n + \dot{\mathbf{R}}_n \cdot (t - t_n)) + \\ (\mathbf{K}_n + \dot{\mathbf{K}}_n \cdot (t - t_n))] \mathbf{i} = \mathbf{e}(t) \quad t \in [t_n, t_{n+1}]. \end{aligned} \quad (5)$$

- Integrating with a trapezoidal-like rule we obtain the corrected values of the currents at the instant t_{n+1} . We write:

$$\int_{t_n}^{t_{n+1}} (\mathbf{L}_n + \dot{\mathbf{L}}_n \cdot (t - t_n)) \frac{d\mathbf{i}}{dt} + \int_{t_n}^{t_{n+1}} [(\mathbf{R}_n + \dot{\mathbf{R}}_n \cdot (t - t_n)) + (\mathbf{K}_n + \dot{\mathbf{K}}_n \cdot (t - t_n))] \mathbf{i} dt = \int_{t_n}^{t_{n+1}} \mathbf{e}(t), \quad (6)$$

- and after the numerical integration:

$$\begin{aligned} \mathbf{L}_n(\mathbf{i}_{n+1} - \mathbf{i}_n) + \frac{\Delta t \dot{\mathbf{L}}_n}{2}(\mathbf{i}_{n+1} + \mathbf{i}_n) + \frac{\Delta t(\mathbf{R}_n + \mathbf{K}_n)}{2}(\mathbf{i}_{n+1} + \mathbf{i}_n) + \\ + \frac{\Delta^2 t(\dot{\mathbf{R}}_n + \dot{\mathbf{K}}_n)}{2} \mathbf{i}_{n+1} = \frac{\Delta t(\mathbf{e}_{n+1} + \mathbf{e}_n)}{2}. \end{aligned} \quad (7)$$

- Collecting terms finally gives a linear system where the unknowns are the corrected currents at the instant t_{n+1} :

$$\begin{aligned} \left(\mathbf{L}_n + \frac{\Delta t \dot{\mathbf{L}}_n}{2} + \frac{\Delta t(\mathbf{R}_n + \mathbf{K}_n)}{2} + \frac{\Delta^2 t(\dot{\mathbf{R}}_n + \dot{\mathbf{K}}_n)}{2} \right) \mathbf{i}_{n+1} = \\ \frac{\Delta t(\mathbf{e}_{n+1} + \mathbf{e}_n)}{2} + \left(\mathbf{L}_n - \frac{\Delta t \dot{\mathbf{L}}_n}{2} - \frac{\Delta t(\mathbf{R}_n + \mathbf{K}_n)}{2} \right) \mathbf{i}_n. \end{aligned} \quad (8)$$

- Once (8) is solved, force and torque are evaluated again with the corrected values of the currents $\mathbf{i}(t_{n+1})$ just obtained. The integration of the mechanical equations yields the corrected position of the moving body.

The integration method has been validated and the results exhibit a very good accuracy respect to the experimental data found in literature.

IV. SIMULATION RESULTS

We considered a device with an average toroid radius of 8 cm. We performed a set of simulations driving the rotor at different rotational speeds. At low speeds (less than 3000 rpm), we observed a small stabilizing effect; at speed greater than 4000 rpm the magnetic drag force reduces and the stabilizing effect is appreciable. Results correspondent to a speed of 4800 rpm are reported here.

Referring to Fig. 2 (which is not in scale), the red and cyan radial magnetized sectors have an angle of 67.50° , the green and yellow ones have an angle of 45° , while the brown and blue azimuth magnetized sectors have an angle of 33.75° . The radial width is 0.5 cm for the red and yellow sectors, 1 cm for the green and cyan ones, and 0.3 cm for the brown and blue ones. The thickness of the conductive (aluminum) sheet is 2 mm and its average radius is 2.2 cm; the clearance between rotor and stator is 7 mm.

The numerical formulation described in Section 3 has been used to perform the analysis of the described device operating under different conditions.

We started considering the device without the conductive sheet and having an initial position characterized by the rotation shaft x-displacement of 1.5 mm with respect to the symmetry axis.

The results of simulation are shown in Figs. 3 and 4. The levitation force is 450 N. As expected the system is unstable with respect to the radial direction and with respect the rotation around the x and the y axes. The contact between the rotor and the stator happens after about 3 ms.

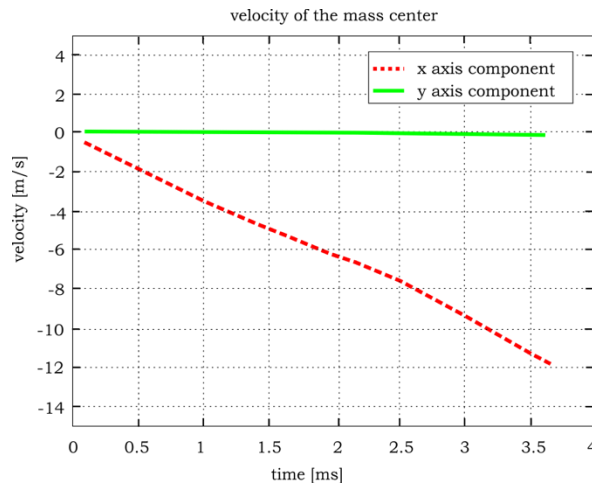


Fig. 3. Velocity of the center of mass of the rotor.

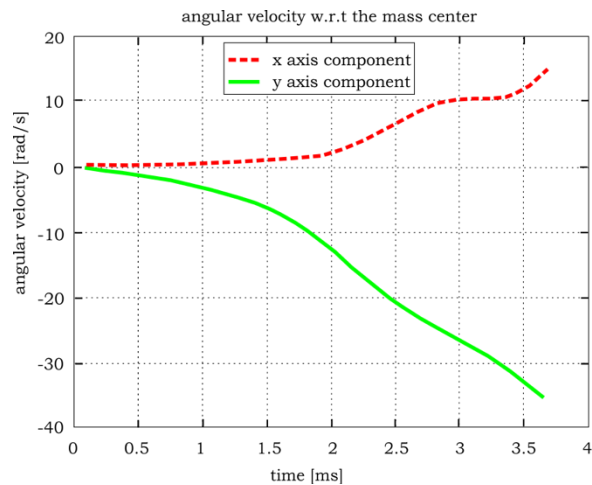


Fig. 4. Components of the angular velocity.

Figures 5 and 6 refer to the configuration with the conductive sheet. The levitation force is raised to 470 N because of the effect of the eddy current. Even in this case the rotor touches the stator because of the unstable

behavior of the system. Comparing the behavior described by Figs. 5 and 6 (presence of the conductive sheet) with the one in Figs. 3 and 4 (absence of conductive sheet), we can see that the eddy currents on the conductive sheet are able to slower the unstable dynamics; the rotor takes a longer time (about 17 ms) to touch the stator. Although the eddy currents are not able to stabilize the device, they can be used to reduce the complexity of the control system. In fact, a lower dynamic requires a slower control action, easier to be designed.

Further simulations have been performed on the device with a reduced number of DOFs preventing rotations with respect to x and y axes.

Figure 7 shows the waveforms of the three components of the velocity of the center of mass of the rotor, while Fig. 8 shows waveforms of the force components; the simulations correspond to the same initial lateral displacement $dx = 1.5 \text{ mm}$.

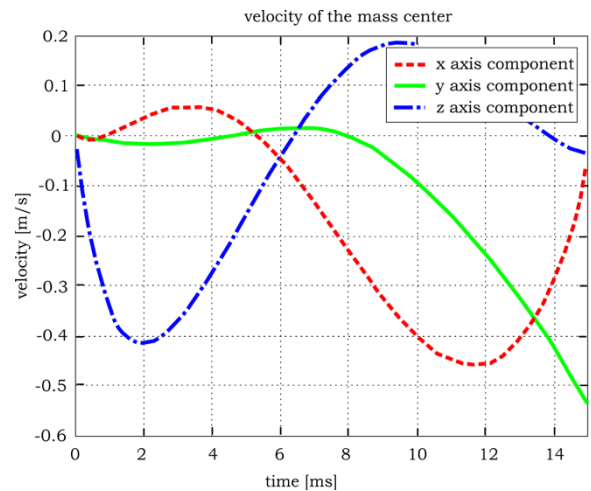


Fig. 5. Velocity of the center of mass of the rotor.

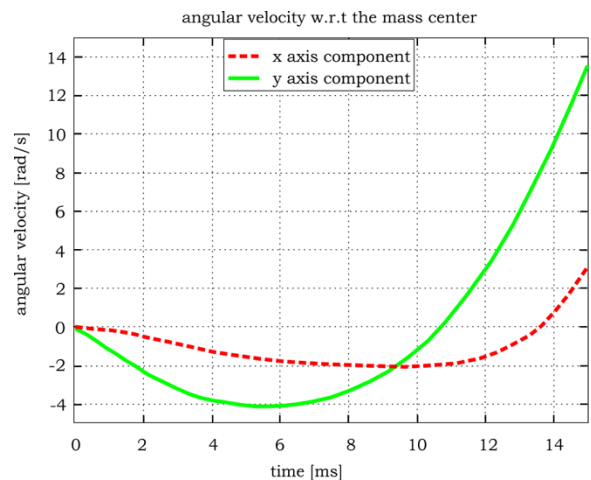


Fig. 6. Components of the angular velocity.

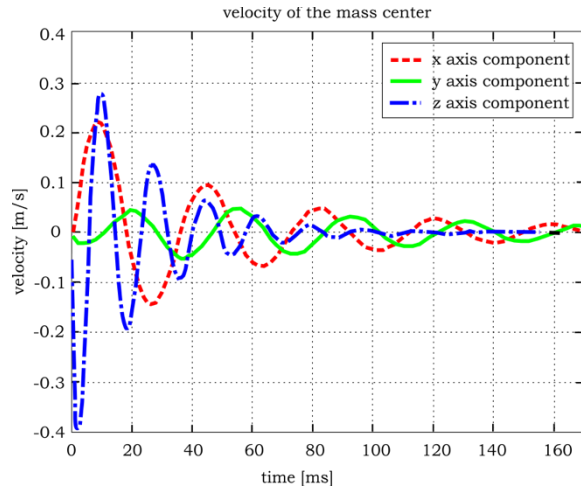


Fig. 7. Velocity of the center of mass of the rotor with 3 DOFs.

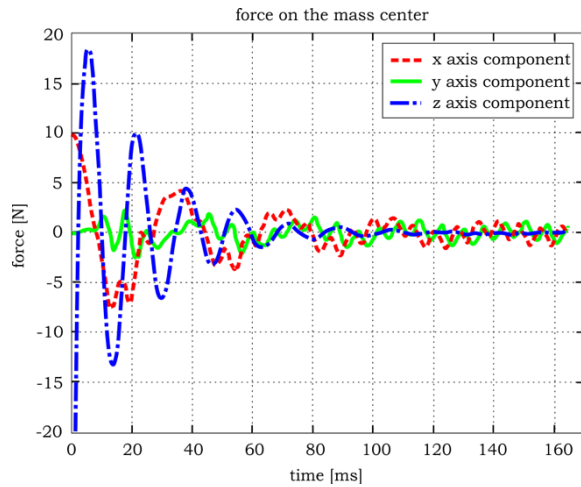


Fig. 8. Force of the center of mass of the rotor with 3 DOFs.

The results of the simulations show that the dynamic of the system is stable. This is actually a good result if we think that in this kind of devices, stability has to be discussed in the contest of dynamics. This means that the robustness requirements previously mentioned, involve concepts of dynamic stability in presence of modeling error due to uncertainties (modern nonlinear dynamics). This theory, usually, not only requires the knowledge of how the forces and torques change with the position and orientation but also of how they changes with both linear and angular velocities. The control systems are consequently usually really complex: this result is then really interesting because it permits a simpler synthesis of the active controller and so reducing the cost. Another similar simulation has been done applying a lateral force of 10 N to the rotor. The results are shown in Figs. 9 and 10; the system is able to compensate the lateral force as

well as for the lateral displacement.

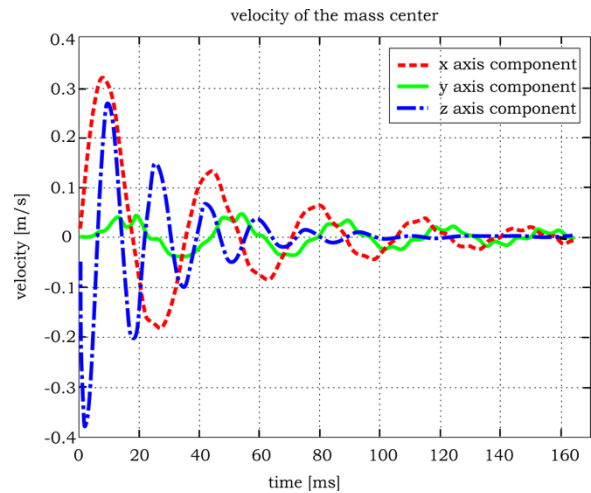


Fig. 9. Velocity of the center of mass of the rotor with 3 DOFs.

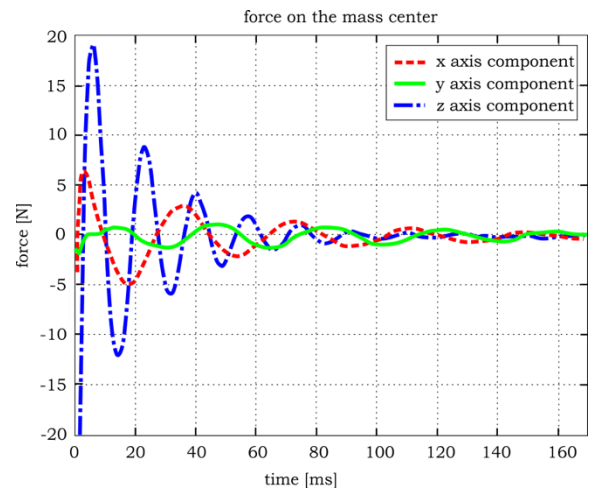


Fig. 10. Force of the center of mass of the rotor with 3 DOFs.

V. CONCLUSIONS

An exhaustive simulation activity has been performed on a PMs bearing based on Halbach array configurations. The conductive sheet is not sufficient to stabilize to system, but it makes slower the unstable dynamics, actually simplifying the control systems action. Since the actuators basically consist of coils, a slower dynamics will need slower control actions, and then smaller voltages. The main result of our analysis relies in the intrinsic stability with respect to the mass center translation, once the rotations with respect x and y axes are prevented. This means that a stabilization system is needed only to maintain the direction of the rotation axis parallel to the z-axis, while the system is able to self-stabilize the position of the rotation axis.

Equivalently, if the stabilizing action results in a net force beside the needed torque, the system is able to compensate this force by adjusting its position.

ACKNOWLEDGMENT

The authors would like to thank the NVIDIA's Academic Research Team for the donation of two NVIDIA Tesla K20c GPUs that have been extensively exploited for the simulations.

REFERENCES

- [1] V. Kozorez and O. Cheborin, "On stability of equilibrium in a system of two ideal current rings," in *Dokl. Akad. Nauk UkrSSR*, Ser. A, vol. 4, pp. 80-81, 1988.
- [2] F. C. Moon, *Chaotic and Fractal Dynamics: Introduction for Applied Scientists and Engineers*. John Wiley & Sons, 2008.
- [3] H.-W. Lee, K.-C. Kim, and J. Lee, "Review of maglev train technologies," *IEEE Trans. Mag.*, vol. 42, no. 7, pp. 1917-1925, 2006.
- [4] J. Meins, L. Miller, and W. Mayer, "The high speed maglev transport system transrapid," *IEEE Trans. Mag.*, vol. 24, no. 2, pp. 808-811, 1988.
- [5] N. Amati, A. Tonoli, F. Impinna, and J. Girardello Detoni, "A solution for the stabilization of electrodynamic bearings: Modeling and experimental validation," *Journal of Vibration and Acoustics*, vol. 133, pp. 021 004-1, 2011.
- [6] A. Tonoli, N. Amati, F. Impinna, J. G. Detoni, H. Bleuler, and J. Sandtner, "Dynamic modeling and experimental validation of axial electrodynamic bearings," in *Proc. of the 12th Int. Symposium on Magnetic Bearings*, pp. 68-73, 2011.
- [7] M. Ono, S. Koga, and H. Ohtsuki, "Japan's superconducting maglev train," *IEEE Instrum. & Measur. Magazine*, vol. 5, no. 1, pp. 9-15, 2002.
- [8] E. Diez-Jimenez, J.-L. Perez-Diaz, and J. C. Garcia-Prada, "Local model for magnet-superconductor mechanical interaction: Experimental verification," *Journal of Applied Physics*, vol. 109, no. 6, (063901), 2011.
- [9] M. Ceraolo, G. Lutzemberger, and D. Poli, "Aging evaluation of high power lithium cells subjected to micro-cycles," *Jour. of Energy Storage*, vol. 6, pp. 116-124, 2016.
- [10] S. Barsali, M. Ceraolo, R. Giglioli, and D. Poli, "Storage applications for smartgrids," *Electric Power System Research (EPSR)*, vol. 120, pp. 109-117, Mar. 2015.
- [11] A. Musolino, R. Rizzo, M. Tucci, and V. M. Matrosov, "A new passive maglev system based on eddy current stabilization," *IEEE Trans. Mag.*, vol. 45, no. 3, pp. 984-987, 2009.
- [12] A. Musolino, M. Raugi, R. Rizzo, and E. Tripodi, "Stabilization of a permanent-magnet MAGLEV system via null-flux coils," in *IEEE Trans. on Plasma Sci.*, vol. 43, no. 5, pp. 1242-1247, 2015.
- [13] S. Earnshaw, "On the nature of the molecular forces which regulate the constitution of the luminiferous ether," *Trans. Camb. Phil. Soc.*, vol. 7, pp. 97-112, 1842.
- [14] K. Halbach, "Application of permanent magnets in accelerators and electron storage rings," *Journal of Applied Physics*, vol. 57, no. 8, pp. 3605-3608, 1985.
- [15] S. Barmada, A. Musolino, M. Raugi, and R. Rizzo, "Analysis of the performance of a combined coil-rail launcher," *IEEE Trans. Mag.*, vol. 39, no. 1, pp. 103-107, Jan. 2003.
- [16] A. Musolino, M. Raugi, and B. Tellini, "3-D field analysis in tubular induction launcher with armature transverse motion," *IEEE Trans. Magn.*, vol. 35, no. 1, pp. 154-159, Jan. 1999.
- [17] R. Albanese, M. Canali, A. Musolino, M. Raugi, G. Rubinacci, and S. Stangherlin, "Analysis of a transient nonlinear 3-D eddy current problem with differential and integral methods," *IEEE Trans. Magn.*, vol. 32, no. 3, pp. 776-779, May 1996.
- [18] E. Tripodi, A. Musolino, R. Rizzo, and M. Raugi, "A new predictor-corrector approach for the numerical integration of coupled electromechanical equations," *Int. J. for Num. Meth. in Eng.*, vol. 105, no. 4, pp. 261-285, 2016.
- [19] S. Quondam Antonio, A. Faba, G. Carlotti, and E. Cardelli, "Vector hysteresis model identification for iron-silicon thin films from micromagnetic simulations," *Physica B: Condensed Matter*, vol. 486, pp. 97-100, 2016.
- [20] S. Barmada, A. Musolino, M. Raugi, and R. Rizzo, "Analysis of the performance of a multi-stage pulsed linear induction launcher," in *IEEE Trans. on Magn.*, vol. 37, no. 1, pp. 111-115, Jan. 2001.
- [21] A. Musolino, R. Rizzo, and E. Tripodi, "The double-sided tubular linear induction motor and its possible use in the electromagnetic aircraft launch system," in *IEEE Trans. on Plasma Sci.*, vol. 41, no. 5, pp. 1193-1200, 2013.
- [22] A. Musolino, R. Rizzo, and E. Tripodi, "Tubular linear induction machine as a fast actuator: Analysis and design criteria," *Progress In Electromag. Research*, vol. 132, pp. 603-619, 2012.
- [23] A. Musolino, R. Rizzo, and E. Tripodi, "Travelling wave multipole field electromagnetic launcher: An SOVP analytical model," in *IEEE Trans. on Plasma Sci.*, vol. 41, no. 5, pp. 1201-1208, 2013.